# Robust Control
## for
# High Speed Atomic Force Microscopy

**Sajal K. Das**

A thesis submitted in fulfilment
of the requirements of the degree of
**Doctor of Philosophy**

Joint Supervisors:
**A/Prof. Hemanshu R. Pota & Prof. Ian R. Petersen**


**School of Engineering and Information Technology**
**University of New South Wales, Canberra**
**Australia**

November 2014

# Abstract

Atomic force microscopes (AFMs) are used in many nanopositioning applications in order to measure the topography of various specimens at an atomic level through surface imaging. The imaging of samples in AFMs is carried out by using a three degree-of-freedom positioning unit called a piezoelectric tube scanner (PTS). The majority of the commercially available AFMs use PTS for $x$, $y$ and $z$ positioning because of its simplicity, large achievable scan range (>100 µm) and smaller capacitance. In spite of having such good qualities, there are some limitations of the PTS which adversely affect the scanning speed and limit the overall performance of the AFM. The PTS of the AFM suffers from the problem of vibration, cross coupling effects between the axes of the scanner and nonlinear effects such as creep and hysteresis. This thesis presents several ways to compensate for the above mentioned problems of the PTS to improve the speed and accuracy of the PTS for high speed atomic force microscopy using robust control.

The first contribution of this dissertation is the design of damping controllers to compensate for the effect of vibrations induced by the PTS. The first design uses a damping controller namely the resonant controller to damp the first resonant mode of the scanner. The design of the controller is presented both in single-input single-output (SISO) and multiple-input multiple-output (MIMO) forms. Experimental results show that the resonant controller significantly damps the first resonant mode of the scanner. One of the limitations of the use of the resonant controller is its high pass nature. The high pass nature of the resonant controller may add high frequency sensor noise and destabilise the system if there are unmodelled high frequency dynamics.

In order to make the system robust to high frequency dynamics we next propose the design of a passive damping controller to damp the resonant modes of the scanner. The motivation to design a passive damping controller for the PTS is its bandpass nature. The bandpass nature of the passive damping controller not only reduces the addition of high frequency sensor noise but also results in large gain and phase margins. In order to design the passive damping controller for the PTS we have proposed a new analytical framework. The analytical framework examines the finite gain stability for a positive feedback interconnection between two stable linear

systems where one system has mixed negative-imaginary (NI), passivity, and small-gain properties and the other system has mixed NI, negative-passivity (NP) and small-gain properties. The closed-loop system with this passive damping controller is robust against changes in the plant dynamics. Although the closed-loop system using the passive damping controller is robust, the performance of this controller is not same for all possible changes in plant dynamics.

In order to achieve robust performance against changes in the plant dynamics, we propose another damping controller namely a minimax linear quadratic Gaussian (LQG) controller to compensate for induced vibrations in the PTS. This type of controller not only provides robust performance against changes in the plant dynamics but also results in large gain and phase margins. Due to its bandpass nature the minimax LQG controller also reduces the addition of high frequency sensor noise.

A second contribution of this thesis is the design of an integral minimax LQG controller to improve the tracking performance of the PTS. The tracking accuracy of the PTS is hampered due to the low resonance frequency of the PTS. Here, we have proposed the design of a minimax LQG controller with integral action to track the reference triangular signal used for raster scanning in most commercial AFMs. The design of the controller includes uncertainty which arises due to the spill over dynamics of the system at high frequencies. Experimental results are compared with an integral controller to demonstrate the effectiveness of the proposed controller. The experimental results show that the integral minimax LQG controller achieves four times better performance as compared to the integral controller.

The third and final contribution of this thesis is the design of a multi-variable controller for damping, tracking and cross coupling reduction of PTSs. At first we propose a design of multi-variable NI controllers for damping and cross coupling reduction of the PTS using a resonant and an integral resonant controller. Secondly, we propose a design of a double resonant controller with integral action to damp the resonant mode of the scanner, reduce the cross coupling effects of the scanner and improve the tracking performance of the PTS. The design of controllers in this case is done using a reference model matching approach.

In all cases a performance comparison is made by implementing the controllers on the PTS. Experimental results presented in the thesis show that the proposed controllers provide significant improvement in the performance of the AFM.

# Acknowledgements

During my stay in the period of my PhD research at the University of New South Wales, Canberra I have received lots of help and support from many peoples. I would like to take this opportunity to give my thanks to the following individuals.

Foremost, I would like to express my sincere gratitude and appreciation to my supervisors, Associate Professor Hemanshu Roy Pota and Professor Ian R. Petersen for their support, patience and encouragement throughout my PhD study. Their technical and editorial advice has been essential for the completion of this dissertation. It would not be possible for me to submit my PhD thesis without their assistance. Thanks to Associate Professor Hemanshu Roy Pota for his grateful review comments on my paper which made my paper more stronger. A special thanks to Professor Ian R. Petersen for managing and giving his time to me during the meetings and giving his valuable suggestions and comments on my works.

I am also grateful to Associate Professor Mark Pickering who was the panel chair in the review board during my Masters review. It was Associate Professor Mark Pickering who first offered me to do PhD instead of the Masters. Thanks to my supervisor Hemanshu Roy Pota for helping me a lot to take decision at that time. I would also like to give many thanks to Miss Masuma Akter for her suggestion and helping me to take decision for PhD instead of Masters. Miss Masuma Akter never told me to do Masters instead of the PhD. I thank Miss Masuma Akter again for her help in Matlab coding and other support in my whole PhD life.

I would like to thank my group mates Mr. Habibullah and Mr. Md. Sohel Rana for their discussions on system identification. On a personal note, I like to thank Md. Sohel Rana again for helping me during the application process of my PhD in Bangladesh. My special thanks to my dear friend Nahida Akter, her husband Dr. A. B. M. Nasiruzzaman and Dr. Apel Mahmud for their helpful activity during my arrival in Australia.

My sincere thanks to research associate Dr. Obaid Ur Rehman and Dr. Abhijit Kallapur for their valuable directions in the design of the minimax LQG controller for the piezoelectric tube scanner. My thanks to Dr. Mohamed Mabrok for his help in my research. My special and many many thanks to Engr. Shane Brandon for his assistance and lesson for the AFM system.

Furthermore, I want to extend my heartiest thanks to my current house mate and previous room mate Md. Humyun Fuad Rahman for giving me such a good company in my research. His contribution in cooking food for us during my PhD candidature is really appreciable. Thanks to him for being with me in every stage of my PhD life. I will surely miss his cooking and shopping.

Thanks to my previous house mates Md. Abdul Barik, Mohammad Omar Khyam, Md. Mahmudul Hasan and Md. Mohiuddin Ahmed for their support, patience and believe on me. My appreciation goes to all bengali community members for making my journey a memorable over the past few years. Words are not enough to express my thanks to each of the bengali community members for all the love and support that I have received over the years. Their expressions have brought joy to my heart and at times a tear to my eye.

On a personal note, I want to thank my parents Mr. Bishnu Chandra Das and Mrs. China Rani Das for their blessing, love and affection to me. I would also like to thank my lovely sister Miss Purnima Das for her calmness and believe on me.

Thanks to Sanjoy Paul, Sajib Saha, Mafruha M. Hossain Tarafder, Mehedi Hasan, Smita Tasneem for being with me and giving me support and recreation in the situations when I get depressed in my research. Their continuous support helps me a lot to concentrate on my research.

Finally I would like to extend my warmest thanks to the members of the SEIT, UNSW, Canberra for being with me throughout my entire PhD life. I would also like to thank UNSW, Canberra for their financial support in my research.

*Dedicated to my parents, sister*
*and*
*my supervisors.*

# List of Publications

## Refereed Book Chapters

1. Sajal K. Das, Hemanshu R. Pota and Ian R. Petersen, "Advanced Vibration Control of Atomic Force Microscope Scanner," *Advanced Intelligent Control Engineering and Automation*, IGI Global, USA, 2014.
2. Sajal K. Das, Hemanshu R. Pota and Ian R. Petersen, "Intelligent Tracking Control System for Fast Image Scanning of Atomic Force Microscopes", *Computational Intelligence applications in Modeling and Control*, Springer-Verlag, Germany, 2014.

## Refereed Journal Papers

3. Sajal K. Das, Hemanshu R. Pota and Ian R. Petersen, "Resonant Controller Design for a Piezoelectric Tube Scanner: A "Mixed" Negative-Imaginary and Small-Gain Approach," *IEEE Transactions on Control Systems Technology*, Vol. 22, no. 5, September 2014
4. Sajal K. Das, Hemanshu R. Pota and Ian R. Petersen, "Damping Controller Design for Nanopositioners: A Mixed Passivity, Negative-Imaginary and Small-Gain Approach", *IEEE/ASME Tansactions on Mechatronics*, In Press.
5. Sajal K. Das, Hemanshu R. Pota and Ian R. Petersen, "Multivariable Negative-Imaginary Controller Design for Damping and Cross Coupling Reduction of Nanopositioners: A Reference Model Matching Approach", *IEEE/ASME Tansactions on Mechatronics*, (Minor Revision).
6. Sajal K. Das, Hemanshu R. Pota and Ian R. Petersen, "A MIMO Double Resonant Controller Design for Nanopositioners", *IEEE Tansactions on Nanotechnology*, (Under Revision).
7. Sajal K. Das, Hemanshu R. Pota and Ian R. Petersen, "Design and Experimental Implementation of Integral Minimax LQG Controller for Tracking Control of Piezoelectric Tube Scanners ", *IEEE Tansactions on Control System Technology*, (Under Review).

8. Sajal K. Das, Hemanshu R. Pota and Ian R. Petersen, "A Test to Determine Mixedness of Mixed Passive, Negative-Imaginary and Small-Gain Systems with Poles on the Imaginary Axis and Stability Analysis ", *IEEE Tansactions on Automatic Control*, (Under Review).

## Refereed Conference Papers

9. Sajal K. Das, Hemanshu R. Pota and Ian R. Petersen, "Resonant Controller for Fast Atomic Force Microscopy," *Proceedings of the 51st IEEE Conference on Decision and Control*, 10–13 December, 2012, Maui, Hawaii, USA, pp. 2471–2476.
10. Sajal K. Das, Hemanshu R. Pota and Ian R. Petersen, "Multi-variable Resonant Controller for Fast Atomic Force Microscopy", *Proc. Australian Control Conference* , 15–16 Nov, 2012, Sydney, Australia, pp. 448–453.
11. Sajal K. Das, Hemanshu R. Pota and Ian R. Petersen, "Double Resonant Controller for Fast Atomic Force Microscopy", *Proc. Aisan Control Conference*, 23–26, June, 2013, Istanbul, Turkey, pp. 1–6.
12. Sajal K. Das, Hemanshu R. Pota and Ian R. Petersen, "Multi-Variable Double Resonant Controller for Fast Image Scanning of Atomic Force Microscope", *Proc. Aisan Control Conference*, 23–26, June, 2013, Istanbul, Turkey, pp. 1–6.
13. Sajal K. Das, Hemanshu R. Pota and Ian R. Petersen, "High Bandwidth Multivariable Combined Resonant and Integral Resonant Controller for Fast Image Scanning Atomic Force Microscope", *Proc. IEEE/ASME International Conference on Advanced Intelligent Mechatronics*, 9–12, July, 2013, Wollongong, Australia, pp. 838–843.
14. Sajal K. Das, Hemanshu R. Pota and Ian R. Petersen, "Velocity Feedback Controller for Piezoelectric Tube Scanner: A "Mixed" Negative-Imaginary and Small-Gain Approach", *Proc. Chinese Control Conference*, 26–28, July, 2013, Xian, China, pp. 5281–5286.
15. Sajal K. Das, Hemanshu R. Pota and Ian R. Petersen, "Resonant Control of Atomic Force Microscope Scanner: A "Mixed" Negative-Imaginary and Small-Gain Approach", *Proceedings of the American Control Conference*, 17–19 June, 2013, Washington, DC, USA, pp. 5476–5481.
16. Sajal K. Das, Hemanshu R. Pota and Ian R. Petersen, "Multi-variable Velocity

Feedback Controller for Piezoelectric Tube Scanner: A "Mixed" Negative-Imaginary and Small-Gain Approach", *Proc. Chinese Control Conference*, 26-28, July, 2013, Xian, China, pp. 5287–5292.

17. Sajal K. Das, Hemanshu R. Pota and Ian R. Petersen, "A Double VFC for Fast Image Scanning of Atomic Force Microscope", *Proc. IEEE Multi-conference on Systems and Control*, 28-30, August, 2013, Hyderabad, India, pp. 449–454.
18. Sajal K. Das, Hemanshu R. Pota and Ian R. Petersen, "Stability Analysis for Interconnected Systems with "Mixed" Passivity, Negative-Imaginary and Small-Gain Properties", *Proceedings of the Australian Control Conference*, 4-5 November, Perth, Australia, pp. 201–206.
19. Sajal K. Das, Hemanshu R. Pota and Ian R. Petersen, "Stability Analysis for Interconnected Systems with "Mixed" Negative-Imaginary and Passivity Properties", *Proceedings of the Australian Control Conference*, 4-5 November, Perth, Australia, pp. 445–449.
20. Sajal K. Das, Hemanshu R. Pota and Ian R. Petersen, "A MIMO Controller Design for Damping, Tracking, and Cross Coupling Reduction of Nanopositioners", *Proceedings of the Australian Control Conference*, 4-5 November, Perth, Australia, pp. 467–472.
21. Sajal K. Das, Hemanshu R. Pota and Ian R. Petersen, "A New Robust Damping and Tracking Controller for High Speed Nanopositioning", *Proceedings of the Australian Control Conference*, 4-5 November, Perth, Australia, pp. 473–478.
22. Sajal K. Das, Hemanshu R. Pota and Ian R. Petersen, "Passive Damping Controller Design for Nanopositioners", *Proceedings of the American Control Conference*, 4-6 June, 2014, Portland, USA.
23. Sajal K. Das, Hemanshu R. Pota and Ian R. Petersen, "Minimax LQG Controller Design for Nanopositioners", *Proceedings of the European Control Conference*, 24-27 June, 2014, Strasbourg, France.

# Contents


Copyright Statement i

Authenticity Statement ii

Originality Statement iii

Abstract iv

Acknowledgements vi

List of Publications ix

List of Symbols xxiv

Chapter 1 Introduction 1
- 1.1 Thesis Objectives . . . 2
- 1.2 Thesis Outlines . . . 3

Chapter 2 Atomic Force Microscopy 5
- 2.1 Introduction . . . 5
- 2.2 Operating Principle of the AFM . . . 7
- 2.3 Operating Modes of the AFM . . . 10
  - 2.3.1 Contact mode . . . 10
  - 2.3.2 Non-contact mode . . . 12
  - 2.3.3 Tapping mode . . . 14
- 2.4 Piezoelectric Tube Scanner . . . 16
- 2.5 Limiting Factors for High Speed Nanopositioning of the PTS . . . 21
  - 2.5.1 Hysteresis . . . 22
  - 2.5.2 Creep . . . 24
  - 2.5.3 Induced vibration . . . 24
  - 2.5.4 Cross coupling . . . 25
- 2.6 Chapter Summary . . . 26

Chapter 3 Resonant Control of Piezoelectric Tube Scanners 30
3.1 Introduction . . . 31
3.2 Experimental Setup . . . 33
3.3 System Identification . . . 34
3.4 Controller Design . . . 38
3.5 Selection of the Controller Parameters and Stability of the Closed-loop System . . . 41
3.6 Experimental Verification . . . 43
3.7 Chapter Summary . . . 46

Chapter 4 Passive Damping Controller Design for Piezoelectric Tube Scanners 49
4.1 Introduction . . . 49
4.2 Mathematical Definitions of Systems . . . 53
4.3 Test for Determining Mixedness of a System Using Hamiltonian Matrices . . . 55
4.3.1 NI test for multiple-input multiple-output (MIMO) LTI systems 55
4.3.2 Passivity test for MIMO LTI systems . . . 57
4.3.3 Test procedures . . . 58
4.4 Interconnection of Two Mixed Systems with Positive Feedback . . . 59
4.5 Numerical Example . . . 64
4.5.1 Test for mixedness . . . 64
4.5.2 Stability analysis . . . 65
4.6 Passive Damping Controller Design . . . 66
4.7 Performance of the Controller . . . 67
4.8 Chapter Summary . . . 71

Chapter 5 Minimax LQG Control of Piezoelectric Tube Scanners 75
5.1 Introduction . . . 76
5.2 System Identification and Problem Formulation . . . 77
5.2.1 Dynamics of the piezoelectric tube scanner . . . 77
5.2.2 Uncertainty modelling . . . 80
5.2.3 Weighting transfer function selection . . . 82
5.3 Minimax LQG Control Theory . . . 83
5.4 Controller Design and Selection . . . 87
5.5 Performance of the Controller . . . 89

5.6 Integral Minimax LQG Control Theory . . . . . 92
5.7 Performance of the Integral Minimax LQG Controller . . . . . 99
5.8 Chapter Summary . . . . . 105

Chapter 6 Damping, Tracking and Cross Coupling Reduction of Piezoelectric Tube Scanners 106
6.1 Introduction . . . . . 107
6.2 System Identification . . . . . 107
6.3 Controller Design . . . . . 111
6.3.1 Design of IRC and combined IRC with the resonant controller 114
6.3.2 Design of the MIMO controller . . . . . 116
6.4 Performance of the Controllers . . . . . 118
6.5 Discussion and Advantages of the Proposed Method Over the Existing Approaches . . . . . 127
6.6 Double Resonant Controller Design . . . . . 128
6.6.1 Comparison of performances between the proposed SISO and MIMO double resonant controller . . . . . 131
6.7 Chapter Summary . . . . . 135

Chapter 7 Conclusions 138

# List of Tables

4.1 Open- and closed-loop bandwidth and gain margin for different loads on the scanner together . . . . . 71
6.1 Advantage of the proposed method over the existing approaches . . . 128

# List of Figures


2.1 Block diagram of the AFM working principles. . . . . 8
2.2 Force vs. distance curve in contact mode of the AFM imaging. . . . . 13
2.3 Plot of force as a function of probe-sample separation. . . . . 15
2.4 A typical illustration of a piezoelectric tube scanner. (a) Side view and (b) top view. . . . . 17
2.5 Piezoelectric tube scanner used in the experiment. . . . . 19
2.6 Raster scanning method in AFM imaging. (a) Triangular signal applied to $x$-axis, (b) staircase signal applied to $y$-axis and (c) raster scanning method. . . . . 20
2.7 Hysteresis terminology. . . . . 21
2.8 Effect of hysteresis in imaging. (a) Measured scanners's displacements (solid line) for a 10 Hz triangular signal input (dashed line), (b) the resulting image of a calibration grating sample. . . . . 23
2.9 Effect of creep in AFM imaging. . . . . 25
2.10 Effect of vibration on the PTS. Scanner displacements when driven by (a) 10 Hz, (b) 100 Hz, (c) 150 Hz and (d) 200 Hz triangular wave signals. . . . . 26
2.11 Open-loop scanned images (a) 15.62 Hz (b) 31.25 Hz (c) 62.5 Hz (d) 125 Hz. . . . . 27
2.12 Effect of cross coupling in AFM imaging. (a) Required $x$ sensor output, (b) required $y$ sensor output, (c) $x$ sensor output with cross coupling, (d) $y$ sensor output with cross coupling, and (e) raster scanning without the cross coupling effect, and (f) raster scanning with the cross coupling effect. . . . . 28
3.1 Experimental setup used in the present work. . . . . 34
3.2 Measured (– the solid line) and identified model (- - the dashed line) frequency responses of $G_{xx}(s)$ . . . . . 35

3.3 Open-loop frequency responses relating the inputs $[V_x, V_y]^T$ and the outputs $[D_x, D_y]^T$. The solid line (–) represents the measured frequency responses and the dashed line (- -) represents the identified model frequency responses. (a) Frequency response of $G_{xx}(s)$, (b) frequency response of $G_{yx}(s)$, (c) frequency response of $G_{xy}(s)$, and (d) frequency response of $G_{yy}(s)$. . . . . 36
3.4 Minimum eigenvalues of $j(G(j\omega) - G^*(j\omega))$. . . . . 37
3.5 Closed-loop system with resonant controller. . . . . 38
3.6 Frequency intervals in the SISO design (NI: negative-imaginary, FG1: finite-gain for system $M_1$, FG2: finite-gain for system $M_2$). . . . . 39
3.7 Maximum singular value ($\bar{\sigma}(G(j\omega))$) plot of $M_1(s)$. . . . . 40
3.8 Frequency intervals in the MIMO design (NI: negative-imaginary, FG1: finite-gain for system $M_1$, FG2: finite-gain for system $M_2$). . . . 41
3.9 Measured open- (– the solid line) and closed-loop (- - the dashed line) frequency responses of the plant output for SISO design. . . . . 42
3.10 Measured magnitude frequency responses relating the inputs $[V_x, V_y]^T$ and the outputs $[D_x, D_y]^T$. The solid line (–) represents the measured open-loop frequency responses and the dashed line (- -) represents the measured closed-loop frequency responses. (a) Frequency response of $G_{xx}(s)$, (b) frequency response of $G_{yx}(s)$, (c) frequency response of $G_{xy}(s)$, and (d) frequency response of $G_{yy}(s)$. . . . . 44
3.11 Open- (red solid line) and closed-loop (black solid line) X sensor output signals for (a) 50 Hz, (b) 100 Hz, (c) 150 Hz, and (d) 200 Hz triangular input signals in SISO design. . . . . 45
3.12 Open- (- - the dashed line) and closed-loop (– the solid line) X sensor output signals for (a) 1 Hz, (b) 10 Hz, (c) 50 Hz, and (d) 100 Hz pulse input signals in SISO design. . . . . 46
3.13 Loop-gains $M_1(j\omega)M_2(j\omega)$ for SISO cases when the resonant controller is designed using the small-gain only approach (– the solid line) and the mixed negative-imaginary and small-gain approach (- - the dashed line). . . . . 47

3.14 Measured open- (– the solid line) and closed-loop frequency responses of $G_{xx}(s)$ for SISO case when the resonant controller is designed using the small-gain approach (-. dashed dot line) and the mixed negative-imaginary and small-gain approach (- - the dashed line). . . . . 48
4.1 Interconnection of systems with positive feedback. . . . . 50
4.2 (a) Nyquist diagram of $M_1(s)$ of (4.1) for positive frequencies, (b) Nyquist diagram of $M_2(s)$ of (4.2) for positive frequencies. . . . . 52
4.3 Magnitude Bode diagram of $M_1(s) * M_2(s)$. . . . . 53
4.4 Frequency intervals (NI1: negative-imaginary region for system $M_1(s)$, NP1: negative-passive region for system $M_1(s)$, P1: Passive region for system $M_1$, FG1: finite-gain region for system $M_1(s)$, NI2: negative-imaginary region for system $M_2(s)$, NP2: negative-passive region for system $M_2(s)$, FG1: finite-gain region for system $M_2(s)$). . . . . 64
4.5 Open- (the solid line –) and closed-loop (the dashed line - -) magnitude frequency response of $M_{xx}(s)$ . . . . . 68
4.6 Magnitude Bode diagram of the controller. . . . . 68
4.7 Open- (blue solid line) and closed-loop (red solid line) X sensor output signals for (a) 1 Hz, (b) 10 Hz, (c) 50 Hz, and (d) 100 Hz triangular input signals. . . . . 69
4.8 Open- ( blue solid line – ) and closed-loop ( red dashed line - - ) X sensor output signals for (a) 1 Hz, (b) 10 Hz, (c) 50 Hz, and (d) 100 Hz pulse input signals. . . . . 70
4.9 Robustness analysis of the interconnected systems for different loads L1, L2 and L3 on the scanner. . . . . 72
4.10 Loop-gains $M_1(j\omega)M_2(j\omega)$ when the controller is designed using the small-gain only approach (. . the dotted line) and the proposed analytical framework (– the solid line). . . . . 72
4.11 Measured open- (the solid line –) and closed-loop frequency responses in the X-axis of the scanner using proposed approach (the dashed dot line -.) and small-gain only approach ( the dashed line - -). . . . . 73
5.1 Uncertainty representation between $G_1(j\omega)$ and $G_2(j\omega)$. . . . . 78
5.2 Comparisons between the two measured frequency responses of $G_1(j\omega)$ and $G_2(j\omega)$ obtained at different times. . . . . 79

5.3 Comparisons between the measured and identified frequency responses of $[G_1(j\omega) + G_2(j\omega)]/2$. The blue solid line represents frequency response obtained from the measured $G_1(j\omega)$ and $G_2(j\omega)$ and the red solid represents the identified model frequency response. . . . . 81
5.4 System representation with uncertainty. . . . . 82
5.5 Multiplicative uncertainty bound. The dotted (. .) line represents $\frac{max\{|G_m(j\omega)-G_1(j\omega)|,|G_m(j\omega)-G_2(j\omega)|\}}{|G_m(j\omega)|}$ and the solid line represents $|W_m(j\omega)|$. 84
5.6 Block diagram of uncertain stochastic system. . . . . 85
5.7 $W_\tau$ versus $\tau$. . . . . 88
5.8 Measured uncontrolled open-loop (blue and red solid line) and controlled closed-loop (black solid line) magnitude frequency responses. . 89
5.9 Bode diagram of the minimax LQG controller for damping. . . . . 90
5.10 Bode diagram of the identified loop-gain. . . . . 91
5.11 Nyquist diagram of the identified loop-gain for positive frequencies. . 92
5.12 Measured open-loop (blue solid line) and closed-loop (red solid line) sensor output signals with a triangular wave reference input using minimax LQG controller. . . . . 93
5.13 Measured open-loop (blue solid line) and closed-loop (red solid line) responses with a square wave reference input using minimax LQG controller. . . . . 94
5.14 Block diagram of uncertain stochastic uncertain system. . . . . 95
5.15 $W_\tau$ versus $\tau$ for designing integral minimax LQG controller. . . . . 97
5.16 Comparison of Bode diagram between the high and low order integral minimax LQG controller. . . . . 98
5.17 Setup to measure the closed-loop response. . . . . 99
5.18 Open- and closed-loop magnitude frequency response using integral minimax LQG controller in the X-axis of the scanner. The solid line (–) represents the open-loop magnitude frequency response and the dashed line (- -) represents the closed-loop magnitude frequency response. . . . . 100
5.19 Open-loop X-sensor output for 8 µm × 8 µm scanning area at (a) 50 Hz, (b) 100 Hz, (c) 200 Hz. . . . . 101
5.20 Closed-loop X-sensor output for 8 µm × 8 µm scanning area at (a) 50 Hz, (b) 100 Hz, (c) 200 Hz using integral minimax LQG controller. 102

5.21 Closed-loop system for the implementation of the integral controller. . 103
5.22 Performance of integral controller for different gains of the integral controller. . . . . 103
5.23 Tracking error at (a) 50 Hz, (b) 100 Hz, (c) 200 Hz. The solid line (–) is the tracking error obtained by using the integral minimax LQG controller and the dashed line (- -) is the tracking error obtained by using the integral controller. . . . . 104
6.1 The measured and the identified model frequency response of $G_{xx}(s)$. The dashed line (- -) represents the identified model response and the solid line (–) represents the measured frequency response. . . . . 108
6.2 Open-loop frequency responses relating to the inputs $[V_x, V_y]^T$ and the outputs $[D_x, D_y]^T$. The solid line (–) represents the measured frequency responses and the dashed line (- -) represents the identified model frequency responses of (6.2). (a) Frequency response of $G_{xx}(s)$, (b) frequency response of $G_{yx}(s)$, (c) frequency response of $G_{xy}(s)$, and (d) frequency response of $G_{yy}(s)$. . . . . 109
6.3 Block diagram of the integral resonant control scheme. (a) illustrative version, (b) simplified version. . . . . 110
6.4 Block diagram of closed-loop system with IRC $C(s)$ and resonant controller $R(s)$. . . . . 111
6.5 Root locus plot of (a) $(G_{xx}(s)+d)*\frac{K}{s}$ with d=1.3 for $K>0$ and (b) root locus plot of $G_{xx}(s)*\frac{K}{s}$ for $K<0$, and (c) root locus plot of $G_{xx}(s)*\frac{K}{s}$ for $K>0$. . . . . 112
6.6 Comparisons between the identified open- (the dashed line - -) and closed-loop (the solid lines –) frequency responses of $G_{xx}(s)$ using IRC for $K = i \times 1.85 \times 10^4$ where $i$=1 to 5 and $d = 1.3$. . . . . 115
6.7 Comparisons of the measured closed-loop frequency responses obtained by implementing SISO IRC (solid line –) and combined SISO resonant controller and IRC (dashed line - -). . . . . 115

6.8 Comparison of the open-loop and closed-loop frequency response (FR) relating to the inputs $[V_x, V_y]^T$ and the outputs $[D_x, D_y]^T$. The solid line (–) represents the measured open-loop FR and the dashed line (- -) represents closed-loop FR obtained by implementing proposed combined SISO resonant and IRC and the dashed dot line (- .) represents closed-loop FR obtained by implementing proposed combined MIMO resonant and IRC. (a) Frequency response of $G_{xx}(s)$, (b) frequency response of $G_{yx}(s)$, (c) frequency response of $G_{xy}(s)$, and (d) frequency response of $G_{yy}(s)$. . . . . 117

6.9 Scanned images at 15.62 Hz obtained by using (a) open-loop, (b) built-in PI controller of the AFM, (c) proposed combined SISO IRC and resonant controller and (d) proposed combined MIMO IRC and resonant controller. . . . . 119

6.10 Scanned images at 31.25 Hz obtained by using (a) open-loop, (b) built-in PI controller of the AFM, (c) proposed combined SISO IRC and resonant controller and (d) proposed combined MIMO IRC and resonant controller. . . . . 120

6.11 Scanned images at 62.5 Hz obtained by using (a) open-loop, (b) built-in PI controller of the AFM, (c) proposed combined SISO IRC and resonant controller and (d) proposed combined MIMO IRC and resonant controller. . . . . 121

6.12 Scanned images at 125 Hz obtained by using (a) open-loop, (b) built-in PI controller of the AFM, (c) proposed combined SISO IRC and resonant controller and (d) proposed combined MIMO IRC and resonant controller. . . . . 122

6.13 Error images obtained by using the combined SISO resonant and IRC (left) and the combined MIMO resonant and IRC (right). Error image (a) (left) obtained by subtracting Fig. 6.9(c) and 6.10(c), (right) obtained by subtracting Fig. 6.9(c) and 6.11(c) and (b) (left) obtained by subtracting Fig. 6.9(d) and 6.10(d), (right) obtained by subtracting Fig. 6.9(d) and 6.11(d) . . . . . 125

6.14 Cross-section (solid line –) and reference (dash line - -) curves of the AFM images of the Z-direction calibration grid of the sample obtained by using (right) proposed combined SISO resonant and IRC and obtained by using (left) proposed combined MIMO resonant and IRC at (a) 15.62 Hz, (b) 15.62 Hz, (c) 31.25 Hz, (d) 31.25 Hz, (e) 62.50 Hz, (f) 62.50 Hz, (g) 125 Hz, (h) 125 Hz. . . . . 126
6.15 Open-loop (dashed-line) and closed-loop (solid-line) magnitude frequency response (MFR) from the reference input voltage in the X-axis of the scanner to the measured X sensor voltage for different loads on the scanner. The same color represents the corresponding open- and closed-loop MFR. . . . . 127
6.16 Block diagram of the closed-loop system for resonant mode damping, tracking and bandwidth improvement. . . . . 129
6.17 Comparison of the open- and closed-loop magnitude frequency responses (MFRs) relating the inputs $[V_x, V_y]^T$ and the outputs $[D_x, D_y]^T$ obtained by using the proposed SISO and MIMO double resonant controller of the scheme of Fig. 6.16. The solid line (–) represents the open-loop system MFR, the dashed line (- -) represents closed-loop MFR obtained by using the SISO double resonant controller, and the dashed dot line (-.) represents closed-loop MFR obtained by using the MIMO double resonant controller. . . . . 130
6.18 Open-loop (solid line) (a) and closed-loop (dashed line) magnitude frequency responses (MFRs) of $G_{xx}(s)$ using SISO (b) and MIMO (c) double resonant controller for different loads on the scanner. . . . . 132
6.19 Scanned images obtained by using the proposed SISO double resonant controller at (a) 15.62 Hz, (b) 31.25 Hz, (c) 62.5 Hz, and (d) 125 Hz for 8 µm×8 µm area scanning. . . . . 133
6.20 Scanned images obtained by using the proposed MIMO double resonant controller at (a) 15.62 Hz, (b) 31.25 Hz, (c) 62.5 Hz, and (d) 125 Hz for 8 µm×8 µm area scanning. . . . . 134

6.21 Comparison of error images obtained by using SISO and MIMO double resonant controller. (a) (left) obtained by subtracting Fig. 6.19 (a) and 6.19 (b), (right) obtained by subtracting Fig. 6.19 (a) and 6.19 (c); (b) (left) obtained by subtracting Fig. 6.20 (a) and 6.20 (b), (right) obtained by subtracting Fig. 6.20 (a) and 6.20 (c). . . . . 136

6.22 Comparison of errors signals between input and output signals the using SISO and MIMO double resonant controller for (a) 15.62 Hz, (b) 31.25 Hz, (c) 62.5 Hz, and (d) 125 Hz input signals. The solid line (–) represents the errors obtained using the SISO controller and the dashed line (- -) represents the errors obtained using the MIMO controller. A small phase shift is purposely added to clearly show the plots. . . . . 137

# List of Symbols

**Symbols**

| | |
|---|---|
| $\bar{\sigma}(A)$ | Largest singular values of a matrix $A$ |
| $\underline{\sigma}(A)$ | Smallest singular values of a matrix $A$ |
| $G(s)$ | Transfer function of a system |
| $G^*(s)$ | Complex conjugate transpose of the matrix $G(s)$ |
| $G_{xx}(s)$ | Transfer function of the PTS in the X-axis |
| ${\mathcal{L}_\infty}^{m\times n}$ | Banach space of matrices |
| $\mathcal{R}^{m\times n}$ | Set of all real rational transfer function matrices |
| $\mathcal{RH}_\infty^{m\times n}$ | Set of all real rational stable transfer functions matrices with $m$ rows and $n$ columns |
| ${\mathcal{RL}_\infty}^{m\times n}$ | Set of all proper, real-rational transfer function matrices with no pole in the origin |

**Abbreviations and Acronyms**

| | |
|---|---|
| AFM | Atomic Force Microscope |
| DSA | Digital signal analyser |
| dSPACE | Digital Signal Processing and Control Engineering |
| FG | Finite-gain |
| FR | Frequency response |
| HVA | High voltage amplifier |
| LQG | Linear Quadratic Gaussian |
| MFM | magnetic force microscope |
| MFR | magnitude frequency response |
| MIMO | Multiple input multiple output |
| NI | Negative-imaginary |
| PI | Proportional Integral |
| PTS | Piezoelectric Tube Scanner |
| SAM | Signal Access Module |
| SG | Small-gain |
| SISO | Single-input single-output |
| SPM | Scanning Probe Microscope |
| STM | Scanning Tunneling Microscope |

# Chapter 1

# Introduction

Scanning probe microscopy (SPM) [1] refers to a group of imaging techniques that collect images of sample surfaces through scanning [2,3]. Many types of SPM systems such as the scanning tunneling microscope (STM) [2, 3], atomic force microscope (AFM) [4–6], and magnetic force microscope (MFM) [7] are used to view sample surfaces. The SPM was invented in the form of the STM. The STM uses only conducting samples to scan which limits the use of STM for non-conducting samples. This led to the invention of the AFM. The AFM is a type of SPM system which is used to measure the topography of various specimens down to an atomic level. The AFM generates three dimensional images of both conducting and non-conducting samples in vacuum and non-vacuum environments. In the AFM imaging process the sample is placed on a positioning unit termed a nanopositioner. The nanopositioner is designed to achieve fine mechanical displacements at an atomic scale [3, 8, 9].

Different types of nanopositioners such as piezoelectric tube scanners (PTSs) [4–6], serial-kinematic [10], and flexure based [11] are used in SPM systems depending on the applications. The nanopositioners used in most commercial SPM systems are of two types and the types are (a) the scan-by-sample [4] and (b) the scan-by-head [12]. Both types of nanopositioners are equally used in nanopositioning applications. In the case of the scan-by-sample the scanner moves during the operation whereas the scan-by-head scanner remains fixed during operation [4, 12].

Nanopositioners are designed to cover a large scanning area which is accomplished by having a large length-to-diameter ratio of the nanopositioner [4, 13–15]. A major disadvantage of having a large length-to-diameter ratio is the low mechanical resonance frequency of the scanner [15]. In practice, in most cases, the nanopositioner is actuated in a raster pattern, which uses a triangular signal in the fast axis, i.e., the X-axis of the scanner [9,16]. One of the disadvantages of using the triangular signal in the X-axis of the scanner is that the triangular signal contains all odd harmonics of its fundamental frequency [4, 13]. Therefore, when PTSs are actuated by a triangular signal, the odd harmonics of the fundamental frequency of the triangular signal excites the mechanical resonance of nanopositioners. This

excitation of the resonant modes of nanopositioners results in a loss of precision positioning in the scanner [13–15].

Nanopositioners used in SPM systems are multiple-input multiple-output (MIMO) systems. There exists a cross coupling [17] between the lateral and longitudinal axes of the piezo scanner. Due to these cross coupling effects, signal applied to one of the axes of the scanner results in a displacement in both axes of the scanner. If the magnitude of the cross coupling is high then the X and Y sensors show modulated triangular signals, i.e., triangular signals with the addition of staircase signals in both sensor outputs. The resulting images generated from SPMs are rotated if the magnitude of the cross coupling is high.

The precision positioning of nanopositioners is also affected due the nonlinear behavior of the piezoelectric actuator. The nonlinear behavior of the nanopositioner can be observed in the hysteresis and creep effects. Hysteresis arises in applications such as PTSs, hard disk drives. The hysteresis nonlinearity of a piezoelectric actuator affects the positioning accuracy of the piezo scanner. The effects of hysteresis become visible in PTSs with an increase of the frequency or amplitude of the applied voltage signals [6]. A deviation of 15% between the forward and backward movements of the applied signal can occur due to the effect of hysteresis [15, 18].

## 1.1 Thesis Objectives

The main objective of this research is to improve the high speed positioning performance of a PTS using a feedback control approach. The first barrier for high speed nanopositioning of the PTS is its induced vibration. The positioning performance of the PTS is greatly affected due to the induced vibration. The first aim of this thesis is the design of a damping controller to damp the resonant modes of the scanner to compensate for the effect of induced vibration. The work done in regard to the design of the damping controller in this thesis is listed below:

1. Resonant controller design for PTSs: a mixed negative-imaginary and small-gain approach;
2. Passive damping controller design for PTSs: a mixed passivity, negative-imaginary and small-gain approach; and
3. Minimax linear quadratic Gaussian (LQG) controller design for PTSs.

The second obstacle for high speed nanopositioning of the PTS is its low tracking performance at high scanning rates. The tracking bandwidth of the PTS is limited

to one percent of its first resonance frequency. The tracking performance is largely affected by the excitation of the mechanical resonant mode of the scanner. The second objective of this research is the design of a tracking controller to improve the tracking performance of the PTS for high speed nanopositioning. This thesis proposes a design of an integral minimax LQG controller to track the triangular reference signal. The second work of this thesis is given below:

1. Integral minimax LQG controller design for tracking control of PTSs.

The third obstacle for high speed nanopositioning of the PTS is the cross coupling effect between the axes of the scanner. The third and final aim of this research is the design of multivariable controllers to attenuate the cross coupling effect between the axes of the scanner. The works in this regard is listed below:

1. Multivariable negative-imaginary controller design for damping and cross coupling reduction of PTSs;
2. Multivariable double resonant controller design for robust damping, tracking and cross coupling reduction of PTSs.

## 1.2 Thesis Outlines

This thesis begins with an introduction to the atomic force microscopy system in Chapter 2. Firstly, it includes a description of the working principles and various operating modes of the AFM. The PTS is considered as the heart of the AFM system. In this chapter a detail introduction to the construction and mechanics of the PTS is discussed. This is then followed by an in-depth discussion of the factors, namely scan induced vibration, hysteresis and creep, that limit the precision positioning of the PTS for high speed nanopositioning.

Chapters 3, 4 and 5 form the first part of this thesis. The first objective of this research is to compensate for the scan-induced vibrations of the PTS. In these chapters we have discussed the design of three damping controllers to compensate for the vibration of the PTS. The first design is the design of a resonant controller for the PTS to damp the first resonant mode of the PTS. The design of the resonant controller for the PTS is presented based on a mixed negative-imaginary and small-gain approach. The resonant controller design is presented both as a single-input single-output (SISO) and multiple-input multiple-output (MIMO) system. The second contribution discussed in Chapter 4 is the design of a passive damping controller for the PTS to damp the first resonant mode of the scanner. This time the design

of the passive damping controller is based on a mixed passivity, negative-imaginary and small-gain approach. In this regard we have proposed a new analytical framework that establishes the finite-gain stability for a positive feedback interconnection between two stable, linear time-invariant systems where one system has mixed passivity, negative-imaginary and small-gain properties and the other system has mixed negative-imaginary, negative-passivity, and small-gain properties. The third contribution in regard to the design of damping controller is proposed in Chapter 5. First Chapter 5 proposes the design of a minimax linear quadratic Gaussian (LQG) controller to damp the first resonant mode of the scanner. The motivation for designing different damping controllers for the PTS is also discussed in these chapters.

The second objective of this thesis is also addressed in Chapter 5. The objective is to design a tracking controller to improve the high speed tracking performance of the PTS for raster scanning. Here we propose the design of a minimax LQG controller with integral action for tracking control of PTSs.

Chapter 6 focuses on the third objective of this thesis. The third objective of this thesis is to compensate for the effect of cross coupling between the axes of the scanner. In order to do so we propose the design of multi-variable controllers for robust damping, tracking and cross coupling attenuation in the PTS. The design of the controllers is presented based on a reference model matching approach.

Chapter 7 presents the concluding remarks and a note on proposed future work.

# Chapter 2

# Atomic Force Microscopy

This chapter presents an overview of the basic principles of the AFM used in this thesis. The first section of this chapter briefly discusses the various kinds of SPMs and their applications to measure surface topography. Section 2.2 describes the operating principle of the AFM. This includes the description and operation of each component used in the AFM. Section 2.3 presents the various operating modes of the AFM used to measure the properties of the sample. In Section 2.4, a detailed description of the main component of this thesis, i.e., the piezoelectric tube scanner (PTS) is presented. This description includes the electrical and mechanical behavior of the PTS and the construction and mechanics of the scanner. Section 2.5 summarizes the limiting factors of the PTS for high speed nanopositioning. A detailed discussion on these limiting factors, namely induced vibration, coupling effect, nonlinearities such as hysteresis, is presented in this section. Finally the chapter is concluded with a summary.

## 2.1 Introduction

Nanotechnology is the branch of science which deals with the manipulation of matters on an atomic level. Nanotechnology as defined by size is naturally very broad, including fields of science as diverse as surface science, organic chemistry, molecular biology, semiconductor physics, and microfabrication. The viewing of surface texture at an atomic level with high resolution was a great challenge until the introduction of the scanning tunneling microscope (STM) [2, 3, 19, 20]. The STM was developed by Gerd Binning and his colleagues in 1981 at the IBM Zurich Research Laboratory in Switzerland [2, 3]. The STM was the first SPM technique capable of directly obtaining three-dimensional (3-D) images of solid surfaces. The discovery of the STM has brought a Nobel Prize to Binning and Rohrer in Physics in 1986. The STM can only be used to measure the topography of surfaces which are electrically conductive to some degree. This limits the use of the STM for the surfaces which are non-conductive in nature.

The invention of the AFM has opened a new era in the field of nanotechnology to study non-conductive sample surfaces. The AFM is used to measure the topography of surfaces, whether it is electrically conductive or insulating. The invention of the AFM has also led to the invention of a family of scanning probe microscopy techniques. These include scanning electrostatic force microscopy [21], scanning force acoustic microscopy (or atomic force acoustic microscopy (AFAM)) [22, 23], magnetic force microscopy [24, 25], scanning near field optical microscopy [26, 27], scanning thermal microscopy [28, 29], scanning electromechanical microscopy [30], scanning Kelvin probe microscopy [31, 32], scanning chemical potential microscopy [33], scanning ion conductance microscopy [34, 35] and scanning capacitance microscopy [36, 37].

The reason for calling them SPMs is because of the use of a probe in these devices for investigation and manipulation of matter. The commercial use of the SPM was started in 1987 with the STM and in 1989 with the AFM by Digital Instruments Inc. The basic stages for the development of the SPM system is as follows:

1. 1981- *Scanning tunneling microscope.* G. Binning ang H. Rohrer. Atomic resolution images of conducting surfaces.
2. 1982- *Scanning near-field optical microscope.* D. W. Pohl. Resolution of 50 nanometers in optical images
3. 1984- *Scanning capacitive microscope.* J. R. Matey, J. Blanc. 500 nm (lateral resolution) images of capacitance variation.
4. 1985- *Scanning thermal microscope.* C. C. Williams, H. K. Wickramasinghe. Resolution of 50 nm in thermal images.
5. 1986- *Atomic force microscope.* G. Binning, C. F. Quate, Ch. Gerber. Atomic resolution on non-conducting (and conducting) samples.
6. 1987- *Magnetic force microscope.* Y. Martin, H. K. Wickramasinghe. Resolution of 100 nm in magnetic images.
7. 1988- *Inverse photoemission microscope.* J. H. Coombs, J. K. Gimzewski, B. Reihl, J. K. Sass, R. R. Schlittler. Detection of luminescence spectra on nanometer scales.
8. 1989- *Near-field acoustic microscope.* K. Takata, T. Hasegawa, S. Hosaka, S. Hosoki, T. Komoda. Low frequency acoustic measurements with the resolution of 10 nanometers.

9. 1990- *Scanning chemical potential microscope.* C. C. Williams, H. K. Wickramasinghe. Atomic scale images of chemical potential variation.
10. 1991- *Kelvin probe force microscope.* N. Nonnenmacher, M. P. O'Boyle, H. K. Wickramasinghe. Measurements of surface potential with 10 nm resolution.
11. 1994- *Apertureless near-field optical microscope.* F. Zenhausern, M. P. O'Boyle, H. K. Wickranmasinghe. Optical microscopy with 1 nm resolution.

## 2.2 Operating Principle of the AFM

The AFM is a very high-resolution type of SPM with demonstrated resolution on the order of a fraction of a nanometer. The STM can investigate only the conductive or semi-conductive samples. This disadvantage was overcome by the invention of the AFM. Like the STM, the AFM relies on a scanning technique to produce very high resolution 3-D images of sample surfaces. The AFM is based upon the principle of sensing the forces between a sharp tip and the surface to be investigated. The forces can be attractive or repulsive depending on the operating modes. When tip to sample distance is large the interactive force is attractive and when the tip to sample distance is small the interactive force is repulsive. The forces are measured by measuring the motion of a very small cantilever beam. During the operation of the AFM the sample is scanned instead of the tip (unlike the STM) because the AFM measures the relative displacement between the cantilever surface and the reference surface.

A schematic of the AFM is presented in Fig. 2.1. The basic components include a micro-cantilever with a sharp tip mounted on a micromachined cantilever, a positioning unit, a laser source, and a laser photodetector. In the imaging process of the AFM, a sample is placed on a positioning unit. There are different types of positioning units used in the AFM such as piezoelectric tube scanners, serial-kinematic scanners, flexure based scanners. The choice of the positioning unit depends on the application of the AFM. A detail discussion on the various types of the positioning unit used in the AFM is given later. The displacement of the positioning unit during the imaging is measured by sensor. In most of the cases capacitive sensors are used to measure the displacement of the scanner.

When the sample is placed on the positioning unit, a cantilever beam with a sharp tip is brought in close proximity of the sample. Various types of cantilevers are used in the AFM. The cantilever used in the AFM should meet the following

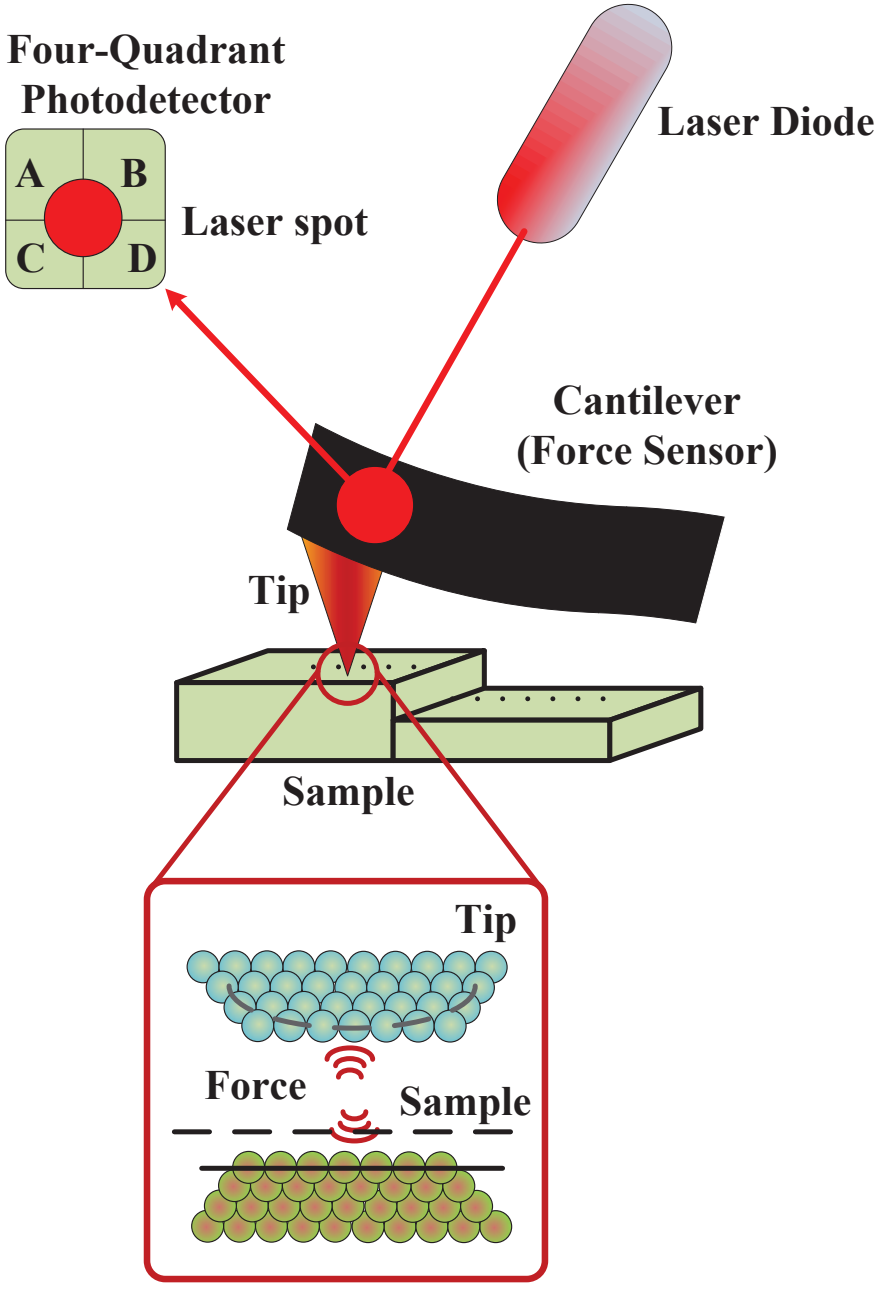


**Figure 2.1:** Block diagram of the AFM working principles.

criteria: (1) low normal spring constant (stiffness); (2) high resonant frequency; (3) high cantilever quality factor Q; (4) high lateral spring constant (stiffness); (5) short cantilever length; (6) incorporation of components (such as mirror) for deflection sensing; and (7) a sharp protruding tip. The cantilevers used in the AFM system also have different shapes and in most of the cases a tip is attached with the cantilever.

In order to achieve a large imaging bandwidth the cantilever should have a high resonant frequency. The Youngs modulus and the density are the material parameters that determine the resonant frequency, aside from the geometry. This makes the cantilever the least sensitive part of the system. In order to register a measurable deflection with small forces it is also required that the cantilever should have low spring constant. The combined requirement of having a high resonance frequency and a low spring constant is met by reducing the mass of the cantilever. The tip used with the cantilever should have radius much smaller than the radii of the corrugations in the sample in order for these to be measured accurately. The cantilever is typically silicon or silicon nitride with a tip radius of curvature on the order of nanometers. Silicon nitride cantilevers are less expensive. They are very rugged and well suited to imaging in almost all environments. They are especially compatible with organic and biological materials.

Common methods to detect cantilever deflections are the optical lever method, the interferometric method, and the electronic tunneling method. The optical lever method is the most used, since it is the most simple to implement. It consists of focusing a laser beam on the back side of the cantilever and in detecting the reflected beam by means of a position sensor, that is usually a quartered photodiode. Both cantilever deflection and torsion signals may be collected.

When the sample is placed on the positioning unit of the AFM, the cantilever is placed in the close contact to the sample. In this process, an electric field is applied across the positioning unit of the AFM. This induces a displacement of the positioning unit. The displacement of the positioning unit is measured using a sensor such as a capacitive sensor. A laser beam is transmitted to and reflected from the cantilever for measuring the cantilever orientation. The reflected laser beam is detected with a position-sensitive detector consisting of two closely spaced photodiodes whose output signal is collected using a differential amplifier. In most cases, the photo detector has four quadrants. A photodiode is a type of photodetector capable of converting light into either current or voltage, depending upon the mode

of operation. The output of the photodetector is provided to a computer for processing of the data for providing a topographical image of the surface with atomic resolution. The currently used position-sensitive detectors are four-sectional which allows measuring not only longitudinal motion but torsion of bending too.

## 2.3 Operating Modes of the AFM

The operating mode of the AFM can be classified into different types depending on the different measurement parameters used in sensing the interactive forces. Three basic fundamental operating modes of the AFM are: (1) contact mode; (2) non-contact mode; and (3) tapping mode.

### 2.3.1 Contact mode

In contact mode, the tip of the cantilever is placed in contact with the sample. This mode is the most commonly used mode for the AFM. The force acting in this mode is repulsive force in the order of $10^{-9}$ N. The force is set by pushing the cantilever against the sample surface. In this mode, the deflection of the cantilever is first sensed and than compared to some desired value of the deflection. The repulsion force $F$ acting upon the tip is related to the cantilever deflection value $x$ under Hooke's law: $F = -kx$, where $k$ is the cantilever spring constant. The spring constant value for different cantilevers usually varies from 0.01 to several N/m. The deflection of the cantilever is converted into an electrical signal DFL. The DFL is the difference signal between top and bottom halves of the photo diode. The DFL signal is used to characterize the interection force between the tip and the surface.

During contact mode when the atoms are gradually brought together, they first weakly attract each other. This attraction increases until the atoms are so close together that their electron clouds begin to repel each other electrostatically. This electrostatic repulsion progressively weakens the attractive force as the interatomic separation continues to decrease. The force goes to zero when the distance between the atoms reaches a couple of Angstroms, about the length of a chemical bond. When the total Van der Waals force becomes positive (repulsive), the atoms are in contact.

The slope of the Van der Waals curve is very steep in the repulsive or contact regime. As a result, the repulsive Van der Waals force balances almost any force that attempts to push the atoms closer together. In the AFM this means that when the cantilever pushes the tip against the sample, the cantilever bends rather than forcing

the tip atoms closer to the sample atoms. Two other forces are generally present during contact AFM operation: a capillary force exerted by the thin water layer often present in an ambient environment, and the force exerted by the cantilever itself. The capillary force arises when water surrounds the tip, applying a strong attractive force (about $10^{-8}$ N) that holds the tip in contact with the surface. The magnitude of the capillary force depends upon the tip-to-sample separation. The force exerted by the cantilever is like the force of a compressed spring. The magnitude and sign (repulsive or attractive) of the cantilever force depends upon the deflection of the cantilever and upon its spring constant.

As long as the tip is in contact with the sample, the capillary force should be constant because the tip and the sample are virtually incompressible. It is assumed that the water layer is reasonably homogeneous. The variable force in contact with the AFM is the force exerted by the cantilever. The total force that the tip exerts on the sample is the sum of the capillary plus the cantilever forces, and must be balanced by the repulsive Van der Waals force for contact AFM. The magnitude of the total force exerted on the sample varies from $10^{-8}$ N to the more typical operating range of $10^{-7}$ to $10^{-6}$ N. Most AFMs detect the position of the cantilever with optical techniques. In the most common scheme, a laser beam bounces off the back of the cantilever onto a position-sensitive photodetector (PSPD). As the cantilever bends, the position of the laser beam on the detector shifts. The PSPD itself can measure displacements of light as small as 10 Angstroms. The ratio of the path length between the cantilever and the detector to the length of the cantilever itself produces a mechanical amplification. As a result, the system can detect sub-Angstrom vertical movement of the cantilever tip.

If the deflection of the cantilever does not match with the predefined value of the deflection a voltage across the positioning unit of the AFM is applied to raise or lower the sample relative to the cantilever to restore the desired value of deflection. The voltage that the feedback amplifier applies to the positioning unit is a measure of the height of features on the sample surface. The predefined value of the cantilever deflection depends on the operating mode. Two types of mode are used in contact mode atomic force microscopy, (a) constant force mode; and (b) constant height mode. In constant force mode, the force between the tip and sample remains fixed. This means that the deflection of the cantilever remains fixed. By maintaining a constant cantilever deflection (using the feedback loops) the force between the probe

and the sample remains constant and an image of the surface is obtained. In this mode vertical deflection, i.e., the control voltage applied to Z electrode is measured. The vertical deflection is used to plot the surface topography. The advantage of the constant force mode is that this method allows us to measure the surface topography with high resolution. Constant force mode is also good for rough samples, used in friction analysis

Constant force mode also has some disadvantages. The scanning speed of the AFM in constant force mode is restricted by the response time of the feedback system. The soft samples such as polymers and biological samples can be destroyed due to interaction between the sharp probe and sample. The local flexure of the soft sample surfaces may be varied. The existence of the substantial capillary forces between the probe and the sample can decrease the resolution as well.

During scanning in constant height mode the distance between the tip of the cantilever and sample remains fixed. The cantilever base moves at a constant height from the sample surface. In constant-height mode, the spatial variation of the cantilever deflection can be used directly to generate the topographic data set because the height of the scanner is fixed as it scans. The main advantage of the constant height mode is high scanning speeds. The scanning speed at constant height mode is restricted only by resonant frequency of the cantilever. Constant height mode also has some disadvantages. In constant height mode the samples are required to be sufficiently smooth. A soft sample can be destroyed because the tip is in direct contact with the surface of the sample.

The operation of the contact mode atomic force microscopy is described in Fig. 2.2 by the force vs. distance curve. The line in Fig. 2.2 indicates the position of the cantilever. The flat line indicates that the cantilever is away from the sample. When cantilever approaches the sample an attractive force is generated as shown in the point A. The point B indicates that the cantilever touches the sample surface. At point C, the tip of the cantilever moves further from the sample. At this point a repulsive force is generated to deflect the cantilever away from the sample. Again during the retraction period of the sample an attractive force is generated as shown by point D.

### 2.3.2 Non-contact mode

In non-contact mode the probe does not contact the sample surface, but oscillates above the adsorbed fluid layer on the surface during scanning. This mode belongs to

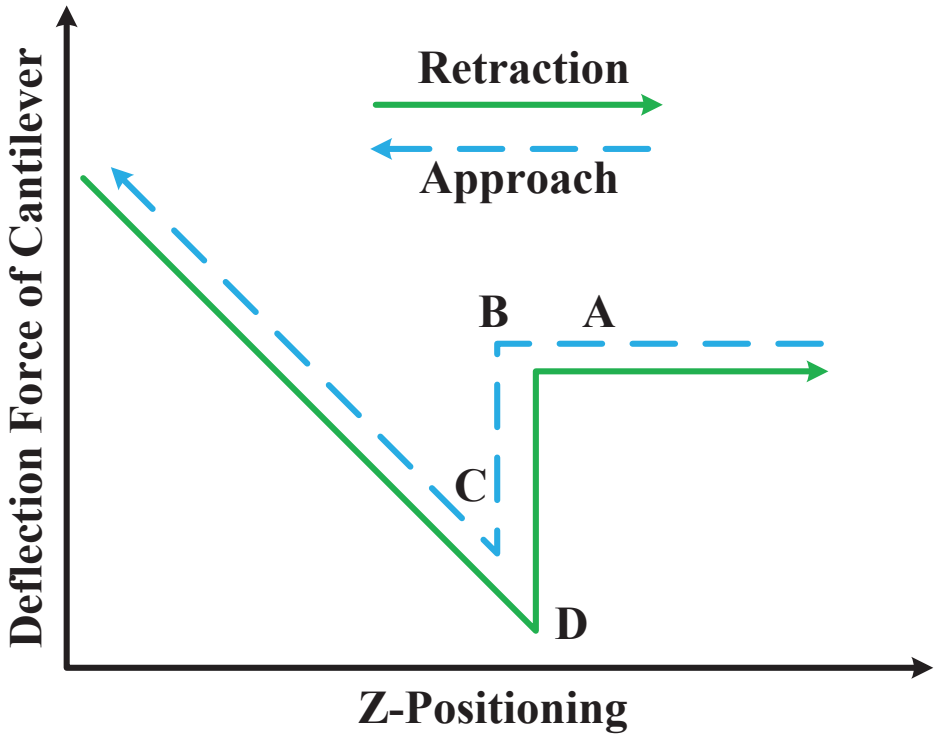


**Figure 2.2:** Force vs. distance curve in contact mode of the AFM imaging.

a family of modes which refers to the use of an oscillating cantilever. The non-contact mode is used in situations where tip contact might alter the sample in subtle ways. In this mode the tip hovers 50-150 Angstrom above the sample surface. Normally the cantilever used in the non-contact mode has higher stiffness and high spring constant in the order of 10 to 100 $\mathrm{N\,m^{-1}}$. This is to avoid sticking to the sample surface. The forces between the tip and sample are quite low, on the order of pN (10−12 N). In this mode the cantilever is usually vibrated at its resonant frequency. The amplitude of the oscillation is kept less than 10 nm. Attractive Van der Waals force is acted between the tip and sample. This attractive force is substantially weaker than the forces used by contact mode. That is why the tip is given a small oscillation so that the AC detection methods can be used to detect the small forces between the tip and the sample. This is done by measuring the change in amplitude, phase, or frequency of the oscillating cantilever in response to force gradients from the sample. The detection scheme is based on measuring changes to the resonant frequency or amplitude of the cantilever due to its interaction with the sample.

The imaging resolution using non-contact mode depends of the distance between

tip-sample. The tip-sample distance could be reduced further to achieve AFM images with high resolution. This can also be achieved in a ultra-high vacuum (UHV) environment instead of the ambient condition. One of the limitations of operating the AFM in an ambient condition is that the tip-sample must be set at a larger distance to avoid the tip from being trapped in the ambient water layer on the sample surface. Non-contact modes of the AFM are classified into two catagories, namely amplitude modulation (AM) and and frequency modulation (FM). In amplitude modulation mode, an external signal with constant amplitude and phase is applied to the piezo actuator of the cantilever to excite and vibrate the cantilever. In this mode, the amplitude of the cantilever is affected by the repulsive force acting on the tip during operation. In frequency modulation mode, the cantilever is always excited to vibrate at its resonance frequency. The advantage of non-contact mode is that in this mode a very low force is exerted on the sample about $10^{-12}$ N. This extends the lifetime of the probe. The non-contact mode usually results in lower resolution; contaminant layer on surface can interfere with oscillation; usually need ultra high vacuum (UHV) to have best imaging.

### 2.3.3 Tapping mode

The tapping mode is also called semi-contact mode. This is an important mode in AFM imaging. This is because this method allows for high resolution imaging of sample surfaces that are easily damaged, loosely held to their substrate, or difficult to image by other AFM techniques. In this mode the cantilever is oscillated at its resonant frequency. Tapping mode overcomes problems associated with friction, adhesion and other difficulties. This is done by alternatively placing the tip in contact with the surface to provide high resolution. Then the tip is lifted off the surface to avoid dragging the tip across the sample. The oscillation of the cantilever in tapping mode is done using a piezoelectric crystal at the base of the cantilever. When the piezoelectric crystal comes into motion the cantilever oscillates. The amplitude of the oscillation of the cantilever is nearly in the order of 20 nm.

Selection of the optimal oscillation frequency is software-assisted and the force on the sample is automatically set and maintained at the lowest possible level. When the tip passes over a bump in the surface, the cantilever has less room to oscillate and the amplitude of the oscillation decreases. Conversely, when the tip passes over a depression, the cantilever has more room to oscillate and the amplitude increases. The oscillation amplitude of the tip is measured by the detector and input

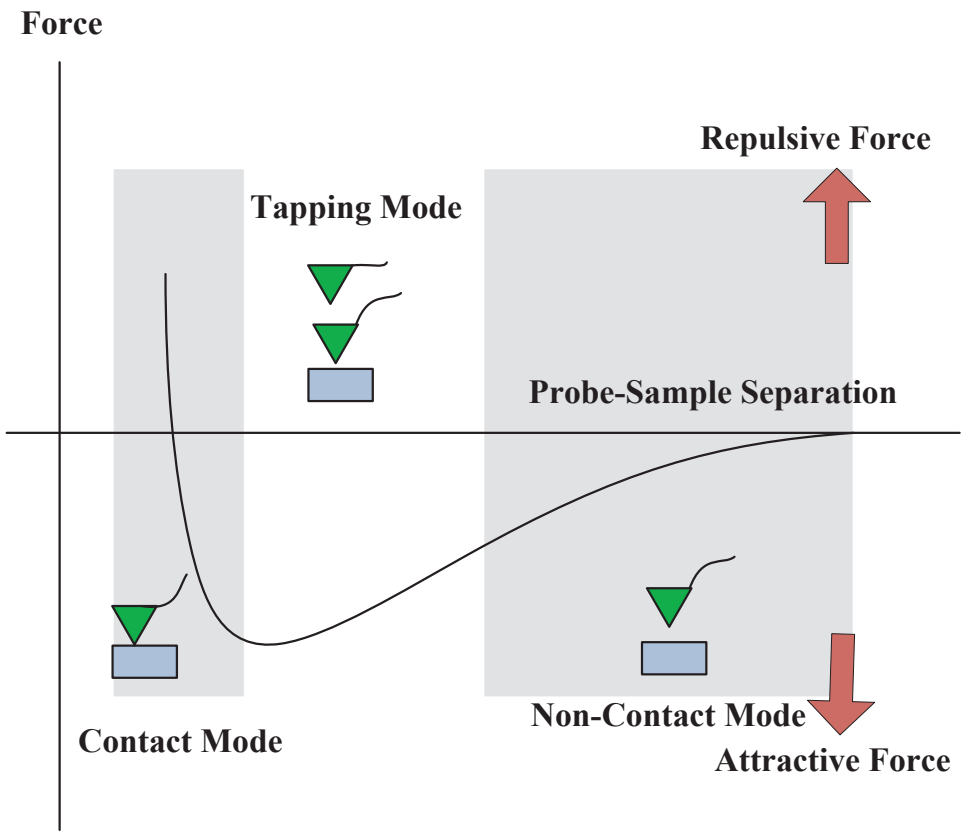


**Figure 2.3:** Plot of force as a function of probe-sample separation.

to the controller electronics. The digital feedback loop then adjusts the tip-sample separation to maintain a constant amplitude and force on the sample.

During scanning, the vertically oscillating tip alternately contacts the surface and lifts off, generally at a frequency of 50,000 to 500,000 cycles per second. As the oscillating cantilever begins to intermittently contact the surface, the cantilever oscillation is necessarily reduced due to energy loss caused by the tip contacting the surface. The reduction in oscillation amplitude is used to identify and measure surface features.

Tapping mode inherently prevents the tip from sticking to the surface and causing damage during scanning. Unlike contact and non-contact modes, when the tip contacts the surface, it has sufficient oscillation amplitude to overcome the tip-sample adhesion forces. Also, the surface material is not pulled sideways by shear forces since the applied force is always vertical. Another advantage of the tapping mode technique is its large, linear operating range. This makes the vertical feedback

system highly stable, allowing routine reproducible sample measurements.

Tapping mode operation in fluid has the same advantages as in the air or vacuum. However imaging in a fluid medium tends to damp the cantilever's normal resonant frequency. In this case, the entire fluid cell can be oscillated to drive the cantilever into oscillation. This is different from the tapping or non-contact operation in air or vacuum where the cantilever itself is oscillating. When an appropriate frequency is selected (usually in the range of 5,000 to 40,000 cycles per second), the amplitude of the cantilever will decrease when the tip begins to tap the sample, similar to Tapping mode operation in air. Alternatively, very soft cantilevers can be used to get the good results in fluid. The spring constant is typically 0.1 N/m compared to the tapping mode in air where the spring constant may be in the range of 1-100 N/m.

The description of three modes of the AFM in terms of force vs. probe-sample distance is shown in Fig. 2.3. The dominant force acting in the short probe-sample distance of the AFM is the Van der Waals force. Long-range interactions such as capillary, electrostatic, magnetic are significant further away from the surface. During contact with the sample, the probe predominately experiences repulsive Van der Waals forces (contact mode). This leads to the tip deflection described previously. As the tip moves further away from the surface attractive Van der Waals forces are dominant (non-contact mode).

## 2.4 Piezoelectric Tube Scanner

A Piezoelectric tube scanner is an important feature of the AFM. The PTS is used as the positioning unit in the AFM. In most cases, the PTS is usually fabricated from lead zirconium titanate by pressing together a powder, then sintering the material. The PTS is designed to achieve fine mechanical displacement in the $x$, $y$, and $z$ axis. Earlier before the invention of the PTS, the three dimensional positioning of the AFM was achieved by using a tripod scanner. But due to lateral bending, it causes cross coupling and low mechanical resonance which limit the scanning speed of the AFM. Later using the piezoelectricity technology, PTSs were made. The PTS works based on the piezoelectric effect. About 100 years before than the time of the invention of the STM, the Curie brothers, Pierre Curie and Jacques Curie (1880) discovered the piezoelectric effect in the materials.

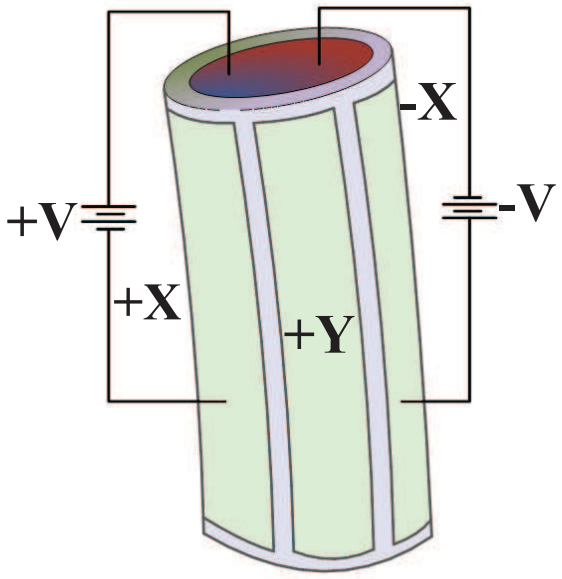


(a)

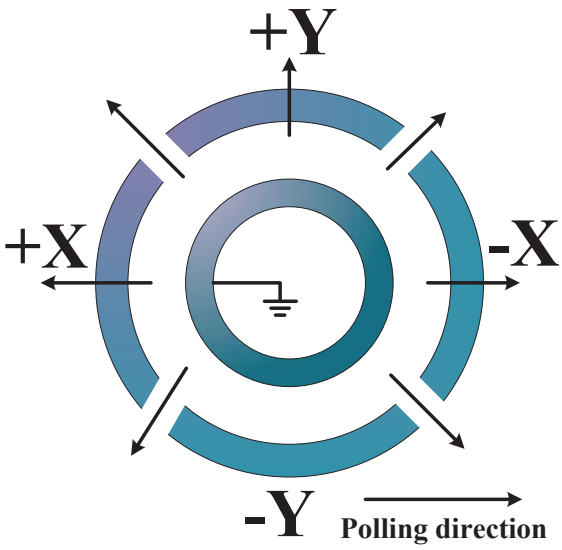


(b)

**Figure 2.4:** A typical illustration of a piezoelectric tube scanner. (a) Side view and (b) top view.

Piezoelectric materials are ceramics that change dimensions in response to an applied voltage and conversely, they develop an electrical potential in response to mechanical pressure. Piezoelectric materials are polycrystalline solids. Each of the crystals in a piezoelectric material has its own electric dipole moment. These dipole moments are responsible to move the piezo in response to an applied voltage. The dipole moments within the scanner are randomly aligned after sintering. The ability of the scanner to move depends on the align of the dipole. If the dipole moments are not aligned, the scanner has almost no ability to move. The align of the dipole moment is done by using a process called poling.

The process of poling in the scanner is done at 200 degree Celsius to free the dipoles. At this moment, a direct current voltage source is applied. It takes few hours to align the dipoles. After the aligning process the scanner is cooled to freeze the dipoles into their aligned state. Then electrodes are attached to the outside of the tube, segmenting it electrically into vertical quarters, for $+x$, $+y$, $-x$, and $-y$ travel. The electrode in the $z$ direction of the scanner is attached in the center of the scanner. A typical illustration of a PTS is presented in Fig. 2.4.

The PTS given in Fig. 2.4 shows that the PTS typically consists of a cylindrical tube made of radially poled piezoelectric materials. The PTS is fixed at one end and free at other end. The PTS is segmented into four equal size electrodes. The electrodes are marked as +X, −X, +Y in the figure. Another electrode is not marked in the picture because the electrode is at the opposite end of the figure. The top part of the electrode is unsegmented. Usually a sample holder is placed on the top of the scanner to hold the sample.

Alternating voltages are applied to the $+x$ and $-x$ electrodes of the scanner. The application of this voltage induces strain into the tube which causes it to bend back and forth in the lateral, i.e., the $x$ direction. A similar method is used to apply voltage in the $y$ direction of the scanner. The expansion and contraction of the PTS depends on the polarity of the applied voltage with respect to the polling direction of the material. The PTS expands when the polarity of the applied voltage coincides with the polling direction. The PTS contracts when the the polarity of the applied voltage is opposite to the polling direction. Voltages applied to the z electrode cause the scanner to extend or contract vertically. The displacement of the scanner is measured by using sensors. In most cases, capacitive sensors are used


**Figure 2.5:** Piezoelectric tube scanner used in the experiment.

to measure the displacement of the scanner. The reason for using capacitive sensors is their high speed response.

The maximum scan size of the PTS depends on many factors. These include the length of the scanner tube, the diameter of the tube, its wall thickness, and the strain coefficients of the particular piezoelectric ceramic from which it is fabricated. Typically the PTS can scan from tens of angstroms to over 100 microns in the lateral and longitudinal directions. In the vertical direction, it can scan from the sub-angstrom range to about 10 microns. One of the PTS used in this thesis is illustrated in Fig. 2.5. In this thesis, we have used three scanners. We started our experiments with one scanner. Then after the damaging of the first resonant mode of the scanner we have used a second scanner and ordered a new scanner. Some of the work in this thesis are done using the new scanner as well.

In most cases the scanning operation in the AFM is performed by using a raster scanning pattern. Raster scanning is performed by moving the PTS in the forward and backward directions along the $x$-axis and moving the PTS in a small step in $y$-axis. This is done by applying triangular signal in the $x$-axis and staircase signal in the $y$-axis as shown in Fig. 2.6 (a) and Fig. 2.6 (b). When a triangular signal is applied to $x$-axis and a staircase signal is applied to $y$-axis, a raster scanning pattern is generated as shown in Fig. 2.6 (c).

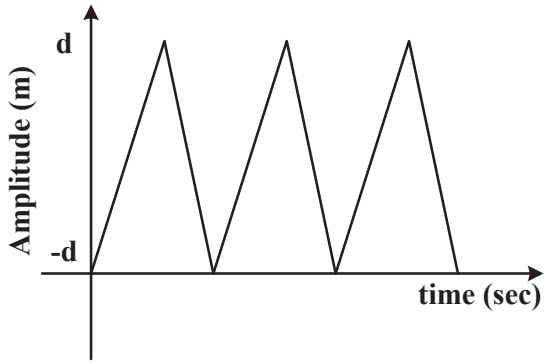


(a)

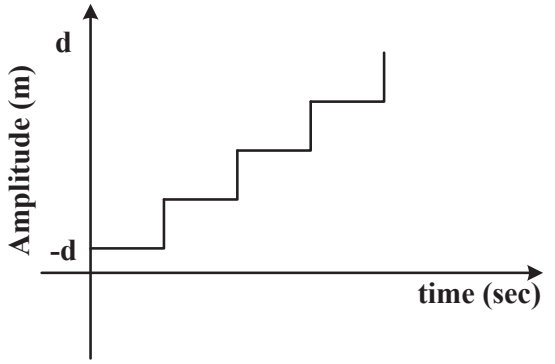


(b)

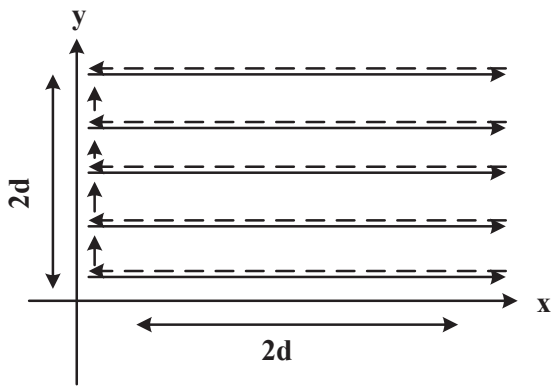


(c)

**Figure 2.6:** Raster scanning method in AFM imaging. (a) Triangular signal applied to $x$-axis, (b) staircase signal applied to $y$-axis and (c) raster scanning method.

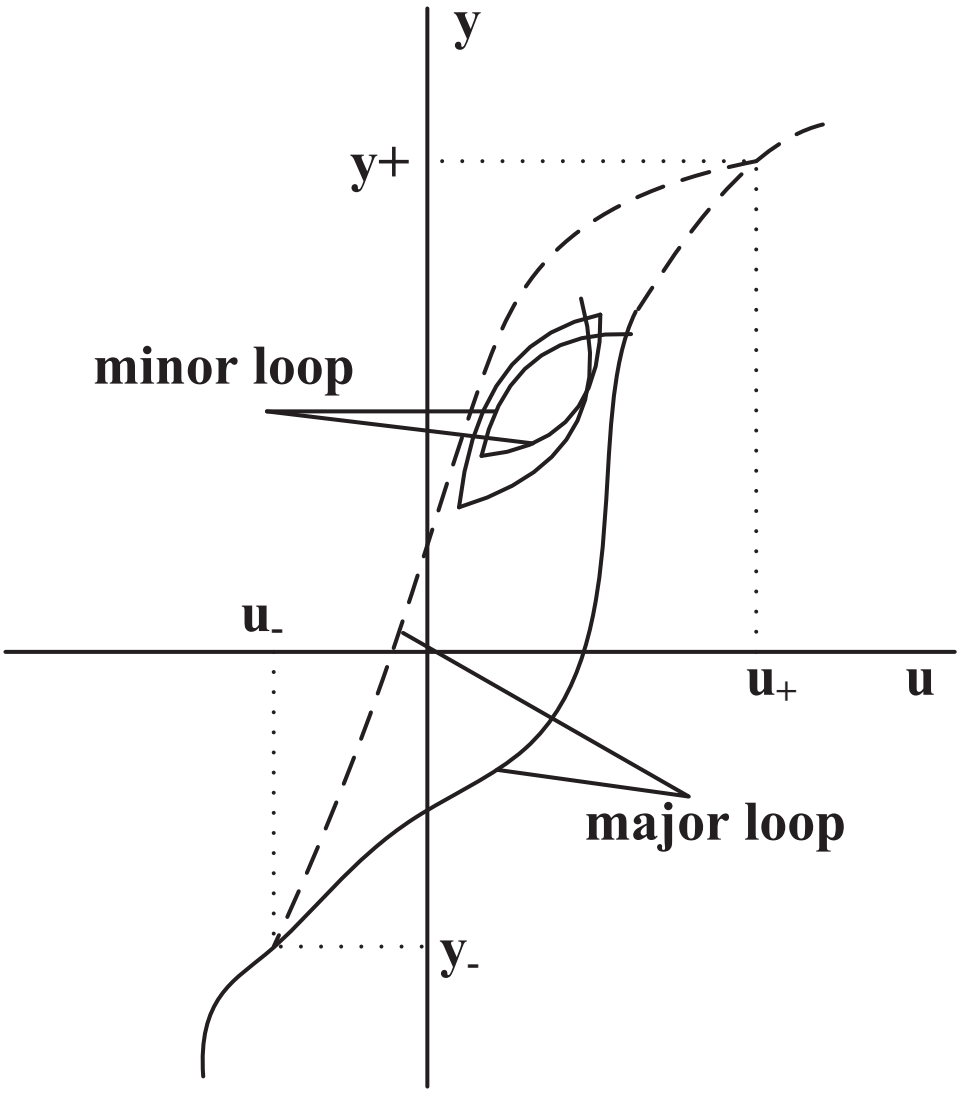


**Figure 2.7:** Hysteresis terminology.

## 2.5 Limiting Factors for High Speed Nanopositioning of the PTS

Accurate positioning of the PTS is required to achieve high quality images of the sample. The high speed imaging performance of the AFM is limited due to some inherent properties of the PTS such as hysteresis, induced vibration and cross coupling. In the following section these issues are further discussed.

### 2.5.1 Hysteresis

The term "hysteresis" is derived from an ancient Greek word "hustereia" meaning "deficiency" or "lagging behind". It was Sir James Alfred Ewing who described the behavior of magnetic materials around 1890. Hysteresis is the dependence of a system which not only depends on its current environment but also on its past environment. This dependence arises because the system can be in more than one internal state. It is the lag in response exhibited by a body in reacting to changes in the forces.

Hysteresis can be represented graphically as a relation in the $u-y$ plane. Fig. 2.7 shows an example of an hysteresis relation along with a sample path. The loop which bounds the region where $y(t)$ is multi-valued is called major loop. The domain of input values $u$ corresponding to this region is $[u_-, u_+]$; the range of outputs $[y_-, y_+]$. Each new segment of the output path in the $u-y$ plane is called a branch. Successive branches which cross inside the major loop form minor loops.

Hysteresis arises in diverse applications such as magnetic hysteresis is a typical example. Hysteresis occurs in ferromagnetic materials and ferroelectric materials, as well as in the deformation of some materials (such as rubber bands and shape-memory alloys) in response to a varying force. The PTS is also fabricated from piezoelectric materials which are ferromagnetic in nature. The ferromagnetic nature of the PTS introduces hysteresis in the PTS. In most cases, the PTS in the AFM is driven by a voltage source. This voltage source is responsible for introducing hysteresis in the PTS.

The effect of hysteresis increases with an increase in the magnitude and frequency of the applied voltage signal. Due to the hysteresis effect distortion occurs in the scanned images of the AFM. As the fast axis of the PTS is driven by a triangular signal, a deviation of fifteen percent can occur due to hysteresis [38]. This effect can be minimized by allowing scan only for low range. This limits the scanners ability for long range scan.

A number of research papers are available in the literature to model hysteresis. The most commonly presented hysteresis models can be summarised as follows: Electromechanical models [39]; Preisach models [40]; Prandtl-Ishlinskii (PI) models [41]; Bouc-Wem models [42]; Rate-dependent or rate-independent hysteresis models [43]. The compensation of hysteresis is important because this effect tends to move the PTS from accurate nanopositioning. One way to compensate for hysteresis is

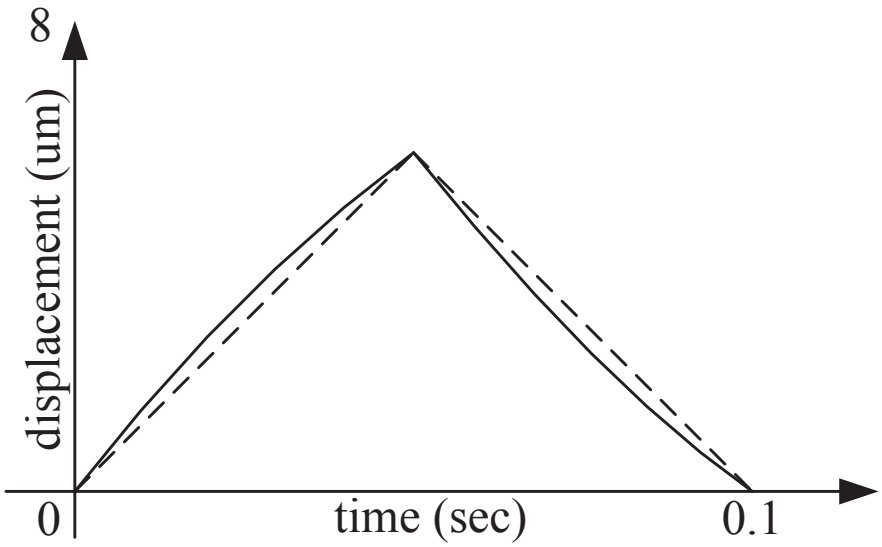


(a)

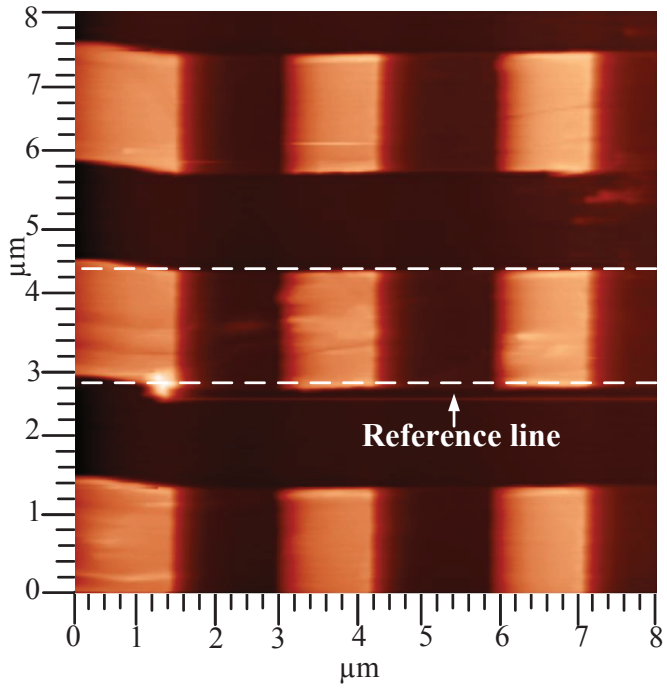


(b)

**Figure 2.8:** Effect of hysteresis in imaging. (a) Measured scanners's displacements (solid line) for a 10 Hz triangular signal input (dashed line), (b) the resulting image of a calibration grating sample.

to model it as a nonlinear function and then eliminate it by cascading its inverse with piezoelectric tube actuator. Though this is useful for open loop, it requires accurate modeling of the system to compensate for hysteresis as it may change with the parameter variation. Current and charge sources can also be used to reduce the hysteresis instead of a voltage source. One of the disadvantages of using a charge source is that, it leads to drift and saturation problem which greatly reduce the range of piezoactuators [38].

Feedback control techniques have also been applied to reduce the hysteresis. Integral or proportional integral (PI) controllers are used in most AFM systems because of their simplicity and ease of implementation. Another advantage of the use of integral or PI controllers is that these controllers apply high gain at low frequency. This high gain of the integral controller results in a reduction of the effect of hysteresis.

### 2.5.2 Creep

Piezoelectric creep effect is another major constraint for high speed nanopositioning of the PTS. The creep effect is mainly prominent at a slow scanning rate. The creep effect distorts the generated images from the AFM. When a voltage signal is applied across the PTS to move the piezo in a direction, the piezo continue to displace even after the removal of the voltage induced. This generates the creep effect in the PTS. The creep effect can be minimized by allowing a sufficient amount of time. Fig. 2.9 illustrates the effects of the creep in imaging. It can be seen that the scanned image is skew down at the bottom of the image due to the creep effect.

### 2.5.3 Induced vibration

The X axis of the PTS is actuated by using a triangular signal. When the PTS is actuated using a triangular signal, the odd harmonics of the triangular signal excite the mechanical resonant mode of the PTS. This causes the scanner to vibrate and trace a distorted triangular waveform which can significantly distort the generated AFM image. This image distortion is particularly objectionable when positioning accuracy is required in a very small range such as nanometer. The induced vibration often limits the positioning accuracy of the PTS to one percent of its first resonance frequency [38]. Therefore it is necessary to compensate the effect of scan induced vibration of the PTS due to the resonant nature of the PTS.

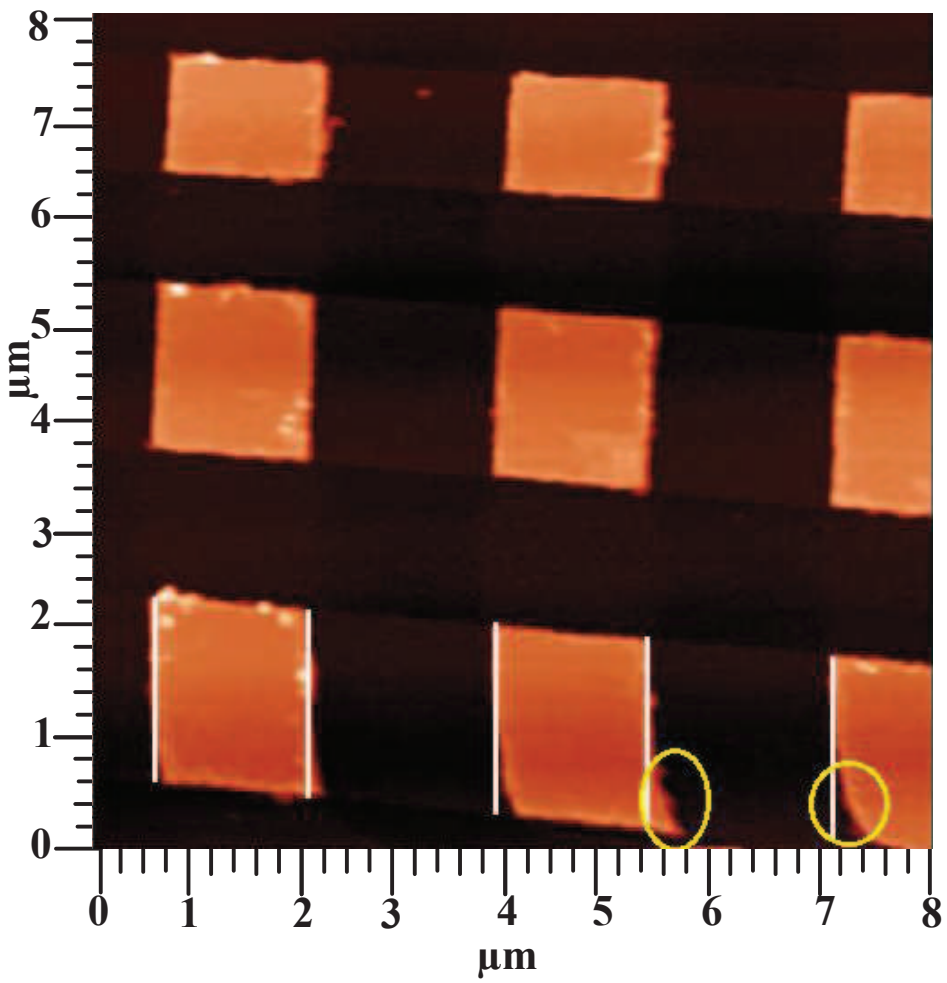


**Figure 2.9:** Effect of creep in AFM imaging.

Fig. 2.10 illustrates the effect of scan-induced vibrations on a scanners displacement. The scanner was excited by using triangular wave signals at 10 Hz, 100 Hz, 150 Hz and 200 Hz. The figures show that the scanner exhibits a large amount of distortion due to the induced vibration of the scanner at high scanning rates. This hampers the tracking accuracy of the PTS. The effect of the induced vibration on AFM imaging is presented in Fig. 2.11. The comparison shows that the generated images are more distorted at high frequencies as compared to the low scanning speeds.

### 2.5.4 Cross coupling

In practice, the axes of scanners are not independent SISO systems. There exists a cross coupling effect between the axes of the scanner. The cross coupling between

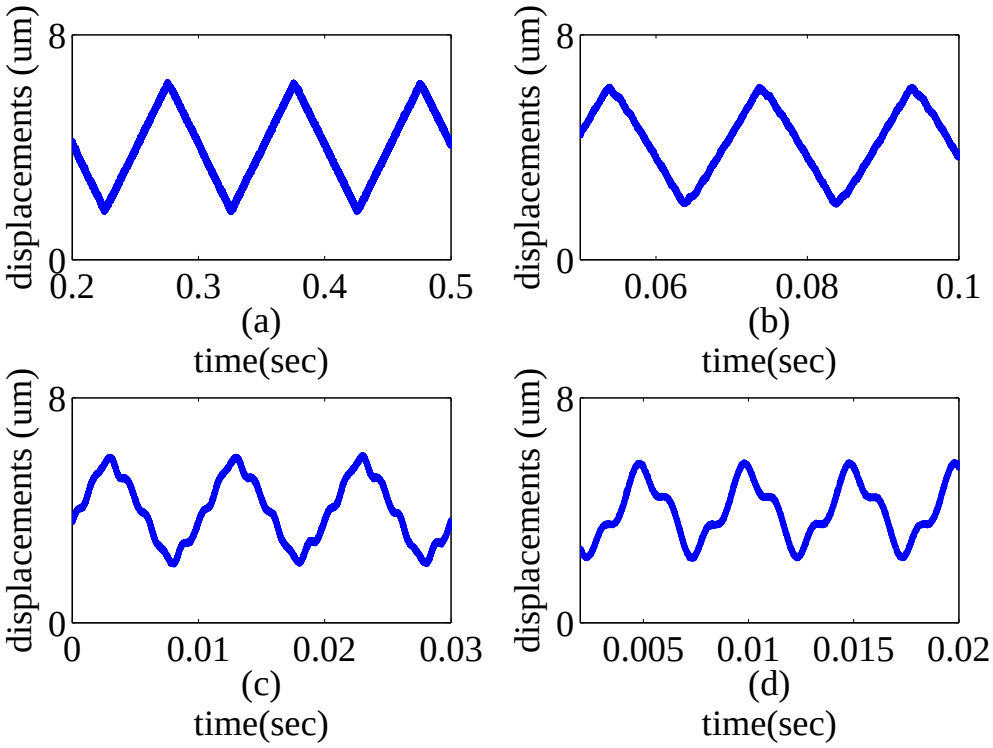


**Figure 2.10:** Effect of vibration on the PTS. Scanner displacements when driven by (a) 10 Hz, (b) 100 Hz, (c) 150 Hz and (d) 200 Hz triangular wave signals.

the axes of the nanopositioner may introduce large amounts of error for high speed precision positioning [44]. This plays an important role in degrading the performance of the scanner. It affects the tracking accuracy of the scanner. The low tracking performance of the scanner results in large artifacts on the scanned images. Such large image artifacts sometime miss the true sample topography. This is particularly objectionable when the sample topography features have a similar size as the coupling caused artifacts. Due to the cross coupling effect the signal applied to one of the axes of PTSs results in displacements in both axes of scanners (see Fig. 2.12 (a,b,c,d)) and if the magnitude of the cross coupling effect is high then the resulting images generated from AFMs are tilted (see Fig. 2.12 (e,f)) [4].

## 2.6 Chapter Summary

In this chapter, first a brief discussion on the invention of various types of SPM systems were presented. Next, the working principles of the AFM system were discussed. Different types of the operating modes of the AFM were also discussed.

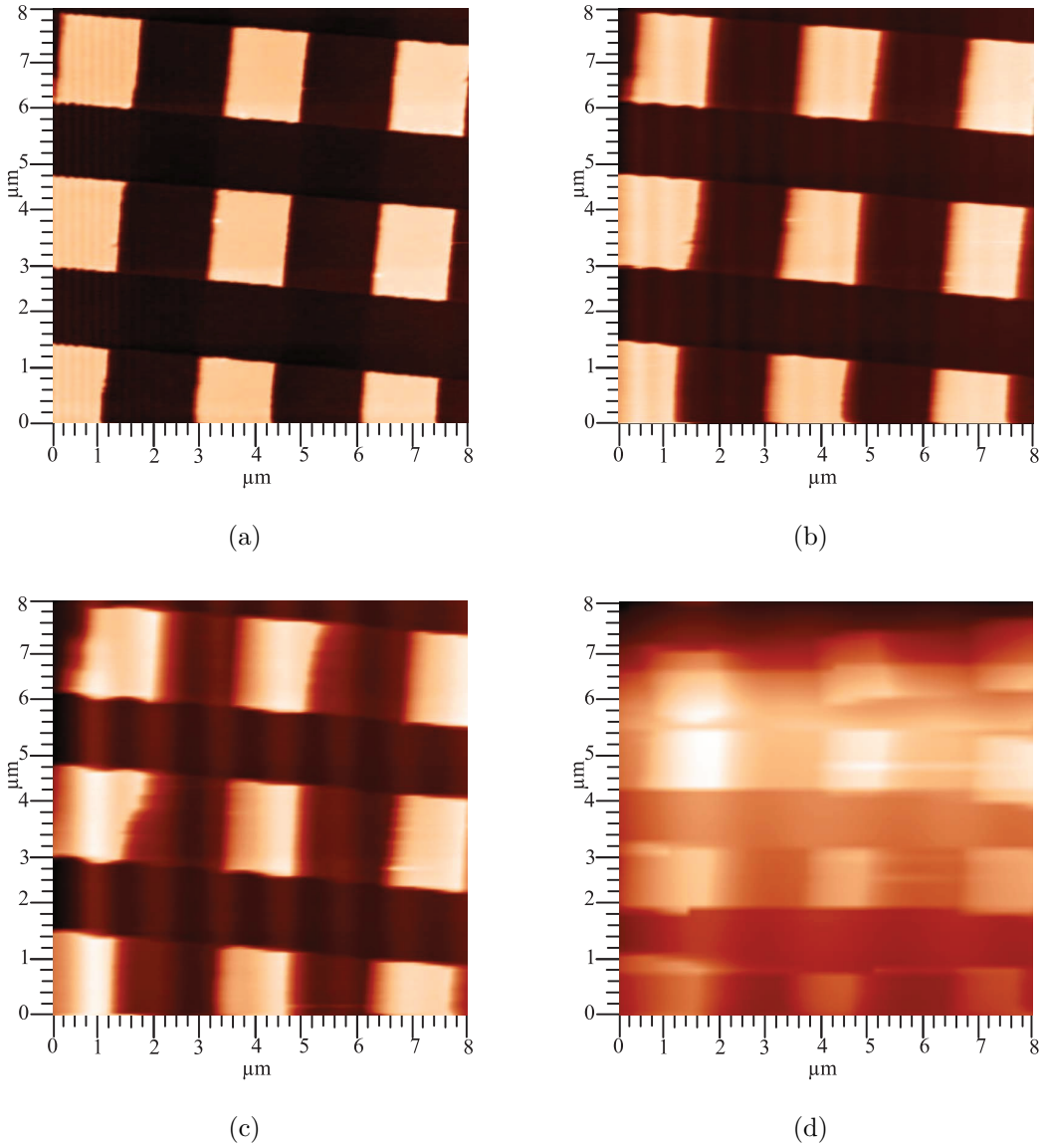


**Figure 2.11:** Open-loop scanned images (a) 15.62 Hz (b) 31.25 Hz (c) 62.5 Hz (d) 125 Hz.

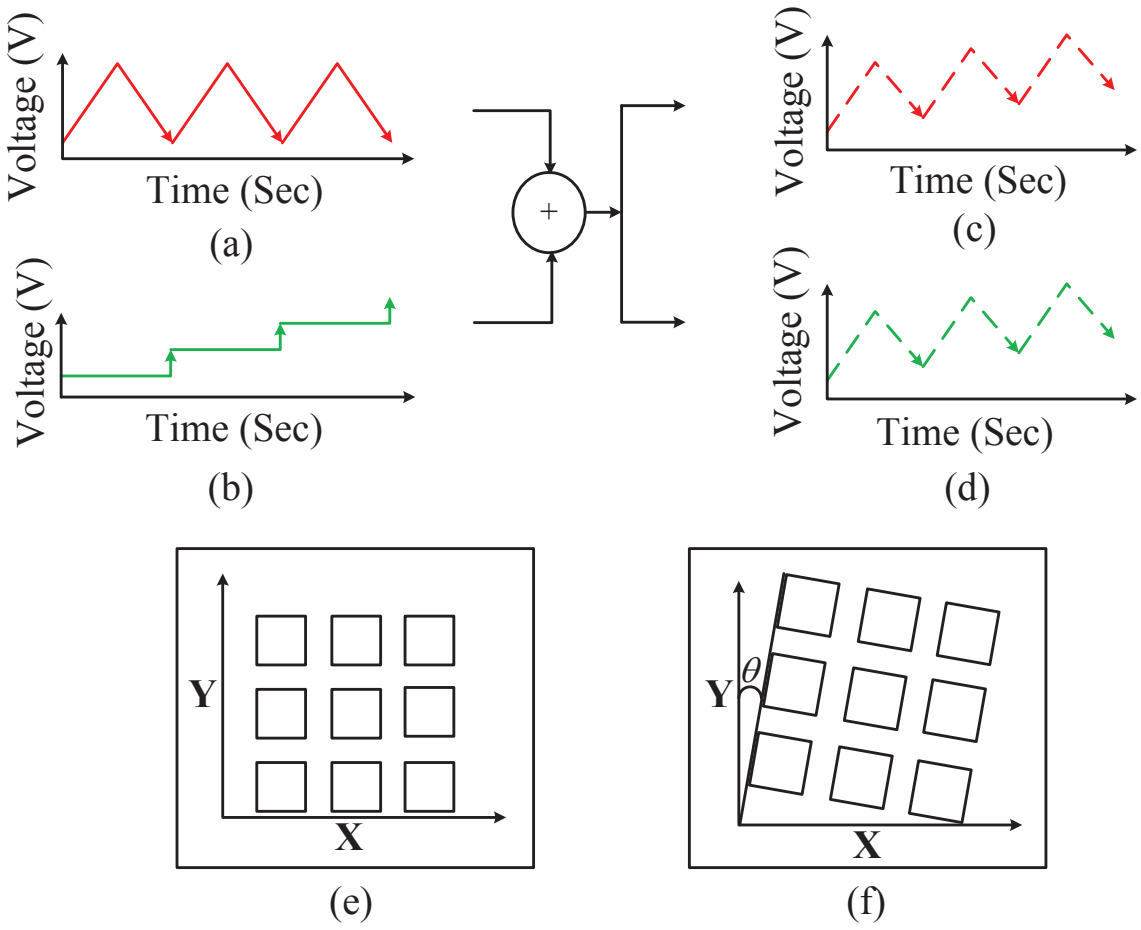


**Figure 2.12:** Effect of cross coupling in AFM imaging. (a) Required $x$ sensor output, (b) required $y$ sensor output, (c) $x$ sensor output with cross coupling, (d) $y$ sensor output with cross coupling, and (e) raster scanning without the cross coupling effect, and (f) raster scanning with the cross coupling effect.

This was subsequently followed by an in depth description of the positioning unit of the AFM. Then, the chapter continued to discuss the various limiting factors to high speed nanopositioning in the PTS. It was shown that these factors reduce the performance of the PTS substantially in high speed nanopositioning. The following chapters discuss the various methods using a feedback control approach to compensate for these effects to increase the positioning accuracy of the PTS at high scanning rates.

# Chapter 3

# Resonant Control of Piezoelectric Tube Scanners

This chapter describes the use of a feedback control approach to achieve high-speed and high-precision positioning in a piezoelectric tube scanner (PTS) by compensating for induced vibration in the PTS. The aim of the design is to achieve a large degree of damping of the first resonant mode of the scanner with large gain and phase margins. In order to guarantee closed-loop stability and achieve a large level of damping of the first resonant mode of the scanner, a mixed negative-imaginary (NI) and small-gain approach [45] is exploited in this chapter. The motivation behind the mixed NI and small-gain approach is that this approach can not only establish the finite-gain stability of the interconnection between the PTS and resonant controller, but also allows for a higher gain of the resonant controller as compared to a small-gain only approach. This leads to a large level of damping of the first resonant mode of the scanner. The design of the resonant controller is presented in two parts. The first design is for a single-input single-output (SISO) controller for the lateral axis, i.e., the X-axis of the PTS and the second design is a multi-input multi-output (MIMO) controller for the combined lateral and longitudinal axes of the scanner.

The rest of the chapter is organized as follows. In the first section of this chapter, a review of existing feedback and feedforward control techniques and the motivation for this work are presented. The experimental setup and the identification of the dynamics of the PTS are described in Section 3.2 and 3.3. Section 3.4 presents the design of the SISO and MIMO resonant controllers for the PTS, Section 3.5 gives a stability analysis of the interconnected systems. The experimental validation of the proposed controller is described in Section 3.6. The chapter is concluded with brief remarks in Section 3.7.

## 3.1 Introduction

There has been a consistent effort in recent years to improve the accuracy and speed of PTSs using feedback control techniques. The approaches to the design of damping controllers to control the resonant mode of nanopositioners can be classified into two categories and the categories are (a) open-loop control [9, 16] and (b) closed-loop control [4, 13–15].

The design of open-loop damping controllers [9, 16] is popular because of their noise efficiency as they do not require any additional sensors during implementation. The identification of the dynamics of nanopositioners in open-loop control is done by using additional sensor and hardware. One of the major drawbacks of the use of open-loop control techniques is their low performance against variations in the plant transfer function. The transfer function of nanopositioners vary for many reasons such as due to the changing of loads on a scan-by-sample scanner. The transfer function of scan-by-head scanners can also change due to changes in environmental condition such as temperature and humidity.

The design of feedback controllers [4–6] to damp the resonant modes of the scanner is of interest as they provide robustness against changes in the plant transfer function. High bandwidth robust controllers such as $H_\infty$ [46–50] controllers are designed to achieve a bandwidth near to the first resonance frequency of the system. The order of controllers using $H_\infty$ methods depend on the order of the system which increases the complexity in the design process for high order systems. The implementation of high order controllers requires advanced DSP systems. The design of $H_\infty$ controllers is done for finite number of resonant modes of systems. If the system has a lot of resonant modes and the design of the controller is based on only small number of modes, then that controller may result in instability because the gain of the controller can still be high at the frequencies corresponding to those un-modeled modes. This may excite the unmodeled dynamics of the scanner during implementation.

Most commercial SPM systems use integral or proportional integral (PI) controllers in the axes of nanopositoners because of their simplicity and the ease of implementation [46, 47]. The closed-loop system using a PI controller is sensitive to changes in the plant transfer functions and can make the closed-loop system unstable for a small-change in plant transfer functions. Another major drawback of integral

controllers is the achievable closed-loop bandwidth [51]. Due to the low gain of integral controllers at high frequencies, the resultant closed-loop system corresponding to the nanopositioner and an integral controller results in a low closed-loop bandwidth. This limits the use of integral controllers for high speed nanopositioning of the PTS.

Piezoelectric shunt damping [52] is another type of damping technique where a shunt circuit which consists of an inductor is added in series with the nanopositioner to damp resonant modes. The amount of damping in shunt control depends on the inductor. This value of inductor sometime reaches hundreds of Henries in low-frequency domains. This shunt damping method is also sensitive to environmental factors such as outside temperature, which may cause drift in the structures resonance frequencies.

Positive position feedback (PPF) controllers [5] and integral resonant controllers (IRCs) [6] are damping controllers used to damp the resonant modes of PTSs. PPF controllers and IRCs are low pass controllers with a sharp roll-off at high frequencies. In spite of providing good damping, PPF controllers and IRCs may suffer from the problem of low gain and phase margins. One of the objectives of the proposed controller is to suppress the first resonant mode of the scanner with little effect at other frequencies in order to achieve large gain and phase margins. The resonant controller [53, 54] provides excellent damping with large gain and phase margins.

Two important properties of PPF controllers, integral resonant controllers, and resonant controllers are that the phases of the transfer functions of these damping controllers lie between $-180^\circ$ and $0^\circ$ and the imaginary parts of these controllers transfer functions are negative at all frequencies. A transfer function which has negative-imaginary part at each frequency is to be referred as NI [55]. A multi-input multi-output transfer function matrix $G(s)$ is said to be NI if $j[G(j\omega) - G^*(j\omega)] \geq 0$ for all $\omega \in (0, \infty)$ [55, 56]. Here, $G^*(j\omega)$ is the complex conjugate transpose of the matrix $G(j\omega)$. The transfer function matrix $G(s)$ is said to have the negative-imaginary property at frequency $\omega$ if $j[G(j\omega) - G^*(j\omega)] \geq 0$ at frequency $\omega$.

PPF controllers, integral resonant controllers, and resonant controllers can be used to damp the resonant modes of structures with collocated position sensors and force actuators [5, 6, 53]. Structures with collocated position sensors and force actuators are also NI systems. The transfer functions of lightly damped structures with collocated position sensors and force actuators can be modeled by a sum of

second order transfer functions of the form $N(s) = \sum_{i=1}^{M} \frac{\phi\phi^T}{s^2+2\xi_i\omega_i s+\omega_i^2}$, where $\xi_i > 0$ is the damping coefficient of ith mode, $\omega_i > 0$ is the resonance frequency of the ith mode, $M$ is the number of modes of the structure and $\phi$ is a column vector [53,54]. The feedback interconnection between a structure with collocated position sensors and force actuators and PPF controllers, integral resonant controllers, and resonant controllers is guaranteed to be finite-gain stable if the DC loop-gain is strictly less than unity as the plant and the controller are both NI with one of them being strictly NI [55].

In practice, the transfer function matrix between the force actuators and the position sensors of PTSs is not NI [4]. Possible reasons for the PTS system not being NI are delays in the sensor or actuator electronics or the collocation of the sensors and actuators may not be perfect. The electronic systems to which a PTS is connected can also add additional phase lag to the system.

Previous work associated with the design of NI damping controllers [6] for PTSs is based on the NI approach [55], i.e., PTSs are also considered as NI systems. Since the PTS is in practice not NI, the design of NI damping controllers for the PTS based on the NI approach [55] cannot guarantee closed-loop stability.

A small-gain approach is a possible solution to guarantee finite-gain stability of the interconnection between the PTS and NI damping controllers. The small-gain theorem states that the feedback interconnection between two stable linear systems is stable if the loop-gain of the two systems is strictly less than one [57,58]. Typically PTSs have large gain near the resonance frequency. Thus the small-gain approach requires that the gain of the controller must be low in order to make the loop-gain less than one to satisfy the stability condition of the small-gain theorem. The low gain of the controller results in a low level of damping of the resonant modes of the scanner. This chapter presents the design of an NI controller for a system which is not negative-imaginary. The system and controller considered in the chapter are a PTS and a resonant controller.

## 3.2 Experimental Setup

The experimental setup consists of (i) a PTS housed in an SPM, (ii) a digital signal analyzer (DSA) to measure the frequency response of the PTS, (iii) a high voltage amplifier (HVA) with a gain of 15 to apply voltage to the PTS, (iv) a signal access

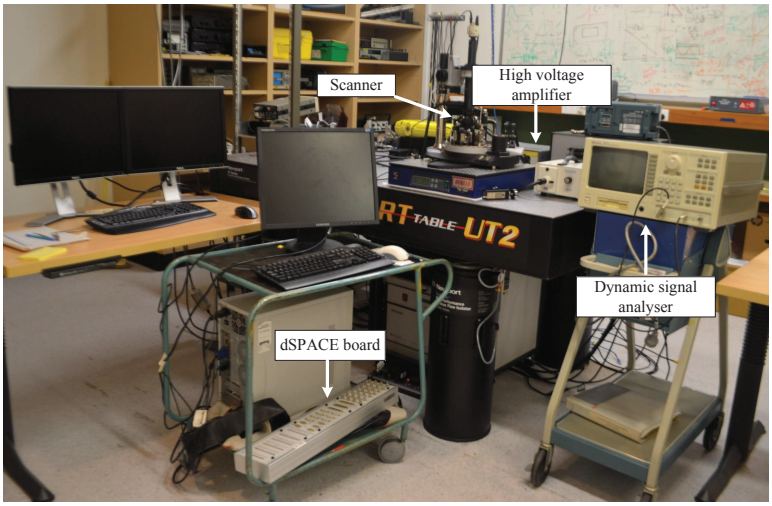


**Figure 3.1:** Experimental setup used in the present work.

module (SAM) which allows direct access to the electrodes of the scanner, and (v) a dSPACE system for the digital implementation of the controller as shown in Fig. 3.1.

The experimental implementation of the controller is performed at the University of New South Wales, Canberra, Australia. The experiments were executed on a NT-MDT scan-by-sample scanner with a scan range of 100 µm × 100 µm × 12 µm. The scanner has positioning resolution of 50 nm and linear dimension error ±0.5%. The resonance frequency of the scanner in the XY directions is 900 Hz and in the Z direction is 5 kHz, approximately.

## 3.3 System Identification

### SISO System Identification

A dual channel signal analyzer (HP35760A) is used to apply a swept sine input of 100 mV rms to the HVA to drive the piezoelectric actuator along the X-axis and the corresponding position response from the X capacitive sensor is recorded. A system identification method is used to obtain a transfer function for the X-axis dynamics of the PTS. The system identification is done using a frequency domain prediction-error minimization method [59] [60] by using the Matlab function 'PEM' to capture the first resonant mode of the scanner with a low order transfer function. The following transfer function $G_{xx}(s)$ is obtained in the identification process:

$$G_{xx}(s) = \frac{D_x(s)}{V_x(s)} = \frac{-186.6s^2 + 1.348 \times 10^6 s - 2.412 \times 10^{10}}{s^3 + 1755s^2 + 3.452 \times 10^7 s + 4.459 \times 10^{10}} \tag{3.1}$$

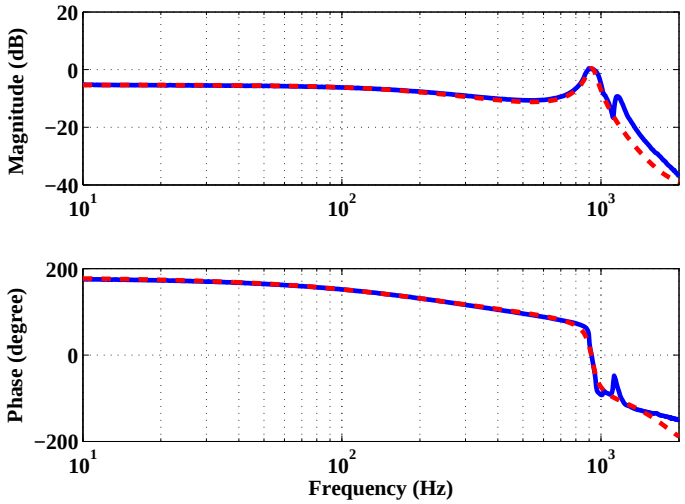


**Figure 3.2:** Measured (– the solid line) and identified model (- - the dashed line) frequency responses of $G_{xx}(s)$ .

where $D_x(s)$ is the Laplace transform of the output voltage from the X sensor and $V_x(s)$ is the Laplace transform of the input voltage to the HVA driving the X-axis of the piezo. Fig. 3.2 shows the match between the measured frequency response and the frequency response of the identified model $G_{xx}(s)$. The system given in Fig. 3.2 has the NI property between 918.3 Hz and $1.91 \times 10^3$ Hz as the phase of the identified model is between 0 and -180° in that range of frequencies.

### MIMO System Identification

The transfer function matrix of the MIMO PTS positioning system can be described by the following equation:

$$\begin{bmatrix} D_x(s) \\ D_y(s) \end{bmatrix} = G(s) \begin{bmatrix} V_x(s) \\ V_y(s) \end{bmatrix} \tag{3.2}$$

where $G(s) = \begin{bmatrix} G_{xx}(s) & G_{xy}(s) \\ G_{yx}(s) & G_{yy}(s) \end{bmatrix}$. The transfer function matrix in 3.2 has a state space realization of the form

$$\dot{x}(t) = Ax(t) + Bu(t);$$

$$y(t) = Cx(t) + Du(t) \tag{3.3}$$

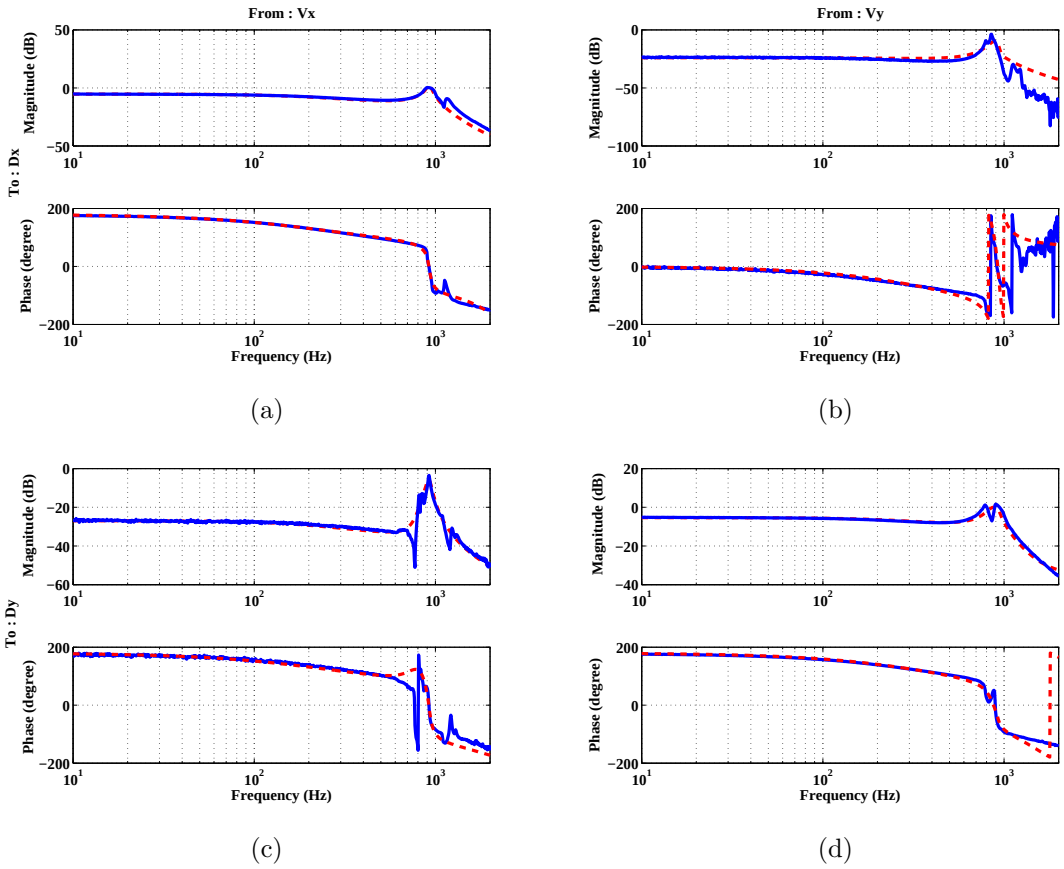


**Figure 3.3:** Open-loop frequency responses relating the inputs $[V_x, V_y]^T$ and the outputs $[D_x, D_y]^T$. The solid line (–) represents the measured frequency responses and the dashed line (- -) represents the identified model frequency responses. (a) Frequency response of $G_{xx}(s)$, (b) frequency response of $G_{yx}(s)$, (c) frequency response of $G_{xy}(s)$, and (d) frequency response of $G_{yy}(s)$.

where $u$ is a vector of the inputs to the HVA and $y$ is a vector of the outputs from capacitive sensors of the scanner.

Swept sine inputs of 100 mV rms were applied to the HVA to drive the piezoelectric scanner along the X- and Y-axis from the dual channel DSA and the corresponding capacitive sensor responses were recorded. The following values of the $A$, $B$, $C$, and $D$ matrices of the above state space model are obtained by using a system identification method:

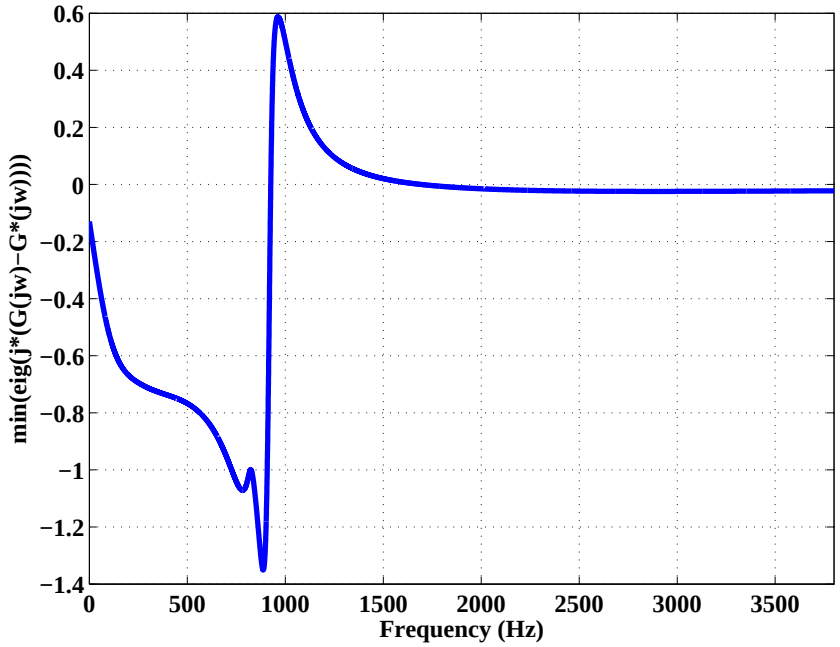


**Figure 3.4:** Minimum eigenvalues of $j(G(j\omega) - G^*(j\omega))$.

$$A = \begin{bmatrix} -427.6 & -5583.6 & -1521.1 & 840.01 & -874.82 & 1074 \\ 4963.2 & -423.76 & -1040.6 & -1245.1 & -1828.2 & 1693.9 \\ 959.85 & 1010.9 & -690.68 & 5435.9 & 474.96 & 1528 \\ -587.17 & 1161.8 & -4395.2 & -508.85 & -2304.2 & -2166.5 \\ -102.38 & 609.98 & 458.09 & 1351.9 & -946.65 & 149.69 \\ 251.11 & -708.42 & 71.644 & 1020.2 & -8.7797 & -1686.1 \end{bmatrix},$$

$$B = \begin{bmatrix} 1.6893 & 12.168 \\ 12.022 & 10.622 \\ -0.42926 & 2.964 \\ 8.0813 & -10.904 \\ -17.019 & 1.1707 \\ 0.58665 & 18.898 \end{bmatrix},$$

$$C = \begin{bmatrix} 9.0521 & 16.8150 & -27.5329 & 20.7708 & 35.2925 & 2.4245 \\ 25.6510 & 19.0371 & 30.2869 & -16.1956 & 6.4775 & -58.5076 \end{bmatrix},$$

$$D = \begin{bmatrix} 0 & 0 \\ 0 & 0 \end{bmatrix}.$$

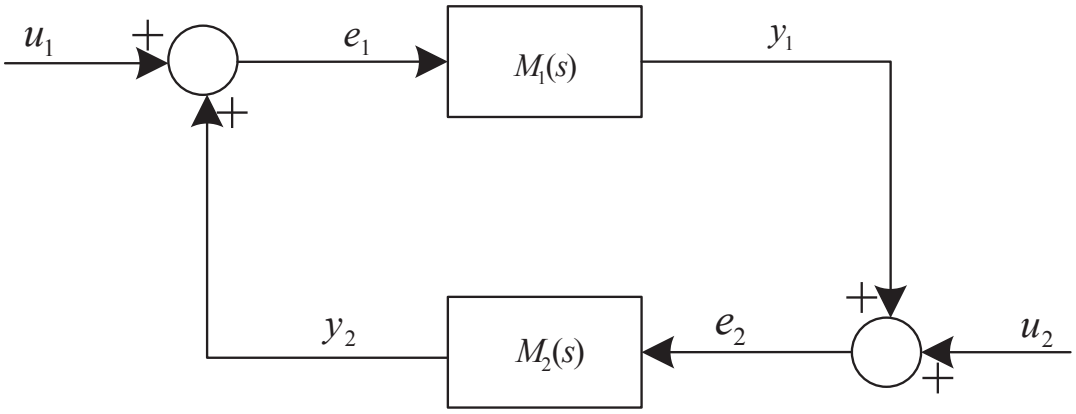


**Figure 3.5:** Closed-loop system with resonant controller.

The MIMO system identification process is done using a frequency domain prediction-error minimization method to capture the first resonant mode of the PTS with a low order model. A comparison between the frequency responses of the measured MIMO data and the identified model (3.3) is given in Fig. 3.3. In order to display the range of frequencies for which the MIMO system (3) has the negative-imaginary property, a plot of the minimum eigenvalues of $j[G(j\omega) - G^*(j\omega)]$ for positive frequencies is given in Fig. 3.4. The eigenvalues of $j[G(j\omega) - G^*(j\omega)]$ are greater than or equal to zero between 925.8 Hz and $1.69 \times 10^3$ Hz, which indicates that the MIMO PTS has the NI property between 925.8 Hz and $1.69 \times 10^3$ Hz. The first four orders of the model represent the first resonant modes in the X- and Y-axis of the scanner and the rest of the model represents all other dynamics of the system including any delay.

## 3.4 Controller Design

This section presents a brief discussion of the design of the SISO and MIMO resonant controllers to damp the first resonant mode of the PTS. The structure of the closed-loop system is given in Fig. 3.5 where $M_1(s)$ and $M_2(s)$ are the plant transfer function and the resonant controller transfer function, respectively, $u_1$ is the reference signal and $y_1$ is the output from the capacitor sensor. The general form of the transfer function of a SISO resonant controller is as follows:

$$M_2(s) = -k_v \frac{s^2 + 2\xi_v \omega_v s}{s^2 + 2\xi_v \omega_v s + \omega_v^2} \tag{3.4}$$

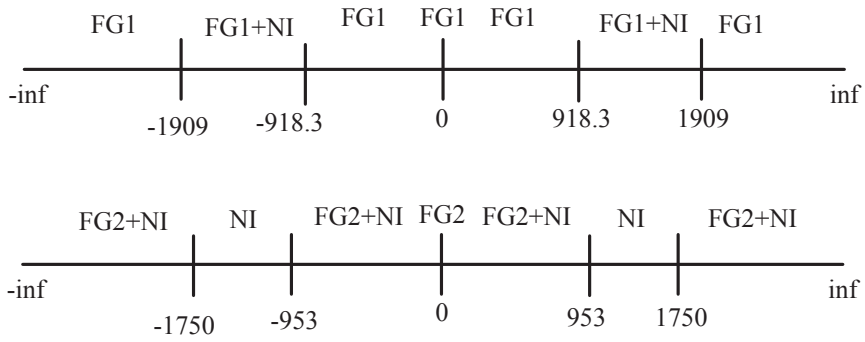


**Figure 3.6:** Frequency intervals in the SISO design (NI: negative-imaginary, FG1: finite-gain for system $M_1$, FG2: finite-gain for system $M_2$).

where $k_v > 0$ is the gain of the controller, $\xi_v > 0$ and $\omega_v > 0$ are the damping constant and the frequency at which resonant mode needs to be damped.

In the design process, choosing the right value of $\omega_v$ is important. It is required that $\omega_v$ is chosen to be equal or nearly equal to the first resonance frequency of the scanner. The amount of damping of the resonant mode depends on $\xi_v$ and $k_v$. Choosing a low value of $\xi_v$ would introduce a notch and undesirable phase shift in the closed-loop. For a high value of $\xi_v$, there is hardly any damping. The value of $k_v$ has an important effect on damping and stability. A low value of $k_v$ leads to a low level of damping of the resonant mode and a high value of $k_v$ can make the closed-loop system unstable.

A MIMO resonant controller has a transfer function matrix of the following form:

$$M_2(s) = -k_v \frac{s^2 + 2\xi_v\omega_v s}{s^2 + 2\xi_v\omega_v s + \omega_v^2}\beta_{m\times m} \tag{3.5}$$

where $\beta_{m\times m} \geq 0$ is a matrix of order $m \times m$. Here, $m$ is the number of inputs and outputs of the system. For the PTS, $\beta_{m\times m}$ is a $2 \times 2$ matrix.

In order to guarantee the closed-loop stability of the feedback interconnection between the PTS and resonant controller and to achieve a large degree of damping of the resonant mode of the scanner, this design of the resonant controller is based on the framework of [45]. It is shown in [45] that, the positive feedback interconnection as given in Fig. 3.5 between two strictly proper, causal and linear time invariant systems $M_1(s)$ and $M_2(s)$ with mixed NI and finite-gain properties bounded by gains $k_1$ and $k_2$, respectively is stable if the following conditions are satisfied:

(1) $\lim_{\omega\to\infty} M_1(j\omega)M_2(j\omega) = 0$.

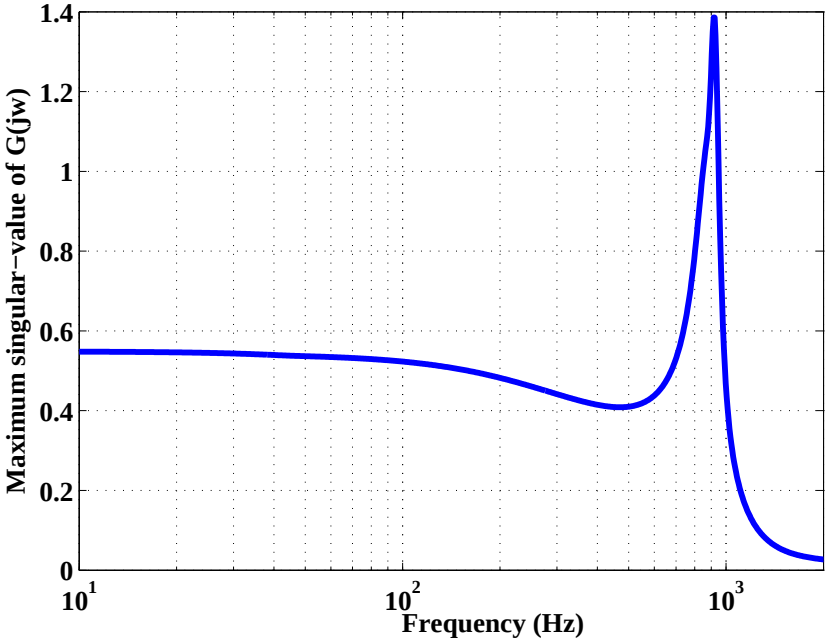


**Figure 3.7:** Maximum singular value ($\bar{\sigma}(G(j\omega))$) plot of $M_1(s)$.

(2) The systems $M_1(s)$ and $M_2(s)$ are bounded by gains $k_1$ and $k_2$, respectively such that, $k_1 > |M_1(0)|$, $k_2 > |M_2(0)|$, and $k_1 k_2 < 1$.

(3) In the intervals, $\omega \in [\omega_i, \omega_{i+1}]$, if $M_1(j\omega)$ does not have the NI property, both $M_1(j\omega)$ and $M_2(j\omega)$ must be bounded by gains $k_1$ and $k_2$, i.e., $|M_1(j\omega)| < k_1$ and $|M_2(j\omega)| < k_2$ for all $\omega \in [\omega_i, \omega_{i+1}]$.

(4) In the intervals, $\omega \in [\omega_p, \omega_{p+1}]$, if $M_1(j\omega)$ has the NI property and bounded by the gain $k_1$, $M_2(j\omega)$ must either have NI property or be bounded by the gain $k_2$ or both.

In order to translate the mixed negative-imaginary and small-gain approach into a suitable design process for the PTS and a resonant controller the following steps are carried out:

(i) Find the frequency intervals at which the system $M_1(s)$ has the NI property.

(ii) Select a gain $k_1$ such that at the frequency intervals where $M_1(s)$ does not have the NI property the system is bounded by the gain $k_1$.

(iii) Make the gain $k_1$ as low as possible such that, $M_1(s)$ has either the NI property or has a finite-gain bounded by the gain $k_1$ or both at each frequency interval in order to achieve a large gain of the controller.

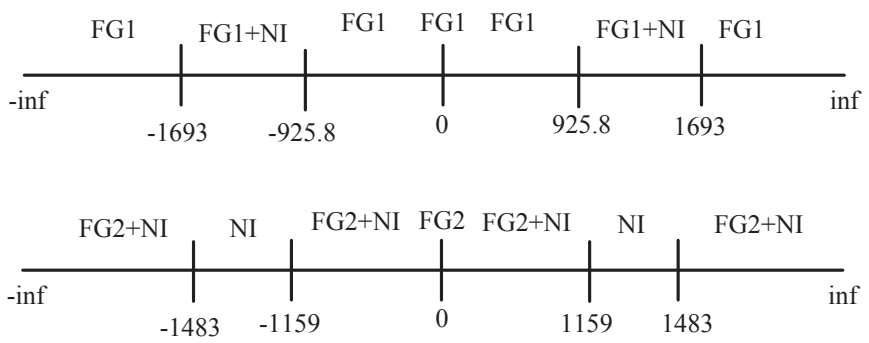


**Figure 3.8:** Frequency intervals in the MIMO design (NI: negative-imaginary, FG1: finite-gain for system $M_1$, FG2: finite-gain for system $M_2$).

(iv) Find the frequency intervals at which $M_1(s)$ has only the NI property, only the finite-gain property bounded by the gain $k_1$ and both.

(v) Select the controller $M_2(s)$ parameters and find the frequencies at which $M_2(s)$ has the NI property.

(vi) Increase the gain of the controller $M_2(s)$ to be as large as possible and select the gain $k_2$ for $M_2(s)$ such that, (a) $k_1k_2 < 1$, (b) $M_2(s)$ has only the NI property at the frequency intervals where $M_1(s)$ has only the NI property, (c) $M_2(s)$ has only the finite-gain property bounded by the gain $k_2$ at the frequency intervals where $M_1(s)$ has only the finite-gain property bounded by the gain $k_1$, and (d) $M_2(s)$ has either the NI or finite-gain properties bounded by $k_2$ at the frequencies where $M_1(s)$ has both the NI and finite-gain properties bounded by the gain $k_1$.

Details of selecting the parameters of the controllers along with a corresponding stability analysis are given in the next section.

## 3.5 Selection of the Controller Parameters and Stability of the Closed-loop System

### The SISO Case

The PTS used in this chapter has its first resonance frequency in the X-axis at 918 Hz (see Fig. 3.2). In this section, the transfer function model (3.1) is treated as system 1 ($M_1(s)$) and (3.4) is treated as system 2 ($M_2(s)$). System 1 has the NI property in the frequency interval between 918.3 Hz and $1.91 \times 10^3$ Hz. The DC gain $M_1(0)$ of (3.1) is 0.54. It is required to select the gain $k_1$ above 0.54 for system 1. Also, the gain $k_1$ has to be selected in a way such that the system 1 has either

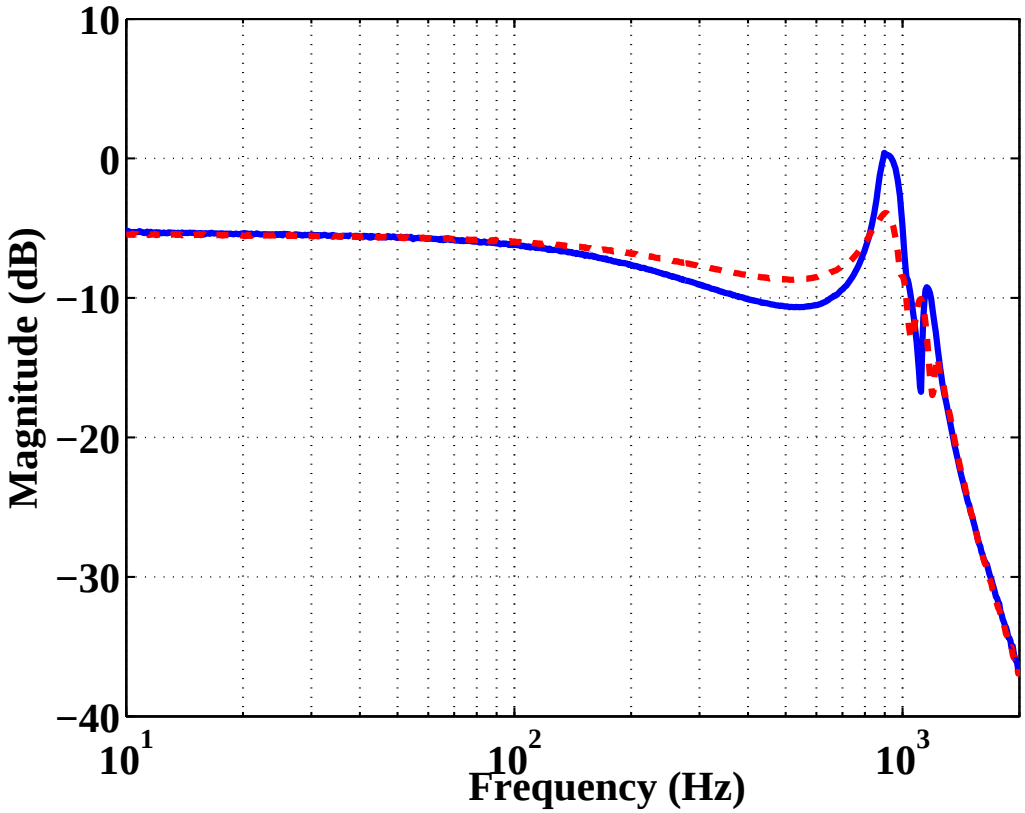


**Figure 3.9:** Measured open- (– the solid line) and closed-loop (- - the dashed line) frequency responses of the plant output for SISO design.

the NI or finite-gain (FG) properties bounded by gain $k_1$ or both at each frequency. A value of the gain $k_1$ less than 1.03 introduces a frequency interval where system 1 has neither the NI nor FG properties bounded by gain $k_1$. Therefore, the value of gain $k_1$ is selected as 1.05.

Now in order to meet the requirement discussed above for the SISO controller design, the values of the controller parameters are selected as $k_v = 0.8$, $\omega_v = 954.9$ Hz, and $\xi_v = 0.56$. Selecting the gain $k_2 = 0.95$, the mixed properties for system 2 is shown in Fig. 3.6. System 2 has only the NI property in the frequency interval between 953.3 Hz and 1750 Hz and in the frequency interval between $-1750$ Hz and $-953.3$ Hz. System 2 has both the NI and FG properties bounded by gain $k_2$ for the remaining frequencies. At each frequency both systems have the same properties, i.e., either the NI or FG and $k_1 k_2 < 1$. Hence, the closed-loop system corresponding to interconnection between $M_1(s)$ and $M_2(s)$ is stable.

**The MIMO Case**

The MIMO controller design is based on the maximum singular value of the plant $M_1(s)$ and the controller $M_2(s)$. For a square matrix $P$, the square roots of the eigenvalues of $P^*P$, where $P^*$ is the complex conjugate transpose of P, are called singular values. In this section, the system (3.5) is treated as system 1 ($M_1(s)$) and the system (3.5) is treated as system 2 ($M_2(s)$). A plot of the maximum singular values of the MIMO plant (3.3) given in Fig. 3.7 shows that the maximum singular value of the MIMO plant at zero frequency ($\bar{\sigma}(M_1(0))$) is 0.55. From Fig. 3.4 it can be observed that the MIMO PTS system has the NI property between 925.8 Hz and $1.69 \times 10^3$ Hz. The gain $k_1$ is required to be selected above 0.55 so that at each frequency system 1 has either the NI or FG properties bounded by the gain $k_1$ or both. Selecting the gain $k_1 = 1.37$ for the MIMO system (3.3), the mixed properties are shown in Fig. 3.8. The MIMO system (3.3) has both the NI and FG properties bounded by gain $k_1$ in the frequency interval between 925.8 Hz and $1.69 \times 10^3$ Hz and in the frequency interval between $-925.8$ Hz and $-1.69 \times 10^3$ Hz. It has only the FG property bounded by the gain $k_1$ in the remaining frequencies.

To meet the requirements discussed above for the MIMO resonant controller design, the values of the MIMO controller parameters are selected as $k_v = 0.8$, $\omega_v = 954.9$ Hz, $\xi_v = 0.56$, and $\beta_{m\times m} = \begin{bmatrix} 0.61 & 0.005 \\ 0.005 & 0.61 \end{bmatrix}$. Selecting the gain $k_2 = 0.725$, the mixed properties for system (3.5) are shown in Fig. 3.8. System (3.5) has only the NI property in the frequency interval from 1159 Hz and 1483 Hz and in the frequency interval from $-1159$ Hz and $-1483$ Hz. It has both the NI and FG properties bounded by gain $k_2$ in the remaining frequencies. Now at each frequency both systems have the same properties, i.e., either the NI or FG and $k_1k_2 < 1$. Hence, the closed-loop system corresponding to interconnection between $M_1(s)$ and $M_2(s)$ for MIMO case is stable.

## 3.6 Experimental Verification

The performance of the proposed controller is examined first by measuring the open- and closed-loop frequency responses in the X- and Y-axis of the scanner. Comparisons of the SISO and MIMO open- and closed-loop frequency responses are given in Fig. 3.9 and Fig. 3.10, which show that the resonant controller is able to provide

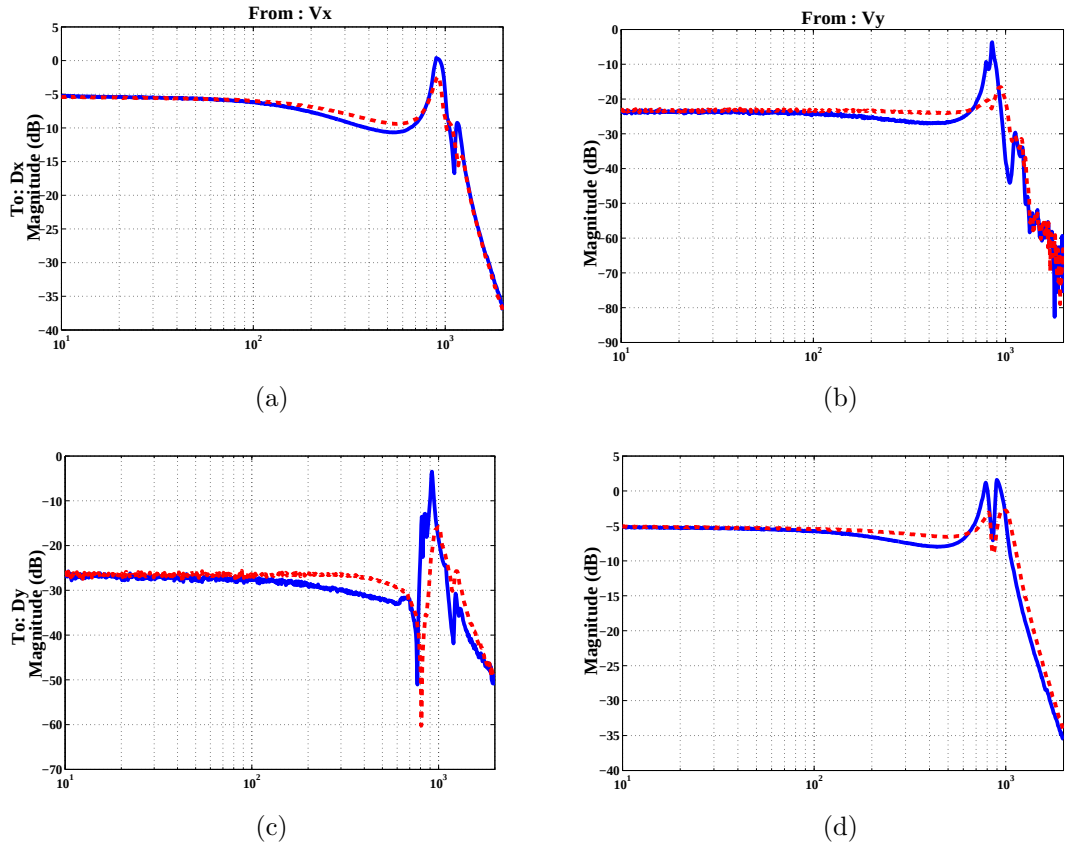


**Figure 3.10:** Measured magnitude frequency responses relating the inputs $[V_x, V_y]^T$ and the outputs $[D_x, D_y]^T$. The solid line (–) represents the measured open-loop frequency responses and the dashed line (- -) represents the measured closed-loop frequency responses. (a) Frequency response of $G_{xx}(s)$, (b) frequency response of $G_{yx}(s)$, (c) frequency response of $G_{xy}(s)$, and (d) frequency response of $G_{yy}(s)$.

3.5 dB and 3.0 dB damping of the first resonant mode of the scanner in the X-axis for the SISO and MIMO cases, respectively.

To illustrate the controller performance in the time domain, triangular voltage signals of different frequencies (50 Hz, 100 Hz, 150 Hz, 200 Hz) are applied to the X-axis of the scanner in the open- and closed-loop cases and the corresponding X sensor outputs are recorded. Fig. 3.11 shows the outputs from the X sensor in open- and closed-loop cases for different frequencies obtained by using the SISO resonant controller in the X-axis of the scanner. A small time delay was purposely added to the open- and closed-loop sensor outputs in order to clearly display the open- and closed-loop time responses. The closed-loop X sensor output shows less vibration than the open-loop sensor output.

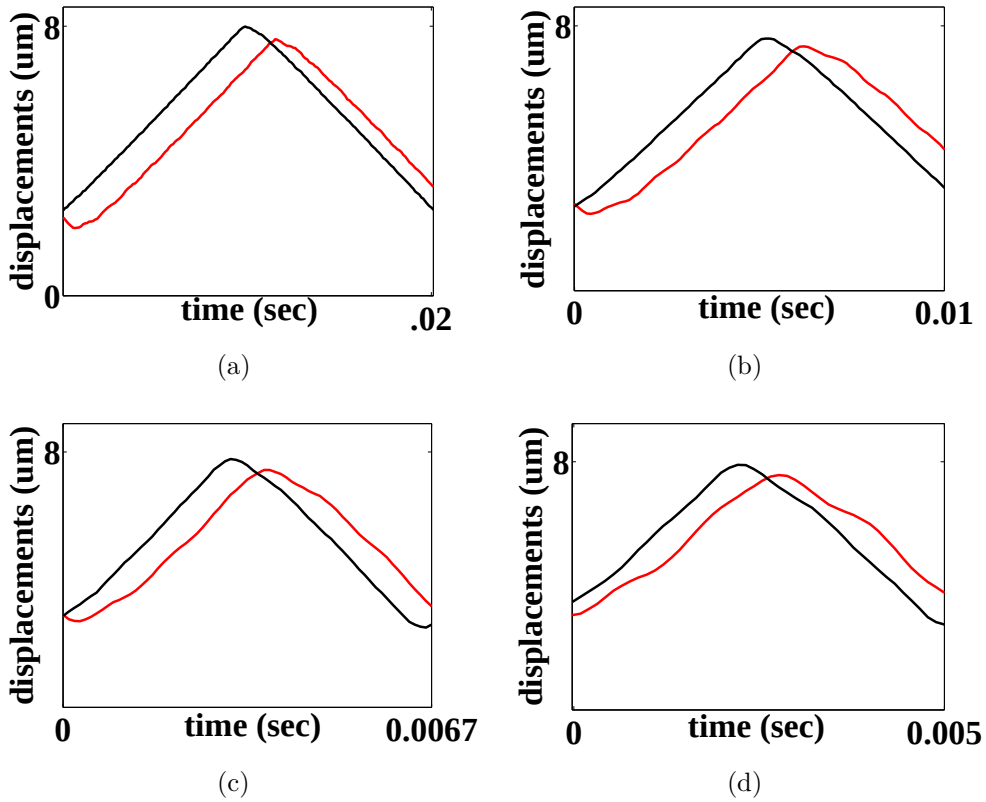


**Figure 3.11:** Open- (red solid line) and closed-loop (black solid line) X sensor output signals for (a) 50 Hz, (b) 100 Hz, (c) 150 Hz, and (d) 200 Hz triangular input signals in SISO design.

The time domain performance of the proposed controller is further examined by applying pulse signals of 1 Hz, 10 Hz, 50 Hz, and 100 Hz to the X-axis of the scanner for the SISO case. The X sensor outputs in open- and closed-loop cases for different frequencies of the pulse signals are given in Fig. 3.12 which shows that the proposed controller is able to reduce the settling time to 17 percent of each pulse period at low frequencies with a significant reduction of vibration.

In order to show the advantage of the mixed NI and small-gain approach as compared to the small-gain only approach, a design of the SISO resonant controller using the small-gain only approach is presented. The resonant controller design using the small-gain only approach limits the loop-gain to be strictly less than one, whereas the mixed NI and small-gain approach allows the loop-gain to be greater than one as shown in Fig. 3.13. The gain of the resonant controller obtained in the small-gain only approach is 0.66, whereas the gain of the resonant controller

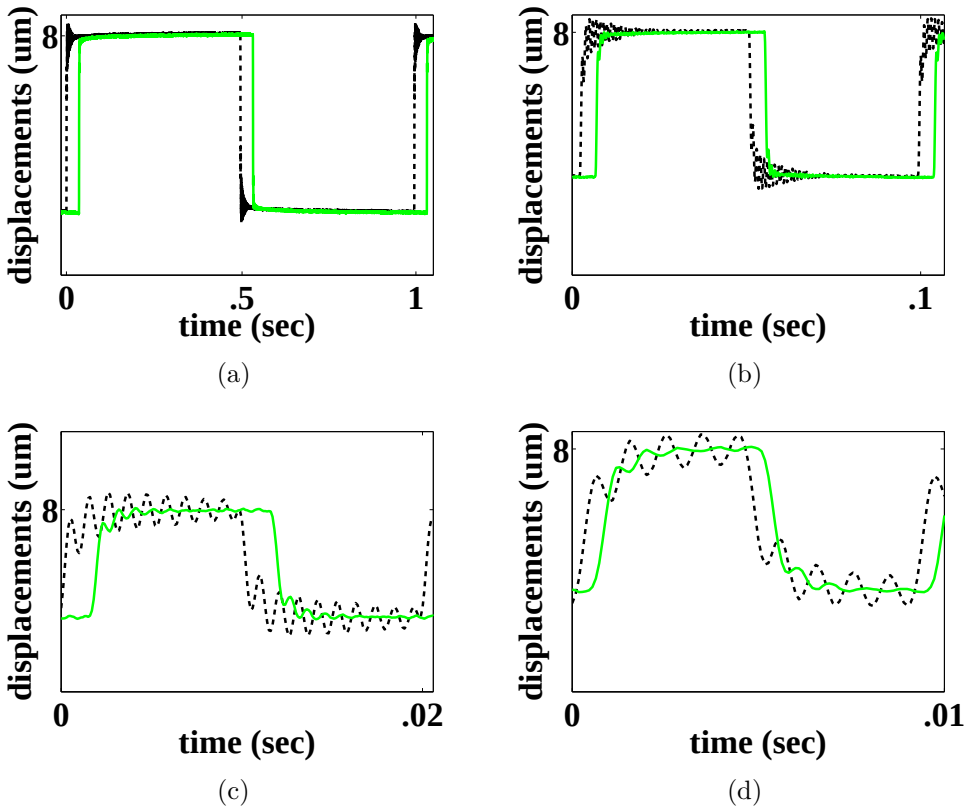


**Figure 3.12:** Open- (- - the dashed line) and closed-loop (– the solid line) X sensor output signals for (a) 1 Hz, (b) 10 Hz, (c) 50 Hz, and (d) 100 Hz pulse input signals in SISO design.

obtained in the mixed negative-imaginary and small-gain approach is 0.8. The resonant controller with gain 0.8 achieved a reduction of resonant peak 3.5 dB and the resonant controller with gain 0.66 achieved a reduction of resonant peak 2.85 dB as shown in Fig. 3.14.

## 3.7 Chapter Summary

In this chapter, a SISO and a MIMO NI damping controller, i.e., the resonant controller is designed to damp the first resonant mode of a PTS which is not NI. The controller design presented is based on a mixed NI and small-gain approach, which not only establishes the finite-gain stability of the closed-loop system but also achieves larger damping of the first resonant mode of the scanner compared to the small-gain only approach. The experimental results show that the resonant controller provides 3.5 dB and 2.85 dB damping of the first resonant mode of the

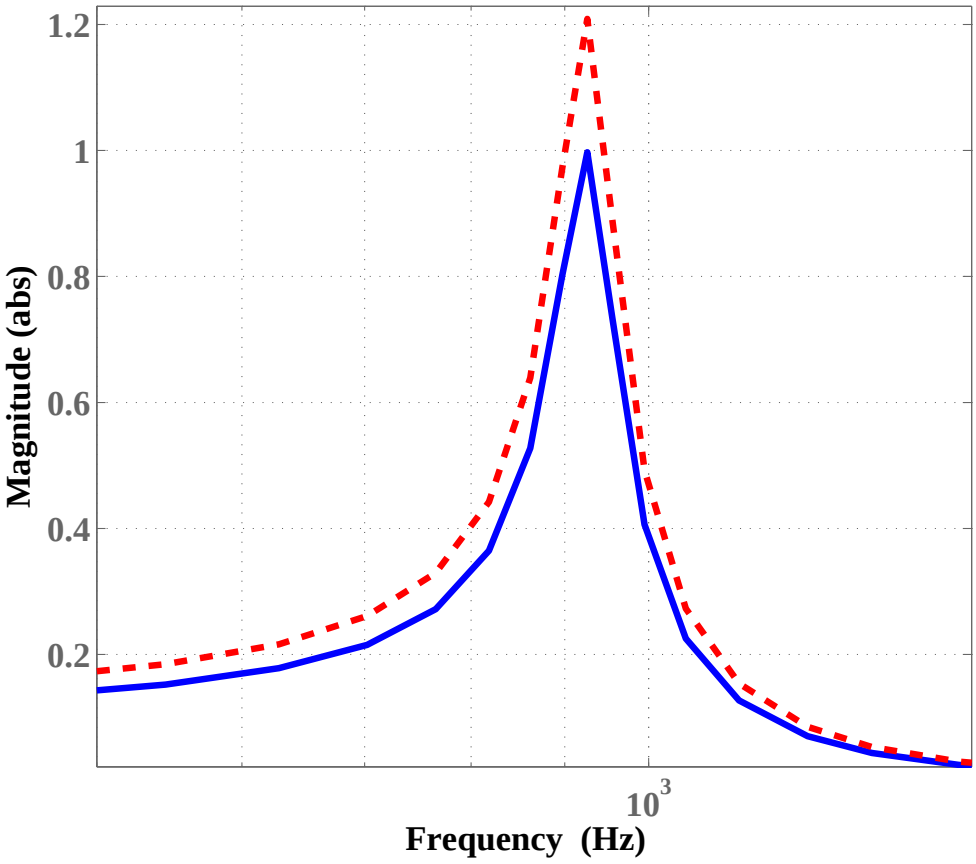


**Figure 3.13:** Loop-gains $M_1(j\omega)M_2(j\omega)$ for SISO cases when the resonant controller is designed using the small-gain only approach (– the solid line) and the mixed negative-imaginary and small-gain approach (- - the dashed line).

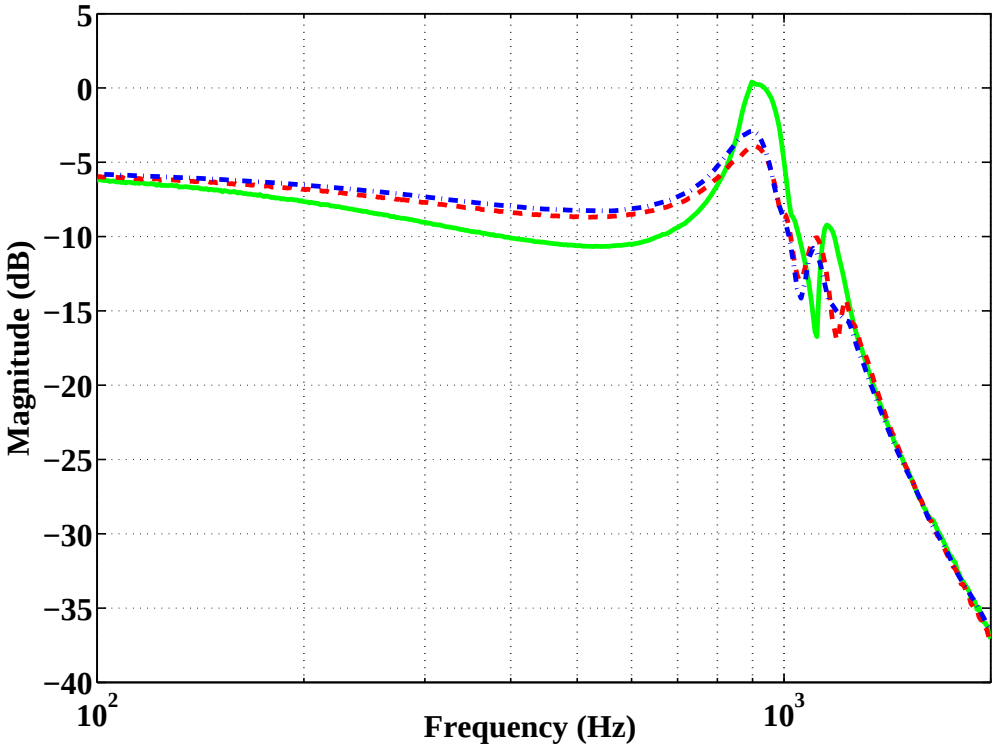


**Figure 3.14:** Measured open- (– the solid line) and closed-loop frequency responses of $G_{xx}(s)$ for SISO case when the resonant controller is designed using the small-gain approach (-. dashed dot line) and the mixed negative-imaginary and small-gain approach (- - the dashed line).

scanner when the resonant controller is designed based on the mixed NI and small-gain approach [45] and the small-gain only approach, respectively.

Resonant controller provides large gain and phase margins as compared to other NI damping controllers such as PPF controller and IRC controller. Resonant controller is a high pass controller. Due to its high pass nature the resultant closed-loop system may suffer from the problem of addition of high frequency sensor noise. This addition of high frequency sensor noise can limit the performance of the controller where an extreme level of precision is required. In order to compensate for the addition of high frequency sensor noise we have proposed a design of another damping controller namely a passive damping controller in the next chapter.

# Chapter 4

# Passive Damping Controller Design for Piezoelectric Tube Scanners

This chapter describes the design of another damping controller namely a passive damping controller for the PTS to damp the first resonant mode. One of the limitation of using the resonant controller discussed in Chapter 3 for the PTS is its high pass nature which results in large high frequency sensor noise. The motivation for designing a passive damping controller for a nanopositioner is its bandpass nature which not only results in large gain and phase margins but also results in low level of sensor noise. The design of the controller is carried out by proposing a novel analytical framework. The analytical framework examines the finite-gain stability for a positive feedback interconnection between two stable, linear time-invariant systems where one system has mixed passivity, negative-imaginary and small-gain properties and the other system has mixed negative-imaginary, negative-passivity, and small-gain properties. The motivation to propose a mixed passivity, negative-imaginary and small-gain approach as compared to the mixed negative-imaginary and small-gain approach is to achieve a large gain of the controller, which allows a large level of damping of the resonant mode of the scanner.

## 4.1 Introduction

A linear system $P(s)$ is said to be passive if $Re[P(j\omega)] \geq 0$ for all $\omega > (0, \infty)$ [57]. If a square transfer function matrix $P(s)$ is passive then it follows that $P(j\omega)+P^*(j\omega) \geq 0$, for all $\omega \in \mathbb{R}$ such that $s = j\omega$ is not a pole of $P(s)$ [56] where $P^*(j\omega)$ is the complex conjugate transpose of the matrix $P(j\omega)$. If $P(s)$ is a single-input single-output (SISO) passive transfer function, then, this is equivalent to the phase condition $\angle P(j\omega) \in [-\pi/2, \pi/2]$ for all $\omega > (0, \infty)$. A transfer function matrix $P(s)$ is said to have the passivity property at frequency $\omega$ if $P(j\omega) + P^*(j\omega) \geq 0$ at $\omega$.

Passive systems are of interest because of their many practical applications, e.g., lightly damped flexible structures with collocated velocity sensors and force actuators [56, 61]. The term collocated refers to the fact that the sensors and the

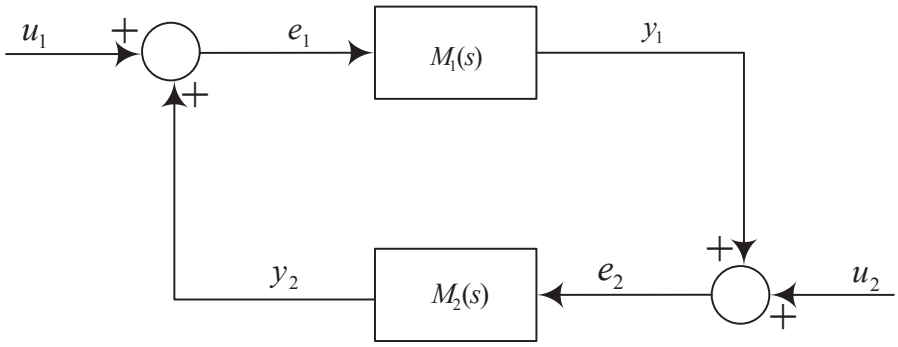


**Figure 4.1:** Interconnection of systems with positive feedback.

actuators have the same location and same direction [53]. Collocated control with velocity measurements is referred to as negative-velocity feedback and can be used directly to increase the effective damping of structures [56]. The transfer functions of such flexible structures with collocated velocity sensors and force actuators are modeled by a sum of second order transfer functions $G(s) = \sum_{i=1}^{M} \frac{\phi\phi^T s}{s^2+2\xi_i\omega_i s+\omega_i^2}$, where $\xi_i > 0$ is the damping coefficient associated with the ith mode, $\omega_i > 0$ is the resonance frequency of the $i^{th}$ mode, $M$ is the total number of modes and $\phi$ is a column vector obtained from the boundary conditions on the corresponding partial differential equations [56, 61]. A guarantee of the closed-loop stability between systems with collocated velocity sensors and force actuators and passive controllers can be established using the passivity theorem [61].

The passivity theorem states that the negative feedback interconnection between two stable linear time invariant passive systems is stable where one of the system is strictly passive [57]. The theoretical properties of negative-velocity feedback are based on the idealized assumption of collocation and require the availability of velocity sensors [56]. An alternative approach to negative-velocity feedback is positive-position feedback, where position sensors are used in place of velocity sensors [56]. The use of position sensors in flexible structures corresponds to a class of systems called negative-imaginary (NI) system [55, 56, 62].

A transfer function $G(s)$ is said to be NI if $j[G(j\omega) - G^*(j\omega)] \geq 0$ for all $\omega \in (0, \infty)$ [55, 56]. A transfer function matrix $G(s)$ is said to have the NI property at frequency $\omega$ if $j[G(j\omega)-G^*(j\omega)] \geq 0$ at frequency $\omega$. For a SISO NI system $G(s)$, this is equivalent to the phase condition $\angle G(j\omega) \in [-\pi, 0]$ for all $\omega \in (0, \infty)$. A necessary and sufficient condition for the stability of the positive feedback interconnection

between two NI systems $M_1(s)$ and $M_2(s)$ as shown in Fig.4.1 is a condition on the dc loop gain and one of the systems is required to be strictly NI [55, 62]. A transfer function $G(s)$ is said to be strictly negative-imaginary if $j[G(j\omega) - G^*(j\omega)] > 0$ for all $\omega \in (0, \infty)$ [62].

There are many cases where interconnected systems do not have either the passivity or NI properties over all frequencies [45]. Rather, the systems have mixed properties; i.e., the passivity or NI properties are satisfied only on certain frequency intervals. The systems may have small-gain property at other frequencies. A system $G(s)$ is said to have the small-gain property at frequency $\omega$ if $|G(j\omega)| < 1$ at frequency $\omega$. The small-gain theorem states that the feedback interconnection of two linear stable time invariant systems $M_1(s)$ and $M_2(s)$ as shown in Fig.4.1 is stable if $|M_1(j\omega)|\ |M_2(j\omega)| < 1$ for all $\omega \in (0,\ \infty)$ [57].

A mixed NI and small-gain approach [45] can be used to establish the closed-loop stability between PTSs and NI damping controllers. A mixed NI and small-gain approach allows only a low gain of the controller which in turn results in a low level damping of the resonant mode of the scanner. Another limitation of the mixed NI and small-gain approach [45] is that, it cannot guarantee the closed-loop stability for PTSs with passive damping controllers such as velocity feedback controllers [61]. The proposed framework enables the closed-loop stability in both cases.

Consider the following two transfer functions where $M_1(s)$ is the transfer function between a force actuator and a position sensor of a PTS obtained from [4] and $M_2(s)$ is the transfer function of a velocity feedback controller:

$$M_1(s) = \frac{-186.6s^2 + 1.348 \times 10^6 s - 2.412 \times 10^{10}}{s^3 + 1955s^2 + 3.452 \times 10^7 s + 4.459 \times 10^{10}} \tag{4.1}$$

$$M_2(s) = \frac{-12000s}{s^2 + 6474s + 3.341 \times 10^7} \tag{4.2}$$

Consider $M_1(s)$ and $M_2(s)$ are connected in a positive feedback as shown in Fig. 4.1. The Nyquist plots of these systems given in Fig. 4.2 show that $M_1(s)$ and $M_2(s)$ are neither NI nor passive systems. The internal stability of the interconnection between the systems $M_1(s)$ and $M_2(s)$ can not be established by using the negative-imaginary theorem or passivity theorem alone. The magnitude of the loop-gain $|M_1(j\omega)||M_2(j\omega)|$ is also not less than one over all frequencies as can be

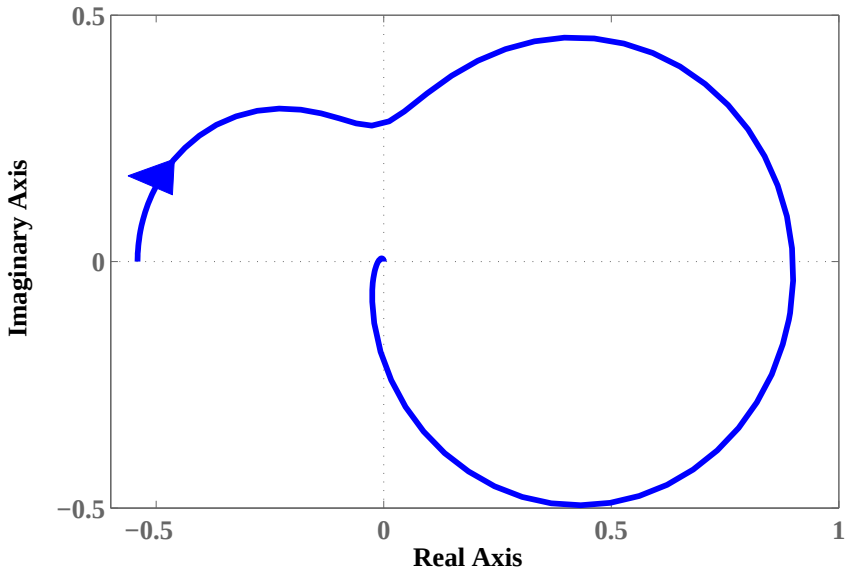


(a)

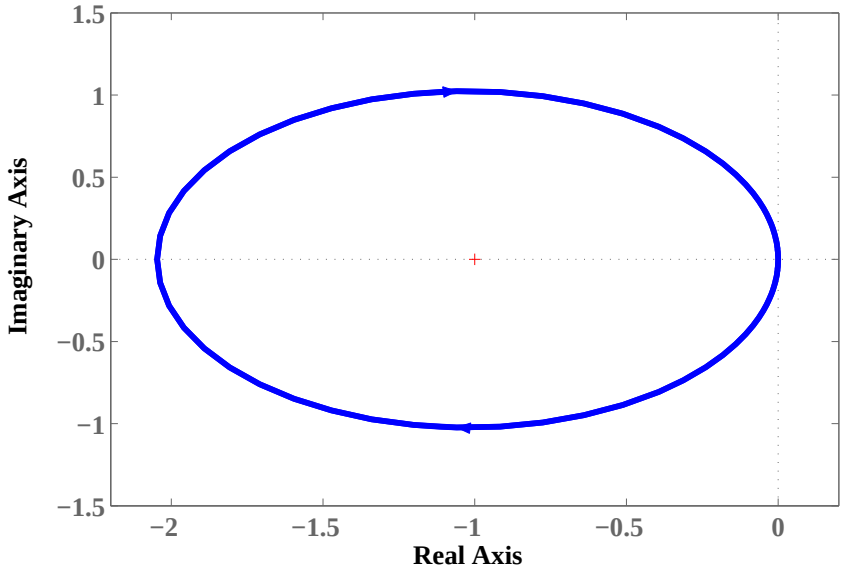


(b)

**Figure 4.2:** (a) Nyquist diagram of $M_1(s)$ of (4.1) for positive frequencies, (b) Nyquist diagram of $M_2(s)$ of (4.2) for positive frequencies.

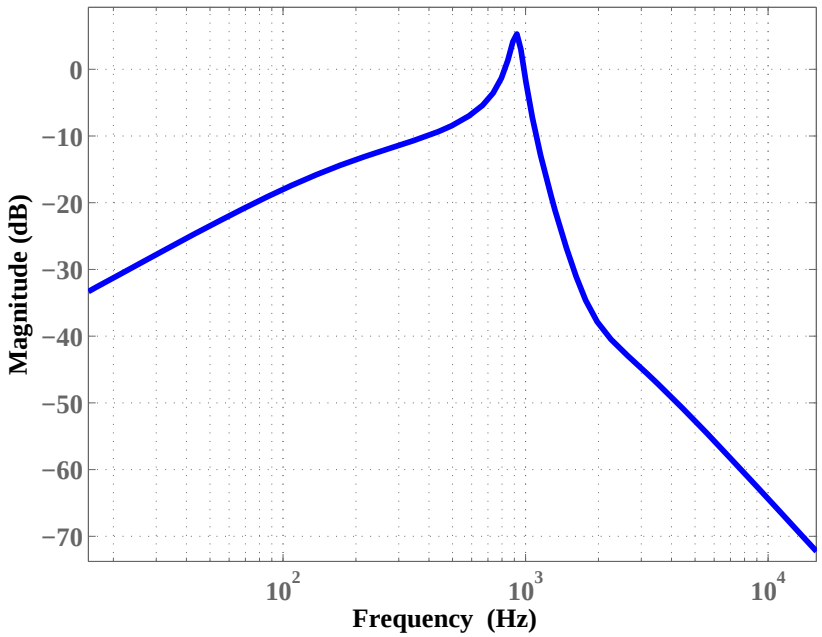


**Figure 4.3:** Magnitude Bode diagram of $M_1(s) * M_2(s)$.

seen from Fig. 4.3 which means that the small-gain theorem cannot be applied in this case.

Motivated by the above practical example of PTSs, we propose a result which merges the passivity, NI, and small-gain theorems in order to establish the closed-loop stability of the positive feedback interconnection between a system with mixed passivity, NI, and small-gain properties and a system with mixed NI, negative-passivity, and small-gain properties.

## 4.2 Mathematical Definitions of Systems

Let $\mathcal{R}^{m\times n}$ be the set of all real rational transfer function matrices and $\mathcal{RH}_\infty^{m\times n}$ be the set of all real rational stable transfer functions matrices with $m$ rows and $n$ columns. ${\mathcal{RL}_\infty}^{m\times n}$ is the set of all proper, real-rational transfer function matrices with no pole in the origin and ${\mathcal{L}_\infty}^{m\times n}$ is a Banach space of matrices. For a transfer function matrix $G(s) \in \mathcal{R}^{m\times n}$, $G^*(s)$ is the complex conjugate transpose of $G(s)$ which is defined as $G(-s)^T$. The largest and smallest singular values of a matrix $A$ are denoted by $\bar{\sigma}(A)$ and $\underline{\sigma}(A)$.

***Definition 1.*** Consider a causal linear time invariant (LTI) system with transfer function matrix $M(s) \in \mathcal{RH}_\infty^{m\times m}$. This system is said to be passive system in the frequency interval $[a, b]$ with $a \geq 0$ if there exists $\gamma$, $\delta \geq 0$ such that

$$-\gamma M^*(j\omega)M(j\omega) + M^*(j\omega) + M(j\omega) - \delta I \geq 0.$$

The system in Definition 1 is said to be input strictly passive if Definition 1 is satisfied with $\gamma = 0$; output strictly passive if Definition 1 is satisfied with $\delta = 0$ and passive if Definition 1 is satisfied with $\gamma = \delta = 0$ for all $\omega \in [a, b]$.

***Definition 2.*** A linear causal time invariant system with transfer function matrix $M(s) \in \mathcal{RH}_\infty^{m\times m}$ is said to be negative passive in the frequency interval $[a, b]$ with $a \geq 0$ if there exists $\gamma$, $\delta \geq 0$ such that

$$-\gamma M^*(j\omega)M(j\omega) - M^*(j\omega) - M(j\omega) - \delta I \geq 0.$$

The system in Definition 2 is said to be input strictly negative passive if Definition 2 is satisfied with $\gamma = 0$; output strictly negative passive if Definition 2 is satisfied with $\delta = 0$ and negative passive if Definition 2 is satisfied with $\gamma = \delta = 0$ for all $\omega \in [a, b]$.

***Definition 3.*** A linear causal time invariant system with transfer function matrix $M(s) \in \mathcal{RH}_\infty^{m\times m}$ is said to be negative-imaginary in the frequency interval $[a, b]$ with $a \geq 0$ if there exists $\alpha$, $\beta \geq 0$ such that

$$-\alpha\omega^2 M^*(j\omega)M(j\omega) + j\omega M(j\omega) - j\omega M^*(j\omega) - \beta I \geq 0.$$

The system in Definition 3 is said to be input strictly negative-imaginary if Definition 3 is satisfied with $\alpha = 0$; output strictly negative-imaginary if Definition 3 is satisfied with $\beta = 0$ and negative-imaginary if Definition 3 is satisfied with $\alpha = \beta = 0$ for all $\omega \in [a, b]$.

***Definition 4.*** A linear causal time invariant system with transfer function matrix $M(s) \in \mathcal{RH}_\infty^{m\times m}$ is said to be finite-gain system bounded by a gain $k \geq 0$ in the frequency interval $[a, b]$ with $a \geq 0$ if

$$k := inf\{\bar{k} \in \mathbb{R}_+ : -M^*(j\omega)M(j\omega) + \bar{k}^2 I \geq 0\}$$

for all $\omega \in [a, b]$.

***Definition 5.*** A linear causal time invariant system with transfer function matrix $M(s) \in \mathcal{RH}_\infty^{m\times m}$ is said to be a system with mixed negative-imaginary, passivity and finite-gain properties bounded by a gain $k \geq 0$ if, for each frequency $\omega \in \mathbb{R}\cup\{\pm\infty\}$ : either (i) $-\alpha\omega^2 M^*(j\omega)M(j\omega)+j\omega M(j\omega)-j\omega M^*(j\omega)-\beta I \geq 0$; or (ii) $-\gamma M^*(j\omega)M(j\omega)+M^*(j\omega)+M(j\omega)-\delta I \geq 0$; or (iii) $-M^*(j\omega)M(j\omega)+k^2 I \geq 0$, where $\alpha, \beta, \gamma, \delta, k \geq 0$.

***Definition 6.*** A linear causal time invariant system with transfer function matrix $M \in \mathcal{RH}_\infty^{m\times m}$ is said to be a system with mixed negative-imaginary, negative-passivity and finite-gain properties bounded by a gain $k \geq 0$ if, for each frequency $\omega \in \mathbb{R}\cup\{\pm\infty\}$ : either (i) $-\alpha\omega^2 M^*(j\omega)M(j\omega)+j\omega M(j\omega)-j\omega M^*(j\omega)-\beta I \geq 0$; or (ii) $-\gamma M^*(j\omega)M(j\omega)-M^*(j\omega)-M(j\omega)-\delta I \geq 0$; or (iii) $-M^*(j\omega)M(j\omega)+k^2 I \geq 0$, where $\alpha, \beta, \gamma, \delta, k \geq 0$.

## 4.3 Test for Determining Mixedness of a System Using Hamiltonian Matrices

In order to apply the robust stability results on the interconnection between two stable, linear time-invariant systems where one system has mixed passivity, negative-imaginary, and small-gain properties and the other system has mixed negative-imaginary, negative-passivity, and small-gain properties, it is necessary to test the property of systems at each frequency. In this chapter, for a given transfer function matrix $G(s)$, we compute the spectrum of the corresponding Hamiltonian matrices to test the property of systems at each frequency.

### 4.3.1 NI test for multiple-input multiple-output (MIMO) LTI systems

Here, we present a test which characterizes a spectral method based on the Hamiltonian matrix to test the property of an NI system at each frequency.

Consider a square transfer function matrix $G(s)$ with minimal state-space representation

$$\dot{x}(t) = Ax(t) + Bu(t), \tag{4.3}$$

$$y(t) = Cx(t) + Du(t), \tag{4.4}$$

where $A \in \mathbb{R}^{n\times n}, B \in \mathbb{R}^{n\times m}, C \in \mathbb{R}^{m\times n}$, and $D \in \mathbb{R}^{m\times m}$.

We start with the following lemma.

**Lemma 1** *Consider a square transfer function matrix $G(s)$ with minimal state space realization* $\left[\begin{array}{c|c} A & B \\ \hline C & D \end{array}\right]$. *Suppose $A$ has no pure imaginary eigenvalues, $D = D^T$, and $\gamma \geq 0$ is not an eigenvalue of the matrix $(CB + B^TC^T)$. Then, $\gamma \in \lambda(T(j\omega_0))$ if and only if $j\omega_0 \in \lambda(N_\gamma)$. Here, $\lambda(T(j\omega))$ denotes the set of eigenvalues of the matrix $T(j\omega) = j\omega(G(j\omega) - G(j\omega)^*)$ and the Hamiltonian matrix $N_\gamma$ is defined as*

$$N_\gamma = \begin{bmatrix} A + BQ_\gamma^{-1}CA & BQ_\gamma^{-1}B^T \\ -A^TC^TQ_\gamma^{-1}CA & -A^T - A^TC^TQ_\gamma^{-1}B^T \end{bmatrix} \tag{4.5}$$

*with $Q_\gamma = \gamma I - CB - B^TC^T$.*

**Case 1**

In this case $CB+B^TC^T > 0$ and the Hamiltonian matrix can be constructed directly to check the NI property of the given MIMO LTI system.

**Theorem 1** *Consider an LTI system with square transfer function matrix $G(s)$ and minimal state space realization (4.3)-(4.4). Also, suppose that $CB+B^TC^T > 0$, $A$ is Hurwitz and $D = D^T$. Then the transfer function matrix $G(s)$ is NI over $\omega \in [a, b]$ if and only if*

1. *the Hamiltonian matrix,*

$$N_0 = \begin{bmatrix} A + BQ_0^{-1}CA & BQ_0^{-1}B^T \\ -A^TC^TQ_0^{-1}CA & -A^T - A^TC^TQ_0^{-1}B^T \end{bmatrix} \tag{4.6}$$

*has no pure imaginary eigenvalues with odd multiplicity in $\omega \in (a, b)$. Here, $Q_0 = -(CB + B^TC^T)$.*

2. *There exist at least one* $\omega_0 \in [a, b]$ *such that* $j\omega_0(G(j\omega_0) - G(j\omega_0)^*) > 0$.

The proof of this theorem will be similar to the proof of Theorem 1 in [63].

**Case 2**

We now consider the case where $CB + B^T C^T$ is singular. Here, the Hamiltonian method needs to be modified in order to derive spectral conditions for the NI property.

**Theorem 2** *Consider an LTI system with square transfer function matrix* $G(s)$ *and minimal state-space realization* (4.3)-(4.4). *Also, suppose that* $A$ *is Hurwitz,* $\det(CB + B^T C^T) = 0$, $D = D^T$, *and* $j\omega_0(G(j\omega_0) - G(j\omega_0)^*) > 0$ *for some* $\omega_0 \in \omega \in [a, b]$. *Then,* $G(s)$ *is NI over* $\omega \in [a, b]$ *if and only if the Hamiltonian matrix*

$$N = \begin{bmatrix} \bar{A} + \bar{B}\bar{Q}^{-1}\bar{C} & \bar{B}\bar{Q}^{-1}\bar{B}^T \\ -\bar{C}^T\bar{Q}^{-1}\bar{C} & -\bar{A}^T - \bar{C}^T\bar{Q}^{-1}\bar{B}^T \end{bmatrix} \tag{4.7}$$

*has no pure imaginary eigenvalues with odd multiplicity. Here,* $\bar{Q} = -(\bar{D} + \bar{D}^T)$, $\bar{A} = \tilde{A}^{-1}, \tilde{A} = A - j\omega_0 I, \bar{B} = -\tilde{A}^{-1}B, \bar{C} = CA\tilde{A}^{-1}$, *and* $\bar{D} = CB - CA\tilde{A}^{-1}B$.

The proof of this theorem will be similar to the proof of Theorem 2 in [63].

### 4.3.2 Passivity test for MIMO LTI systems

In this section, we recall the results from [64] which characterize a spectral method based on the Hamiltonian matrices to verify whether or not a given system satisfies the passivity property and the small gain theorem in a finite frequency interval.

**Passivity test**

**Theorem 3** *Consider an LTI system with transfer function matrix* $G(s)$ *and minimal state space realization* (4.3)-(4.4). *Suppose* $l \in \mathbb{R}$. *The matrix* $G(j\omega_0) + G(j\omega_0)^* - lI$ *has no zero eigenvalues over* $\omega \in [a, b]$ *if and only if* $H_1$ *does not have eigenvalues on the imaginary axis between and including* $-ja$ *and* $-jb$, *where*

$$H_1 = \begin{bmatrix} -A + BX_1^{-1}C & -BX_1^{-1}B^T \\ -C^T X_1^{-1}C & A^T - C^T X_1^{-1}B^T \end{bmatrix}, \tag{4.8}$$

$X_1 = D^T + D - lI$ *is invertable.*

**Small gain test**

**Theorem 4** *Consider an LTI system with transfer function matrix $G(s)$ and minimal state space realization* (4.3)-(4.4)*. Suppose $\epsilon \in \mathbb{R}$. The matrix $-G(j\omega_0)G(j\omega_0)^* + \epsilon^2 I$ has no zero eigenvalues over $\omega \in [a, b]$ if and only if $H_2$ dose not have eigenvalues on the imaginary axis between and including $-ja$ and $-jb$, where*

$$H_1 = \begin{bmatrix} -A - BX_2^{-1}D^TC & -BX_2^{-1}B^T \\ C^TDX_2^{-1}D^TC & A^T - C^TDX_2^{-1}B^T \end{bmatrix}, \tag{4.9}$$

*$X_2 = -D^TD + \epsilon^2 I$ is invertable.*

### 4.3.3 Test procedures

For a given system in a state-space description, we wish to determine whether or not the system is mixed. Here we present a step by step algorithm to characterize the mixedness of the system.

1. First, compute the matrix $CB + B^TC^T$, if it is invertible; then use Theorem 1 to determine the pure imaginary eigenvalues of the Hamiltonian matrix (4.6). Then, sort these purely imaginary eigenvalues with odd multiplicity such that $\omega_1 < \omega_2 < ... < \omega_k$, where $k$ is the number of purely imaginary eigenvalues of the Hamiltonian matrix. In case of $CB + B^TC^T$, is not invertible; we use Theorem 4.7 instead. Note that if $k = 0$, this implies that the system is either NI or not NI for all frequencies.

   For every frequency interval $(\omega_i, \omega_{i+1})$ compute $j(G(j\omega_m) - G(j\omega_m)^*)$ where $\omega_m \in (\omega_i, \omega_{i+1})$, i.e., a suitable choice is $\omega_m = \frac{\omega_i + \omega_{i+1}}{2}$. If $j(G(j\omega_m) - G(j\omega_m)^*) \geq 0$ then the system has the NI property in the frequency interval $(\omega_i, \omega_{i+1})$, otherwise the system does not have NI property in this frequency range. Note that if $k = 0$, this implies that the system is either NI or not NI.
2. Next, we use Theorem 3 to determine the pure imaginary eigenvalues of the Hamiltonian matrix (4.8) by choosing $l$ to be very small positive integer in the case of $D^T + D$ is singular or $l = 0$ in the case $D^T + D$ is nonsingular. Then, sort these purely imaginary eigenvalues with odd multiplicity such that $\tilde{\omega}_1 < \tilde{\omega}_2 < ... < \tilde{\omega}_{\tilde{k}}$, where $\tilde{k}$ is the number of purely imaginary eigenvalues of the Hamiltonian matrix (4.8).

   For every frequency interval $(\tilde{\omega}_i, \tilde{\omega}_{i+1})$ compute $(G(j\omega_{\tilde{m}}) + G(j\omega_{\tilde{m}})^*)$ where $\omega_{\tilde{m}} \in (\tilde{\omega}_i, \tilde{\omega}_{i+1})$, i.e., a suitable choice is $\omega_{\tilde{m}} = \frac{\tilde{\omega}_i + \tilde{\omega}_{i+1}}{2}$. If $G(\omega_{\tilde{m}}) + G(j\omega_{\tilde{m}})^*) \geq 0$

then the system has passivity property in the frequency interval $(\tilde{\omega}_i, \tilde{\omega}_{i+1})$, otherwise the system does not have the passivity property in this frequency range. Note that if $\tilde{k} = 0$, this implies that the system is either passive or not passive.

3. In the next step, we use Theorem 4 to determine the pure imaginary eigenvalues of the Hamiltonian matrix (4.9) by choosing $\epsilon < 1$. Then, sort these purely imaginary eigenvalues such that $\bar{\omega}_1 < \bar{\omega}_2 < ... < \bar{\omega}_{\bar{k}}$, where $\bar{k}$ is the number of purely imaginary eigenvalues of the Hamiltonian matrix (4.9).
   For every frequency interval $(\bar{\omega}_i, \bar{\omega}_{i+1})$ compute $G(\omega_{\bar{m}})G(\omega_{\bar{m}})^* < \epsilon I$ where $\omega_{\bar{m}} \in (\bar{\omega}_i, \bar{\omega}_{i+1})$, i.e., a suitable choice is $\omega_{\bar{m}} = \frac{\bar{\omega}_i + \bar{\omega}_{i+1}}{2}$. If $G(\omega_{\bar{m}})G(\omega_{\bar{m}})^* < \epsilon I$ then the system has the the small gain property in the frequency interval $(\bar{\omega}_i, \bar{\omega}_{i+1})$, otherwise the system does not have the small gain property in this frequency range. Note that if $\bar{k} = 0$, this implies that the system either satisfies the small gain property or not for all frequencies.
4. Finally, we compute the intersection of the intervals in step 1,2 and 3. If the intersection interval is $\phi$, then the system is mixed, otherwise the system is not mixed.

## 4.4 Interconnection of Two Mixed Systems with Positive Feedback

Consider the positive feedback interconnection between $M_1(s)$ and $M_2(s)$ as shown in Fig. 4.1, where $M_1(s)$ is a system with mixed passivity, negative-imaginary, and finite-gain properties bounded by gain $k_1$ and $M_2(s)$ is a system with mixed negative-imaginary, negative-passivity and finite-gain properties bounded by gain $k_2$ on different frequency intervals.

In the following we will show some preliminary results in order to establish the main results:

**Lemma 2** *Suppose* $M_1(j\omega) \in {\mathcal{RL}_\infty}^{m\times m}$ *and* $M_2(j\omega) \in {\mathcal{RL}_\infty}^{m\times m}$ *are two transfer function matrices where at some* $\omega \in \mathbb{R} \cup \{\pm\infty\}$, $M_1^*(j\omega) + M_1(j\omega) > 0$ *and* $-M_2^*(j\omega) - M_2(j\omega) \geq 0$, *then* $det[I - M_1(j\omega)M_2(j\omega)] \neq 0$ *and* $det[I - \frac{1}{g}M_1(j\omega)M_2(j\omega)] \neq 0$ *for any* $g \geq 1$.

*Proof:* Since $M_1^*(j\omega) + M_1(j\omega) > 0$ and $-M_2^*(j\omega) - M_2(j\omega) \geq 0$, hence, $\Re[\lambda_i[M_1(j\omega)]] > 0$ and $\Re[\lambda_i[-M_2(j\omega)]] \geq 0$ for all $\lambda_i$. Here, $\lambda_i[.]$ is the ith eigenvalue. Therefore, $M_1(j\omega)$ is nonsingular. Now, $M_1^*(j\omega) + M_1(j\omega)$ and $M_1^{-*}(j\omega) + M_1^{-1}(j\omega)$ are Hermitian congruent [65], hence, $M_1^{-*}(j\omega) + M_1^{-1}(j\omega) > 0$ which implies that, $M_1^{-*}(j\omega) - M_2^*(j\omega) + M_1^{-1}(j\omega) - M_2(j\omega) > 0$. Hence, $\Re[\lambda_i[M_1^{-1}(j\omega) - M_2(j\omega)]] > 0$ for all $\lambda_i$ and $\det[M_1^{-1}(j\omega) - M_2(j\omega)] \neq 0$ which also implies that, $\det[I - M_1(j\omega)M_2(j\omega)] \neq 0$, since, $\det[I - M_1(j\omega)M_2(j\omega)] = \det[M_1(j\omega)]\det[M_1^{-1}(j\omega) - M_2(j\omega)]$ and $M_1(j\omega)$ is nonsingular.

Now, since $M_1^{-*}(j\omega) + M_1^{-1}(j\omega) > 0$, therefore, $g(M_1^{-*}(j\omega) + M_1^{-1}(j\omega)) > 0$ for any $g \geq 1$. Also, $-M_2^*(j\omega) - M_2(j\omega) \geq 0$, hence, $gM_1^{-1}(j\omega)) - M_2(j\omega) + gM_1^{-*}(j\omega) - M_2^*(j\omega) > 0$. Therefore, $\Re[\lambda_i[gM_1^{-1}(j\omega) - M_2(j\omega)]] > 0$ for all $\lambda_i$ and $\det[gM_1^{-1}(j\omega) - M_2(j\omega)] \neq 0$ which also implies that, $\det[I - \frac{1}{g}M_1(j\omega)M_2(j\omega)] \neq 0$ for all $g \geq 1$. □

**Lemma 3** *Suppose $M_1(j\omega) \in \mathcal{RL}_\infty^{m\times m}$ and $M_2(j\omega) \in \mathcal{RL}_\infty^{m\times m}$ are two transfer function matrices where at some $\omega \in \mathbb{R} \cup \{\pm\infty\}$, $j(M_1(j\omega) - M_1^*(j\omega)) > 0$ and $j(M_2(j\omega) - M_2^*(j\omega)) \geq 0$, then $det[I - M_1(j\omega)M_2(j\omega)] \neq 0$ and $det[I - \frac{1}{g}M_1(j\omega)M_2(j\omega)] \neq 0$ for any $g \geq 1$.*

*Proof:* The above suppositions can be written as $(jM_1(j\omega)) + (jM_1(j\omega))^* > 0$ and $(jM_2(j\omega))^{-1} + (jM_2(j\omega))^{-*} \geq 0$. Hence, $\det[I - M_1(j\omega)M_2(j\omega)] = \det[I + (jM_1(j\omega))(jM_2(j\omega))] = \det[(jM_1(j\omega)) + (jM_2(j\omega))^{-1}]\det[jM_2(j\omega)] \neq 0$. In a similar way as shown in Lemma 1, it can also be shown that, $\det[I - \frac{1}{g}M_1(j\omega)M_2(j\omega)] \neq 0$ for any $g \geq 1$. □

**Theorem 5** *[ [66], Theorem 5.8] Consider a positive feedback interconnection as shown in Fig. 4.1 where $M_1(s) \in \mathcal{RH}_\infty^{m\times m}$, $M_2(s) \in \mathcal{RH}_\infty^{m\times m}$ and the interconnection is well-posed. Then, the feedback interconnection of Fig. 4.1 is stable if and only if the Nyquist plot of $det[I - M_1(j\omega)M_2(j\omega)]$ does not make any encirclements of the origin for $-\infty \leq \omega \leq \infty$.*

The Nyquist plot of $\det[I - M_1(j\omega)M_2(j\omega)]$ belongs to a family of Nyquist plots of $\det[I - \frac{1}{g}M_1(j\omega)M_2(j\omega)]$, where $g \in [1, \infty)$ and the sufficient condition so that $\det[I - M_1(j\omega)M_2(j\omega)]$ does not make an encirclement of the origin for all $\omega \in \mathbb{R} \cup \{\pm\infty\}$ and $g \in [1, \infty)$ is $\det[I - \frac{1}{g}M_1(j\omega)M_2(j\omega)] \neq 0$. In the following theorem, we will explore the conditions for which $\det[I - \frac{1}{g}M_1(j\omega)M_2(j\omega)] \neq 0$ for all $\omega \in \mathbb{R} \cup \{\pm\infty\}$

and $g \in [1, \infty)$ to show the finite-gain stability of the interconnected systems as shown in Fig. 4.1 where $M_1(s)$ is a system with mixed passivity, negative-imaginary and finite-gain properties bounded by gain $k_1$ and $M_2(s)$ is a system with mixed negative-imaginary, negative-passivity and finite-gain properties bounded by gain $k_2$.

Now consider the following three frequency sets:

1. $\Phi_{\rm NI}$ is the set of frequency intervals $[\omega_1, \omega_2]$ where $0 < \omega_1 \leq \omega_2$, contained in $[0, \infty]$ over which both $M_1(s)$ and $M_2(s)$ have the NI property.
2. $\Psi_{\rm P}$ is the set of frequency intervals $[\omega_3, \omega_4]$ where $0 \leq \omega_3 \leq \omega_4$, contained in $[0, \infty]$ over which $M_1(s)$ has the passivity property and $M_2(s)$ has the negative-passivity property or vice versa.
3. $\Omega_{\rm FG}$ is the set of frequency intervals $[\omega_5, \omega_6]$ where $0 \leq \omega_5 \leq \omega_6$, contained in $[0, \infty]$ over which $M_1(s)$ is bounded by a gain $k_1$ and $M_2(s)$ is bounded by a gain $k_2$ such that $k_1 k_2 < 1$.

In the above frequency sets, it should be noted that zero frequency and its neighborhoods are included in the passivity set or negative-passivity set $\Psi_{\rm P}$ or finite-gain set $\Omega_{\rm FG}$ and zero frequency is always excluded from the negative-imaginary set $\Phi_{\rm NI}$.

**Theorem 6** *Suppose $M_1(s) \in \mathcal{RH}_\infty^{m\times m}$ and $M_2(s) \in \mathcal{RH}_\infty^{m\times m}$ are two strictly proper, causal and linear time invariant systems which are connected as shown in Fig. 4.1 where $M_1(s)$ is mixed passive, negative-imaginary, and finite-gain system bounded by a gain $k_1 > \bar{\sigma}(M_1(0))$ and $M_2(s)$ is mixed negative-imaginary, negative-passive, and finite-gain system bounded by a gain $k_2 > \bar{\sigma}(M_2(0))$. Suppose the three sets of frequency intervals are such that $\cup\{\Phi_{NI}, \Psi_P, \Omega_{FG}\} = [0, \infty]$. Here $\cup\{\Phi_{NI}, \Psi_P, \Omega_{FG}\}$ denotes the union of all intervals contained in the sets $\Phi_{NI}$ , $\Psi_P$ , $\Omega_{FG}$. Then the positive feedback interconnection is finite-gain stable if $k_1 k_2 < 1$.*

*Proof:* The proof of Theorem 6 is given by showing $\det[I - \frac{1}{g} M_1(j\omega) M_2(j\omega)] \neq 0$ for all $g \in [1, \infty)$ and all $\omega \in (-\infty, \infty)$. In order to do so, the overall proof is split into three parts: (i) first, it is shown that $\det[I - \frac{1}{g} M_1(j\omega) M_2(j\omega)] \neq 0$ for all $g \in [1, \infty)$ and all $\omega \in \cup\{\Phi_{\rm NI}\}$; (ii) then, it is shown that $\det[I - \frac{1}{g} M_1(j\omega) M_2(j\omega)] \neq 0$ for all $g \in [1, \infty)$ and all $\omega \in \cup\{\Psi_{\rm P}\}$; and (iii) finally, it is shown that $\det[I - \frac{1}{g} M_1(j\omega) M_2(j\omega)] \neq 0$ for all $g \in [1, \infty)$ and all $\omega \in \cup\{\Omega_{\rm FG}\}$.

**Proof of part (i):** When $\omega \in \cup\{\Phi_{\rm NI}\}$, then, there exists $\alpha_i, \beta_i > 0$ for $i = 1, 2$ such that $-\alpha_i\omega^2 M_i^*(j\omega)M_i(j\omega) + j\omega M_i(j\omega) - j\omega M_i^*(j\omega) - \beta_i I \geq 0$, which also implies that, $j\omega M_i(j\omega) - j\omega M_i^*(j\omega) > 0$. Since, $j\omega M_i(j\omega) - j\omega M_i^*(j\omega) > 0$, hence, $\frac{1}{\sqrt{g}}j\omega M_i(j\omega) - \frac{1}{\sqrt{g}}j\omega M_i^*(j\omega) > 0$, for $g > 0$. Hence, from Lemma 2, $\det[I - \frac{1}{g}M_1(j\omega)M_2(j\omega)] \neq 0$ for all $g \in [1, \infty)$.

**Proof of part (ii):** When $\omega \in \cup\{\Psi_{\rm P}\}$, i.e., the frequency interval when $M_1(s)$ has passivity property and $M_2(s)$ has negative-passivity property then there exists $\gamma_1, \gamma_2, \delta_1, \delta_2 > 0$ such that $-\gamma_1 M_1^*(j\omega)M_1(j\omega) + M_1^*(j\omega) + M_1(j\omega) - \delta_1 I \geq 0$ and $-\gamma_2 M_2^*(j\omega)M_2(j\omega) - M_2^*(j\omega) - M_2(j\omega) - \delta_2 I \geq 0$. This implies that, $M_1^*(j\omega) + M_1(j\omega) > 0$ and $-M_1^*(j\omega) - M_1(j\omega) > 0$. Now, since $M_1^*(j\omega) + M_1(j\omega) > 0$ and $-M_1^*(j\omega) - M_1(j\omega) > 0$, therefore, $\frac{1}{\sqrt{g}}M_1^*(j\omega) + \frac{1}{\sqrt{g}}M_1(j\omega) > 0$ and $-\frac{1}{\sqrt{g}}M_1^*(j\omega) - \frac{1}{\sqrt{g}}M_1(j\omega) > 0$ for $g > 0$. Hence from Lemma 1, $\det[I - \frac{1}{g}M_1(j\omega)M_2(j\omega)] \neq 0$ for all $g \in [1, \infty)$.

**Proof of part (iii):** When $\omega \in \cup\{\Omega_{\rm FG}\}$, then there exists $k_i > 0$ for $i = 1, 2$ such that $-M_i^*(j\omega)M_i(j\omega) + \bar{k_i}^2 I \geq 0$. Since $M_1(s)$ and $M_2(s)$ are bounded by gain $k_1$ and $k_2$, i.e., $k_1 > \bar{\sigma}(M_1(0))$ and $k_2 > \bar{\sigma}(M_2(0))$ hence, $\det[I - \frac{1}{g}M_1(j\omega)M_2(j\omega)] \neq 0$ if and only if $k_1 k_2 < 1$ for all $g \in [1, \infty)$. This concludes the proof of Theorem 4. ■

***Remark 1:*** There are seven cases which can arise for the two systems. These cases are:

(i) When $M_1(s)$ and $M_2(s)$ both are only negative-imaginary, then the positive feedback interconnection between the two systems is stable according to the proof of part (i) for Theorem 6.

(ii) When $M_1(s)$ and $M_2(s)$ are only passive and negative-passive, respectively then the positive feedback interconnection between the two systems is stable according to the proof of part (ii) for Theorem 6.

(iii) When $M_1(s)$ and $M_2(s)$ both are only finite-gain system bounded by gains $k_1$ and $k_2$, then the positive feedback interconnection between the two systems is stable if $k_1 k_2 < 1$ according to the proof of part (iii) for Theorem 6.

(iv) When $M_1(s)$ has mixed negative-imaginary and passivity properties and $M_2(s)$ has mixed negative-imaginary and negative-passivity properties, then the positive feedback interconnection between the two systems is stable according to the proof of part (i) and (ii) of Theorem 6.

(v) When $M_1(s)$ and $M_2(s)$ both have mixed negative-imaginary and finite-gain properties bounded by gains $k_1$ and $k_2$, then the positive feedback interconnection

between the two systems is stable if $k_1k_2 < 1$ according to the proof of part (i) and (iii) of Theorem 6.

(vi) When $M_1(s)$ has mixed passivity and finite-gain properties bounded by a gain $k_1 > \bar{\sigma}(M_1(0))$ and $M_2(s)$ has mixed negative-passivity and finite-gain properties bounded by a gain $k_2 > \bar{\sigma}(M_2(0))$, then the positive feedback interconnection between the two systems is stable if $k_1k_2 < 1$ according to the proof of part (i) and (iii) of Theorem 6.

(vii) When $M_1(s)$ has mixed negative-imaginary, passivity and finite-gain properties bounded by a gain $k_1$ and $M_2(s)$ has mixed negative-imaginary, negative-passivity and finite-gain bounded properties by a gain $k_2$, then the positive feedback interconnection between the two systems is stable if $k_1k_2 < 1$ according to the proof of part (i), (ii) and (iii) of Theorem 6.

The combinations given above for the positive feedback interconnection of Fig. 4.1 also satisfy the conditions of the negative-imaginary [56], passivity [57] and small-gain [58] theorems.

*Corollary 1:* Suppose the conditions of Theorem 6 hold and assume both systems are negative-imaginary in the frequency interval $(0, \infty)$. The interconnected systems given in Fig. 4.1 for positive feedback interconnection is finite gain stable if $k_1k_2 < 1$.

The internal stability result for the positive feedback interconnection between two negative-imaginary systems where one system is strictly negative-imaginary is captured by Corollary 1. Since both systems are assumed as strictly proper, $M_1(\infty) = 0$ and $M_2(\infty) = 0$. Also, $\bar{\lambda}(M_1(0)) = \bar{\sigma}(M_1(0))$ and $\bar{\lambda}(M_2(0)) = \bar{\sigma}(M_2(0))$ according to the Lemma 1 of [55] and $\bar{\lambda}(M_1(0))\bar{\lambda}(M_2(0)) < k_1k_1$. Hence the condition $k_1k_2 < 1$ is equivalent to the condition $\bar{\lambda}(M_1(0))\bar{\lambda}(M_2(0)) < 1$. Also the condition $j\omega M(j\omega) - j\omega M^*(j\omega) > 0$ and $j\omega M(j\omega) - j\omega M^*(j\omega) \geq 0$ in Lemma 3 implies that one of the systems is required to be strictly NI. Hence, the conditions of NI theorem [55] are satisfied.

*Corollary 2:* Suppose the conditions of Theorem 6 hold and assume one system is passive and another system is negative-passive in the frequency interval $(0, \infty)$. Then, the positive feedback interconnection of the two systems is finite gain stable.

The internal stability results for the positive feedback interconnection shown in Fig. 4.1 when one system is passive and another system is strictly negative-passive, can be captured by using Corollary 2. Since both systems are assumed as strictly proper, $M_1(\infty) = 0$ and $M_2(\infty) = 0$. Also the condition $M(j\omega) + M^*(j\omega) > 0$

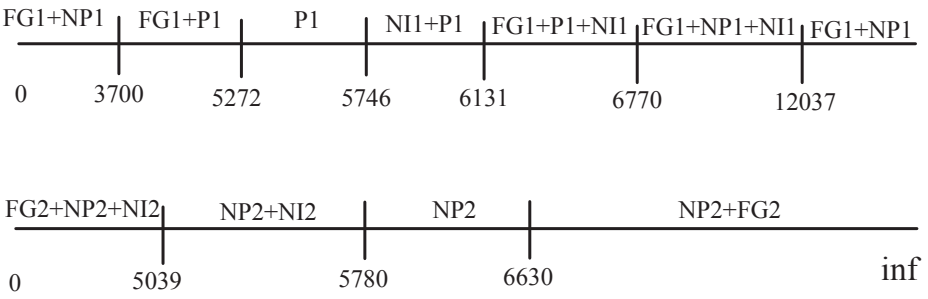


**Figure 4.4:** Frequency intervals (NI1: negative-imaginary region for system $M_1(s)$, NP1: negative-passive region for system $M_1(s)$, P1: Passive region for system $M_1$, FG1: finite-gain region for system $M_1(s)$, NI2: negative-imaginary region for system $M_2(s)$, NP2: negative-passive region for system $M_2(s)$, FG1: finite-gain region for system $M_2(s)$).

and $-M(j\omega) - M^*(j\omega) \geq 0$ in Lemma 2 implies that one of the systems is required to be strictly passive or negative-passive. Therefore, the conditions of the passivity theorem are also satisfied for Theorem 6.

*Corollary 3:* Let the suppositions of Theorem 6 hold and both systems are finite-gain systems bounded by gains $k_1$ and $k_2$. Then, the positive feedback interconnection is finite-gain stable if $k_1 k_2 < 1$.

## 4.5 Numerical Example

Consider the transfer functions $M_1(s)$ and $M_2(s)$ as given in (4.1) and (4.2). The Nyquist plots of these systems given in Fig. 4.2 show that none of the negative-imaginary, passivity or small-gain theorem alone can provide a guarantee of finite-gain stability for the feedback interconnection of the two systems $M_1(s)$ and $M_2(s)$. In the following, first we have shown the test for mixedness of the systems $M_1(s)$ and $M_2(s)$ and then we have presented the stability analysis for the positive feedback interconnection between $M_1(s)$ and $M_2(s)$ as shown in Fig. 4.1.

### 4.5.1 Test for mixedness

In order to check the mixedness of the systems $M_1(s)$ and $M_2(s)$ we have used Theorem 1, Theorem 3, and Theorem 4. In the following we will present a brief procedure to test the mixedness of the system $M_1(s)$. The test for $M_2(s)$ can be done in a similar way. First, we compute the eigenvalues of the Hamiltonian matrix (4.6) for $M_1(s)$ to check the frequency intervals for which $M_1(s)$ have the NI property. We found that the Hamiltonian matrix (4.6) has four purely imaginary eigenvalues, $\pm j5746.4$ and $\pm j12037$. Breaking the frequency range $(0, \infty)$ into the intervals

$(0, 5746.4]$, $[5746.4, 12037]$ and $[12037, \infty)$ and examining the sign definiteness of $j(M_1(j\omega) - M_1^*(j\omega))$ at some single frequency point within the each of these interval as discussed in Section 4.3.3. After examining the sign definiteness of $j(M_1(j\omega) - M_1^*(j\omega))$ in different frequency intervals we found that, $M_1(s)$ has the NI property between $[5746.4, 12037]$. In a similar way, by using the Hamiltonian matrix (4.8) for $l = 0.0001$ we found that, $M_1(s)$ has the passivity property in the frequency interval [3700,6770] and negative-passivity property in the frequency interval $[0, 3700]$ and [6770, $\infty$).

We select $\epsilon = k_1 = 0.55$ for $M_1(s)$. We compute the eigenvalues of Hamiltonian matrix (4.9) and we found that $M_1(s)$ has finite-gain property bounded by gain 0.55 in the frequency intervals [0,5272] and [6131,$\infty$) $\mathrm{rad\,s^{-1}}$. In a similar way, for $\epsilon = k_2 = 1.8$ we found that, $M_2(s)$ has negative-imaginary property in the frequency interval [0,5780], negative-passivity property in the frequency interval [0,$\infty$) and finite-gain property bounded by gain 1.8 in the frequency intervals [0, 5039] and (6630,$\infty$) $\mathrm{rad\,s^{-1}}$.

### 4.5.2 Stability analysis

First the values of the gains $k_1$ and $k_2$ are selected as 0.55 ($> \bar{\sigma}(M_1(0) = 0.54)$) and 1.8 ($> \bar{\sigma}(M_2(0) = 0)$) which satisfy the condition $k_1 k_2 < 1$. The mixed properties of the two systems for gains $k_1$ and $k_2$ are illustrated in Fig. 4.4. The mixed properties given above are only shown for positive frequencies. However, the mixed properties between the systems for positive feedback interconnection can also be obtained for negative frequencies in a similar way.

It can be seen that, at each frequency when $M_1(s)$ has the NI property, $M_2(s)$ also has the NI property; when $M_1(s)$ has the passivity property, $M_2(s)$ has the negative-passivity property, when $M_1(s)$ has the finite-gain property bounded by gain $k_1$, $M_2(s)$ has the finite-gain property bounded by gain $k_2$ and $k_1 k_2 < 1$. Hence, the closed-loop system corresponding to interconnection between $M_1(s)$ and $M_2(s)$ is stable. This is verified by calculating the corresponding closed-loop poles for the positive feedback interconnection between the transfer functions $M_1(s)$ and $M_2(s)$ and the closed-loop poles calculated as $-841.1 + 6210.7i$, $-841.1 - 6210.7i$, $-2314.8 + 3543.7i$, $-2314.8 - 3543.7i$ and $-2116.8$ which shows that the closed-loop system is stable.

## 4.6 Passive Damping Controller Design

The experimental setup to identify the dynamics of the PTS was described in Chapter 3. The sensor of the PTS used in Chapter 3 was not working during this work. We have used a different PTS for this work. The identification of the dynamics of the PTS was done in a similar way as discussed in Chapter 3. The transfer function for the dynamics of the PTS along the X-axis in this case is as follows:

$$M_{xx}(s) = \frac{M_{dx}(s)}{M_{vx}(s)} = \frac{-131.9(s^2-9196s+2.21\times10^8)}{(s+1593)(s^2+134.1s+3.322\times10^7)} \tag{4.10}$$

Consider the block diagram of the closed-loop system shown in Fig. 4.1 where $M_1(s)$ is the plant transfer function, i.e., the transfer function of the positioning system of the PTS and $M_2(s)$ is the transfer function of a passive damping controller. A passive damping controller can be realized by the following transfer function:

$$M_2(s) = -k_p \frac{s}{s^2 + 2\xi_p\omega_p s + \omega_p^2} \tag{4.11}$$

Here, $k_p > 0$ is the gain of the passive damping controller, $\xi_p > 0$ is the damping constant of the controller and $\omega_p > 0$ is the frequency at which resonant mode needs to be damped. The selection of the controller parameters for the PTS is based on the desired aim. The frequency at which the controller provides large gain is frequency $\omega_p$. It is desired that in order to damp the resonant mode of the scanner the value of $\omega_p$ is chosen equal or nearly equal to the first resonant mode of the scanner. The damping constant is chosen in a way to achieve large level of damping. A low value of damping constant $\xi_p$ introduces undesirable phase shift in the closed-loop and a high value of the damping constant hardly has any effect on damping. The controller gain $k_p$ plays a major role to damp the resonant mode of a piezo scanner. The controller gain $k_p$ is selected as large as possible to achieve large level of damping of the first resonant mode of the scanner. It is also important that, the controller gain $k_p$ is chosen such that closed-loop system is stable and achieve large level of damping of the resonant mode. In order to guarantee the closed-loop stability and large level of damping of the first resonant mode of the piezo scanner, the controller design is presented by exploiting Theorem 6.

The overall design process of the controller using Theorem 6 includes following steps:

(i) Find the frequencies at which the system $M_1(s)$ has the negative-imaginary, passivity, and negative-passivity properties, i.e., the phase of the SISO syatem $M_1(s)$ lies between $[0^\circ\ -180^\circ]$, $[90^\circ\ -90^\circ]$, and $[-270^\circ\ 90^\circ]$.

(ii) Select a gain $k_1$ such that at the frequencies where $M_1(s)$ does not have the negative-imaginary, passivity, and negative-passivity properties bounded by a gain $k_1$.

(iii) Make the gain $k_1$ as low as possible such that, $M_1(s)$ has either the negative-imaginary or passivity or negative-passivity properties or has a finite-gain bounded by the gain $k_1$.

(iv) Find the frequencies at which $M_1(s)$ has only the negative-imaginary, passivity, negative-passivity, and finite-gain properties bounded by the gain $k_1$ and both.

(v) Select the controller $M_2(s)$ parameters and find the frequencies at which $M_2(s)$ has the negative-imaginary, passivity, and negative-passivity properties.

(vi) Increase the gain of the controller $M_2(s)$ to be as large as possible and select the gain $k_2$ for $M_2(s)$ such that, (a) $k_1k_2 < 1$, (b) $M_2(s)$ has the NI property at the frequencies where $M_1(s)$ has the NI property, (c) $M_2(s)$ has the passivity property at the frequencies where $M_1(s)$ has the passivity property,

Using the above selection criteria the controller is chosen as follows:

$$M_2(s) = \frac{-12500s}{s^2 + 8484s + 3.672 \times 10^7} \tag{4.12}$$

## 4.7 Performance of the Controller

The performance of the proposed controller is examined by implementing the controller on an experimental PTS. A comparison of the measured open- and closed-loop magnitude frequency responses of $M_{xx}(s)$ is given in Fig. 4.5. The comparison shows that the proposed controller is able to provide 20 dB damping of the first resonant mode of the scanner. From the frequency response of $M_{xx}(s)$ in open-loop it can be observed that, there is a dip in the range of frequencies from 100 Hz to 800 Hz, which means that there is a variation of gain in open-loop. The magnitude of the output voltage in that range will vary even though the magnitude of the input voltage remain same. This will certainly reduce the performance of the PTS for high speed nano-positioning. The closed-loop frequency response of $M_{xx}(s)$ shows less amount of dip in the frequency response as compared to the open-loop frequency

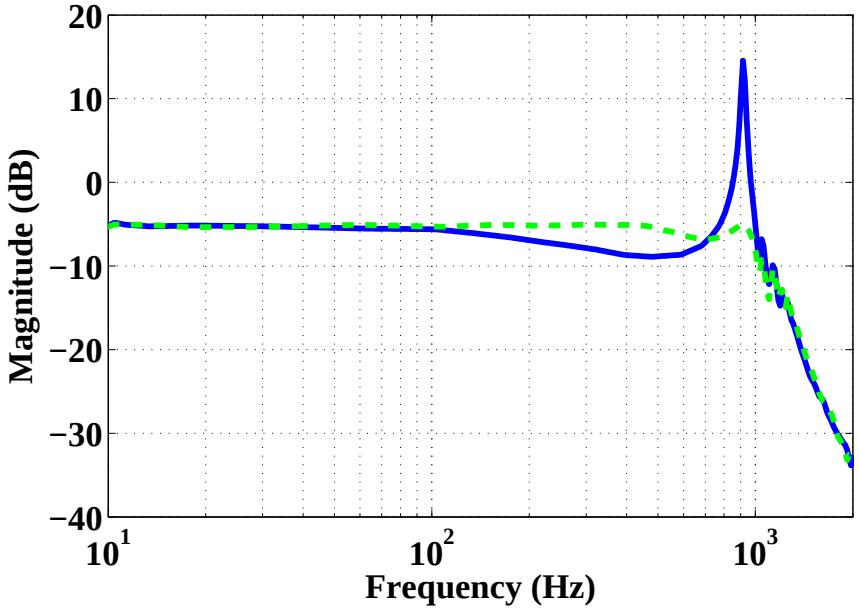


**Figure 4.5:** Open- (the solid line –) and closed-loop (the dashed line - -) magnitude frequency response of $M_{xx}(s)$ .

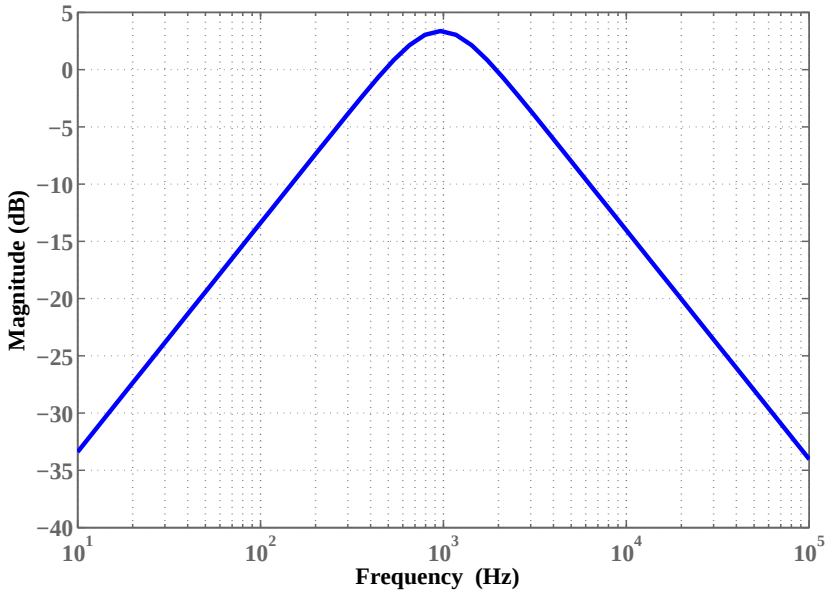


**Figure 4.6:** Magnitude Bode diagram of the controller.

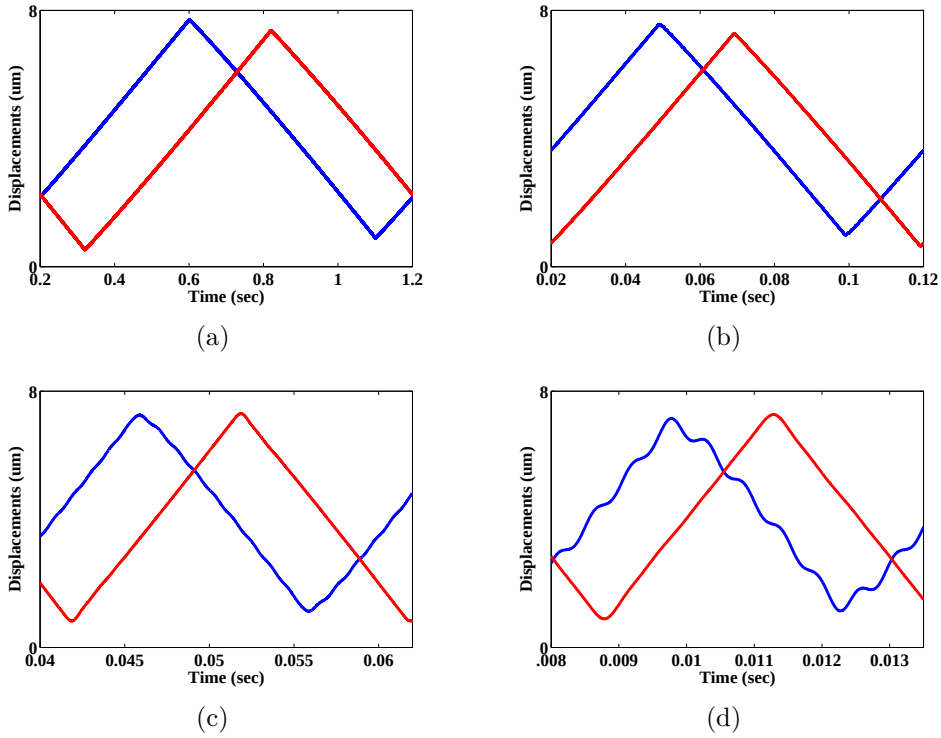


**Figure 4.7:** Open- (blue solid line) and closed-loop (red solid line) X sensor output signals for (a) 1 Hz, (b) 10 Hz, (c) 50 Hz, and (d) 100 Hz triangular input signals.

response. The controller is also able to flatten the frequency response of the PTS. This signifies large bandwidth of the closed-loop system which in turns ensure faster scanning.

A magnitude Bode diagram of the controller is presented in Fig. 4.6. The magnitude Bode diagram of the controller shows that the controller only applies high gain near to the first resonance frequency of the scanner which in turn results in large gain and phase margins. To illustrate controller performance in time domain, triangular voltage signals of different frequencies (1 Hz, 10 Hz, 50 Hz, and 100 Hz) are applied to the X-axis of the scanner in the open- and closed-loop cases and the corresponding X sensor outputs are recorded. Fig. 4.7 shows the outputs from the X sensor in open- and closed-loop cases for different frequencies obtained by using the controller in the X-axis of the scanner. A small time delay was purposely added to the open- and closed-loop sensor outputs in order to clearly display the open- and closed-loop time responses. The closed-loop X sensor output shows less vibration as compared the open-loop sensor output.

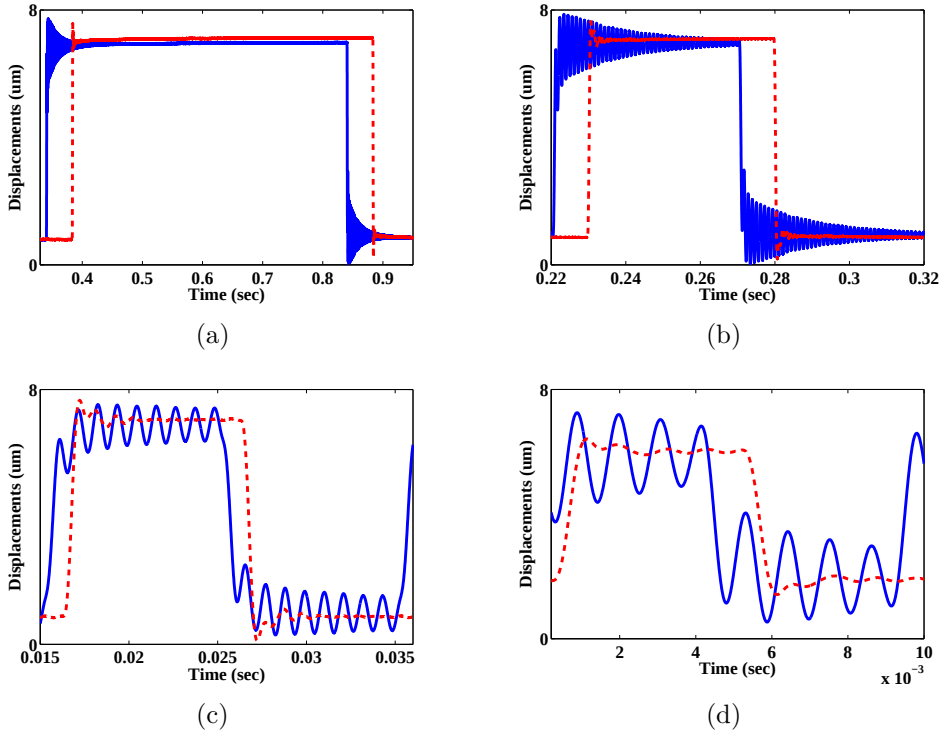


**Figure 4.8:** Open- ( blue solid line – ) and closed-loop ( red dashed line - - ) X sensor output signals for (a) 1 Hz, (b) 10 Hz, (c) 50 Hz, and (d) 100 Hz pulse input signals.

The time domain performance of the proposed controller is further examined by applying pulse signals of 1 Hz, 10 Hz, 50 Hz, and 100 Hz to the X-axis of the scanner. The X sensor outputs in open- and closed-loop cases for different frequencies of the pulse signals are given in Fig. 4.8 which shows that the proposed controller is able to reduce the settling time to 20 percent of each pulse period at low frequencies with a significant reduction of vibration.

The transfer function of the PTS can change during operation due to different loads on the scanner. Controllers design for high speed nano-positioning must be able to maintain closed-loop stability in presence of changes in the plant transfer function. In order to measure the performance of the proposed controller against changes in the plant transfer functions we have placed three samples with different load L1, L2, L3 on the scanner. The open- and closed-loop magnitude frequency responses for the different loads were measured using the same controller. The experimental results presented in Fig. 4.9 show that the controller is robust against

changes in the plant transfer function. A comparison of the gain margins and closed-loop bandwidths for different loads on the scanner is presented in Table 4.1. The comparison shows that the proposed controller achieved more bandwidths in closed-loop for different loads as compared to open-loop. The controller also achieved significant amount of gain margin in the closed-loop as well.

**Table 4.1:** Open- and closed-loop bandwidth and gain margin for different loads on the scanner together

| | Bandwidth for no load (Hz) | Bandwidth for load L1 (Hz) | Bandwidth for load L2 (Hz) | Gain Margin for no load | Gain Margin for load L1 | Gain Margin for load L2 |
|---|---|---|---|---|---|---|
| Open-loop | 600 | 517 | 510 | - | - | - |
| closed-loop | 920 | 850 | 750 | 3.63 | 3.47 | 3.19 |

The advantage of the proposed framework as compared to the small-gain only approach is shown by designing a controller using a small-gain only approach. The small-gain approach limits the loop-gain to be strictly less than one as shown in Fig. 4.10, whereas, the proposed framework allows a loop-gain greater than one. The gain of the controller obtained in the small-gain only approach is 1700, whereas the gain of the controller obtained in the proposed framework is 12500. The controller with gain 1700 achieved 7 dB damping of the first resonant mode of the scanner and the controller with gain 12500 achieved 20 dB damping of the first resonant mode of the scanner as shown in Fig. 4.11.

## 4.8 Chapter Summary

In this chapter a passive damping controller design is presented to damp the first resonant mode of a PTS using a mixed negative-imaginary, passivity and small-gain approach. It is shown that the positive feedback interconnection between the two stable LTI systems, where one system has mixed passive, negative-imaginary and finite-gain properties bounded by a gain $k_1$, and the other system has mixed negative-imaginary, negative-imaginary and finite-gain properties bounded by a gain $k_2$, is guaranteed to be finite-gain stable if $k_1 k_2 < 1$. The stability analysis for the above

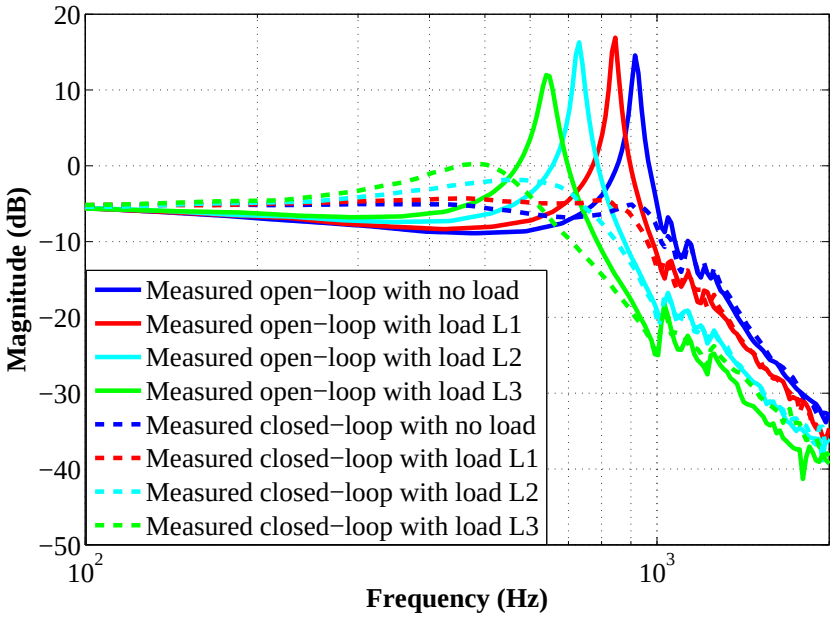


**Figure 4.9:** Robustness analysis of the interconnected systems for different loads L1, L2 and L3 on the scanner.

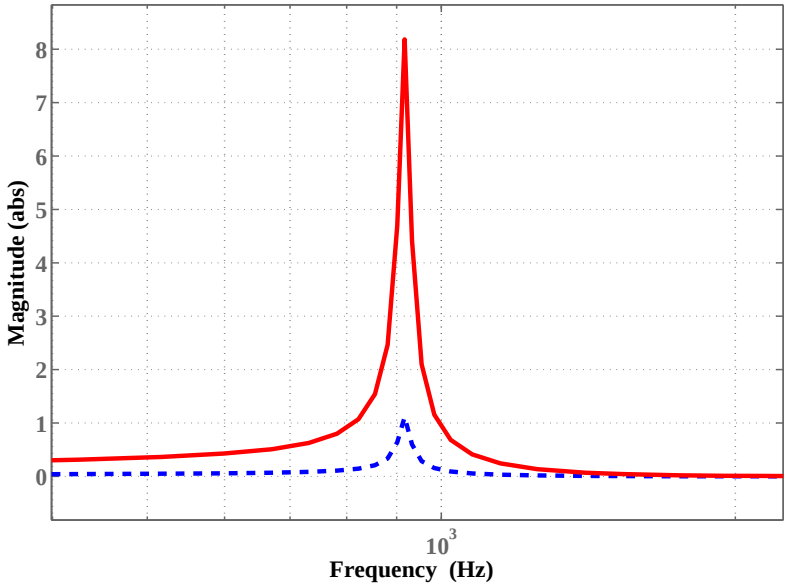


**Figure 4.10:** Loop-gains $M_1(j\omega)M_2(j\omega)$ when the controller is designed using the small-gain only approach (. . the dotted line) and the proposed analytical framework (– the solid line).

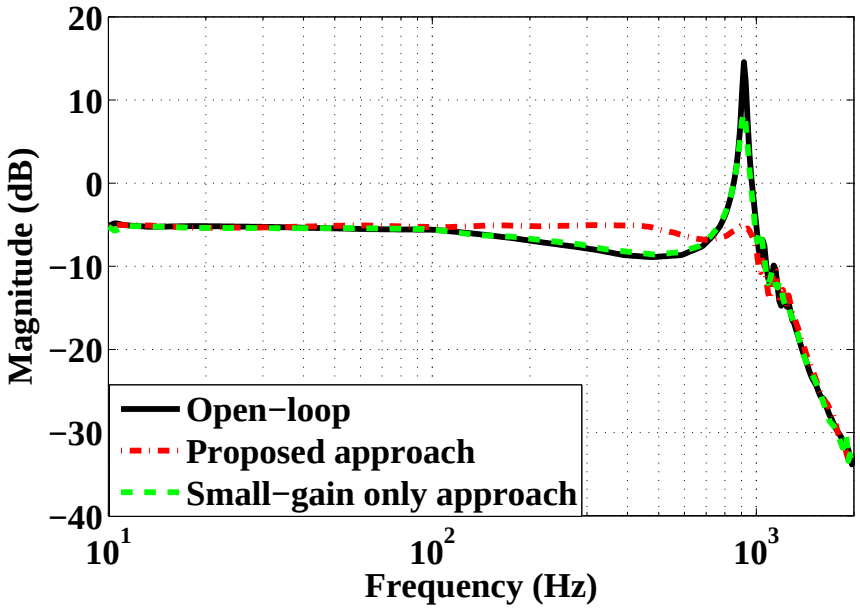


**Figure 4.11:** Measured open- (the solid line –) and closed-loop frequency responses in the X-axis of the scanner using proposed approach (the dashed dot line -.) and small-gain only approach ( the dashed line - -).

mentioned systems is done by using Nyquist stability criteria. The framework proposed in the chapter includes individual theorems of passivity, negative-imaginary and small-gain. A numerical example is provided to validate the proposed framework.

The experimental results presented in the chapter show that the proposed controller is able to flatten the frequency response by achieving 20 dB damping of the first resonant mode of the scanner. The motivation for designing a passive damping controller as compared to the resonant controller as discussed in Chapter 3 is that this type of controller is a band pass controller for which the resultant closed-loop system not only results in large gain and phase margins but also reduces sensor noise at high frequencies. The experimental results also show that the controller is robust against changes in plant transfer functions due to load changes. This signifies another advantage of the proposed passive damping controller.

Although the passive damping controller results in a robust stability for the PTS, however it does not guarantee robust performance in the closed-loop. The design of the controller is not done to provide robust performance. In the next chapter we present the design of the final damping controller of this thesis, where the controller

design is carried out to provide robust performance against changes in the plant transfer functions.

# Chapter 5

# Minimax LQG Control of Piezoelectric Tube Scanners

In the previous chapters, we have presented the design of two damping controllers namely a resonant controller and a passive damping controller to damp the resonant mode of the PTS. Although the resonant controller and the passive damping controller achieve large gain and phase margins and provide robustness against changes in plant transfer functions and unmodelled dynamics, the performance of the resonant controller and the passive damping controller is not robust against changes in plant dynamics.

In order to ensure robust performance of the controller, we present another design of a controller in this chapter. The controller is a minimax linear-quadratic-Gaussian (LQG) controller. The major challenge in high speed precision positioning of the PTS is the presence of mechanical resonance modes at low frequencies. The tracking performance of the PTS at high scanning rates is largely affected due to its low mechanical resonance frequency. The PTS has to track a triangular reference signal during the raster scanning process. The triangular signal contains odd harmonics of its fundamental frequency. When a triangular signal is applied to the PTS, the harmonics of the PTS excites the mechanical resonance of the PTS. This results in poor tracking performance of the PTS. The tracking performance of the PTS is limited to one percent of its first resonance frequency. This is a great challenge to control engineers to enhance the tracking performance of the PTS for high speed nanopositioning.

This chapter presents a design and experimental implementation of a minmax LQG controller for damping and tracking control of the PTS. The first design shows the design of minimax LQG controller for damping the resonant mode of the scanner and the second design shows the design of a minimax LQG controller with integral action for tracking control of the PTS. The performance of the controller is compared with an integral controller. The proposed controller achieves four times greater bandwidth than the integral controller.

The first section of this chapter presents a brief introduction and motivation to design of a minimax LQG controller for the PTS. System identification and the problem formulation is presented in Section 5.2. Section 5.3 presents a detailed description of the minimax LQG theory. Section 5.4 discusses the design and selection of the controller parameters. The performance of the controller for damping is presented in Section 5.5. The design and performance of the integral minimax LQG controller is presented in Sections 5.6 and 5.7. Finally the chapter is concluded in Section 5.8.

## 5.1 Introduction

Different types of damping controllers including open- and closed-loop controllers were discussed in Chapter 3. The main motivation to design a minimax LQG controller for the PTS is its excellent performance in damping the resonant mode of structures and its ability to provide robust performance. Robust $H_2$ and $H_\infty$ controllers have been designed to suppress mechanical vibrations of structures [67, 68]. An appropriate cost function is selected in the $H_2$ and $H_\infty$ methods to eliminate the vibration of a system. Although the use of spatial $H_\infty$ controllers provides a good level of damping of the resonant modes of the structure, the use of the $H_\infty$ norm in the design of $H_\infty$ controllers often leads to a conservative controller for which the resultant closed-loop system may result in a low level of damping. It is often more suitable to use the $H_2$ norm as the performance index. However, the design of robust $H_2$ controllers can be computationally intractable [69].

Most SPM systems use integral controllers for tracking control of the PTS. Integral controllers are used because of their ability to reduce the non-linearities of the PTS. The major drawback of the use of integral controllers for the PTS is their low closed-loop bandwidth. The bandwidth of integral controllers for nanopositioners is limited to $2\omega\xi$, where $\omega$ and $\xi$ are the first resonance frequency and damping constant of the nanopositioner [51].

Negative imaginary (NI) controllers [56] such as positive position feedback (PPF) controllers [18], integral resonant controllers (IRCs) [15] are designed to improve the tracking performance of integral controllers for nanopositioners. The motivation to design NI damping controllers is their robustness against changes in the plant

dynamics [15]. The IRCs and PPF controllers are low pass controllers. The closed-loop system for scanners with IRCs or PPF controllers may have a low gain and phase margin due to the low pass nature of the controllers.

Nonlinear control approaches using impulsive control [70] and signal transformation control [71] have been demonstrated for fast nanopositioning. These two approaches are designed based on a trade-off between the tracking bandwidth and sensitivity to the measurement noise. The impulsive control and signal transformation control approaches achieve good tracking performance, the control systems using impulsive and signal transformation control are sensitive to disturbances and uncertainty in the low frequency gain of the plant.

The minimax linear-quadratic-Gaussian (LQG) control [72–76] technique is a damping technique which uses the $H_2$ norm in the design process to solve two algebraic Riccati equations. A minimax LQG controller is a special case of the LQG controller, where the worst-case LQG performance index is minimized. In this work, we first propose a design of a minimax LQG controller to suppress the vibrations of the PTS.

Next we propose a novel tracking controller namely an integral minimax LQG controller using the minimax LQG theory [72–76]. The integral minimax LQG controller is designed by providing integral action to the minimax LQG controller. Another motivation to design this type of controller is that it uses the $H_2$ norm in the design process for which the resultant controller does not result in a conservative controller like $H_\infty$ controller. This type of controller is robust against changes in plant dynamics and provides greater bandwidth as compared to integral controllers. The controller is designed based on the consideration that the measurement noise is minimum. For this two measurement noises are included in the modelling of the system to account for the effect of measurement noise in the experiments.

## 5.2 System Identification and Problem Formulation

### 5.2.1 Dynamics of the piezoelectric tube scanner

As previously discussed in Section 5.1, the transfer function of PTS varies due to different factors, let $G_1(j\omega)$ and $G_2(j\omega)$ be the two transfer functions of the system at different temperatures between which the true transfer function of the system varies. Now, let $G_m(j\omega) = \frac{G_1(j\omega)+G_2(j\omega)}{2}$ be the nominal model transfer function. Then, the uncertainty due to the modelling error can be represented by (5.1):

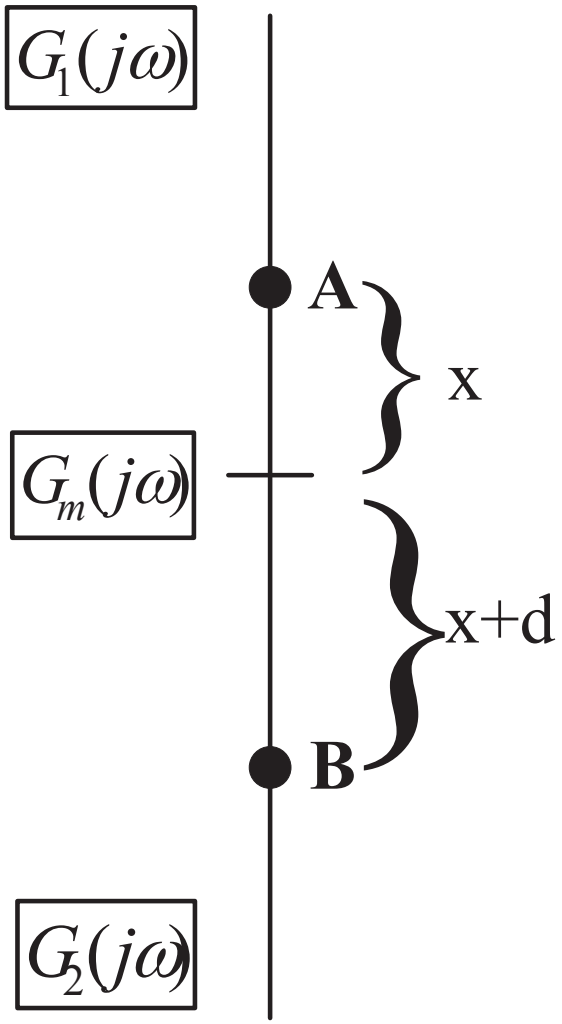


**Figure 5.1:** Uncertainty representation between $G_1(j\omega)$ and $G_2(j\omega)$.

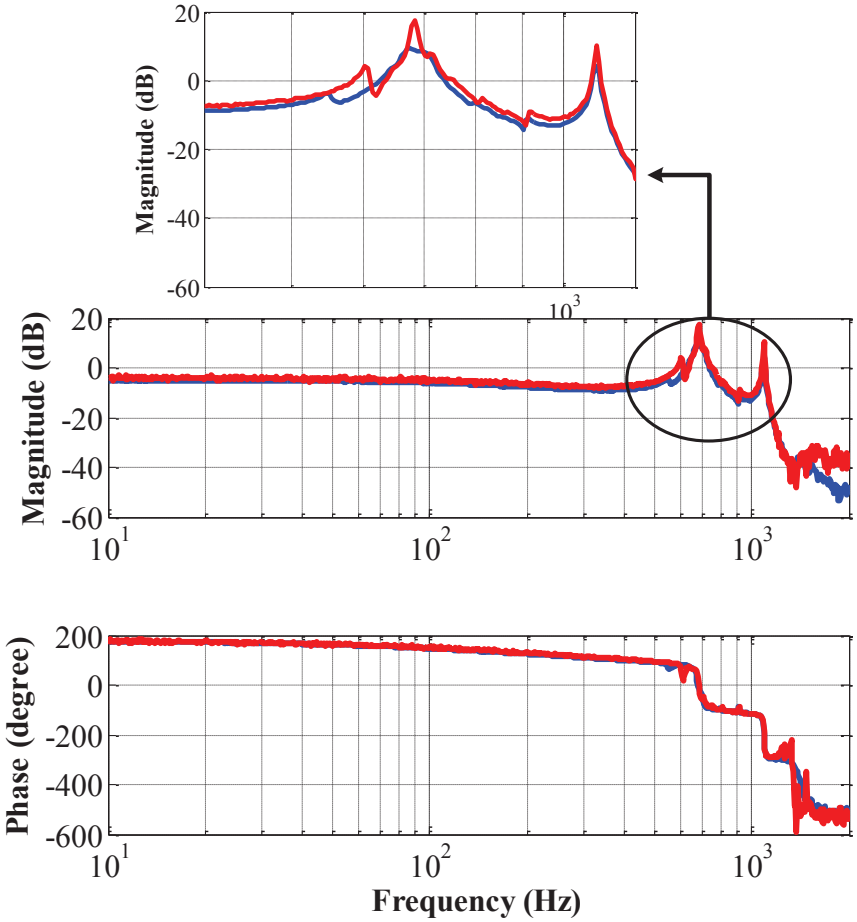


**Figure 5.2:** Comparisons between the two measured frequency responses of $G_1(j\omega)$ and $G_2(j\omega)$ obtained at different times.

$$\Delta G(j\omega) = max\{|G_m(j\omega) - G_1(j\omega)|, |G_m(j\omega) - G_2(j\omega)|\}. \tag{5.1}$$

A schematic view of the representation of the uncertainty between $G_1(j\omega)$ and $G_2(j\omega)$ is presented in Fig. 5.1 and shows that, if the actual true transfer function of the system lies at point B, then the uncertainty is given by $\Delta G(j\omega) = max\{|G_m(j\omega) - G_2(j\omega)|\}$ where $x + d > x$.

In order to identify $G_m(j\omega)$ it is required to know $G_1(j\omega)$ and $G_2(j\omega)$ where $G_1(j\omega)$ and $G_2(j\omega)$ are the transfer functions of the system at different temperatures. The identification of $G_1(j\omega)$ and $G_2(j\omega)$ is done by applying swept sine waves from 10 Hz to 2 kHz to the X-axis of the scanner and recording the corresponding X-sensor output at different times in different temperatures. A comparison of the

measured frequency responses of $G_1(j\omega)$ and $G_2(j\omega)$ given in Fig. 5.2 shows that, the two transfer functions frequency responses are different at different temperatures which clearly signifies the motivation of the present work. After obtaining $G_1(j\omega)$ and $G_2(j\omega)$, we obtain $G_m(j\omega)$ from the relation $G_m(j\omega) = \frac{G_1(j\omega)+G_2(j\omega)}{2}$. Next, we used a subspace based system identification method [77] using Matlab to obtain a model for $G_m(j\omega)$. The identification is done to capture the first two resonant modes of $G_m(j\omega)$ with low a order transfer function matrix. In the identification process, we found the following transfer function is the best fit with the measured $G_m(j\omega)$:

$$G_m(j\omega) = \frac{D_x(s)}{V_x(s)} = \frac{-54.96s^4+1.092\times10^6 s^3-1.101\times10^{10}s^2+4.444\times10^{13}s-5.615\times10^{17}}{s^5+1365s^4+6.52\times10^7 s^3+8.304\times10^{10}s^2+8.705\times10^{14}s+9.804\times10^{17}} \tag{5.2}$$

where $D_x(s)$ is the Laplace transform of the output voltage from the X sensor and $V_x(s)$ is the Laplace transform of the input voltage to the HVA driving the X piezo. A comparison of the measured and identified model frequency responses of $G_m(j\omega)$ is presented in Fig. 5.3. The comparison shows that, the identified model captures the first two resonant modes of the measured frequency response. A higher order model would capture the other modes of the measured frequency response as well. However, we consider a low order transfer function intentionally to show the robustness of the proposed controller against the spill over dynamics.

### 5.2.2 Uncertainty modelling

In the design of minimax LQG controller, the first step is the modelling of the uncertainties. In this design, we consider two types of uncertainties which may arise in a piezoelectric tube scanner. The uncertainties are: (a) the uncertainty due to high order spill over dynamics and (b) the uncertainty which arises due to the changes in the plant transfer function of the scanner due to changes of temperature. These uncertainties are represented as a frequency weighted multiplicative uncertainty as shown in Fig. 5.4. The true transfer function of the system including the uncertainty is assumed to have the following form:

$$G_\Delta(j\omega) = G_m(j\omega)[1 + W_m(j\omega)\Delta G(j\omega)] \tag{5.3}$$

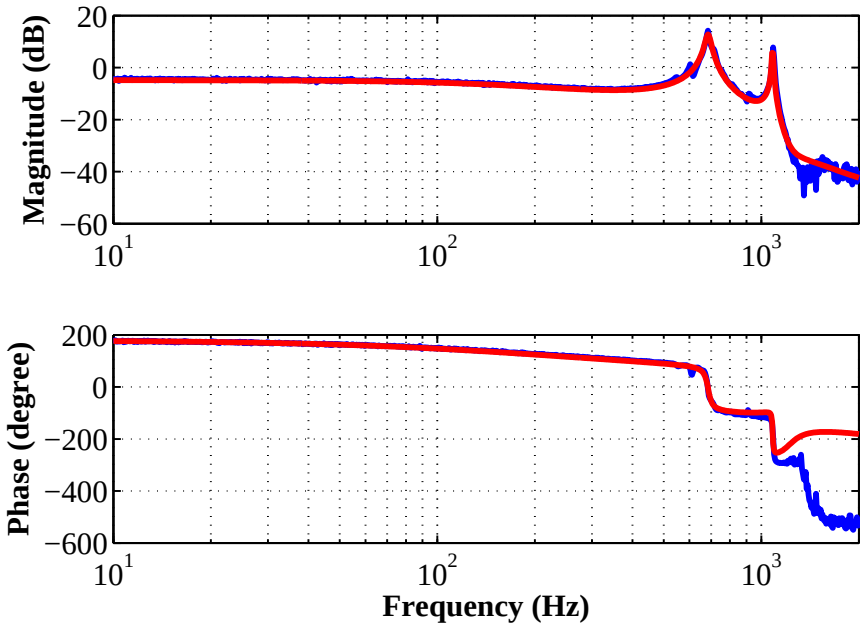


**Figure 5.3:** Comparisons between the measured and identified frequency responses of $[G_1(j\omega) + G_2(j\omega)]/2$. The blue solid line represents frequency response obtained from the measured $G_1(j\omega)$ and $G_2(j\omega)$ and the red solid represents the identified model frequency response.

where $W_m(j\omega)$ is a suitable weighting transfer function, $G_m(j\omega)$ is defined in (5.2) and $\Delta G(j\omega)$ is an uncertain transfer function satisfying the $\mathrm{H}^\infty$ norm bound

$$||\Delta G(j\omega)||_\infty \leq 1. \tag{5.4}$$

The weighting transfer function $W_m(j\omega)$ has a major role in damping the resonant mode of the scanner. The selection of the magnitude of the weighting transfer function $W_m(j\omega)$ depends on the uncertainty. The low the magnitude of $W_m(j\omega)$ the better the performance of the controller and the lower the robustness of the controller. The high the magnitude of $W_m(j\omega)$ the better the robustness and the lower the performance of the controller. Hence, there is always a trade off between the performance and robustness of the controller. One point which should be noted here is that the uncertainty representation in this design is for the uncertainty which arises due to the unmodelled spill over effects and the changing of the plant transfer functions due to changes in the temperature of the scanner. From Fig. 5.4, it can be seen that the output of the uncertainty block enters the system through the same

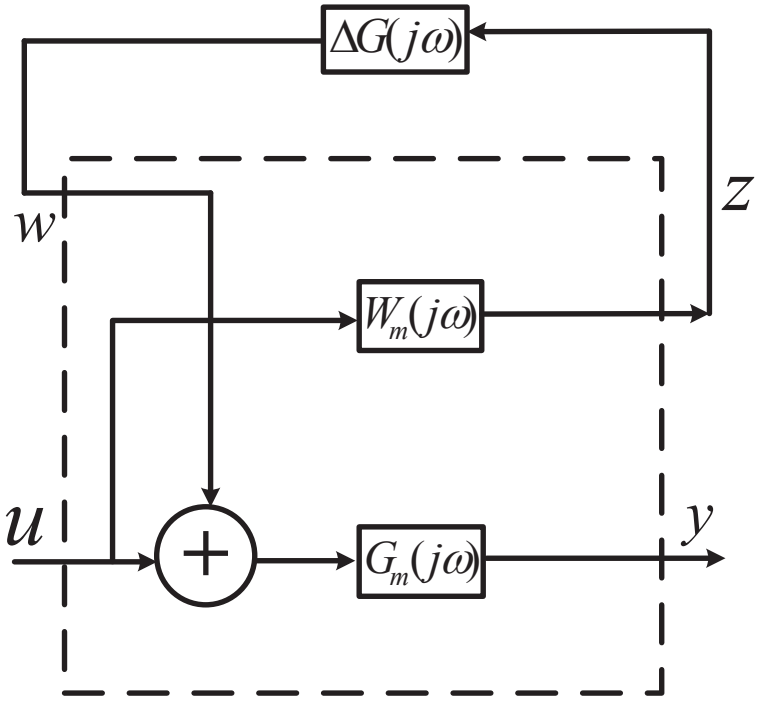


**Figure 5.4:** System representation with uncertainty.

channel as the control input which means that the disturbance signal also enters the system through the same channel as the control input.

### 5.2.3 Weighting transfer function selection

As indicated in the previous section, selecting the weighting transfer function $W_m(j\omega)$ is a key design step to achieve a trade-off between the control system performance and control system robustness. Decreasing the magnitude of $W_m(j\omega)$ at a given frequency $\omega$ improves the performance of the closed-loop system and decreases the closed-loop robustness at that frequency. Also, the order of the controller depends on the order of $W_m(j\omega)$. The larger the order of $W_m(j\omega)$, the higher is the order of the controller. The magnitude of the weighting transfer function can be selected from the following formula:

$$\frac{G_\Delta(j\omega) - G_m(j\omega)}{G_m(j\omega)} = W_m(j\omega)\Delta G(j\omega). \tag{5.5}$$

Since $\Delta G(j\omega) = max\{|G_m(j\omega) - G_1(j\omega)|, |G_m(j\omega) - G_2(j\omega)|\}$, it follows that,

$$\frac{max\{|G_m(j\omega) - G_1(j\omega)|, |G_m(j\omega) - G_2(j\omega)|\}}{|G_m(j\omega)|} \leq |W_m(j\omega)|. \tag{5.6}$$

Therefore, the selection of the magnitude of the weighting transfer function mostly depends on (5.6). The weighing transfer function is selected in such a way that (5.6) is satisfied. The weighting transfer function $W_m(j\omega)$ is chosen as high pass filter since the main uncertainty arises from neglecting the third and higher order dynamics of the system. We want the magnitude $|W_m(j\omega)|$ to be high at high frequencies so that the controller provides robustness at high frequencies as we neglected the high frequency dynamics of the systems. The high pass weighting transfer function also improves the gain and phase margins of the system. In this design, $W_m(j\omega)$ is chosen as a high pass fourth order Chebychev filter with 1 dB ripple in the pass band. In our final design, we used the following transfer function of $W_m(j\omega)$:

$$W_m(j\omega) = \frac{s^4+4442s^3+9.867\times10^6 s^2+1.284\times10^{10}s+8.352\times10^{12}}{s^4+1.045\times10^4 s^3+5.463\times10^7 s^2+1.672\times10^{11}s+2.56\times10^{14}} \tag{5.7}$$

The magnitude Bode plot of $W_m(j\omega)$ and $\frac{max\{|G_m(j\omega)-G_1(j\omega)|,|G_m(j\omega)-G_2(j\omega)|\}}{|G_m(j\omega)|}$ given in Fig. 5.5 shows that, condition (5.6) is satisfied which signifies the performance and robustness of the closed-loop system.

## 5.3 Minimax LQG Control Theory

Minimax LQG control theory is based on a kind of game type optimization problem where the designer is considered as a minimizing player who tries to maintain a certain level of robust performance of the controller against the plant uncertainty. In this game type optimization problem, the uncertainty is treated as the maximizing player. The minimax LQG control strategy is based on finding a controller which minimizes the worst case of the following objective function:

$$J = \lim_{T\to+\infty} \mathbf{E}\frac{1}{2T}\int_0^T (x(t)'Rx(t) + u(t)'Gu(t))dt \tag{5.8}$$

where, $x(t) \in \mathbb{R}^n$ is the state, $u(t) \in \mathbb{R}^m$ is the control input, $R \geq 0$, and $G > 0$. The term $x(t)'Rx(t)$ in the cost function (5.8) corresponds to a requirement to minimize the system variables of interest and the term $u(t)'Gu(t)$ corresponds to a requirement to minimize the size of the control inputs. The matrices $R$ and $G$ associated with

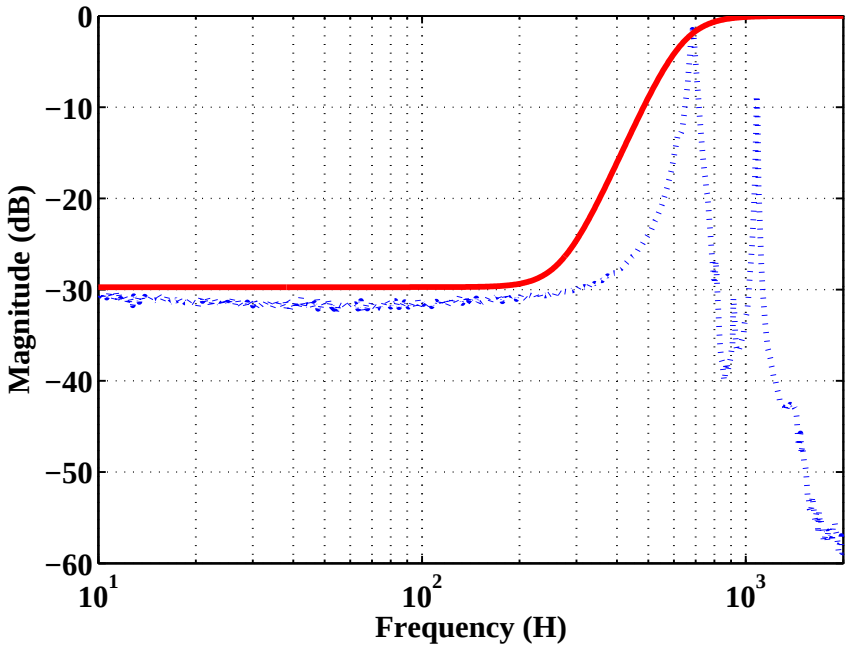


**Figure 5.5:** Multiplicative uncertainty bound. The dotted (. .) line represents $\frac{max\{|G_m(j\omega)-G_1(j\omega)|,|G_m(j\omega)-G_2(j\omega)|\}}{|G_m(j\omega)|}$ and the solid line represents $|W_m(j\omega)|$.

the state and the control input, respectively are chosen such that the cost functional reflects the desired performance objectives of the control system. Here, $E[.]$ is the expected value.

In order to define the minimax LQG control problem consider $G_m(j\omega)$ and $W_m(j\omega)$ to have the following state space realizations:

$G_m(j\omega) = \left[\begin{array}{c|c} A_g & B_g \\ \hline C_g & D_g \end{array}\right]$ and $W_m(j\omega) = \left[\begin{array}{c|c} A_w & B_w \\ \hline C_w & D_w \end{array}\right]$. Hence, from Fig. 5.4

$$\dot{x_g}(t) = A_g x_g(t) + B_g(u(t) + w(t)) \tag{5.9}$$

$$y(t) = C_g x_g + D_g(u(t) + w(t)). \tag{5.10}$$

And

$$\dot{x_w}(t) = A_w x_w(t) + B_w u(t) \tag{5.11}$$

$$z(t) = C_w x_w + D_w u(t). \tag{5.12}$$

Therefore, we can write

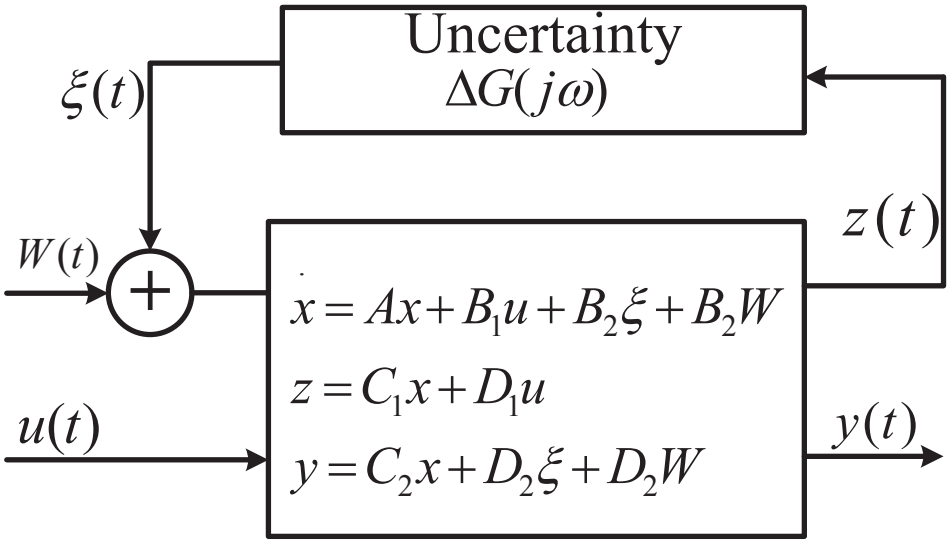


**Figure 5.6:** Block diagram of uncertain stochastic system.

$$\begin{bmatrix} \dot{x_g}(t) \\ \dot{x_w}(t) \end{bmatrix} = \begin{bmatrix} A_g & 0 \\ 0 & A_w \end{bmatrix} \begin{bmatrix} x_g(t) \\ x_w(t) \end{bmatrix} + \begin{bmatrix} B_g \\ B_w \end{bmatrix} u + \begin{bmatrix} B_g \\ 0 \end{bmatrix} w.$$

Consider the uncertain stochastic system given in Fig. 5.6 defined by the following stochastic state equations of the form

$$\begin{aligned} \dot{x} &= Ax + B_1u + B_2\xi + B_2W, \\ z &= C_1x + D_1u, \\ y &= C_2x + D_2\xi + D_2W \end{aligned} \tag{5.13}$$

where, $x(t) \in \mathbb{R}^n$ is the state, $u(t) \in \mathbb{R}^m$ is the control input, $W(t)$ is a unity covariance Gaussian white noise process corresponding to the nominal disturbance input, $z(t) \in \mathbb{R}^q$ is the uncertainty output, $\xi(t) \in \mathbb{R}^p$ is the uncertainty input and $y(t) \in \mathbb{R}^l$ is the measured output. Here, $A = \begin{bmatrix} A_g & 0 \\ 0 & A_w \end{bmatrix}$, $B_1 = \begin{bmatrix} B_g \\ B_w \end{bmatrix}$, $B_2 = \begin{bmatrix} B_g \\ 0 \end{bmatrix}$, $C_1 = \begin{bmatrix} 0 \\ C_w \end{bmatrix}$, $C_2 = \begin{bmatrix} C_g \\ 0 \end{bmatrix}$, $D_1 = D_w$, $D_2 = \begin{bmatrix} 0 & \delta \end{bmatrix}$. Since in the design of LQG theory $D_2D_2' > 0$ [72–76], we chose $D_2 = \begin{bmatrix} 0 & \delta \end{bmatrix}$, where $\delta > 0$ is a small positive number. The uncertainty input $\xi(t)$ and the uncertainty output $z(t)$ are used to define a set

of all addmissible uncertainties and the relationship between the input and output of the uncertainty model is written by the following integral quadratic constraint:

$$\lim_{T\to+\infty}\mathbf{E}\frac{1}{2T}\left[\int_0^T(||\xi(t)||^2-||z(t)||^2)dt\right]\leq d \tag{5.14}$$

where $d>0$ is a given constant that restricts the size of the disturbance signals acting on to the system. The performance index of the minimax LQG controller is expressed by (5.8) where the uncertainty constraint (5.14) is satisfied. In the design, it is required to find a controller which minimizes the worst case of (5.8) satisfying (5.14) and this is done by solving the following two algebraic Riccati equations:

$$\begin{aligned}(A-B_2D_2'(D_2D_2')^{-1}C_2)Y_\infty+Y_\infty(A-B_2D_2'(D_2D_2')^{-1}C_2)'-Y_\infty(C_2'(D_2D_2')^{-1}C2-\\ \frac{1}{\tau}R_\tau)Y_\infty+B_2(I-D_2'(D_2D_2')^{-1}D_2)B_2'=0\end{aligned} \tag{5.15}$$

$$\begin{aligned}X_\infty(A-B_1G_\tau^{-1}\gamma')+(A-B_1G_\tau^{-1}\gamma_\tau')'X_\infty+(R_\tau-\gamma_\tau G_\tau^{-1}\gamma_\tau')-X_\infty(B_1G_\tau^{-1}B_1'-\\ \frac{1}{\tau}B_2B_2')X_\infty=0\end{aligned} \tag{5.16}$$

where, the solutions are required to satisfying following conditions:

$$X_\infty>0 \tag{5.17}$$

$$Y_\infty>0 \tag{5.18}$$

$$I-\frac{1}{\tau}X_\infty Y_\infty>0 \tag{5.19}$$

and

$$R_\tau-\gamma_\tau'G_\tau^{-1}\gamma_\tau\geq 0. \tag{5.20}$$

Here,

$R_\tau := R + \tau C_1' C_1,$
$G_\tau := G + \tau D_1' D_1,$
$\gamma_\tau = \tau C_1' D_1.$

Comparing the above two Riccati equations given in (5.15) and (5.16) with the standard Riccati equation of the form $P'X + XP - XMR^{-1}M'X + N = 0$ we get $M = \begin{bmatrix} C_2' & \sqrt{(}R) \end{bmatrix}$ and $R^{-1} = \begin{bmatrix} (D_2 D_2')^{-1} & 0 \\ 0 & -\frac{I}{\tau} \end{bmatrix}$ for (5.15) and $M = \begin{bmatrix} B_1 & B_2 \end{bmatrix}$ and $R^{-1} = \begin{bmatrix} G_\tau^{-1} & 0 \\ 0 & -\frac{I}{\tau} \end{bmatrix}$ for (5.16), respectively.

Now the minimax LQG optimal controller can be defined by the following equation:

$$\hat{\dot{x}} = (A - B_1 G_\tau^{-1}\gamma_\tau' - \left(B_1 G_\tau^{-1} B_1' - \frac{1}{\tau} B_2 B_2'\right) X_\infty)\hat{x} + \left(I - \frac{1}{\tau} X_\infty Y_\infty\right)^{-1} (Y_\infty C_2' + B_2 D_2')(D_2 D_2')^{-1} \times \left(y - (C_2 + \frac{1}{\tau} D_2 B_2' X_\infty)\hat{x}\right),$$

$$u_t = -G_\tau^{-1}(B_1' X_\infty + \gamma_\tau')\hat{x} \tag{5.21}$$

where, for each value of the parameter $\tau > 0$, the corresponding upper bound on the cost functional is

$$W_\tau = \frac{1}{2} tr\Big[Y_\infty R_\tau + (Y_\infty C2' + B_2 D_2')(D_2 D_2')^{-1} \times (C_2 Y_\infty + D_2 B_2') X_\infty (I - \frac{1}{\tau} Y_\infty X_\infty)^{-1}\Big] + \tau d. \tag{5.22}$$

## 5.4 Controller Design and Selection

The application of minimax LQG control theory starts with the formulation of the uncertain system model. In order to design the minimax LQG controller, it is necessary to specify the uncertainty first. As discussed earlier, the main uncertainties considered in the design are (a) spill over dynamics at high frequencies due to the higher order modes of the system, (b) the uncertainty due to the changes in plant transfer functions due to changes in temperature. The uncertainty modelling along with the selection of the weighing transfer function is presented in earlier. The

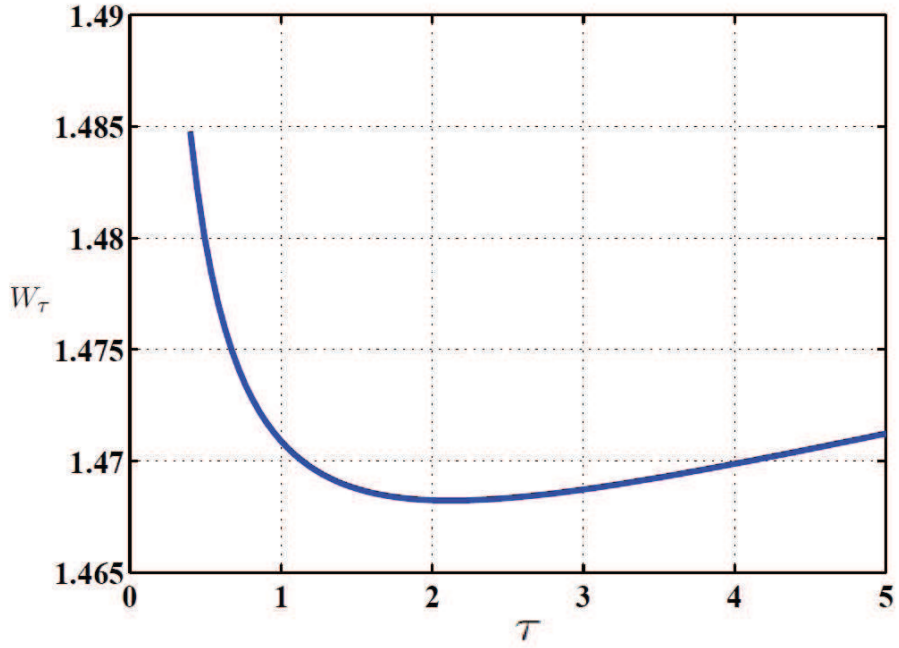


**Figure 5.7:** $W_\tau$ versus $\tau$.

true transfer function of the system is expresses by (5.2) and the weighting transfer function is expressed by (5.7).

The uncertainty presented in the design is stochastic uncertainty and in a stochastic uncertain system Gaussian white noise acts on the same channel as the control input. In the theory of uncertain stochastic systems, the design of the minimax LQG controller is based on the assumption $D_2 D_2' > 0$ [72–76]. Therefore, in order to satisfy the design requirements of the LQG theory, a small measurement noise is added with the system.

As discussed in previous section, the design parameters $R$ and $G$ of (5.8) play a major role in the performance and robustness of the proposed controller. A large value of $R$ increases the performance of the proposed controller. However, a very large value of $R$ would result in controller having a very large bandwidth. A very large bandwidth of the controller limits the implementation of the controller in the rapid prototyping system dSPACE. Therefore, there is a trade-off in selection of $R$ to achieve the desired performance of the controller and the implementation of the controller in dSPACE. The design parameter $G$ determines the size of the control input to the plant. After some trial and error method we select $R = 1000$ I, where

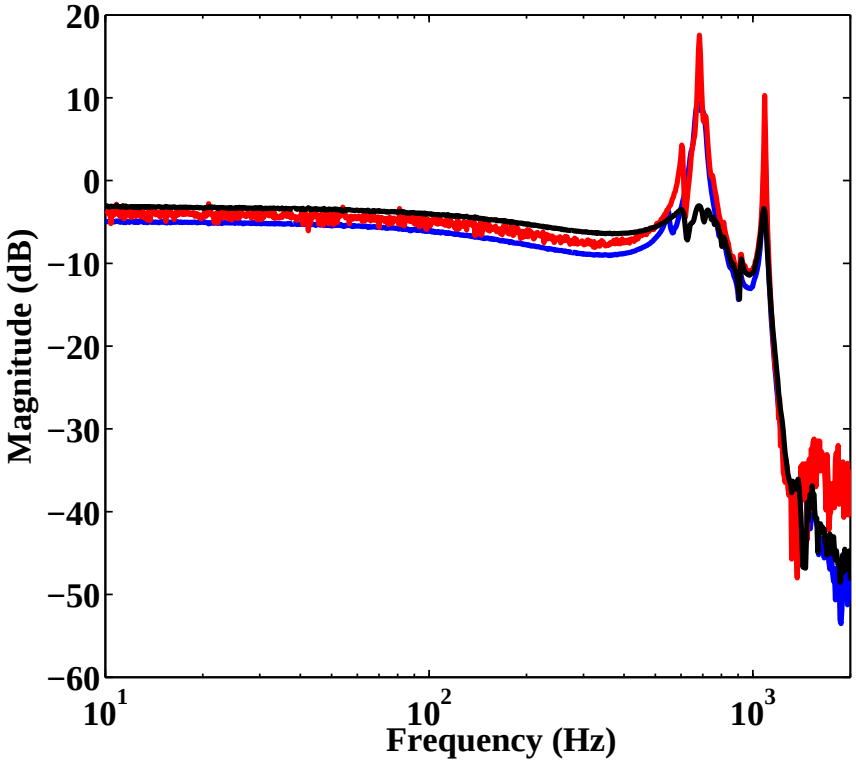


**Figure 5.8:** Measured uncontrolled open-loop (blue and red solid line) and controlled closed-loop (black solid line) magnitude frequency responses.

I is an identity matrix of order $9 \times 9$, G=0.5.

The LQG controller is synthesized first by selecting the constant $\tau > 0$ to minimize the quantity defined in (5.22). A plot of $W_\tau$ versus $\tau$ is given in Fig. 5.7. We select the $\tau = 2.1$ in the design process. This value of $\tau$ is used to construct a controller using the formula (5.21). The transfer function of the controller obtained in the design process is as follows:

$$\frac{-3.905\times10^4 s^8+4.449\times10^9 s^7+5.025\times10^{13} s^6+4.821\times10^{17} s^5+3.226\times10^{21} s^4+1.465\times10^{25} s^3+4.468\times10^{28} s^2+8.268\times10^{31} s+4.568\times10^{34}}{s^9+8.686\times10^4 s^8+2.324\times10^9 s^7+3.542\times10^{13} s^6+3.365\times10^{17} s^5+2.504\times10^{21} s^4+1.251\times10^{25} s^3+4.245\times10^{28} s^2+9.378\times10^{31} s+1.084\times10^{35}} \tag{5.23}$$

## 5.5 Performance of the Controller

The performance of the proposed controller is first measured by examining the closed-loop frequency response of the system. A comparison of the open- and closed-loop magnitude frequency responses is presented in Fig. 5.8. The comparison of the

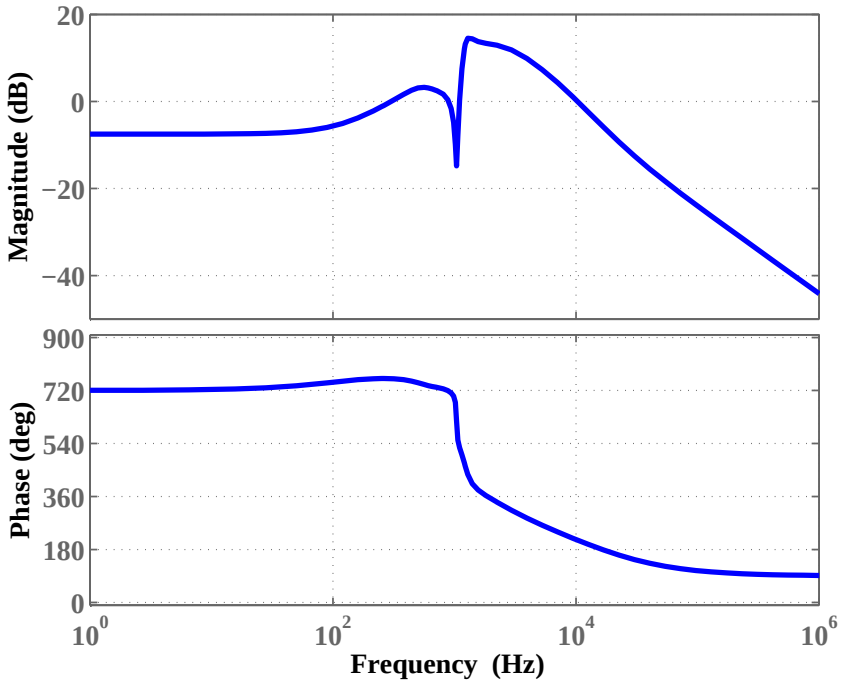


**Figure 5.9:** Bode diagram of the minimax LQG controller for damping.

measured open- and closed-loop magnitude frequency responses show that, the proposed controller is able to flatten the first resonant mode of the scanner by providing 18 dB of damping. The controller also reduce the second resonant peak by 10 dB of the scanner.

The magnitude Bode diagram of the controller transfer function presented in Fig. 5.9 shows that the controller provides high gain near the resonant frequency of the scanner. The gain of the controller at low and high frequencies is low which results in large gain and phase margins. The measured magnitude Bode diagram and Nyquist plot of the measured open loop-gain presented in Fig. 5.10 and Fig. 5.11 shows that, the closed-loop system is stable and the controller achieves large gain and phase margins.

The time domain performance of the proposed controller is considered by applying triangular signals of different frequencies (50 Hz, 100 Hz, 150 Hz, 200 Hz) to the X-axis of the scanner in the open- and closed-loop cases and the corresponding X sensor outputs are recorded. Fig. 5.12 shows the outputs from the X sensor in the open- and closed-loop cases for different frequencies obtained by using the controller

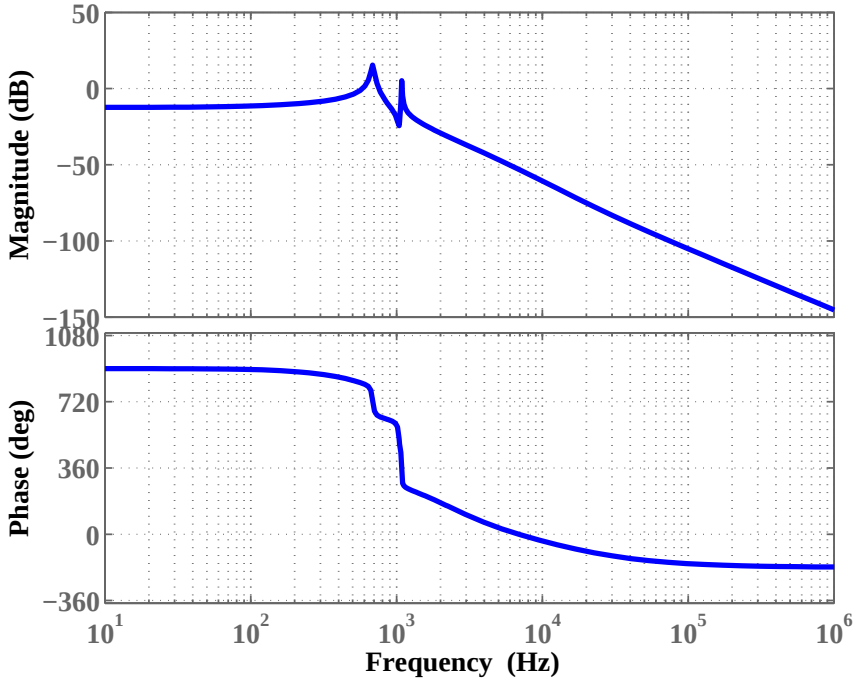


**Figure 5.10:** Bode diagram of the identified loop-gain.

in the X-axis of the scanner. This comparison shows that the open-loop sensor output signal becomes distorted as the scanning frequency increases, whereas, the closed-loop sensor outputs are less distorted as compared to the open-loop sensor outputs.

A further examination of the time domain performance of the controller is considered by applying square wave signals of 1 Hz, 10 Hz, 50 Hz, and 100 Hz to the X-axis of the scanner. The X sensor outputs in the open- and closed-loop cases for different frequencies of the pulse signals are given in Fig. 5.13 which show that the designed controller achieved a significant amount of damping. This increase in damping results in less vibratory sensor outputs in closed-loop as compared to the open-loop case.

The design of the minimax LQG controller presented above was designed for damping the resonant mode of the scanner. In the following we present design of integral minimax LQG controller for tracking control of the PTS.

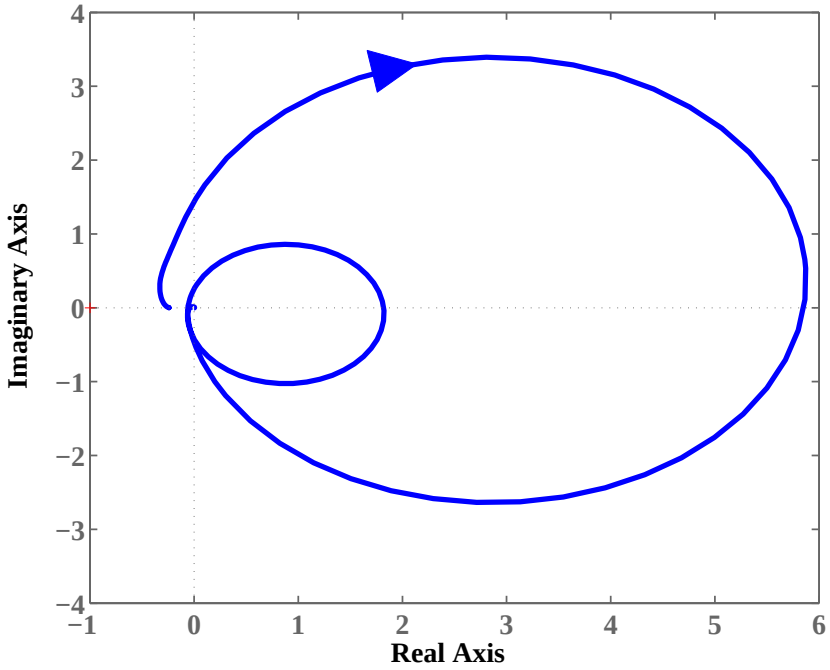


**Figure 5.11:** Nyquist diagram of the identified loop-gain for positive frequencies.

## 5.6 Integral Minimax LQG Control Theory

Consider the uncertain stochastic system given in Fig. 5.14 defined by the following stochastic state equations of the form

$$\begin{aligned} \dot{x} &= Ax + B_1 u + b_2 \xi + B_2 W, \\ z &= C_1 x + D_1 u, \\ y &= C_2 x + D_2 \xi + D_2 W. \end{aligned} \tag{5.24}$$

In Fig. 5.14, $I(s)$ is the transfer function of an integral controller, $y = C_2 x$, $x_i = I(s)y = \int y dt$ and $\dot{x}_i = y = C_2 x$.

Consider

$$\tilde{x} = \begin{bmatrix} x \\ x_i \end{bmatrix} = \begin{bmatrix} x \\ \int y dt \end{bmatrix} \tag{5.25}$$

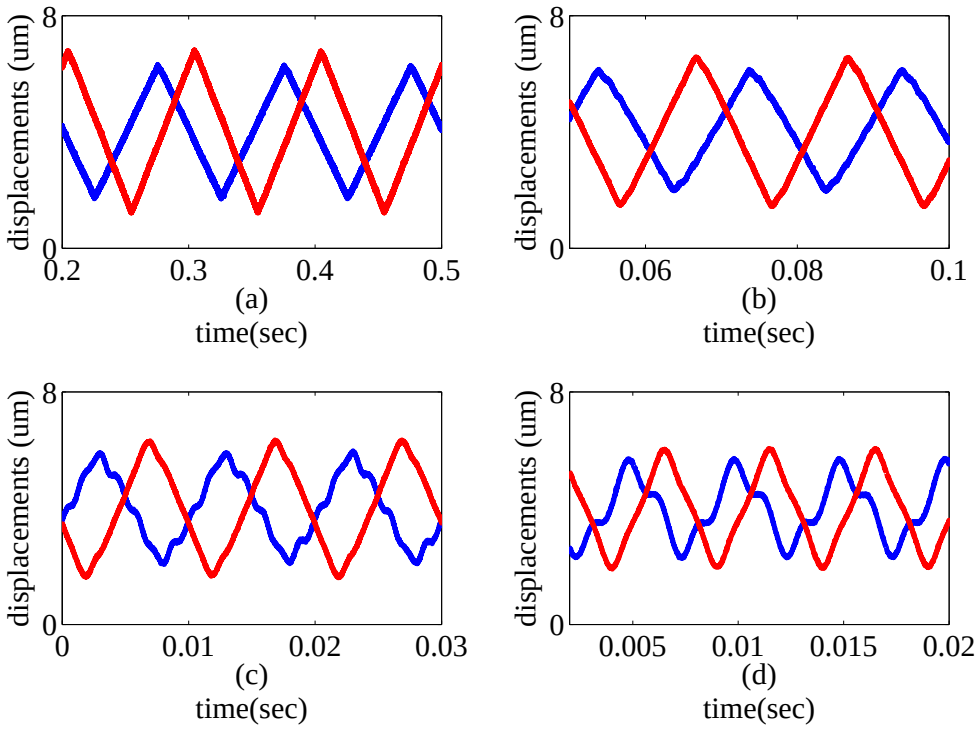


**Figure 5.12:** Measured open-loop (blue solid line) and closed-loop (red solid line) sensor output signals with a triangular wave reference input using minimax LQG controller.

$$\tilde{y} = \begin{bmatrix} y \\ x_i \end{bmatrix} = D_2(\xi + W) \tag{5.26}$$

$$\dot{\tilde{x}}(t) = \begin{bmatrix} \dot{x}(t) \\ \dot{x}_i(t) \end{bmatrix} = \begin{bmatrix} A & 0 \\ C_2 & 0 \end{bmatrix} \begin{bmatrix} x(t) \\ x_i(t) \end{bmatrix} + \begin{bmatrix} B_1 \\ 0 \end{bmatrix} u + \begin{bmatrix} B_2 & 0 & 0 \\ 0 & 0 & 0 \end{bmatrix} (\xi + W); \tag{5.27}$$

$$Z = \begin{bmatrix} C_1 & 0 \end{bmatrix} \tilde{x} + D_1 u; \tag{5.28}$$

$$\tilde{y} = \begin{bmatrix} C_2 & 0 \\ 0 & I \end{bmatrix} \tilde{x} + \begin{bmatrix} 0 & \epsilon_1 & 0 \\ 0 & 0 & \epsilon_2 \end{bmatrix} (\xi + W). \tag{5.29}$$

Let,

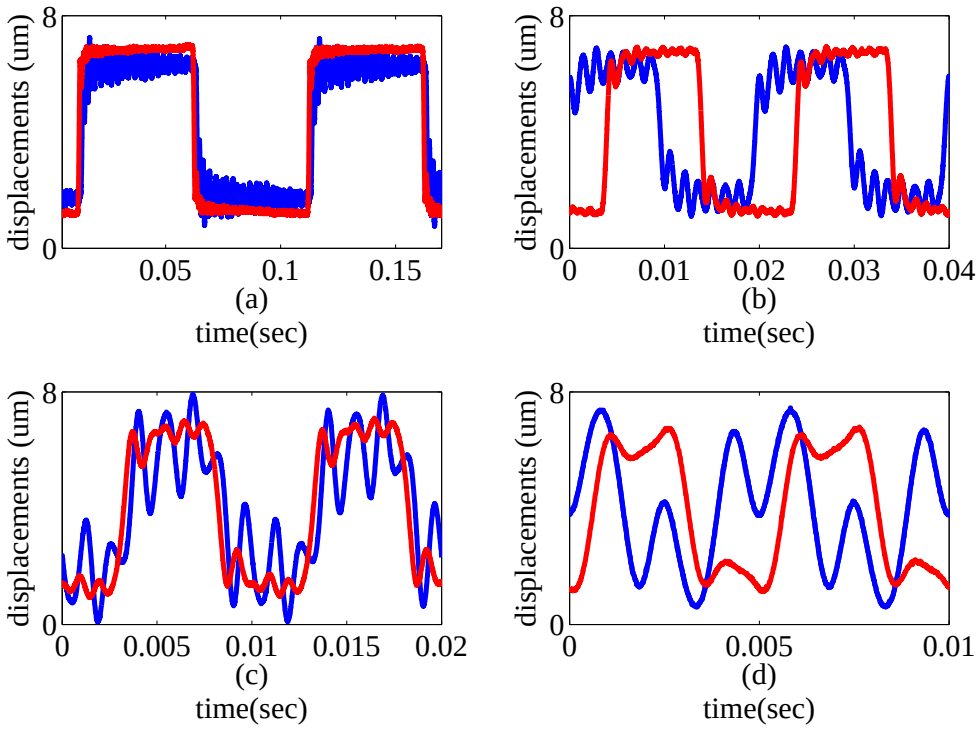


**Figure 5.13:** Measured open-loop (blue solid line) and closed-loop (red solid line) responses with a square wave reference input using minimax LQG controller.

$$A_n = \begin{bmatrix} A & 0 \\ C_2 & 0 \end{bmatrix},\ B_{1n} = \begin{bmatrix} B_1 \\ 0 \end{bmatrix},\ B_{2n} = \begin{bmatrix} B_2 & 0 & 0 \\ 0 & 0 & 0 \end{bmatrix},\ C_{1n} = \begin{bmatrix} C_1 & 0 \end{bmatrix},\ D_{1n} = D_1,\ C_{2n} = \begin{bmatrix} C_2 & 0 \\ 0 & I \end{bmatrix},\ D_{2n} = \begin{bmatrix} 0 & \epsilon_1 & 0 \\ 0 & 0 & \epsilon_2 \end{bmatrix}.$$

For the augmented plant as outlined in (5.27)-(5.29), the integral minimax LQG controller is designed by defining a quadratic cost function of the form

$$J = \lim_{T \to +\infty} \mathbf{E} \frac{1}{2T} \int_0^T (x(t)'Rx(t) + f(y)^T Q_I f(y) + u(t)'Gu(t))dt \tag{5.30}$$

where $f(y) = \int_0^T y(\tau)d\tau$, $R \geq 0$, $Q_I \geq 0$, and $G > 0$ are weighting matrices associated with the state, the integral state, and the control input respectively. Here, $y(t)$ is the output of the plant with zero input. The design of the integral

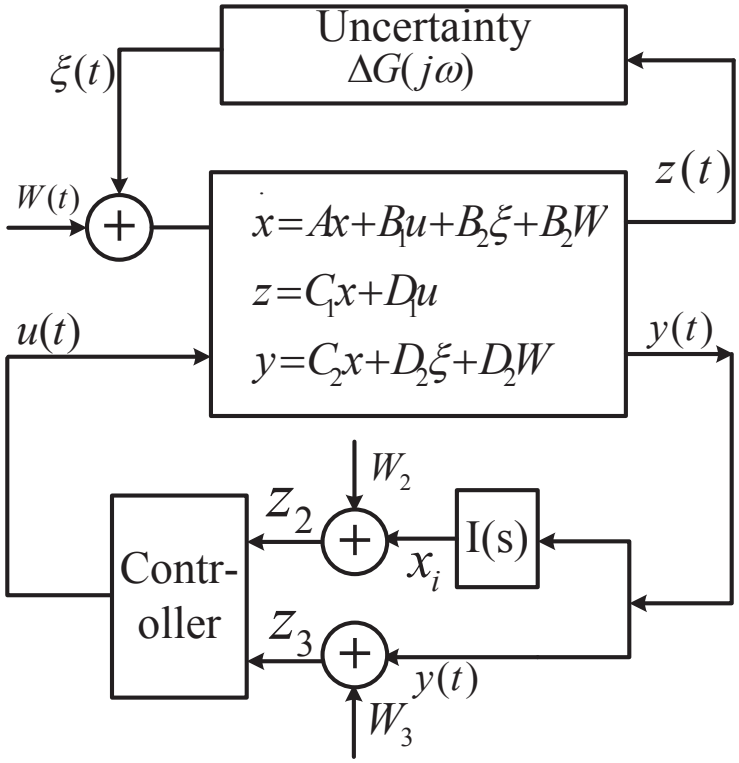


**Figure 5.14:** Block diagram of uncertain stochastic uncertain system.

minimax LQG controller is carried out by solving following two algebraic Riccati equations:

$$\begin{aligned}(A_n - B_{2n}D_{2n}'(D_{2n}D_{2n}')^{-1}C_{2n})Y_\infty + Y_\infty(A_n - B_{2n}D_{2n}'(D_{2n}D_{2n}')^{-1}C_{2n})' \\ -Y_\infty(C_{2n}'(D_{2n}D_{2n}')^{-1}C2n - \frac{1}{\tau}R_\tau)Y_\infty \\ +B_{2n}(I - D_{2n}'(D_{2n}D_{2n}')^{-1}D_{2n})B_{2n}' = 0 \quad (5.31)\end{aligned}$$

$$\begin{aligned}X_\infty(A_n - B_{1n}G_\tau^{-1}\gamma') + (A_n - B_{1n}G_\tau^{-1}\gamma_\tau')'X_\infty + \\ (R_\tau - \gamma_\tau G_\tau^{-1}\gamma_\tau') - X_\infty(B_{1n}G_\tau^{-1}B_{1n}' - \frac{1}{\tau}B_{2n}B_{2n}')X_\infty = 0 \quad (5.32)\end{aligned}$$

where, the solutions are required to satisfy following conditions:

$$X_\infty > 0 \tag{5.33}$$

$$Y_\infty > 0 \tag{5.34}$$

$$I - \frac{1}{\tau} X_\infty Y_\infty > 0 \tag{5.35}$$

and

$$R_\tau - \gamma_\tau' G_\tau^{-1} \gamma_\tau \geq 0. \tag{5.36}$$

Here,
$R_\tau := R + \tau C_{1n}' C_{1n}$,
$G_\tau := G + \tau D_{1n}' D_{1n}$,
$\gamma_\tau = \tau C_{1n}' D_{1n}$.

Now the integral minimax LQG optimal controller can be defined by the following equation:

$$\begin{aligned}\dot{\hat{x}} = (A_n - B_{1n} G_\tau^{-1} \gamma_\tau' - \left( B_{1n} G_\tau^{-1} B_{1n}' - \frac{1}{\tau} B_{2n} B_{2n}' \right) X_\infty) \hat{\dot{x}} \\ + \left( I - \frac{1}{\tau} X_\infty Y_\infty \right)^{-1} (Y_\infty C_{2n}' + B_{2n} D_{2n}')(D_{2n} D_{2n}')^{-1} \\ \times \left( y - (C_{2n} + \frac{1}{\tau} D_{2n} B_{2n}' X_\infty) \hat{\dot{x}} \right)\end{aligned}$$

$$u_t = -G_\tau^{-1} (B_{1n}' X_\infty + \gamma_\tau') \hat{\dot{x}} \tag{5.37}$$

where, for each value of the parameter $\tau > 0$, the corresponding upper bound on the cost functional is

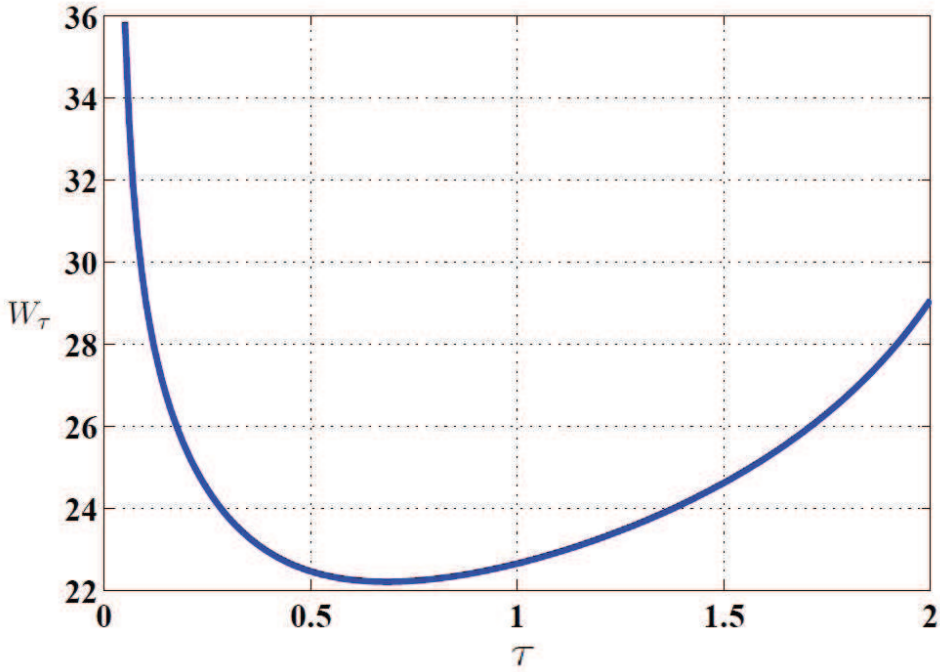


**Figure 5.15:** $W_\tau$ versus $\tau$ for designing integral minimax LQG controller.

$$W_\tau = \frac{1}{2} tr \Big[ Y_\infty R_\tau + (Y_\infty C2n' + B_{2n} D'_{2n})(D_{2n} D'_{2n})^{-1} \times (C_{2n} Y_\infty + D_{2n} B'_{2n}) X_\infty (I - \frac{1}{\tau} Y_\infty X_\infty)^{-1} \Big] + \tau d \tag{5.38}$$

As discussed earlier the design parameters $R$ and $G$ have major role on the performance and robustness of the proposed controller. A large value of $R$ increase the performance of the proposed controller. The design parameter $G$ defines the amount of control input to the plant. A high value of $G$ may lead to a controller with a large gain which may cause saturation problem in the actuator. We select

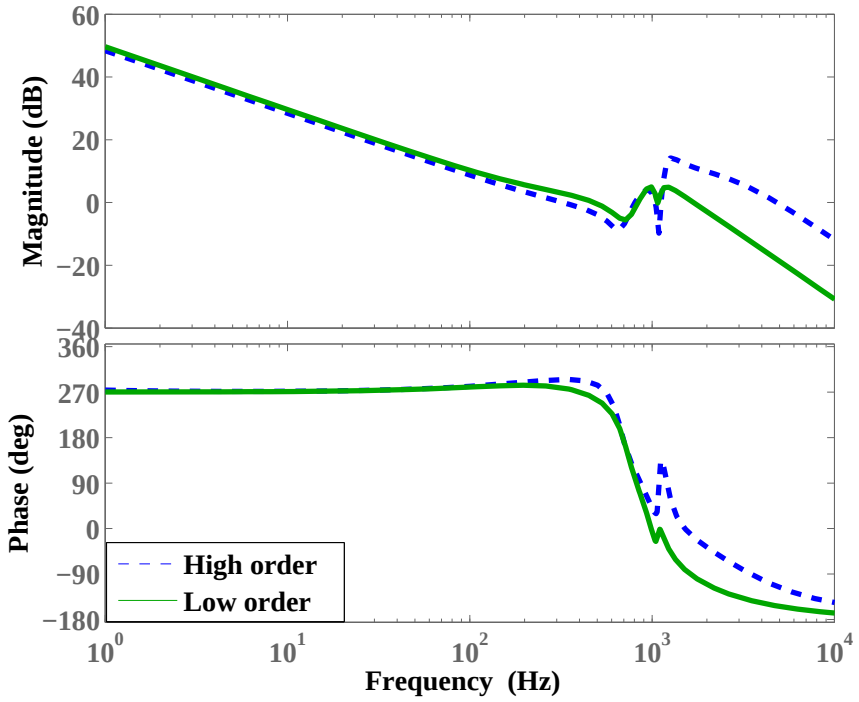


**Figure 5.16:** Comparison of Bode diagram between the high and low order integral minimax LQG controller.

$$R = \begin{bmatrix} 10 & 0 & 0 & 0 & 0 & 0 & 0 & 0 & 0 & 0 \\ 0 & 10 & 0 & 0 & 0 & 0 & 0 & 0 & 0 & 0 \\ 0 & 0 & 10 & 0 & 0 & 0 & 0 & 0 & 0 & 0 \\ 0 & 0 & 0 & 10 & 0 & 0 & 0 & 0 & 0 & 0 \\ 10 & 0 & 0 & 0 & 10 & 0 & 0 & 0 & 0 & 0 \\ 0 & 0 & 0 & 0 & 0 & 10 & 0 & 0 & 0 & 0 \\ 0 & 0 & 0 & 0 & 0 & 0 & 10 & 0 & 0 & 0 \\ 0 & 0 & 0 & 0 & 0 & 0 & 0 & 10 & 0 & 0 \\ 0 & 0 & 0 & 0 & 0 & 0 & 0 & 0 & 10 & 0 \\ 0 & 0 & 0 & 0 & 0 & 0 & 0 & 0 & 0 & 1100 \end{bmatrix}, \text{ G=.5, } D_{2n} = \begin{bmatrix} 0 & .005 & 0 \\ 0 & 0 & .00011 \end{bmatrix}.$$

A plot of $W_\tau$ versus $\tau$ for integral minimax LQG controller is given in Fig. 5.15. We select $\tau = 0.6$ in the design process. This value of $\tau$ is used to construct a controller using the formula (5.37). Using the above selected parameters, the

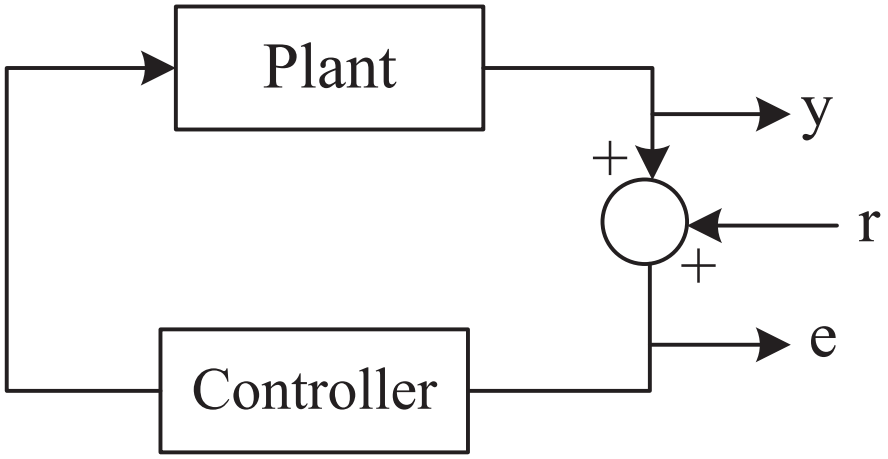


**Figure 5.17:** Setup to measure the closed-loop response.

integral minimax LQG synthesis methodology leads to a 11th-order controller. The digital implementation of such high order controller would require a long sampling interval which would degrade the performance of control system. Model order is reduced using MATLAB. The obtained 7th-order controller was re-tuned to achieve best matching between the high and low order controller. Fig. 5.16 shows the Bode plots of the full-order controller and reduced order controller.

## 5.7 Performance of the Integral Minimax LQG Controller

The proposed integral minimax LQG controller is implemented on a PTS to evaluate the performance of the controller in the frequency domain. Fig. 5.17 shows the setup to measure the frequency response of the closed-loop system where $r$ is the reference signal, $y$ is the output from the sensor and $e$ is the error between the command signal and output signal. A comparison of the open- and closed-loop magnitude frequency responses of $G_m(s)$ is shown in Fig. 5.18. The comparison shows that, the proposed controller is able to achieve a closed-loop bandwidth near to the first resonance frequency of the scanner. The controller is also able to damp both resonant modes of the scanner. The damping achieved by the proposed controller in closed-loop is 15 dB.

The time domain performance of the integral minimax LQG controller is presented by tracking triangular reference signals of different frequencies. Fig. 5.19 shows the outputs from the X sensor in open-loop at different scanning rates for an 8 µm × 8 µm scanning area. The scanning was performed at 50 Hz, 100 Hz and

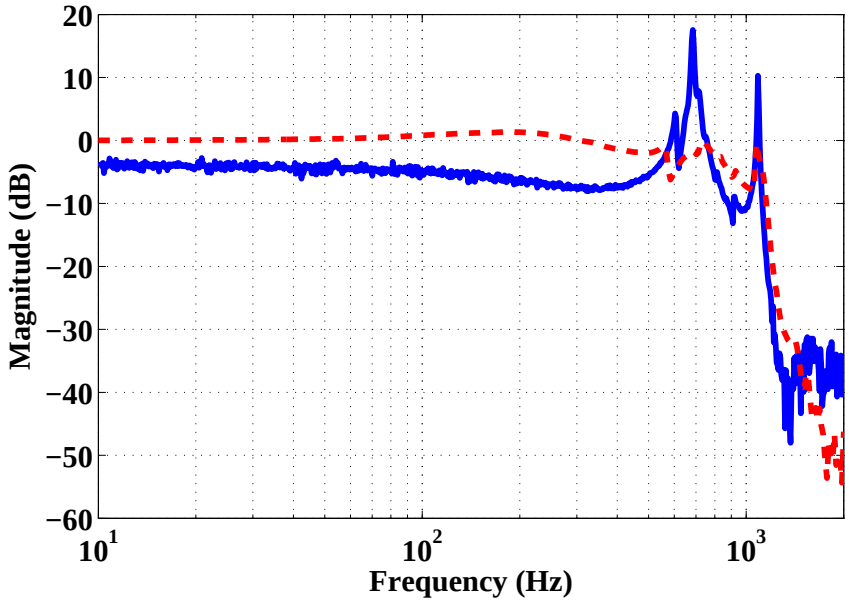


**Figure 5.18:** Open- and closed-loop magnitude frequency response using integral minimax LQG controller in the X-axis of the scanner. The solid line (–) represents the open-loop magnitude frequency response and the dashed line (- -) represents the closed-loop magnitude frequency response.

200 Hz. The open-loop X sensor output shows that the open-loop sensor output are distorted with the increase of scanning frequency. The closed-loop X sensor outputs given in Fig. 5.20 show less distortion as compared to the open-loop X sensor outputs.

In order to show the improvement achieved by the proposed controller as compared to an integral controller we have designed an integral controller for the PTS. Fig 5.21 shows the closed-loop system to implement the integral controller where $G(s)$ is the transfer function of the plant, $C(s) = \frac{K}{s}$ is the transfer function of the integral controller and $K$ is the gain of the controller. The closed-loop magnitude frequency responses between the PTS and integral controller for different gains of the integral controller is presented in Fig. 5.22. The closed-loop magnitude frequency responses given in Fig. 5.22 are obtained for $K = 1000,\ 1200,\ 1400,\ 2000$ and 2500.

The closed-loop system using the integral controller contains a lightly damped resonance mode. The bandwidth achieved by the integral controller with the gain $K = 1000$ for the PTS is 120 Hz. This is four times smaller than the bandwidth achieved by the integral minimax LQG controller. The higher gain of the integral

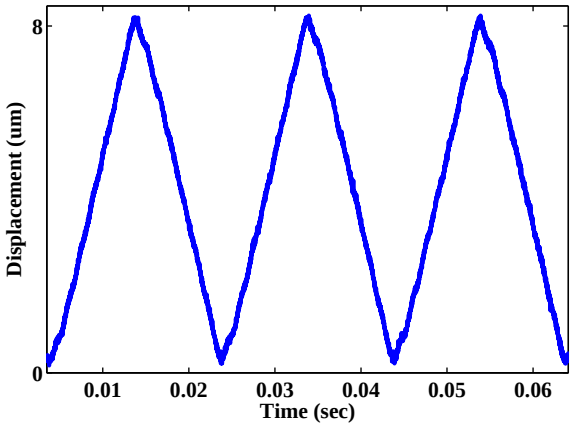


(a)

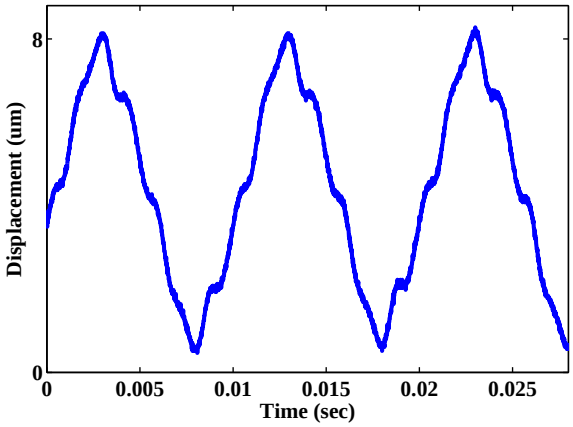


(b)

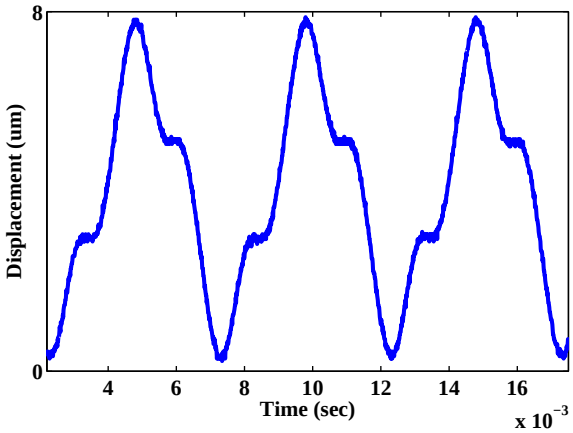


(c)

**Figure 5.19:** Open-loop X-sensor output for 8 µm × 8 µm scanning area at (a) 50 Hz, (b) 100 Hz, (c) 200 Hz.

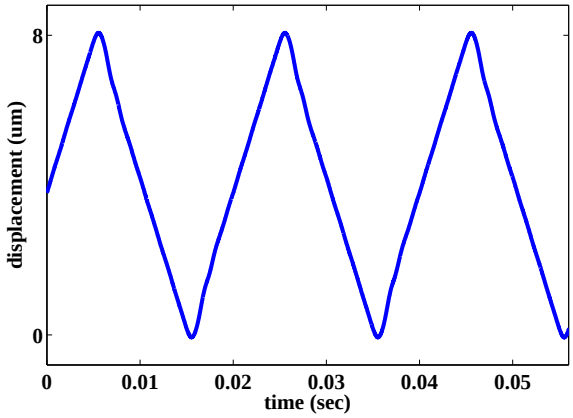


(a)

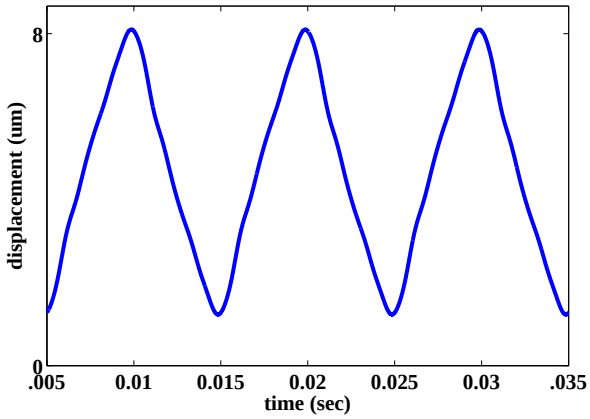


(b)

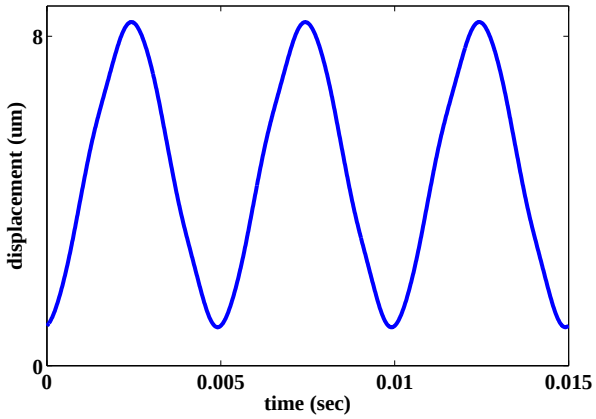


(c)

**Figure 5.20:** Closed-loop X-sensor output for 8 µm × 8 µm scanning area at (a) 50 Hz, (b) 100 Hz, (c) 200 Hz using integral minimax LQG controller.

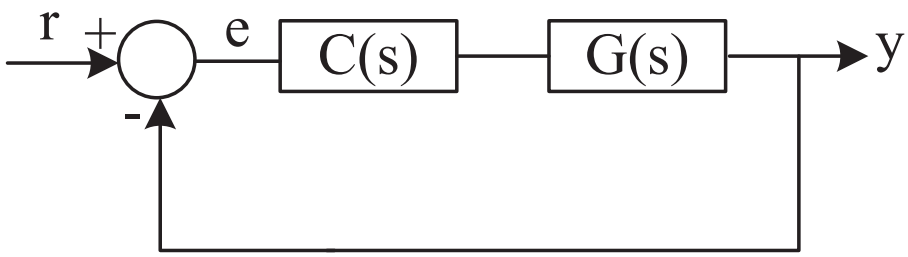


**Figure 5.21:** Closed-loop system for the implementation of the integral controller.

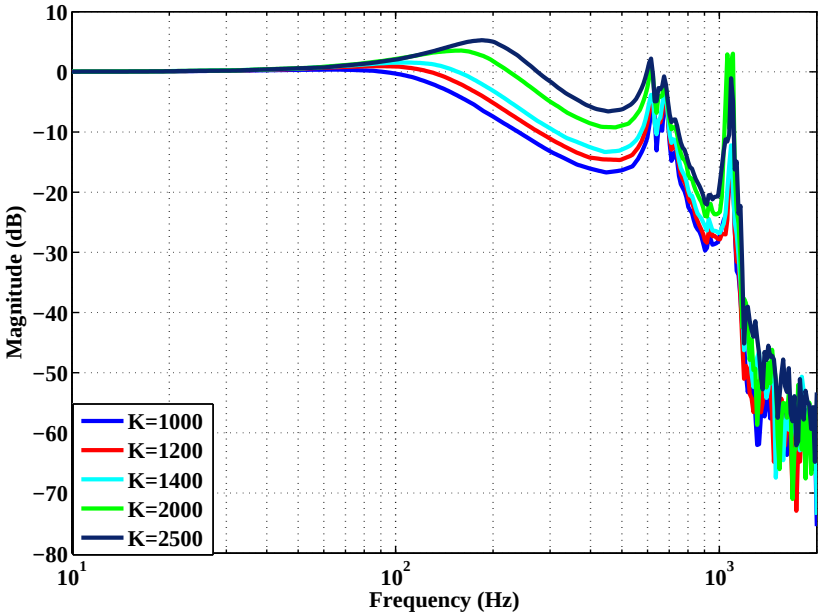


**Figure 5.22:** Performance of integral controller for different gains of the integral controller.

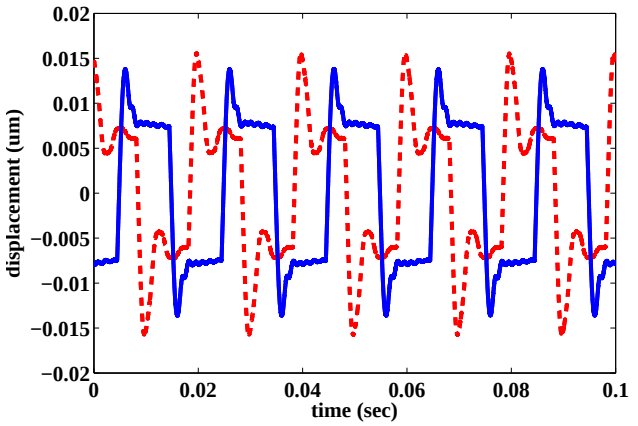


(a)

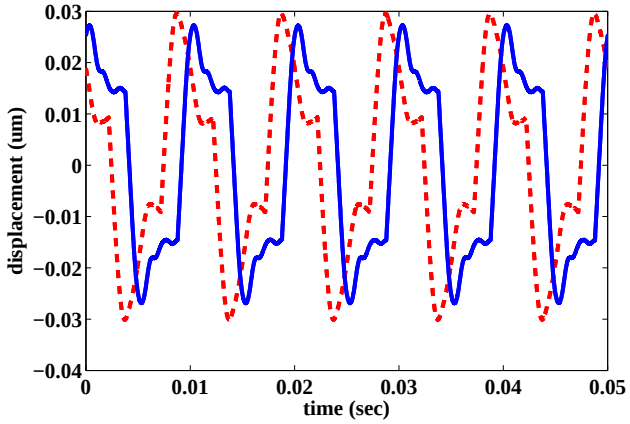


(b)

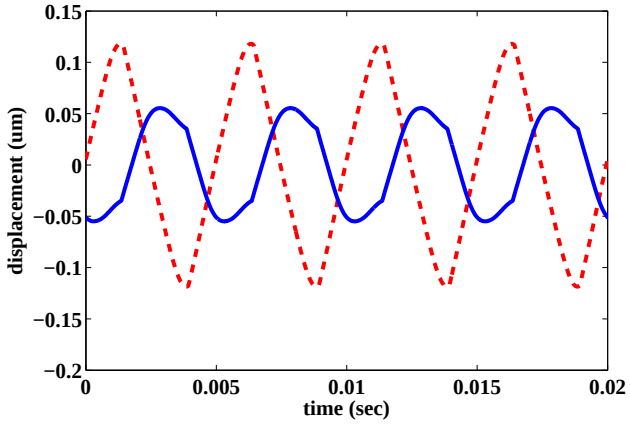


(c)

**Figure 5.23:** Tracking error at (a) 50 Hz, (b) 100 Hz, (c) 200 Hz. The solid line (–) is the tracking error obtained by using the integral minimax LQG controller and the dashed line (- -) is the tracking error obtained by using the integral controller.

controller increases the magnitude of the closed-loop gain at intermediate frequency range and resonance frequency range. This increase of gain is objectionable because this results in poor tracking performance of the integral controller.

Fig. 5.23 shows a comparison of the tracking errors by using the integral controller and integral minimax LQG controller. The gain of the integral controller is chosen as $K = 2500$ in this case. The comparison shows that the error using the integral minimax LQG controller is low as compared to the integral controller. This shows the merit of the proposed integral minimax LQG controller for triangular reference tracking.

## 5.8 Chapter Summary

In this chapter a minimax LQG controller is designed and implemented to improve the high speed performance of a PTS. The design of the controller is done to damp the resonant mode of the scanner and to improve the tracking performance of the PTS. The controller presented in this chapter is able to achieve a bandwidth near to the first resonance frequency of the scanner. The high closed-loop bandwidth of the system ensures the improvement for the fast nanopositioning performance of the scanner. Experimental results show that compared to an integral controller, the proposed controller is able to achieve four times the bandwidth than that of the integral controller.

The design of the controller shown in this chapter is presented for the SISO case. This SISO controller design approach does not guarantee the reduction of the cross coupling between the axes of the PTS. In the next chapter we will present the design of multi-variable controllers to account the effect of cross coupling between the axes of the scanner.

# Chapter 6

# Damping, Tracking and Cross Coupling Reduction of Piezoelectric Tube Scanners

Most nanopositioners used in SPMs are not independent SISO systems. They are multiple-input multiple-output (MIMO) systems. There exists a strong cross coupling effect between the axes of the scanner. The displacement of each axis of the PTS is not independent of the input from the other axis. Due to the cross coupling effect, a signal applied to one of the axes of PTSs results in displacements in both axes of scanners. This results in poor precision positioning of the PTS. The controller which is designed to improve the precision positioning of the PTS should also be able to reduce this cross couple effect between the axes of the PTS.

This chapter presents a design and experimental implementation of multivariable controller for the PTS to compensate for the damping, to improve tracking and to reduce the cross coupling effect between the axes of the scanner. The design of the controller is presented using a MIMO framework. A reference model matching approach is used to design the controller. This chapter also compares the performance of the proposed controller with the performance of the integral controller in terms of reducing the cross coupling effect between the axes of the PTS.

The rest of the chapter is organised as follows. The first section of this chapter presents a brief introduction and motivation for the design of a multi-variable NI controller for the PTS. The system identification process is discussed in Section 6.2. Section 6.3 presents details of the controller design for damping and cross coupling reduction. The performance of the controller for damping and cross coupling reduction is presented in Section 6.4 and the advantage and novelty of the proposed controller as compared to the state of the art is presented Section 6.5.The design and performance of the double resonant controller for damping, tracking and cross coupling reduction of the PTS is presented in Section 6.6. The chapter is concluded with a summary in Section 6.7.

## 6.1 Introduction

The motivation to design NI damping controllers for nanopositioners include their low order transfer function matrices, simplicity, ease of implementation, high bandwidth and robustness against the changes in resonance frequencies of the system. Previous approaches associated with the design of NI damping controllers [6, 18, 51] for the PTS are based on a SISO approach, i.e., the axes of the PTS are considered as independent SISO systems.

A SISO NI controller such as an integral resonant controller (IRC) may reduce the cross coupling effect to some extent at low frequencies but cannot solve the problem of image rotation as shown in Chapter 2. A SISO NI controller [15] that achieves a bandwidth near to the first resonance frequency of a scanner cannot guarantee a reduction of the cross coupling effect in the design process as the SISO controller design has no provision to attenuate the cross coupling effect [78]. The use of a MIMO controller design for PTSs is of interest because of their ability to consider both the bandwidth and cross coupling effect in the design process.

In this chapter, we first propose the design of multivariable NI controller to damp the resonant mode of PTS and to reduce the cross coupling effect between the axes of the scanner using a combination of a resonant controller and an integral resonant controller. Next we propose another design of a multivariable controller using double resonant controller for damping, tracking and cross coupling reduction of the PTS.

## 6.2 System Identification

Details of the identification of the dynamics of the PTS was presented in Chapter 3. In this chapter we will directly use the identified transfer function matrices of the PTS for the SISO and MIMO cases. The identified transfer function of the PTS in the X-axis is as follows:

$$G_{xx}(s) = \frac{D_x(s)}{V_x(s)} = \frac{-186.6s^2 + 1.348 \times 10^6 s - 2.412 \times 10^{10}}{s^3 + 1755s^2 + 3.452 \times 10^7 s + 4.459 \times 10^{10}} \tag{6.1}$$

where $D_x(s)$ is the Laplace transform of the output voltage from the X sensor and $V_x(s)$ is the Laplace transform of the input voltage to the HVA driving the X-axis of the piezo.

Fig. 6.1 compares the measured frequency response and the frequency response of the identified model $G_{xx}(s)$ of the PTS in the X-axis.

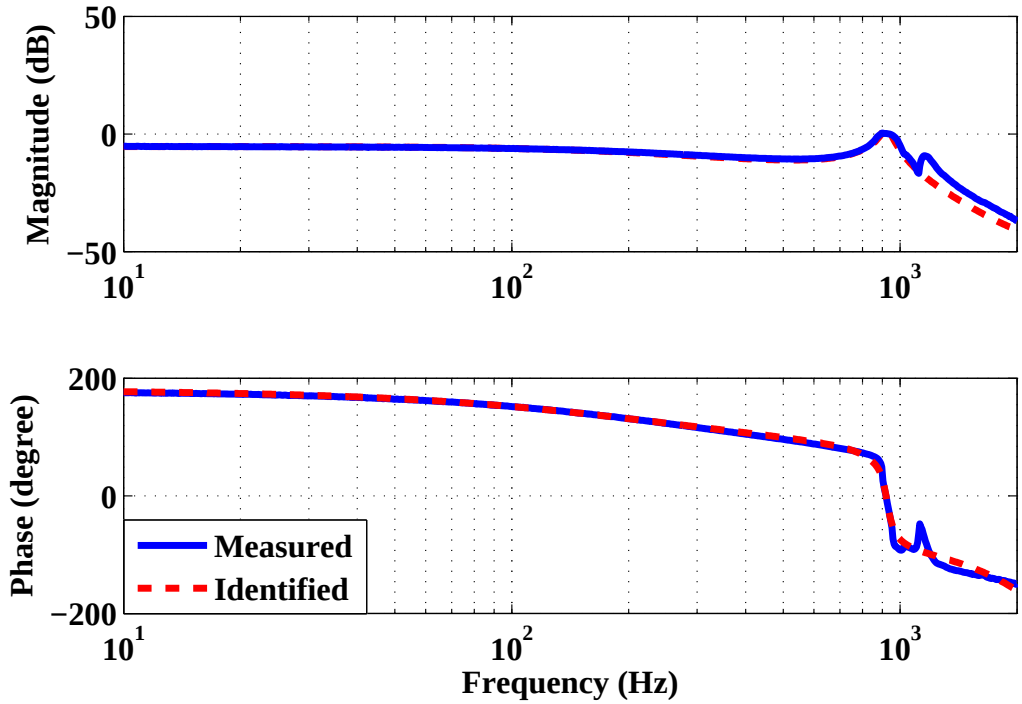


(a)

**Figure 6.1:** The measured and the identified model frequency response of $G_{xx}(s)$. The dashed line (- -) represents the identified model response and the solid line (–) represents the measured frequency response.

The transfer function matrix of the MIMO positioning system of the PTS is described by the following equation:

$$\begin{bmatrix} D_x(s) \\ D_y(s) \end{bmatrix} = G(s) \begin{bmatrix} V_x(s) \\ V_y(s) \end{bmatrix} \tag{6.2}$$

where, $G(s) = \begin{bmatrix} G_{xx}(s) & G_{xy}(s) \\ G_{yx}(s) & G_{yy}(s) \end{bmatrix}$.

The above transfer function matrix in (6.2) has a state space form which is given below:

$$\dot{x}(t) = Ax(t) + Bu(t)$$

$$y(t) = Cx(t) + Du(t) \tag{6.3}$$

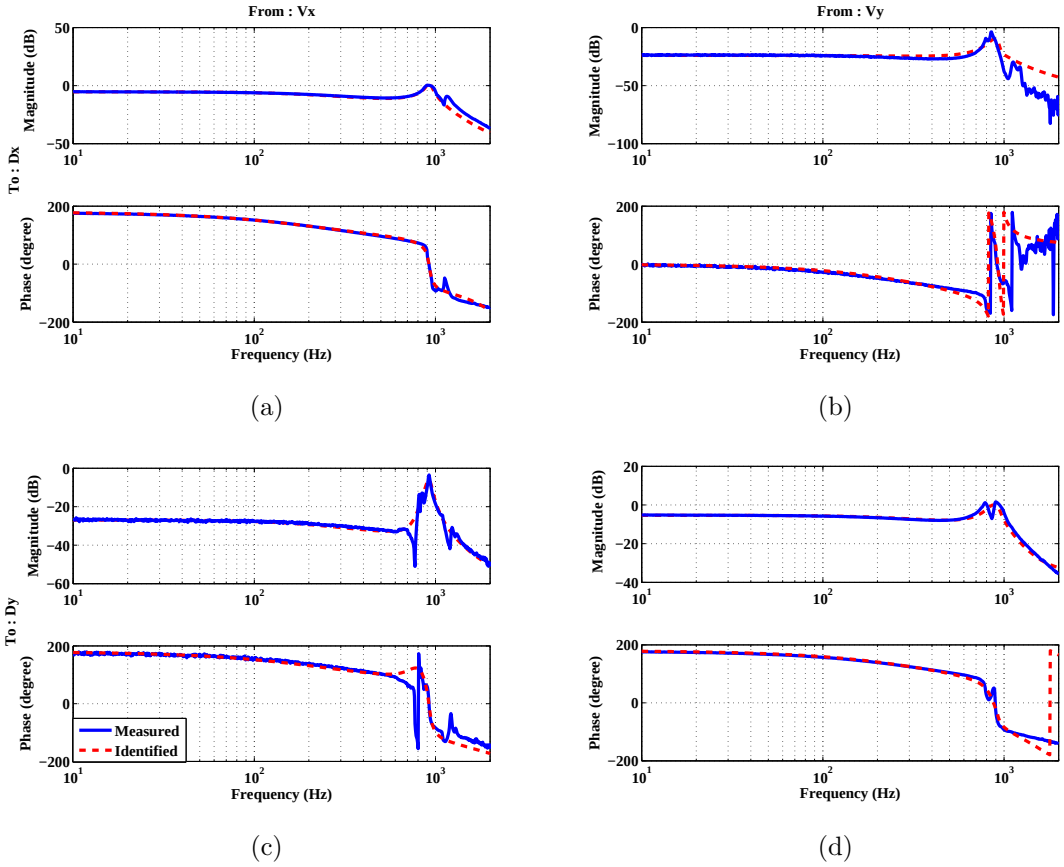


**Figure 6.2:** Open-loop frequency responses relating to the inputs $[V_x, V_y]^T$ and the outputs $[D_x, D_y]^T$. The solid line (–) represents the measured frequency responses and the dashed line (- -) represents the identified model frequency responses of (6.2). (a) Frequency response of $G_{xx}(s)$, (b) frequency response of $G_{yx}(s)$, (c) frequency response of $G_{xy}(s)$, and (d) frequency response of $G_{yy}(s)$.

where $u$ is a vector of the inputs to the HVA and $y$ is a vector of the outputs from the position sensors.

The identified values of the $A$, $B$, $C$,$D$ matrices of the above state space model from Chapter 3 are as follows:

$$A = \begin{bmatrix} -427.6 & -5583.6 & -1521.1 & 840.01 & -874.82 & 1074 \\ 4963.2 & -423.76 & -1040.6 & -1245.1 & -1828.2 & 1693.9 \\ 959.85 & 1010.9 & -690.68 & 5435.9 & 474.96 & 1528 \\ -587.17 & 1161.8 & -4395.2 & -508.85 & -2304.2 & -2166.5 \\ -102.38 & 609.98 & 458.09 & 1351.9 & -946.65 & 149.69 \\ 251.11 & -708.42 & 71.644 & 1020.2 & -8.7797 & -1686.1 \end{bmatrix},$$

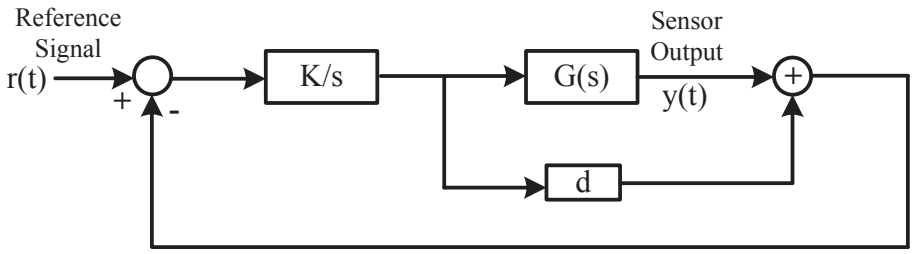


(a)

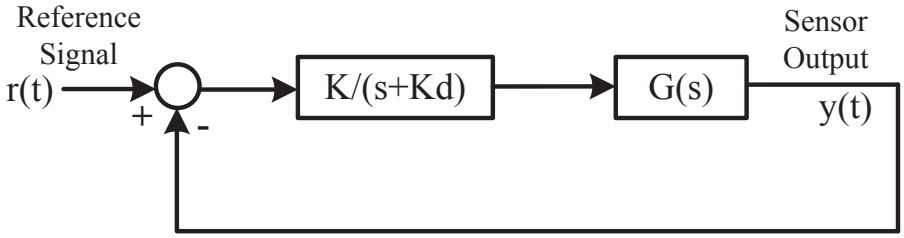


(b)

**Figure 6.3:** Block diagram of the integral resonant control scheme. (a) illustrative version, (b) simplified version.

$$B = \begin{bmatrix} 1.6893 & 12.168 \\ 12.022 & 10.622 \\ -0.42926 & 2.964 \\ 8.0813 & -10.904 \\ -17.019 & 1.1707 \\ 0.58665 & 18.898 \end{bmatrix},$$

$$C = \begin{bmatrix} 9.0521 & 16.8150 & -27.5329 & 20.7708 & 35.2925 & 2.4245 \\ 25.6510 & 19.0371 & 30.2869 & -16.1956 & 6.4775 & -58.5076 \end{bmatrix},$$

$$D = \begin{bmatrix} 0 & 0 \\ 0 & 0 \end{bmatrix}.$$

The matching between the MIMO open-loop measured data and the identified model (6.2) is shown in Fig. 6.2. It should be noted that the frequency responses in the X- and Y-axis of the PTS are not symmetric. The asymmetric properties of the materials from which the PTS is made and imperfections in the location of the sensors relative to the electrodes can cause different output voltages in the axes of the PTS.

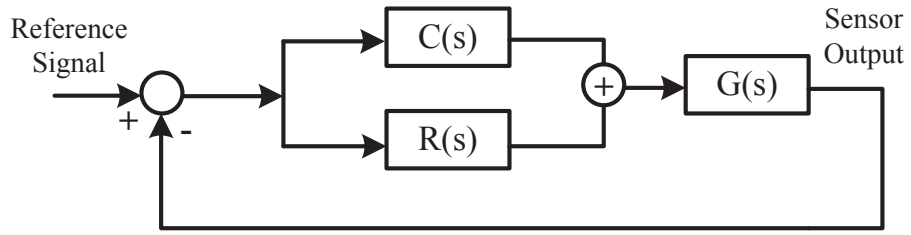


**Figure 6.4:** Block diagram of closed-loop system with IRC $C(s)$ and resonant controller $R(s)$.

## 6.3 Controller Design

The first control objectives of this chapter are to: (i) damp the first resonant mode of the PTS in the lateral and longitudinal axes, (ii) increase the bandwidth close to the first resonance frequency of the scanner, and (iii) reduce the cross coupling effect between the axes of the scanner. In order to achieve the above mentioned objectives, this chapter presents a design with a control architecture using two NI damping controllers namely an IRC and a resonant controller.

An IRC is known for its robust performance. The IRC is designed based on the pole-zero interlacing property of resonant systems such as for co-located smart structures with force actuators and position sensors as outlined in [79]. An IRC is a combined integral controller ($\frac{K}{s}$) and a feed thorough term $d$ with the plant as given in Fig. 6.3(a), where $G(s)$ is the transfer function of the plant. The feed through term $d$ is selected to achieve a zero-pole interlacing property instead of pole-zero interlacing property of the system. The value of $d$ is chosen low to achieve large level of damping of the resonant mode of the system. A simplified block diagram of the IRC $C(s)$ with the plant transfer function $G(s)$ is given in Fig. 6.3(b). The transfer function of the IRC $C(s)$ from Fig. 6.3(b) is:

$$C(s) = \frac{K}{s + Kd} \tag{6.4}$$

Although IRCs are known for their robust performance, the bandwidth of the closed-loop system using an IRC is limited due to their low pass nature at high frequencies. The closed-loop system with the IRC of Fig. 6.3(a) starts to roll-off at $Kd + K$. To see this, consider the following transfer function $G(s)$ of a resonant system:

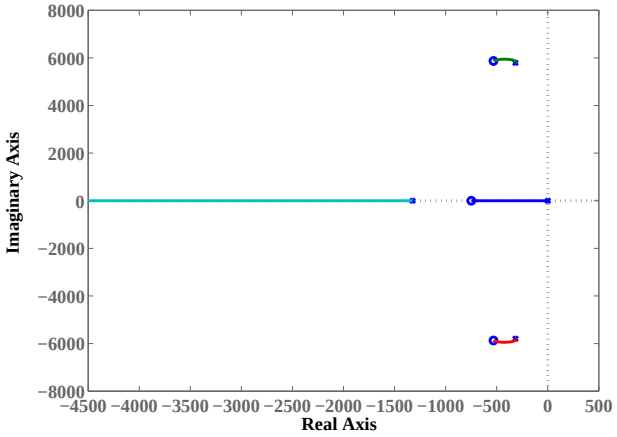


(a)

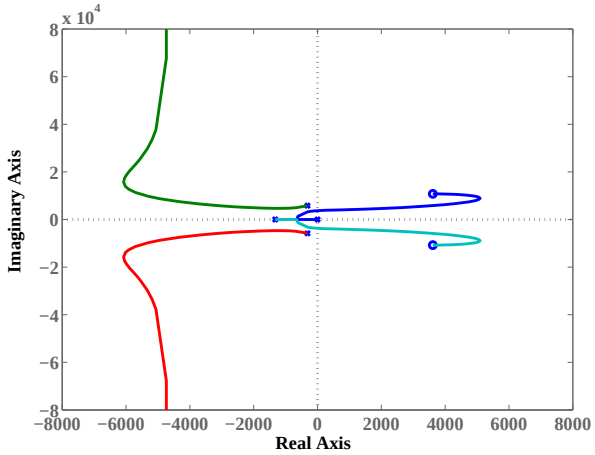


(b)

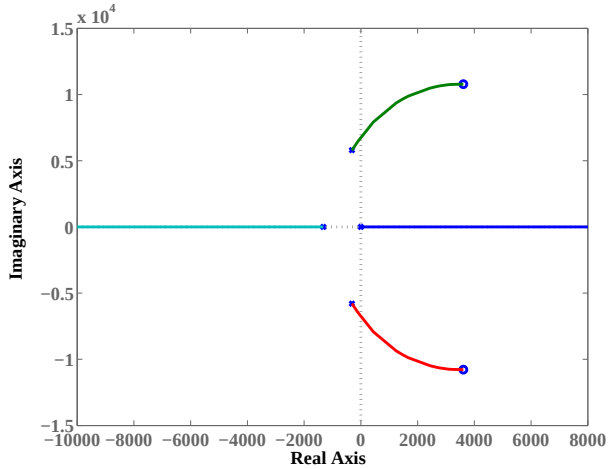


(c)

**Figure 6.5:** Root locus plot of (a) $(G_{xx}(s) + d) * \frac{K}{s}$ with d=1.3 for $K > 0$ and (b) root locus plot of $G_{xx}(s) * \frac{K}{s}$ for $K < 0$, and (c) root locus plot of $G_{xx}(s) * \frac{K}{s}$ for $K > 0$.

$$G(s) = \frac{\omega_p^2}{s^2 + 2\xi\omega_p s + \omega_p^2} \tag{6.5}$$

where $\xi > 0$ and $\omega_p > 0$ are the damping constant and the natural frequency, respectively. Now the closed-loop transfer function for the negative feedback interconnection shown in Fig. 6.3(a) is:

$$S(s) = \frac{C(s)G(s)}{1 + C(s)G(s)} \approx \frac{K}{s + (Kd + K)}. \tag{6.6}$$

The optimal values of the parameters of the IRC obtained from the results of [6] for the system (6.5) are $d = -\frac{4\omega_p^2}{3\omega_p^2}$ and $K = \frac{\sqrt{2}\omega_p}{d}$. The bandwidth of system (6.6) is $Kd + K$, i.e., the system (6.6) rolls-off at $Kd + K$ which is equal to $\frac{\omega_p}{2\sqrt{2}}$. If the first resonance frequency of a resonant structure is 900 Hz, the closed-loop bandwidth that can be achieved by using an IRC is only 318 Hz which is still not high enough for fast nano-positioning.

Since the controller $C(s)$ has a low gain near $\sqrt{2}\omega_p$ due to the integral part we need to have $R(s)$ as given in Fig. 6.4 with $C(s)$ such that it has a high gain near $\sqrt{2}\omega_p$, if we need bandwidth to be close to $\omega_p$. The block $R(s)$ given in Fig. 6.4 is the transfer function of a resonant controller. A resonant controller is a high pass NI controller, i.e., the phase of the transfer function of the resonant controller lies between $[-\pi, 0]$. The transfer function of the resonant controller $R(s)$ is as follows:

$$R(s) = -K_r \frac{s^2 + 2\xi_r\omega_r s}{s^2 + 2\xi_r\omega_r s + \omega_r^2} \tag{6.7}$$

where, $K_r$ is the gain of the resonant controller, $\xi_r$ is the damping constant and $\omega_r$ is the resonance frequency.

In the following, firstly, the design of an IRC and the combination of an IRC with a resonant controller is presented for the SISO case and it is shown that, the combined IRC with the resonant controller achieves a bandwidth three times larger than the bandwidth achieved by the IRC only. Secondly, the design of a combined IRC and resonant controller is presented for the MIMO case to achieve a bandwidth close to the first resonance frequency of the scanner and attenuate the cross coupling effect between the axes of the scanner. The advantage of the MIMO controller over the SISO controller is illustrated by comparing scan images at different scanning rates.

### 6.3.1 Design of IRC and combined IRC with the resonant controller

The design of an IRC is based on the pole-zero interlacing property of the system. The feed through term $d$ shown in Fig. 6.3 is selected to achieve a zero-pole interlacing property for the augmented plant $G(s)+d$. The root locus plot given in Fig. 6.5 shows that the closed-loop system between $G_{xx}(s)+d$ and $\frac{K}{s}$ with $d = 1.3$ for $K > 0$ is always stable whereas the closed-loop system between $G_{xx}(s)$ and $\frac{K}{s}$ for $K < 0$ and $K > 0$ is not always stable. The gain $K$ for the IRC $C(s)$ in Fig. 6.3(b) is selected as $1.85 \times 10^4$ from the root locus plot of Fig. 6.5(a).

The identified closed-loop frequency responses of $G_{xx}(s)$ given in Fig. 6.6 are obtained by implementing the SISO IRC for $K = i \times 1.85 \times 10^4$ where $i$=1 to 5 and $d = 1.3$. The closed-loop system between the IRC and $G_{xx}(s)$ rolls-off at 100 Hz and achieves 7 dB of damping of the first resonant mode of the scanner. The early roll-off strategy of the closed-loop system using the IRC before the open-loop system rolls-off results in a low closed-loop bandwidth which in turns limit the use of IRC for fast nanoscale positioning. The reason for the low closed-loop bandwidth using IRC controller is the low gain of the IRC at high frequencies. In order to provide gain to the IRC at high frequencies, a high pass negative-imaginary controller, namely a resonant controller is included with the IRC to improve the fast nanoscale positioning performance of the IRC.

The resonant controller is chosen such that the closed-loop system starts roll-off at first resonance frequency of the scanner. An optimization is performed to follow a reference transfer function model. A desired closed-loop transfer function is selected according to the aim of the design process, i.e., to achieve a desired bandwidth. The open-loop system $G_{xx}(s)$ starts roll-off after the first resonance frequency at 918 Hz. The aim of the design process is to achieve a closed-loop system which rolls-off at 918 Hz. A closed-loop bandwidth higher than the first resonance frequency of the open-loop system would require high control input energy for which the optimization process might not converge.

The transfer function of the desired closed-loop system for the SISO design is chosen as

$$T(s) = \frac{1}{\tau s + 1} \tag{6.8}$$

where $\tau$ is selected to achieve the desired bandwidth. In the present SISO design $\tau$ is chosen as $\frac{1}{918\text{Hz}}$. A first order model is not a target of the design process, the

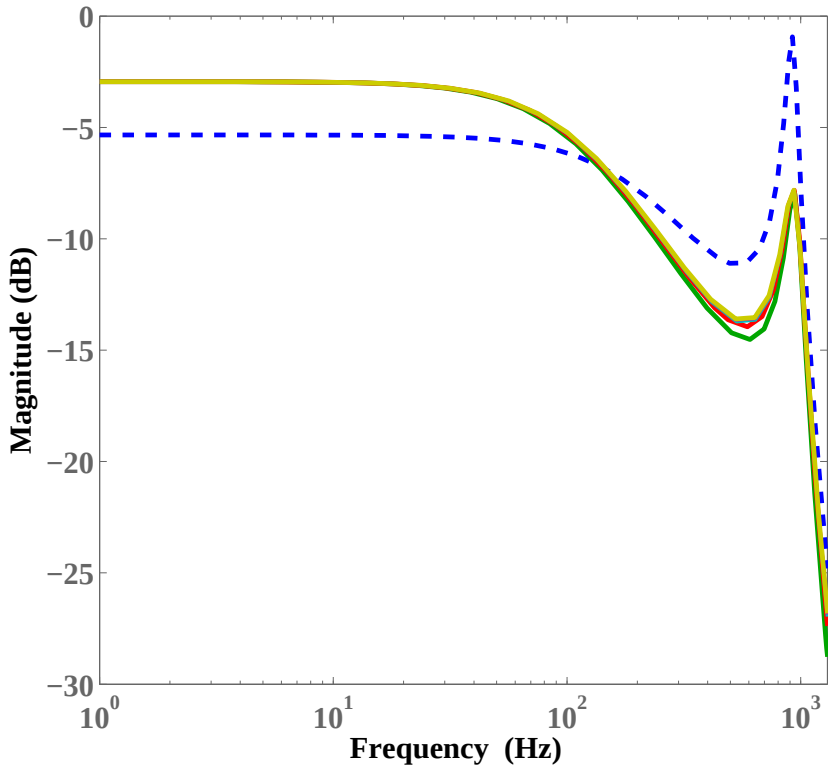


**Figure 6.6:** Comparisons between the identified open- (the dashed line - -) and closed-loop (the solid lines –) frequency responses of $G_{xx}(s)$ using IRC for $K = i \times 1.85 \times 10^4$ where $i$=1 to 5 and $d = 1.3$.

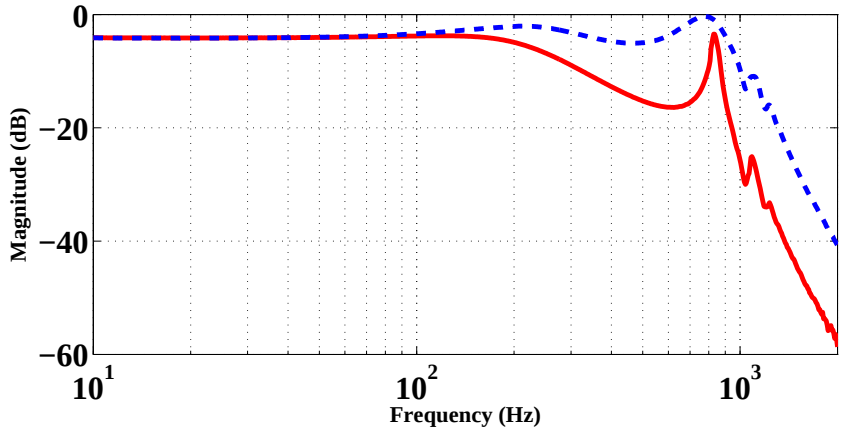


**Figure 6.7:** Comparisons of the measured closed-loop frequency responses obtained by implementing SISO IRC (solid line –) and combined SISO resonant controller and IRC (dashed line - -).

target is to achieve the characteristics of the desired first order model, i.e., we want a closed-loop system with a constant gain to the first resonance frequency of the scanner. Each parameter of the resonant controller is chosen by minimizing the $H_2$ norm of the difference between the desired and the actual closed-loop transfer function. The transfer function of the actual closed-loop system of Fig. 6.4 is

$$T_{cl}(s) = \frac{G(s)(C(s) + R(s))}{1 + G(s)(C(s) + R(s))}.$$

The $H_2$ norm of the error transfer function between the desired and the actual closed-loop transfer function is $\|E(s)\|_2 = \|T(s) - T_{cl}(s)\|_2$. An optimization operation by using fminsearch command from the MATLAB is carried out to obtain the values of the resonant controller parameters by minimizing $\|E(s)\|_2$. A finite value of $\|E(s)\|_2$ guarantees the stability of the closed-loop system [78, 80]. The resultant values of the resonant controller parameters obtained from the optimization process for the X-axis controller design are $K_r = -1.3$, $\xi_r = 0.6$, $\omega_r = 5600$. In the optimization process choosing the initial values of the controller parameters is important for the convergence of the optimization process. In the design the initial values of the resonant controller are selected as $K_r = 1.0$, $\xi_r = .7$, $\omega_r = 6000$.

The performance of the closed-loop system using a SISO combined IRC and resonant controller for the X-axis of the scanner is shown by frequency responses as given in Fig. 6.7. The closed-loop frequency response given in Fig. 6.7 using the proposed combined IRC and resonant controller starts to roll-off at 900 Hz which is three times larger than achieved by the IRC only. This signifies the advantage of the combined IRC and resonant controller over the IRC only for fast nanoscale positioning.

Although the closed-loop system using the combined SISO IRC and resonant controller starts roll-off at 900 Hz, it does not guarantee the reduction of the cross coupling effect between the axes of the scanner. In order to guarantee the reduction of the cross coupling effect between the axes of the scanner in addition to high bandwidth, the following section presents the design of a MIMO controller:

### 6.3.2 Design of the MIMO controller

The transfer functions matrices of the IRC and the resonant controller for MIMO cases are as follows:

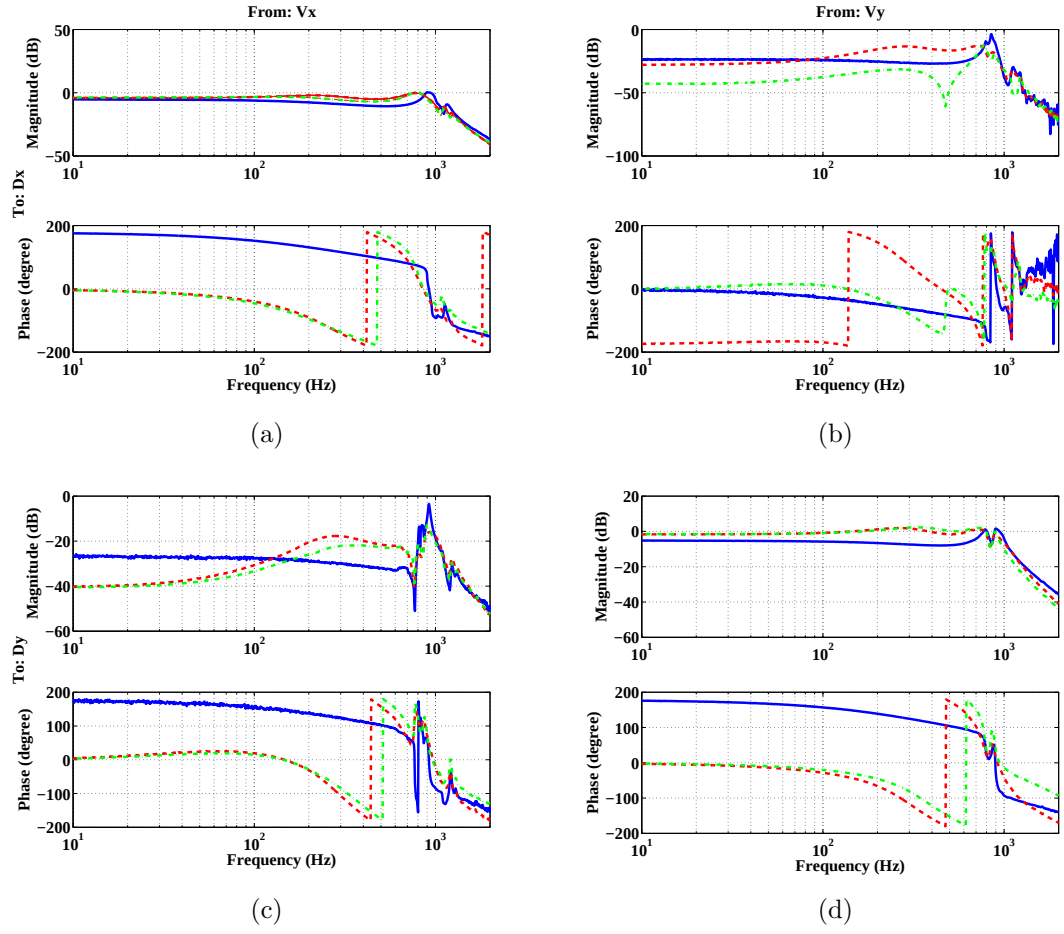


**Figure 6.8:** Comparison of the open-loop and closed-loop frequency response (FR) relating to the inputs $[V_x, V_y]^T$ and the outputs $[D_x, D_y]^T$. The solid line (–) represents the measured open-loop FR and the dashed line (- -) represents closed-loop FR obtained by implementing proposed combined SISO resonant and IRC and the dashed dot line (-.) represents closed-loop FR obtained by implementing proposed combined MIMO resonant and IRC. (a) Frequency response of $G_{xx}(s)$, (b) frequency response of $G_{yx}(s)$, (c) frequency response of $G_{xy}(s)$, and (d) frequency response of $G_{yy}(s)$.

$$C(s) = \frac{K}{s + Kd}\Sigma_{m\times m} \tag{6.9}$$

$$R(s) = -K_r\frac{s(s + 2\xi_r\omega_r)}{s^2 + 2\xi_r\omega_r + \omega_r^2}\Gamma_{m\times m} \tag{6.10}$$

where $\Sigma_{m\times m}$ and $\Gamma_{m\times m}$ are both matrix of order $m \times m$; $m$ is the number of inputs and outputs of the system.

The MIMO controller is designed to achieve a closed-loop system which rolls-off at first resonance frequency of the scanner and to attenuate the cross coupling effect between the axes of the scanner. The transfer function of the desired closed-loop MIMO system is

$$T(s) = \frac{1}{\tau s + 1}\begin{bmatrix} 1 & 0 \\ 0 & 1 \end{bmatrix}.$$

Similar to the SISO design, the value of $\tau$ chosen for the MIMO design is $\frac{1}{918\text{Hz}}$. The bandwidth of the desired MIMO transfer function is 918 Hz and has no cross coupling between the axes. An optimization process as discussed in the design of SISO controller is carried out to obtain the MIMO controller parameter values. The values of the parameters obtained from the optimization process are as follows: $K_r = -0.5$, $\xi_r = 0.602$, $\omega_r = 5890$, $K = -2500$, $Kd = 500$, $\Sigma_{m\times m} = \begin{bmatrix} 0.501 & 0.201 \\ 0.00194 & 1.309 \end{bmatrix}$, $\Gamma_{m\times m} = \begin{bmatrix} 1.986 & 0.005 \\ 0.0049 & 0.512 \end{bmatrix}$.

## 6.4 Performance of the Controllers

A comparison of performance between the SISO and MIMO controller is shown by comparing the measured closed-loop frequency responses and scanned images obtained by using the SISO and MIMO controller. In a similar way as discussed in the design of the combined SISO IRC and resonant controller for the X-axis of the scanner, a combined SISO IRC and resonant controller for the Y-axis is designed and implemented on the scanner. The comparison of the measured closed-loop frequency responses given in Fig. 6.8 shows that the designed SISO and MIMO controller are able to flatten the frequency responses by damping the first resonant mode of the scanner. The closed-loop bandwidths in the X- and Y-axis are increased by 900 Hz both for the SISO and MIMO cases. Although the closed-loop bandwidth achieved

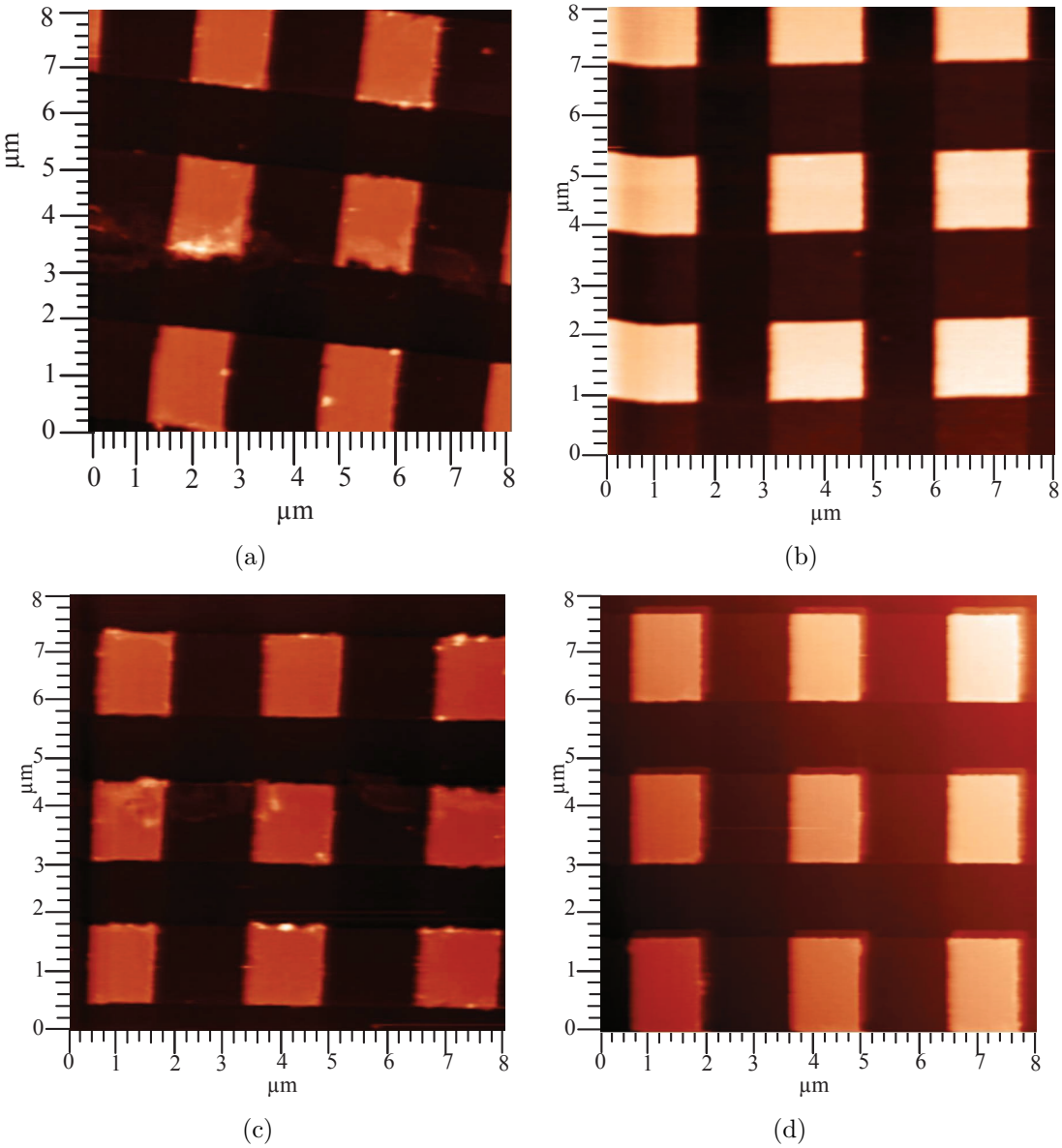


**Figure 6.9:** Scanned images at 15.62 Hz obtained by using (a) open-loop, (b) built-in PI controller of the AFM, (c) proposed combined SISO IRC and resonant controller and (d) proposed combined MIMO IRC and resonant controller.

by the SISO controller and MIMO controller is nearly same, the advantages of using the MIMO controller over the SISO controller can be seen by observing the closed-loop cross coupling effect of Fig. 6.8. The amount of reduction of the cross coupling effect between the axes of the scanner by using the MIMO controller at each frequency is higher except at some frequencies as compared to the SISO controller.

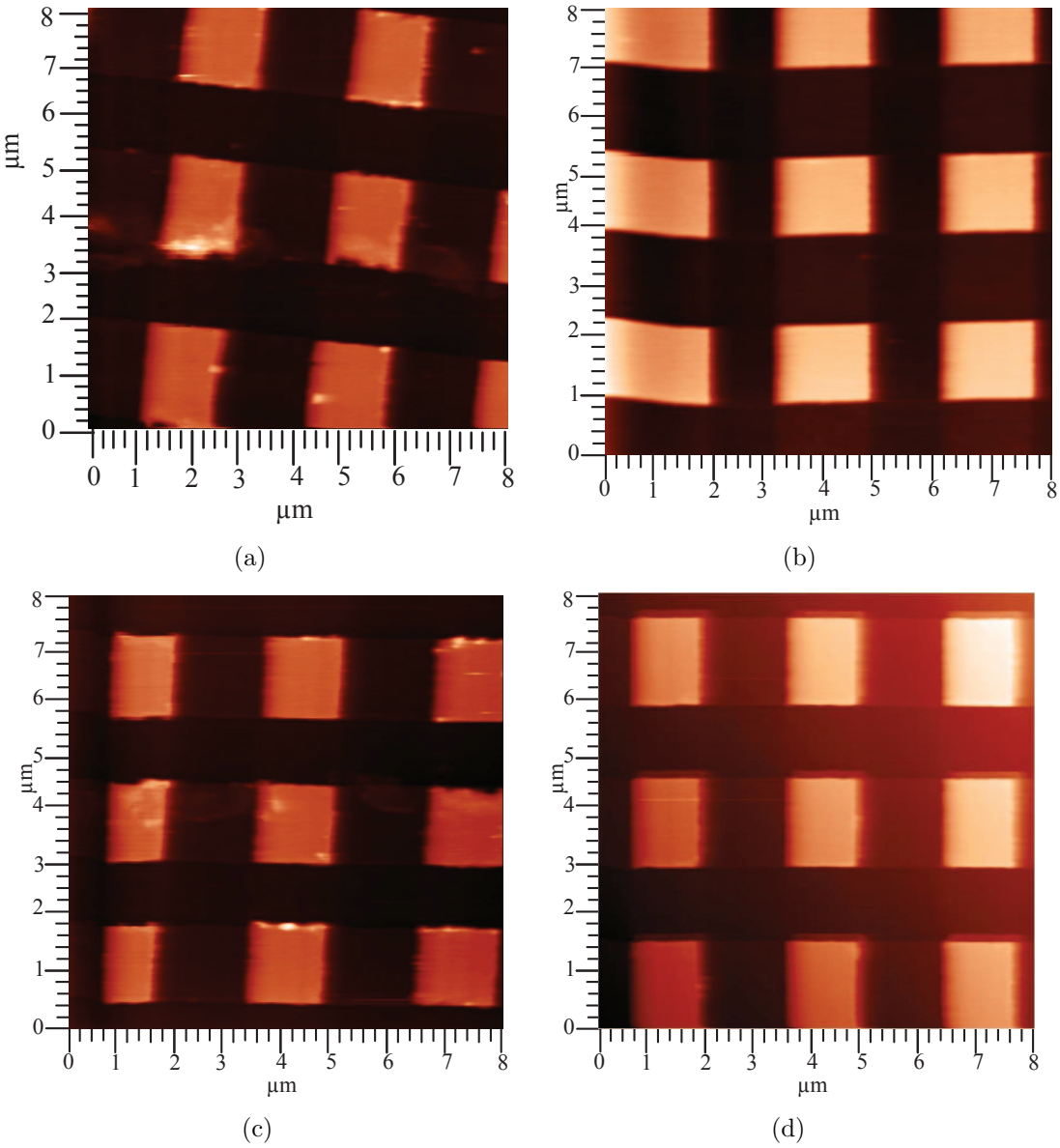


**Figure 6.10:** Scanned images at 31.25 Hz obtained by using (a) open-loop, (b) built-in PI controller of the AFM, (c) proposed combined SISO IRC and resonant controller and (d) proposed combined MIMO IRC and resonant controller.

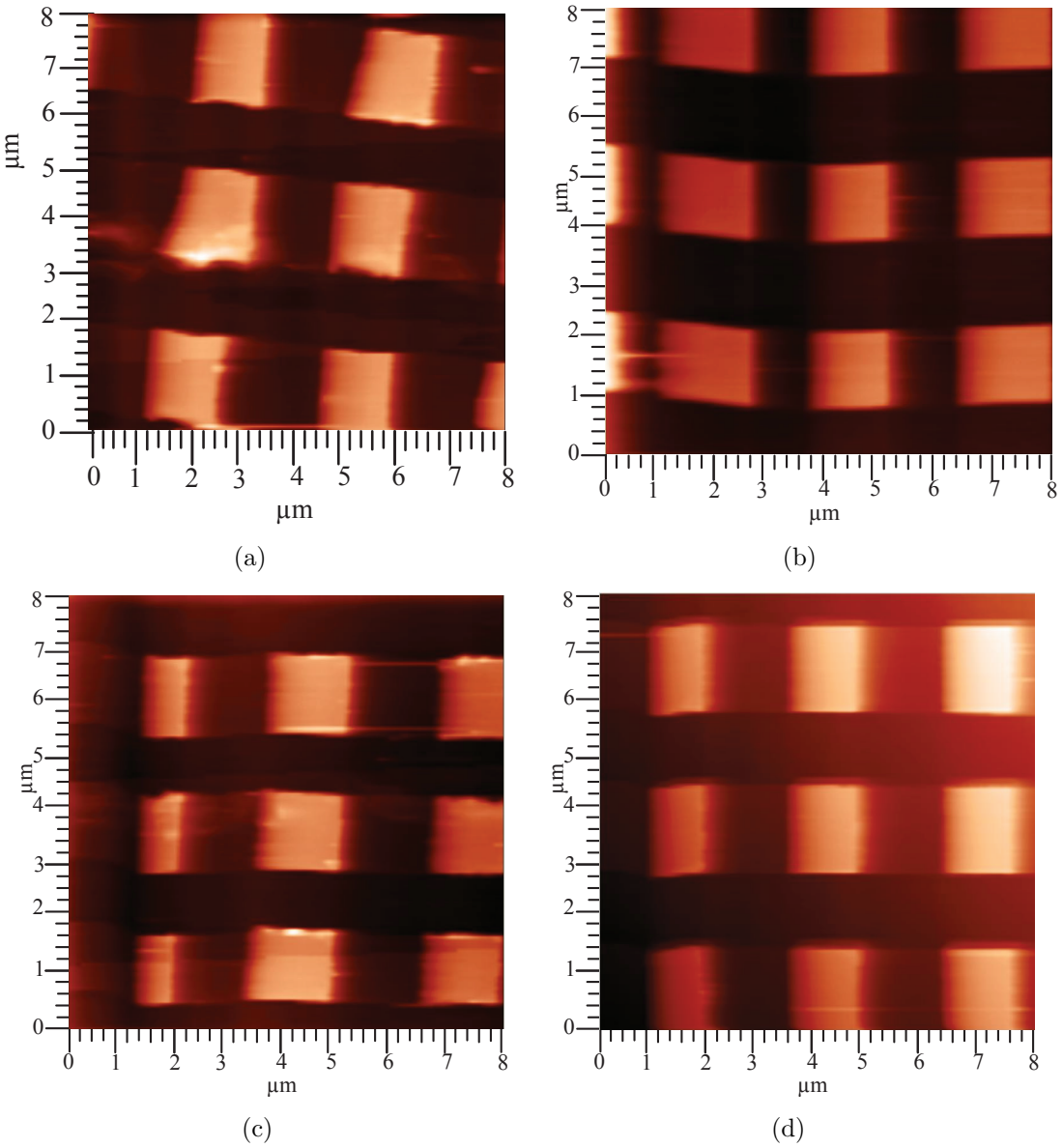


**Figure 6.11:** Scanned images at 62.5 Hz obtained by using (a) open-loop, (b) built-in PI controller of the AFM, (c) proposed combined SISO IRC and resonant controller and (d) proposed combined MIMO IRC and resonant controller.

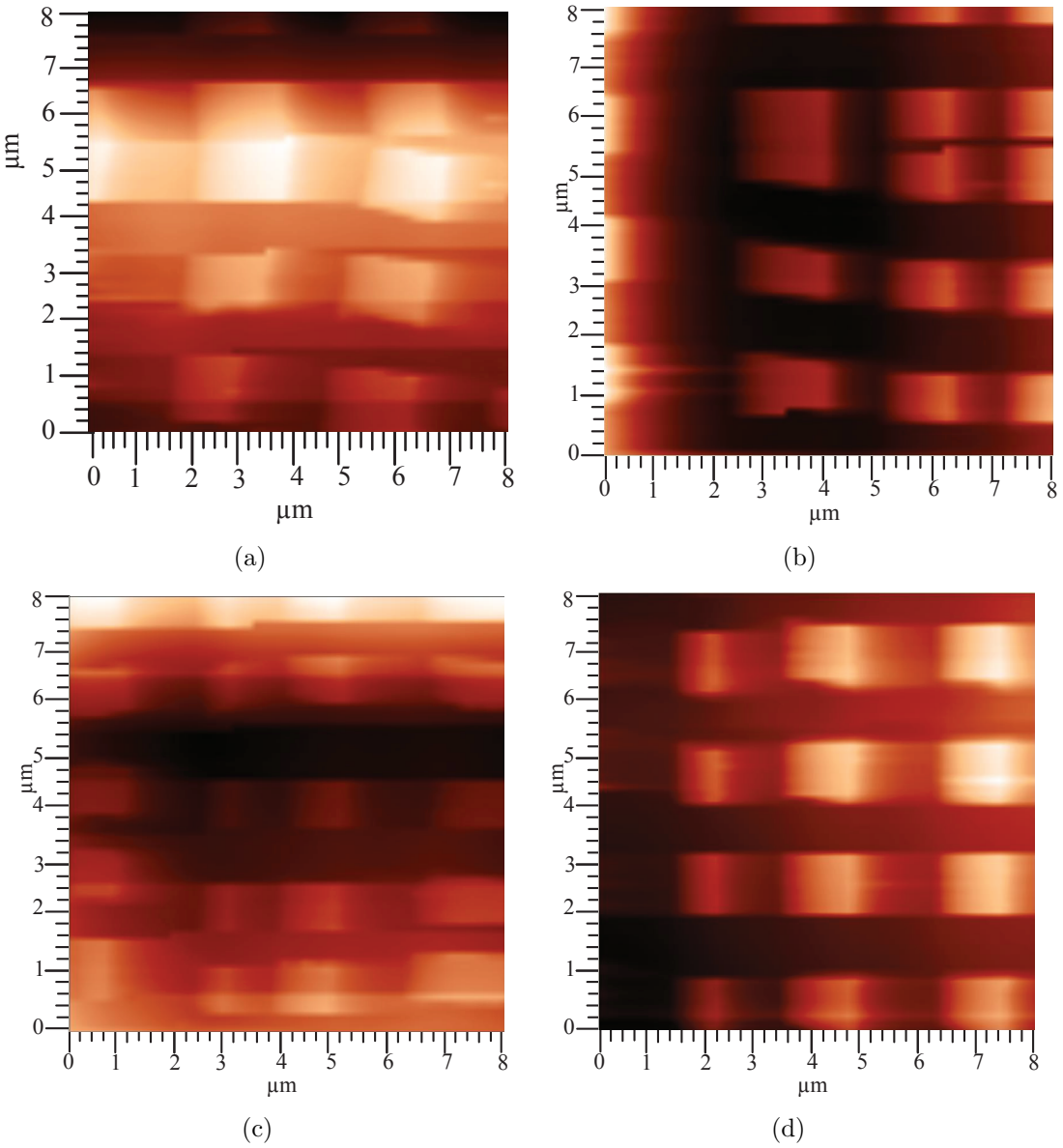


**Figure 6.12:** Scanned images at 125 Hz obtained by using (a) open-loop, (b) built-in PI controller of the AFM, (c) proposed combined SISO IRC and resonant controller and (d) proposed combined MIMO IRC and resonant controller.

The effect of having the large cross coupling effect between the axes of the scanner is shown by comparing scanned images obtained by using open-loop, the in-built PI controller of the AFM, the proposed SISO and MIMO controllers. Experimental images presented in Fig. 6.9 to Fig. 6.12 are obtained by using open-loop, the in-built PI controller of the AFM, the proposed SISO and MIMO controllers at different scanning rates. In the imaging process the grating used for scanning consists of number of squares. Each square has a length of 1.5 µm and the space between successive squares is also 1.5 µm. The imaging using the SISO and MIMO controllers was done for an 8 µm×8 µm area scanning. An 8 µm×8 µm area should consist nine squares.

It can be seen that, the scanned image at 125 Hz (see Fig. 6.12(c)) obtained by using SISO controller has twenty squares for the 8 µm×8 µm area scanning. This is due to the additional cross coupling effect between the scanner, whereas the scanned image at 125 Hz (see Fig. 6.12(d)) obtained by using the MIMO controller has twelve squares for an 8 µm×8 µm area scanning which are due to the low cross coupling effect between the axes of the scanner. This is certainly a great advantage of using MIMO controller as compared to the SISO controller.

Another important observation in the scanned images obtained by using the SISO controller is the rotation of the images. This image rotation also exists in the scanned images obtained in open-loop although the amount of rotation in the scanned images using the SISO controller is lowered as compared to the scanned images obtained by using the open-loop. The closed-loop scanned images obtained by using the MIMO controller have less rotation due to the small cross coupling effect between the axes of the scanner. This shows another advantage of using the MIMO controller over the SISO controller for nanopositioning of the piezoelectric tube scanner. Also, the squares in the scanned images obtained by using the SISO controller are not regular in shape and the squares get small at the edges at high scanning frequency, whereas the squares in the scanned images obtained by using the MIMO controller are more regular in shape as compared to the SISO controller.

The scanned images obtained by using the built-in PI controller of the AFM are less rotated. The squares are not regular in shape, i.e., the blocks are stretched to the left at each scanning frequency. The PI controller is designed to track the reference signal. When the PI controller achieves accurate tracking, that forces the system to decouple. Indeed, the reference signals in the axes of the scanner are

decoupled, which means that the responses due to the reference signals are also decoupled.

It is also desired that the controller performance should be same for all scanning frequencies, i.e, the error between two scanned images for two different scanning frequencies should be minimum. In order to compare the performance between the SISO and MIMO controller in image scanning at low scanning frequencies we show a comparison of error images in Fig. 6.13.

The error images are obtained by subtracting two scanned images. The reference images used for the SISO and MIMO cases are the scanned image obtained at 15.62 Hz. The error image shown in the left of Fig. 6.13(a) is obtained by subtracting Fig. 6.9(c) and 6.10(c) and the error image shown in the right of Fig. 6.13(a) is obtained by subtracting Fig. 6.9(c) and 6.11(c). The error image shown in the left of Fig. 6.13(b) is obtained by subtracting Fig. 6.9(d) and 6.10(d) and the error image shown in the right of Fig. 6.13(b) is obtained by subtracting Fig. 6.9(d) and 6.11(d). The error images given in Fig. 6.13 show that the error images for the SISO case have large error as compared to the MIMO case which signifies the advantage of using MIMO controller over the SISO controller for low scanning speed as well.

Although the controller is designed to roll-off at the first resonance frequency, the performance of the piezoelectric tube scanner is usually limited to one percent of the first resonance frequency of the scanner [6, 15]. This is because the X-axis of the scanner has to track triangular signals. The triangular signal contains all odd harmonics of its fundamental frequency. The images at high scanning rate are distorted due to the high order harmonics of the triangular signal. Also the resonance of the cantilever beam comes into play during the scanning process. Due to the resonant nature of the cantilever beam, the images obtained at high scanning rates are also distorted.

The comparison between the SISO and MIMO controller using the calibration grid for the Z profile of the sample about the center of the X-axis of the AFM images is presented in Fig. 6.14. Though the Z profiles of the sample for the SISO and MIMO cases are nearly same at low scanning speeds, the Z profile of the sample obtained using the SISO controller deteriorates at high scanning speeds as compared to the MIMO controller.

The resonance frequency of the PTS changes with the change in loads on the scanner during the service. The maximum resonance frequency occurs while there

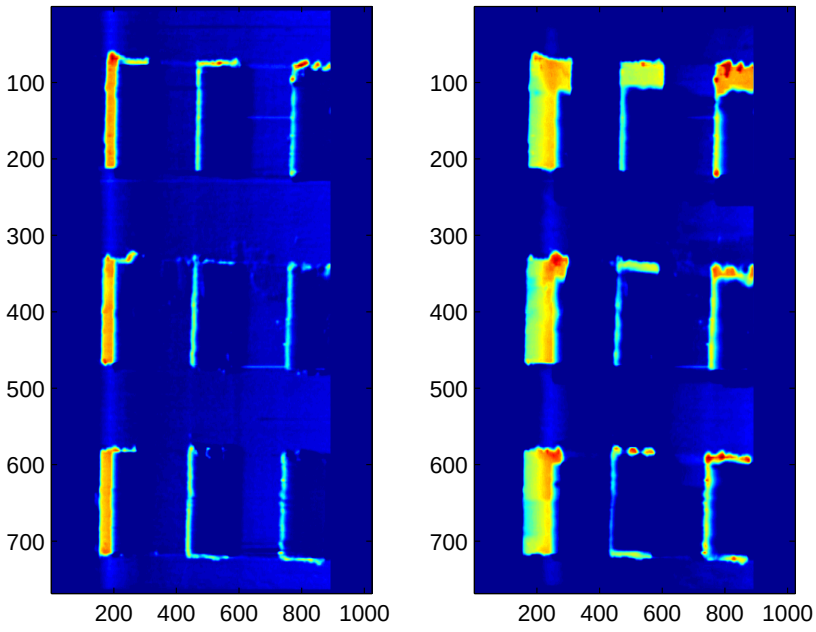


(a)

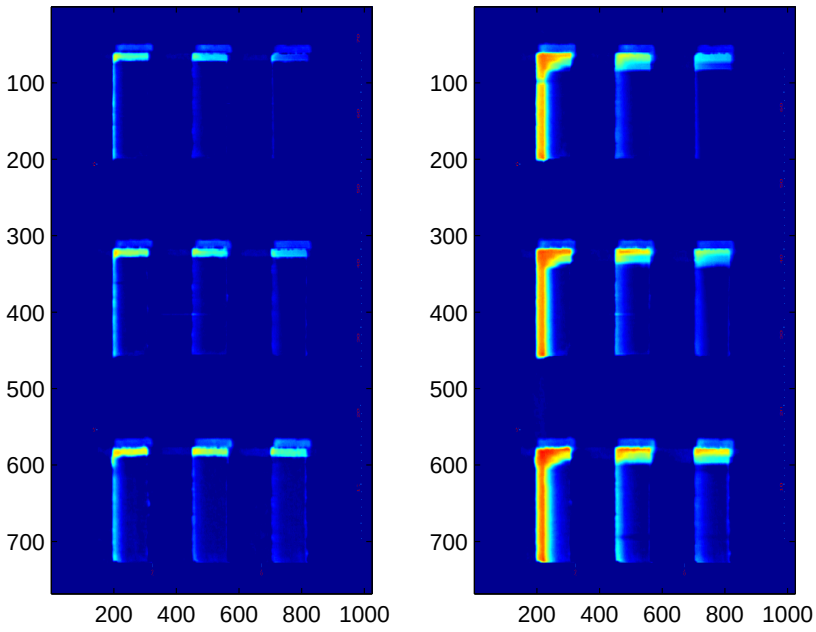


(b)

**Figure 6.13:** Error images obtained by using the combined SISO resonant and IRC (left) and the combined MIMO resonant and IRC (right). Error image (a) (left) obtained by subtracting Fig. 6.9(c) and 6.10(c), (right) obtained by subtracting Fig. 6.9(c) and 6.11(c) and (b) (left) obtained by subtracting Fig. 6.9(d) and 6.10(d), (right) obtained by subtracting Fig. 6.9(d) and 6.11(d)

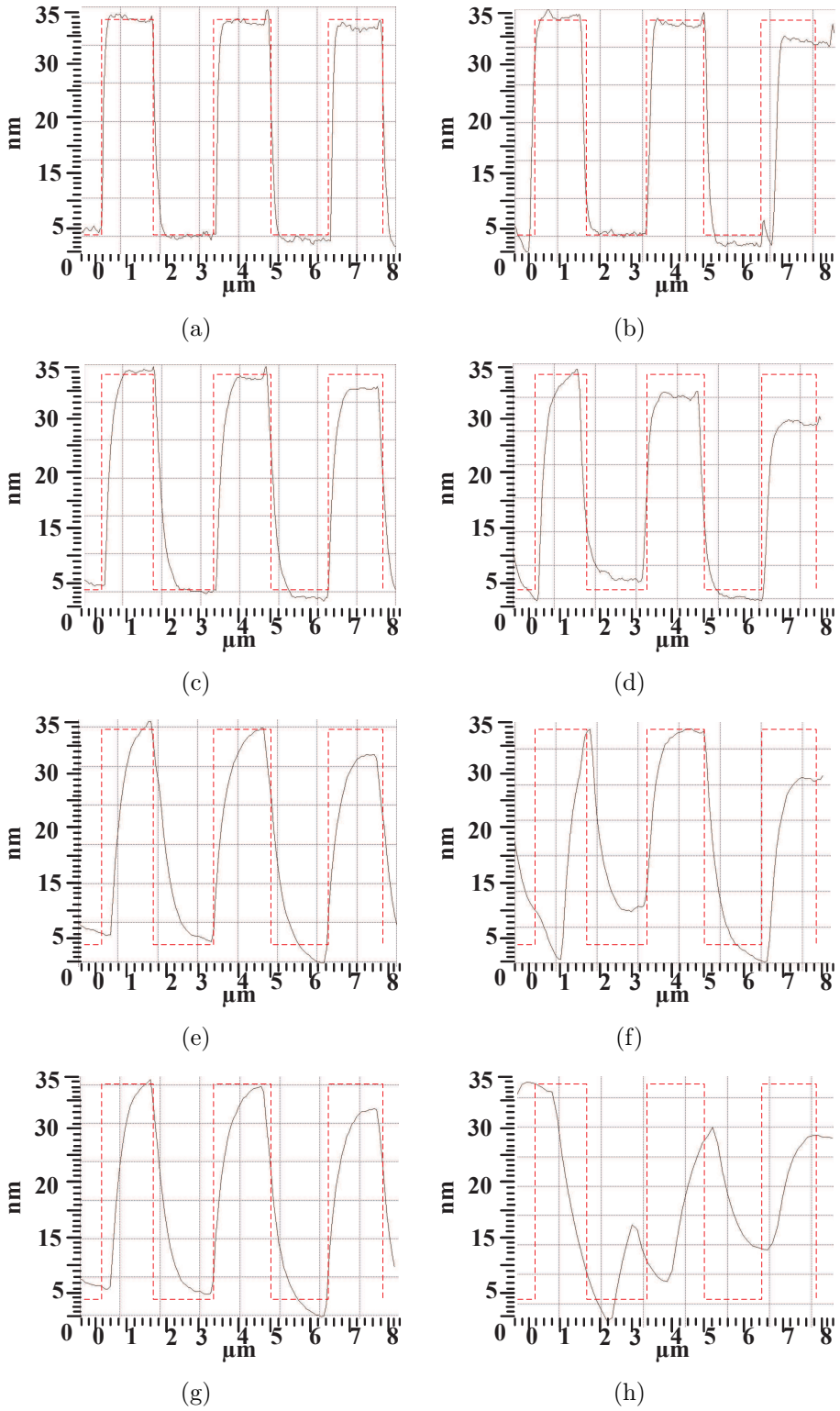


**Figure 6.14:** Cross-section (solid line –) and reference (dash line - -) curves of the AFM images of the Z-direction calibration grid of the sample obtained by using (right) proposed combined SISO resonant and IRC and obtained by using (left) proposed combined MIMO resonant and IRC at (a) 15.62 Hz, (b) 15.62 Hz, (c) 31.25 Hz, (d) 31.25 Hz, (e) 62.50 Hz, (f) 62.50 Hz, (g) 125 Hz, (h) 125 Hz.

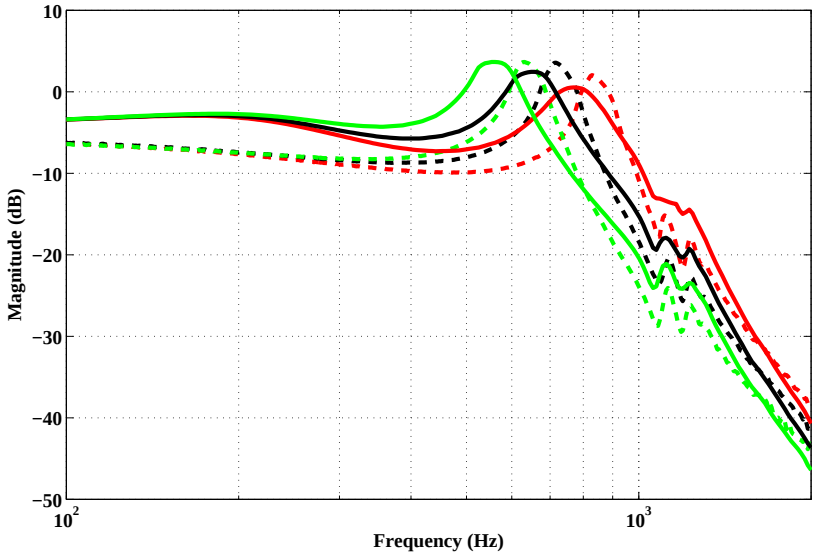


**Figure 6.15:** Open-loop (dashed-line) and closed-loop (solid-line) magnitude frequency response (MFR) from the reference input voltage in the X-axis of the scanner to the measured X sensor voltage for different loads on the scanner. The same color represents the corresponding open- and closed-loop MFR.

is no load on the scanner. Controllers design for high speed nano-positioning must be able to maintain the closed-loop stability against the changes in the resonance frequency. In order to show the performance of the proposed controller in terms of load change on the scanner a comparison of the open- and closed-loop magnitude frequency responses (MFRs) is given in Fig. 6.15 for different loads on the scanner. The closed-loop MFRs are taken by using the MIMO controller in the X-axis of the scanner. As the load on the scanner increases the resonance frequency of the scanner in the X-axis starts moving towards left, i.e., the resonance frequency of the system decreases. In all cases the closed-loop system remain stable and provides a bandwidth near to the first resonance frequency.

## 6.5 Discussion and Advantages of the Proposed Method Over the Existing Approaches

The advantage of the proposed method over existing approaches is given in Table 6.1. Previous approaches designed for high speed nanopositioning of piezo scanner given in Table 6.1 are based on SISO approaches and though the SISO approaches are high bandwidth and robust against the changes in resonance frequency of the plant,

a reduction of the cross coupling effect in the axes of the scanner is not guaranteed using the SISO approach. In this chapter the design of a MIMO controller by combining two negative-imaginary damping controllers is presented which in addition to high bandwidth and robustness against the changes in resonance frequency also guarantees the reduction of the cross coupling effect between the axes of the scanner.

**Table 6.1:** Advantage of the proposed method over the existing approaches

| Control Techniques | Approach | Advantage | Limitation | Year |
|---|---|---|---|---|
| Inversion based feed-forward method [13] | SISO | (i) High bandwidth, (ii) reduce nonlinearities, and (iii) low noise | (i) Sensitive against the changes in resonance frequency | 2007 |
| Damping based controller only [6] | SISO | (i) High bandwidth, (ii) robust against the changes in resonance frequency | (i) Does not guarantee the reduction of the cross coupling effect | 2007 |
| Model based vibration suppression method [81] | SISO | (i) High bandwidth, (ii) reduce the effects of nonlinearities | (i) Depends on accurate system model | 2008 |
| PI controller | SISO | (i) Excellent low frequency tracking performance | (i) Low bandwidth, (ii) sensitive against the changes in resonance frequency | 2009 |
| Damping based controller with integral action [15], [18] | SISO | (i) High bandwidth, (ii) robust against the changes in resonance frequency, and (iii) reduce the effect of nonlinearities at low frequencies | (i) Does not guarantee the reduction of the cross coupling effect, (ii) increase the effect of nonlinearities at high frequencies | 2009-2010 |
| LQG and $H_\infty$ controller [46–50, 82] | SISO | (i) High bandwidth, (ii) robust against the changes in resonance frequency | (i) Does not guarantee the reduction of the cross coupling effect | 2002-2011 |
| Damping based controller with integral action [78] | MIMO | (i) Robust against the changes in resonance frequency, and (ii) reduce the effect of nonlinearities at low frequencies, (iii) guarantee the reduction of the cross coupling effect | (i) Low bandwidth | 2012 |
| **Proposed method** | **SISO and MIMO** | **(i) High bandwidth, (ii) robust against the changes in resonance frequency, and (iii) guarantees the reduction of the cross coupling effect** | **(i) Does not guarantee the tracking of reference signal** | **2014** |

As shown in Table 6.1 although the proposed multivariable IRC and resonant controller reduce cross coupling effect between the axes of the scanner but it does not guarantee the tracking of reference signal. In the following we propose another design of double resonant controller and integral controller for damping, tracking and cross coupling reduction of the PTS.

## 6.6 Double Resonant Controller Design

A block diagram of the closed-loop system using a double resonant controller is presented in Fig. 6.16. Here, $G(s)$ is the transfer function of the plant transfer function, $H_{FB}(s)$ is the transfer function of the feedback resonant controller to damp the resonant mode of the scanner, $C_{FF}(s)$ is the transfer function of the integral controller and $H_{FF}(s)$ is the transfer function of the resonant controller to

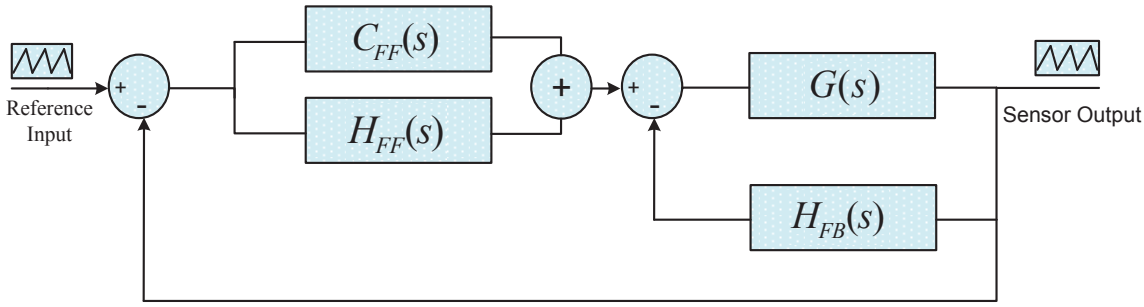


**Figure 6.16:** Block diagram of the closed-loop system for resonant mode damping, tracking and bandwidth improvement.

provide gain to the integral controller at high frequencies. The transfer functions $C_{FF}(s)$, $H_{FB}(s)$ and $H_{FB}(s)$ are as follows:

$$C_{FF}(s) = \frac{k_i}{s} \tag{6.11}$$

$$H_{FB}(s) = k_{\text{fb}} \frac{s^2 + 2\xi_{\text{fb}}\omega_{\text{fb}}s}{s^2 + 2\xi_{\text{fb}}\omega_{\text{fb}}s + \omega_{\text{fb}}^2} \tag{6.12}$$

$$H_{FF}(s) = k_{\text{ff}} \frac{s^2 + 2\xi_{\text{ff}}\omega_{\text{ff}}s}{s^2 + 2\xi_{\text{ff}}\omega_{\text{ff}}s + \omega_{\text{ff}}^2} \tag{6.13}$$

A reference model matching approach as discussed earlier is used to design SISO and MIMO double resonant controller for the PTS. The frequency domain performance of the SISO and MIMO double controller is shown in Fig. 6.17. The MIMO controller is able to reduce cross coupling effect more than the SISO controller at low frequencies while keeping the same closed-loop bandwidth which demonstrates the advantages of the MIMO controller over the SISO controller.

The reason of the large cross coupling effect between the axes of the scanner at intermediate frequency using the SISO double resonant controller is the low gain of the integral controller. However, the MIMO double resonant controller provides a greater reduction of the cross coupling effects between the axes of the scanner at intermediate frequencies as compared to the SISO double resonant controller.

The experimental results are directly related to the theoretical foundation. For example, in the SISO design, the theoretical aim of the design process is to achieve a closed-loop bandwidth near to the first resonance frequency of the scanner and experimentally we have achieved that. Also for the MIMO design, theoretically the

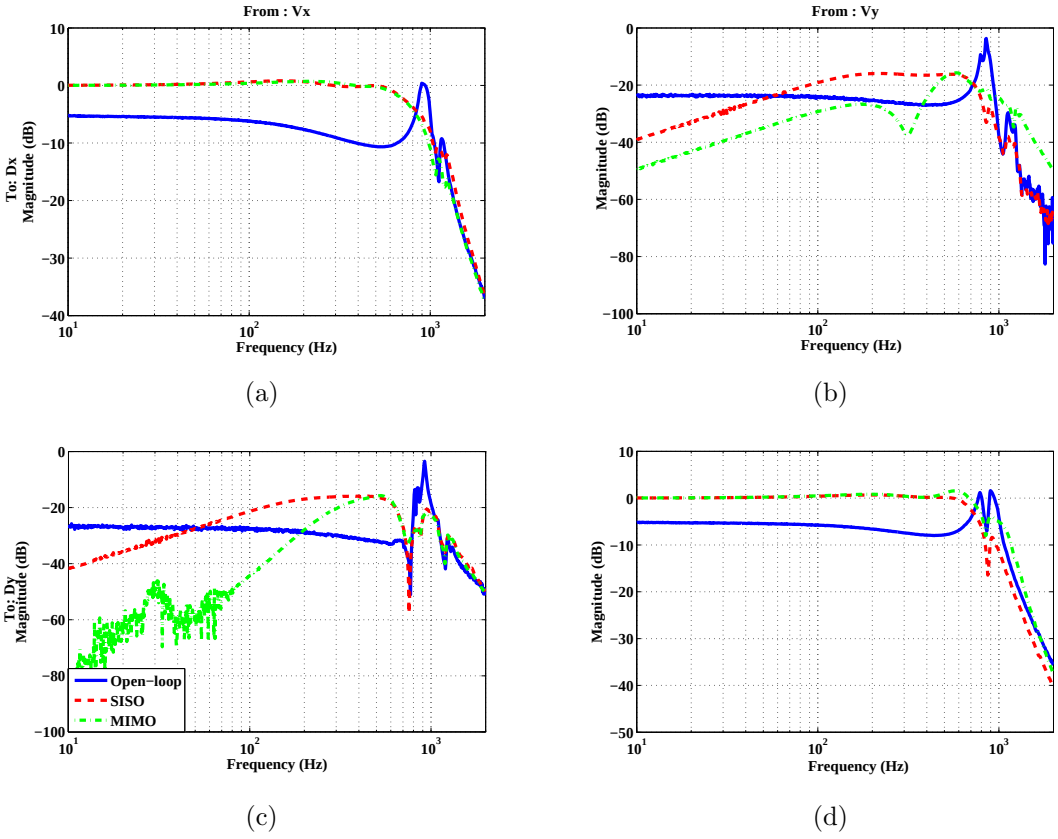


**Figure 6.17:** Comparison of the open- and closed-loop magnitude frequency responses (MFRs) relating the inputs $[V_x, V_y]^T$ and the outputs $[D_x, D_y]^T$ obtained by using the proposed SISO and MIMO double resonant controller of the scheme of Fig. 6.16. The solid line (–) represents the open-loop system MFR, the dashed line (- -) represents closed-loop MFR obtained by using the SISO double resonant controller, and the dashed dot line (-.) represents closed-loop MFR obtained by using the MIMO double resonant controller.

aim of the design process is to achieve a closed-loop bandwidth near to the first resonance frequency and no cross coupling effect between the axes of the scanner. Experimentally for the MIMO design, we have achieved a closed-loop bandwidth near to the first resonance frequency of the scanner and a low cross coupling effect between the axes of the scanner at low frequencies. This shows that the experimental outcome and the theoretical design process are related to each other.

In order to show the performance of the proposed double controller in terms of load changes on the scanner, a comparison of the open- and closed-loop magnitude frequency responses (MFRs) are given in Fig. 6.18. The closed-loop MFRs are taken by using the SISO and MIMO double resonant controller in the X-axis of the scanner. As the load on the scanner increases, the resonance frequency of the scanner in the X-axis starts moving towards left, i.e., the resonance frequency of the system decreases. In all cases the closed-loop system remains stable and provides a bandwidth near to the resonance frequency.

The double resonant controllers designed for the SISO and MIMO cases are implemented on the PTS of an AFM to measure the high speed imaging performance of the AFM. The implementation of the proposed controller is done by replacing the built-in controller of the AFM. The following shows a comparison of performance of the proposed MIMO controller over the SISO controller for imaging:

### 6.6.1 Comparison of performances between the proposed SISO and MIMO double resonant controller

The comparison of the scanned images using SISO and MIMO double resonant controller are presented in Fig. 6.19 and Fig. 6.20. It can be seen that, the scanned image at 125 Hz obtained by using SISO double resonant controller has a total of twenty squares for an 8 µm×8 µm scanning area as shown in Fig. 6.19 (d). This is due to the additional cross coupling effects between the axes of the scanner. The scanned image at 125 Hz shown in Fig. 6.20 (d) obtained by using MIMO double resonant controller has a total of nine squares for an 8 µm×8 µm scanning area which demonstrates the low cross coupling effect between the axes of the scanner.

The comparison of the error images at low frequencies using SISO and MIMO double resonant controller shown in Fig. 6.21 shows that the MIMO double resonant controller performs better as compared to the SISO double resonant controller. Also, a comparison of error signals between the input and output signals using the SISO and the MIMO controller given in Fig.6.22 shows that, the magnitude of the error

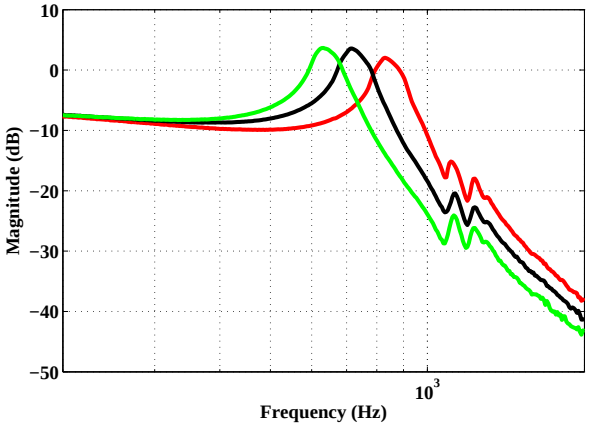


(a)

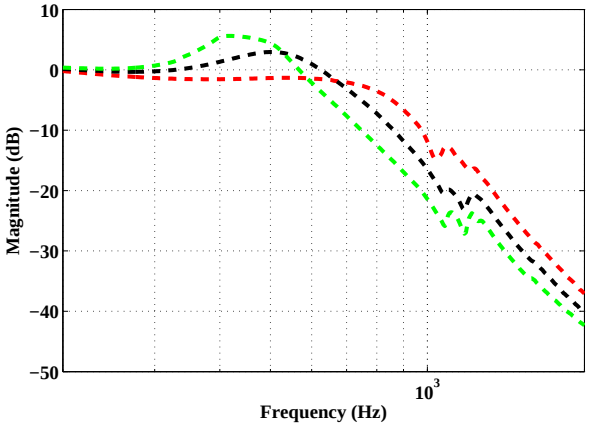


(b)

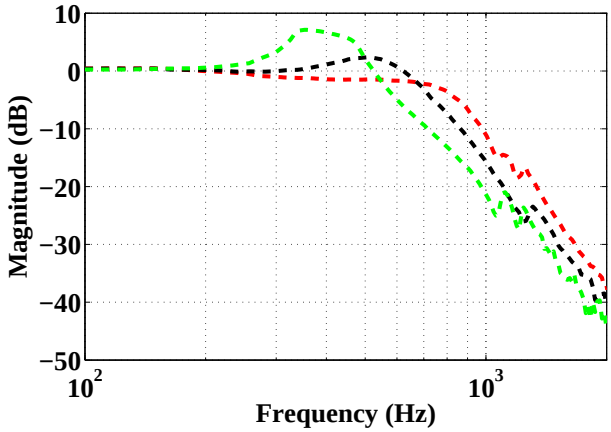


(c)

**Figure 6.18:** Open-loop (solid line) (a) and closed-loop (dashed line) magnitude frequency responses (MFRs) of $G_{xx}(s)$ using SISO (b) and MIMO (c) double resonant controller for different loads on the scanner.

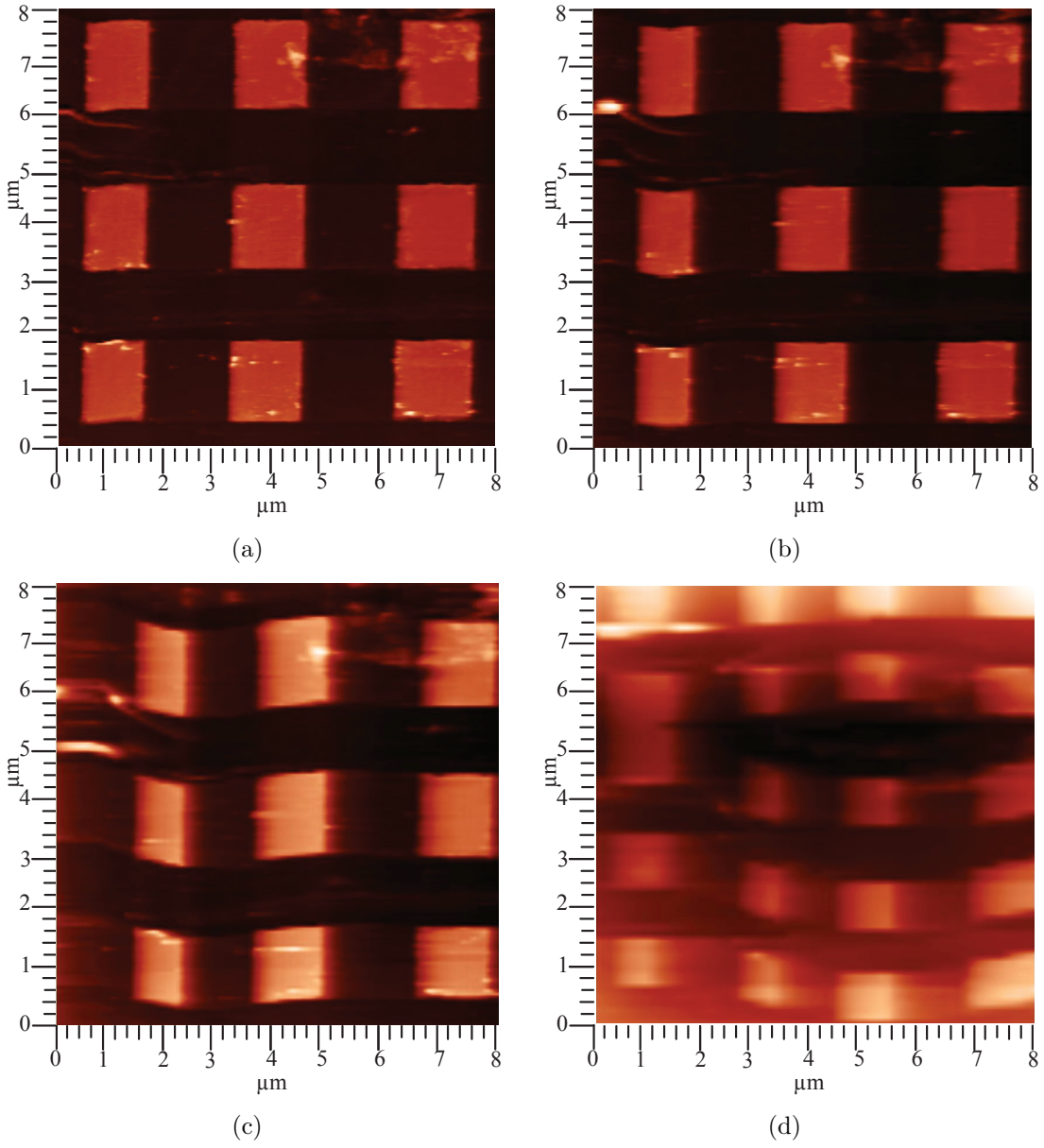


**Figure 6.19:** Scanned images obtained by using the proposed SISO double resonant controller at (a) 15.62 Hz, (b) 31.25 Hz, (c) 62.5 Hz, and (d) 125 Hz for 8 µm×8 µm area scanning.

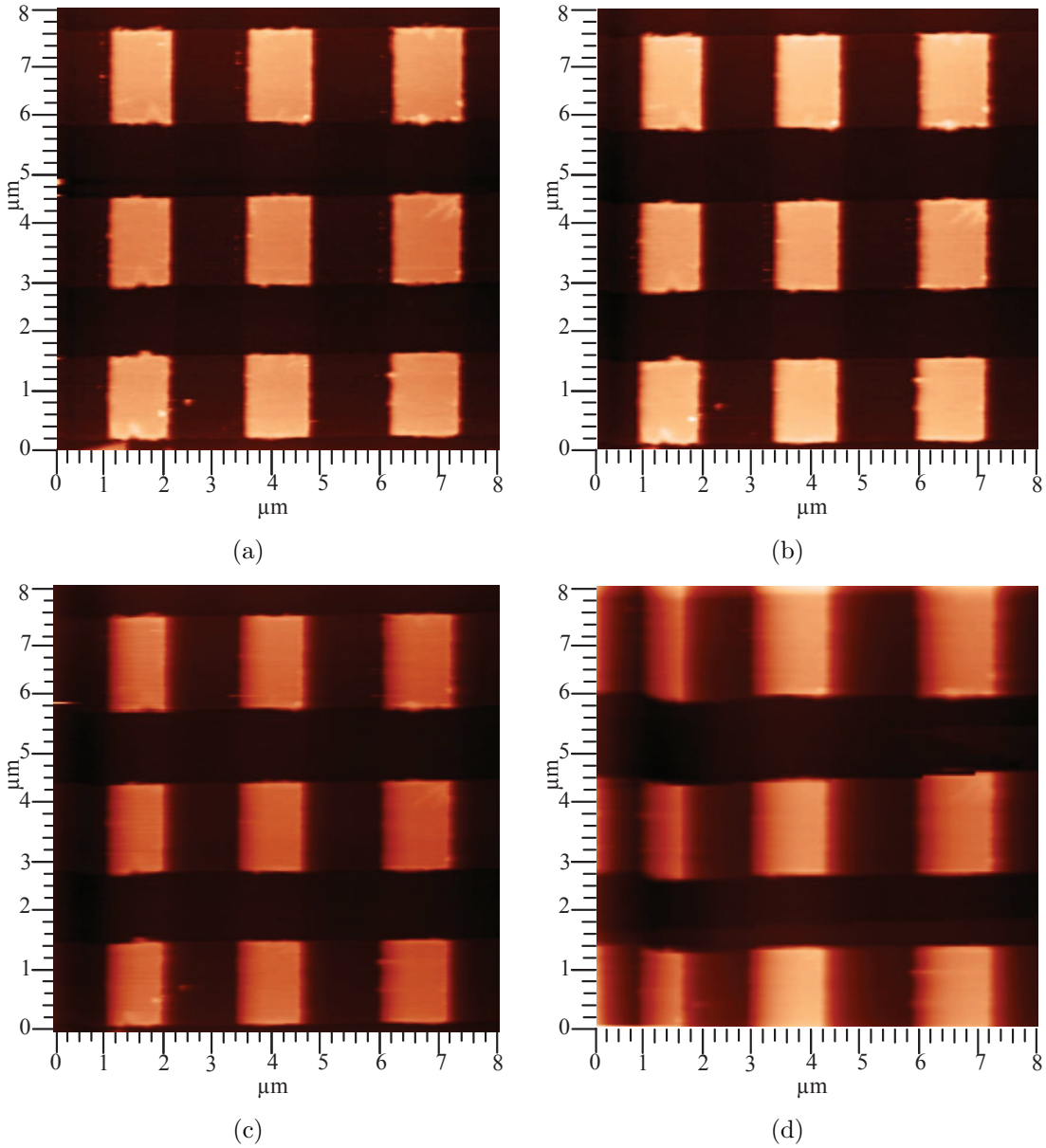


**Figure 6.20:** Scanned images obtained by using the proposed MIMO double resonant controller at (a) 15.62 Hz, (b) 31.25 Hz, (c) 62.5 Hz, and (d) 125 Hz for 8 µm×8 µm area scanning.

signals using the MIMO controller is lowered as compared to the SISO controller at all scanning rates.

## 6.7 Chapter Summary

In this chapter, a damping based controller design framework using negative-imaginary controllers is proposed for a PTS to damp the first resonant mode of the scanner, to improve the tracking performance of the PTS and to attenuate the cross coupling effect. The design of the controller is presented both in SISO and MIMO forms. The controller presented in this chapter is able to achieve a bandwidth near to the first resonance frequency of the scanner with a reduction of cross coupling effects. Compared to an integral controller, the proposed controller is able to achieve five times the bandwidth of the integral controller. Comparisons of the experimental images presented in this chapter obtained by using SISO and MIMO controllers show that the MIMO controller provides two times better improvement in image quality at high scanning rates as compared to the SISO controller.

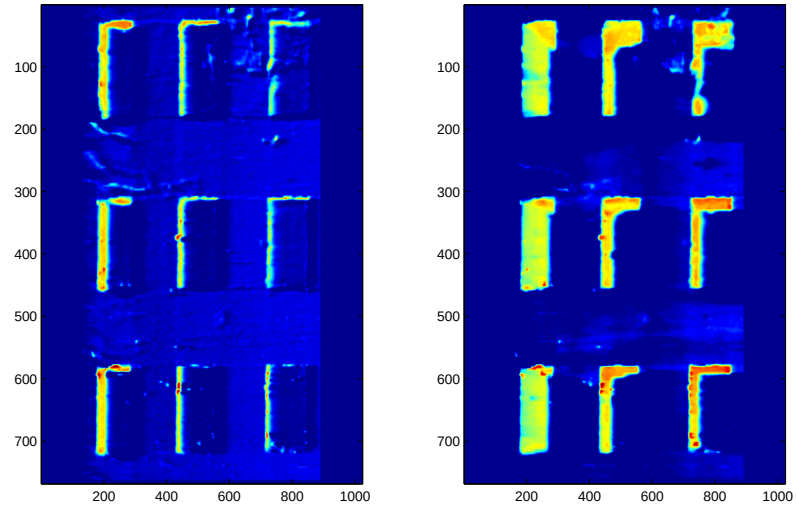


(a)

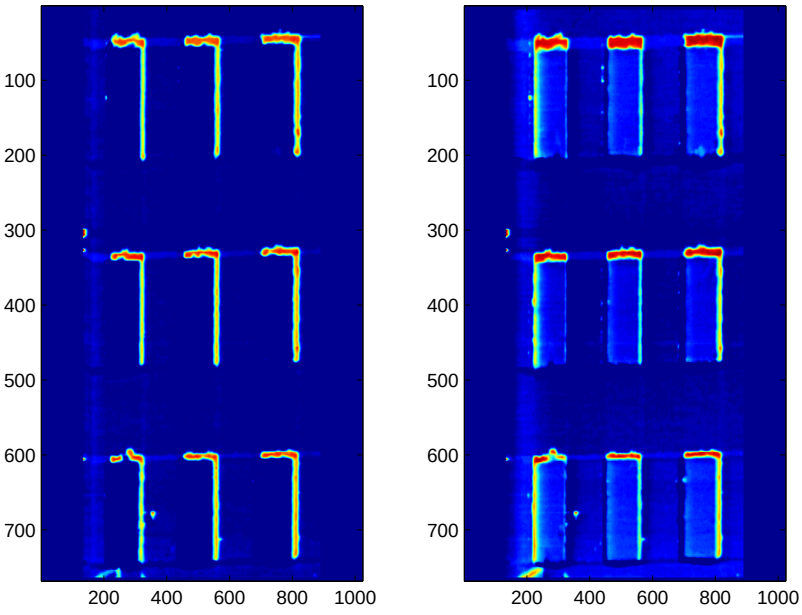


(b)

**Figure 6.21:** Comparison of error images obtained by using SISO and MIMO double resonant controller. (a) (left) obtained by subtracting Fig. 6.19 (a) and 6.19 (b), (right) obtained by subtracting Fig. 6.19 (a) and 6.19 (c); (b) (left) obtained by subtracting Fig. 6.20 (a) and 6.20 (b), (right) obtained by subtracting Fig. 6.20 (a) and 6.20 (c).

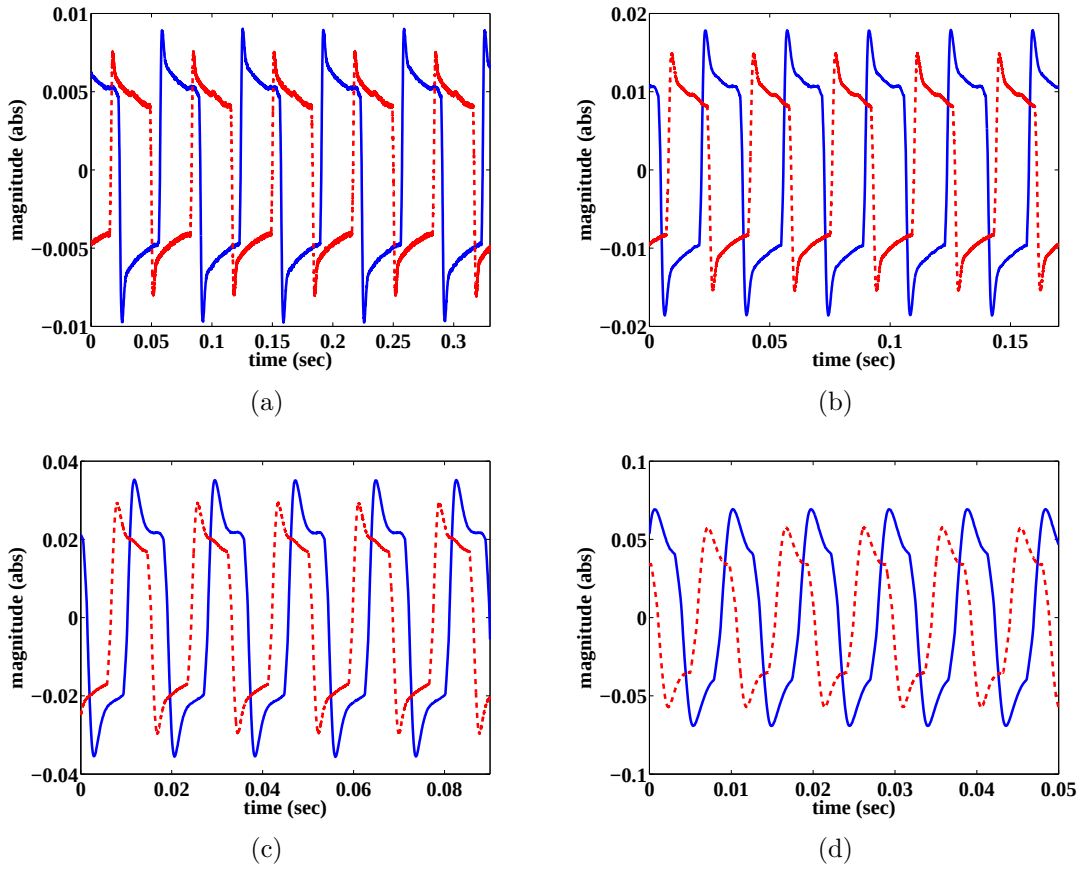


**Figure 6.22:** Comparison of errors signals between input and output signals the using SISO and MIMO double resonant controller for (a) 15.62 Hz, (b) 31.25 Hz, (c) 62.5 Hz, and (d) 125 Hz input signals. The solid line (–) represents the errors obtained using the SISO controller and the dashed line (- -) represents the errors obtained using the MIMO controller. A small phase shift is purposely added to clearly show the plots.

# Chapter 7

# Conclusions

In this thesis, we explored several ways to improve the performance of a PTS for high speed nanopositioning. First we proposed a design of a resonant controller to compensate for the induced vibration of the PTS by damping its resonant modes. The design of the controller was presented based on a mixed NI and small-gain approach. This approach allows us to have a large gain for the controller to achieve a high level of damping of the first resonant mode of the scanner. Next, we designed a passive damping controller for damping the resonant modes of the scanner as the resonant controller is limited due to its high pass nature.

In order to design the passive damping controller for the PTS we proposed an analytical framework which examines the finite-gain stability of the positive feedback interconnection between two linear time-invariant systems where one system has mixed NI, passivity and small-gain properties and the other system has mixed NI, negative-passivity and small-gain properties. The motivation to establish this analytical framework is that the mixed NI and small-gain approach only allow a low gain of the passive damping controller. This results in low level of damping of the resonant mode of the scanner. Finally, the aim of designing a damping controller was concluded by designing the final damping controller namely a minimax LQG controller. The minimax LQG controller was designed with the aim to achieve robust performance for damping the resonant mode of the scanner. Experimental results using minimax LQG controller showed that the controller was able to achieve the desired level of performance.

Secondly the motivation of this thesis also involved improving the tracking performance of the PTS for precision positioning. Here, we designed a robust integral miniamx LQG controller for tracking control of the PTS. The design of the controller was carried out to provide robustness against the unmodelled dynamics of the PTS. The implementation of the integral minimax LQG controller resulted in a high closed-loop bandwidth of 800 Hz. This is four times better than that which can be achieved by using an integral controller.

Finally, multi-variable controllers were designed to achieve damping, tracking and cross coupling reduction in the PTS. Here, first we proposed multi-variable NI controllers for damping and cross coupling reduction of the PTS and then we showed a design of a double resonant controller along with an integral controller for damping, tracking and cross coupling reduction in the PTS. Then experimental results compared between the SISO and MIMO controllers. It was shown that the MIMO controllers performed two times better as compared to the SISO controllers.

Future extensions of this thesis should include the incorporation of the z axis dynamics in the design process. The identification and control of the z axis dynamics is a different control problem. Using a MIMO framework this effect can be incorporated along with the x- and y-axis dynamics.

The performance of the proposed controllers were presented for the raster scanning method. The application of these controllers to other scanning methods such as spiral scanning, cycloid scanning can be a good area of research. The design of the controllers were presented for damping, tracking and cross coupling reduction. The performance of these controllers against the effect of non-linearities will be a good extension of this research.

The analytical framework proposed in this thesis in Chapter 4 can be extended in several ways. The analytical framework was presented for linear time invariant continuous time systems. The first possible extension of this work can be done for non-linear systems. This framework can also be extended for time variant systems. A discrete time version of this framework is also another possible extension.

# References


[1] H. E.Meyer and R. Bennewitz, *Scanning Probe Microscopy.* Heidelberg, Germany: Springer, 2004.

[2] G. Binnig and D. P. E. Smith, "Single-tube three-dimensional scanner for scanning tunneling microscopy," *Review of Scientific Instruments*, vol. 57, no. 8, pp. 1688–1689, 1986.

[3] G. Binnig and H. Rohrer, "Scanning tunneling microscopy from birth to adolescence," *Rev. Mod. Phys.*, vol. 59, pp. 615–625, Jul 1987.

[4] S. K. Das, H. R. Pota, and I. R. Petersen, "Resonant controller for fast atomic force microscopy," in *Proc. Conference on Decision and Control*, Maui, Hawaii, USA, Dec 2012, pp. 2471–2476.

[5] M. Ratnam, B. Bhikkaji, A. Fleming, and S. Moheimani, "PPF control of a piezoelectric tube scanner," in *44th IEEE Conference on Decision and Control and European Control Conference.*, Dec. 2005, pp. 1168 – 1173.

[6] B. Bhikkaji and S. O. Moheimani, "Integral resonant control of a piezoelectric tube actuator for fast nanoscale positioning," *IEEE/ASME Trans. on Mech.*, vol. 13, no. 5, pp. 530–537, 2008.

[7] D. Rugar, H. J. Mamin, P. Guethner, S. E. Lambert, J. E. Stern, I. McFadyen, and T. Yogi, "Magnetic force microscopy: General principles and application to longitudinal recording media," *Journal of Applied Physics*, vol. 68, no. 3, pp. 1169–1183, 1990.

[8] G. Schitter, "Advanced mechanical design and control methods for atomic force microscopy in real-time," in *Proc. American Control Conf.*, pp. 3503–3508, Jul, 2007.

[9] D. Croft and S. Devasia, "Vibration compensation for high speed scanning tunneling microscopy," *Review of Scientific Instruments*, vol. 70, no. 12, pp. 4600–4605, 1999.

[10] S. Wadikhaye, Y. Yong, and S. Moheimani, "Design of a compact serial-kinematic scanner for high-speed atomic force microscopy: An analytical approach," *IET Micro Nano Letters*, vol. 7, no. 4, pp. 309–313, 2012.

[11] Y. Li and Q. Xu, "Design and analysis of a totally decoupled flexure-based xy parallel micromanipulator," *IEEE Transactions on Robotics*, vol. 25, no. 3, pp.

645–657, 2009.

[12] N. Chuang, I. R. Petersen, and H. R. Pota, "Robust $H^\infty$ control in fast atomic force microscopy," in *Proc. American Control Conf. (ACC)*, pp. 2258–2265, 2011.

[13] K. K. Leang and S. Devasia, "Feedback-linearized inverse feedforward for creep, hysteresis, and vibration compensation in afm piezoactuators," *IEEE Transactions on Control Systems Technology*, vol. 15, no. 5, pp. 927–935, 2007.

[14] N. Kodera, H. Yamashita, and T. Ando, "Active damping of the scanner for high-speed atomic force microscopy," *Rev. of Sci. Instrum.*, vol. 76, no. 5, pp. 053 708(1)–053 708(5), 2005.

[15] A. J. Fleming, S. S. Aphale, and S. O. R. Moheimani, "A new method for robust damping and tracking control of scanning probe microscope positioning stages," *IEEE Trans. on Nanotechnology*, vol. 9, no. 4, pp. 438–448, 2010.

[16] D. Croft, G. Shedd, and S. Devasia, "Creep, hysteresis, and vibration compensation for piezoactuators: atomic force microscopy application," in *Proc. American Control Conf*, pp. 2123–2128, 2000.

[17] O. M. El Rifai and K. Youcef-Toumi, "Coupling in piezoelectric tube scanners used in scanning probe microscopes," in *Proc. American Control Conf the 2001*, vol. 4, 2001, pp. 3251–3255.

[18] I. A. Mahmood and S. O. R. Moheimani, "Making a commercial atomic force microscope more accurate and faster using positive position feedback control," *Rev. of Sci. Instrum.*, vol. 80, no. 6, pp. 063 705(1)–063 705(8), 2009.

[19] G. Binnig, C. F. Quate, and C. Gerber, "Atomic force microscope," *Phys. Rev. Lett.*, vol. 56, pp. 930–933, Mar 1986.

[20] ——, "Atomic force microscope 2D and 3D," *Phys. Rev. Lett.*, vol. 56, pp. 930–933, Mar 1986.

[21] J. E. Stern, B. Terris, H. Mamin, and D. Rugar, "Deposition and imaging of localized charge on insulator surfaces using a force microscope," *Applied Physics Letters*, vol. 53, no. 26, pp. 2717–2719, Dec 1988.

[22] V. Scherer, W. Arnold, and B. Bhushan, "Lateral force microscopy using acoustic friction force microscopy," *Surface and Interface Analysis*, vol. 27, no. 5-6, pp. 578–587, 1999.

[23] S. Amelio, A. V. Goldade, U. Rabe, V. Scherer, and B. Bhushan, "Measurments of mechanical propoerties of ultra-thin diamond-like carbon coatings using atomic force acoustic microscopy," *Thin Solid Films*, vol. 392, pp. 75–84, 2001.

[24] C. Schoenenberger and S. Alvarado, "Understanding magnetic force microscopy," *Z. Phys.*, vol. 80, no. 3, pp. 373–383, 1990.

[25] U. Hartmann, "Magnetic force microscopy," *Annu. Rev. Mater. Sci.*, vol. 29, pp. 53–87, 1999.

[26] E. Betzig, P. L. Finn, and J. S. Weiner, "Combined shear force and near-field scanning optical microscopy," *Applied Physics Letters*, vol. 60, no. 20, pp. 2484–2486, 1992.

[27] P. F. Barbara, D. M. Adams, and D. B. O'Connor, "Characterization of organic thin film materials with near-field scanning optical microscopy," *Annual Review of Materials Science*, vol. 29, pp. 433–469, 1999.

[28] A. Majumdar, "Scanning thermal microscopy," *Annual Review of Materials Science*, vol. 29, pp. 505–585, 1999.

[29] C. Williams and H. Wickramasinghe, "Scanning thermal profiler," *Applied Physics Letters*, vol. 49, no. 23, pp. 1587–1589, Dec 1986.

[30] O. E. Husser, D. H. Craston, and A. J. Bard, "Scanning eletromechanical microscopy-high resolution deposition and etching materials," *J. Electrochem. Soc.*, vol. 136, pp. 3222–3229, 1989.

[31] W. Melitz, J. Shen, A. C. Kummel, and S. Lee, "Kelvin probe force microscopy and its application," *Surface Science Reports*, vol. 66, no. 1, pp. 1 – 27, 2011.

[32] D. DeVecchio and B. Bhushan, "Use of a nanoscale kelvin probe for detecting wear precursors," *Review of Scientific Instruments*, vol. 69, no. 10, pp. 3618–3624, 1998.

[33] C. C. Williams and H. K. Wickramasinghe, "Microscopy of chemical-potential variations on an atomic scale," *Nature*, vol. 344, pp. 317–319, 1990.

[34] C. Prater, P. Hansma, M. Tortonese, and C. Quate, "Improved scanning ion-conductance microscope using microfabricated probes," *Review of Scientific Instruments*, vol. 62, no. 11, pp. 2634–2638, Nov 1991.

[35] P. Hansma, B. Drake, O. Marti, S. Gould, and C. Prater, "The scanning ion-conductance microscope," *Science*, vol. 243, no. 4891, pp. 641–643, 1989.

[36] D. T. Lee, J. P. Pelz, and B. Bhushan, "Instrumentation for direct, low frequency scanning capacitance microscopy, and analysis of position dependent stray capacitance," *Rev. Sci. Instrum.*, vol. 73, pp. 3523–3533, 2002.

[37] J. Matey and J. Blanc, "Scanning capacitance microscopy," *Annu. Rev. Mater. Sci.*, vol. 57, pp. 1437–1444, 1999.

[38] B. Bhikkaji, M. Ratnam, A. J. Fleming, and S. O. R. Moheimani, "High-performance control of piezoelectric tube scanners," *IEEE Trans. on Control Sys. Tech.*, vol. 15, no. 5, pp. 853–866, 2007.

[39] H. Adriaens, W. De Koning, and R. Banning, "Modeling piezoelectric actuators," *IEEE/ASME Transactions on Mechatronics*, vol. 5, no. 4, pp. 331–341, Dec 2000.

[40] K. Kuhnen and P. Krejci, "Compensation of complex hysteresis and creep effects in piezoelectrically actuated systems - a new preisach modeling approach," *IEEE Transactions on Automatic Control*, vol. 54, no. 3, pp. 537–550, March 2009.

[41] M. Al Janaideh, S. Rakheja, and C.-Y. Su, "An analytical generalized prandtl-ishlinskii model inversion for hysteresis compensation in micropositioning control," *IEEE/ASME Transactions on Mechatronics*, vol. 16, no. 4, pp. 734–744, Aug 2011.

[42] F. Ikhouane, V. Manosa, and J. Rodellar, "Dynamic properties of the hysteretic bouc-wen model," *Systems & Control Letters*, vol. 56, no. 3, pp. 197 – 205, 2007.

[43] W. T. Ang, F. Garmon, P. Khosla, and C. Riviere, "Modeling rate-dependent hysteresis in piezoelectric actuators," in *Proceedings International Conference on Intelligent Robots and Systems*, vol. 2, Oct 2003, pp. 1975–1980 vol.2.

[44] Y. K. Yong, K. Liu, and S. Moheimani, "Reducing cross-coupling in a compliant xy nanopositioner for fast and accurate raster scanning," *IEEE Transactions on Control Systems Technology*, vol. 18, no. 5, pp. 1172 –1179, sept. 2010.

[45] S. Patra and A. Lanzon, "Stability analysis of interconnected systems with "mixed" negative-imaginary and small-gain properties," *IEEE Transactions on Automatic Control*, vol. 56, no. 6, pp. 1395 –1400, June 2011.

[46] S. Salapaka, A. Sebastian, J. P. Cleveland, and M. V. Salapaka, "High bandwidth nano-positioner: A robust control approach," *Review of Scientific Instruments*, vol. 73, no. 9, pp. 3232–3241, 2002.

[47] G. Schitter, A. Stemmer, and F. Allgower, "Robust 2 dof-control of a piezoelectric tube scanner for high speed atomic force microscopy," in *Proc. American Control Conf the 2003*, vol. 5, 2003, pp. 3720–3725.

[48] G. Schitter, P. Menold, H. F. Knapp, F. Allgwer, and A. Stemmer, "High performance feedback for fast scanning atomic force microscopes," *Rev. Sci. Instrum.*, no. 8, p. 72, June 2001.

[49] A. Sebastian, M. V. Salapaka, and J. P. Cleveland, "Robust control approach to atomic force microscopy," in *Proc. 42nd IEEE Conf. Decision and Control*, vol. 4, 2003, pp. 3443–3444.

[50] A. Sebastian and S. M. Salapaka, "Design methodologies for robust nanopositioning," *IEEE Trans. on Control Sys. Tech.*, vol. 13, no. 6, pp. 868–876, 2005.

[51] A. J. Fleming, "Nanopositioning system with force feedback for high-performance tracking and vibration control," *IEEE/ASME Transactions on Mechatronics*, vol. 15, no. 3, pp. 433–447, 2010.

[52] A. A. Eielsen and A. J. Fleming, "Passive shunt damping of a piezoelectric stack nanopositioner," in *American Control Conference*, Marriott Waterfront, Baltimore, MD, USA, June 2010.

[53] H. Pota, S. Reza Moheimani, and M. Smith, "Resonant controller for smart structures," *Smart Materials and Structures*, vol. 11, pp. 1–8, 2002.

[54] H. Pota, S. R. Moheimani, and M. Smith, "Resonant controllers for flexible structures," in *Proc. Conf. on Decision and Control*, vol. 1, pp. 631–636, 1999.

[55] A. Lanzon and I. R. Petersen, "Stability robustness of a feedback interconnection of systems with negative imaginary frequency response," *IEEE Transactions on Automatic Control*, vol. 53, no. 4, pp. 1042–1046, 2008.

[56] I. Petersen and A. Lanzon, "Feedback control of negative-imaginary systems," *IEEE Control Sys. Mag.*, vol. 30, no. 5, pp. 54 –72, oct. 2010.

[57] C. A. Desoer and M. Vidyasagar, *Feedback Systems: Input-Output Properties*. New York: Academic Press, 1975.

[58] M. Green and D. J. N. Limebeer, *Linear Robust Control*, E. Cliffs, Ed. NJ: Prentice-Hall, 1996.

[59] L. Ljung, "Prediction error estimation methods," *Circuits, Systems and Signal Processing*, vol. 21, no. 3, pp. 11–21, 2002.

[60] ——, *System Identification Toolbox for use with MATLAB*. The Math Works,

Inc, Natick, MA, 2000.

[61] M. J. Balas, "Direct velocity feedback control of large space structures," *Journal of Guidance and Control*, vol. 2, no. 3, pp. 252–253, 1979.

[62] I. R. Petersen, "Negative imaginary systems theory in the robust control of highly resonant flexible structures," in *Australian Control Conference*, Melbourne, Australia, November 2011, pp. 1–6.

[63] M. Mabrok, A. Kallapur, I. Petersen, and A. Lanzon, "Spectral conditions for negative imaginary systems with applications to nanopositioning," *IEEE/ASME Transactions on Mechatronics*, no. 99, pp. 1–9, 2013.

[64] W. M. Griggs, B. D. Anderson, and R. N. Shorten, "A test for determining systems with "mixed" small gain and passivity properties," *Systems & Control Letters*, vol. 60, no. 7, pp. 479 – 485, 2011.

[65] B. Nobale and J. W. Daniel, *Applied Linear Algebra*, N. Englewood Cliffs, Ed. Prentice Hall, 1988.

[66] K. Zhou, J. C. Doyle, and K. Glover, *Robust and Optimal Control*, N. Upper Saddle River, Ed. Prentica Hall, 1996.

[67] D. Halim and S. O. R. Moheimani, "Experimental implementation of spatial H infinity control on a piezoelectric-laminate beam," *IEEE/ASME Transactions on Mechatronics*, vol. 7, no. 3, pp. 346–356, 2002.

[68] ——, "Spatial resonant control of flexible structures-application to a piezoelectric laminate beam," *IEEE Transactions on Control Systems Technology*, vol. 9, pp. 37–53, Jan 2001.

[69] F. Paganini and E. Feron, "LMI methods for robust $H_2$ analysis: a survey with comparisons: a survey with comparisons," *Recent Advances on LMI Methods in Control SIAM*, pp. 129–151, 1999.

[70] T. Tuma, A. Sebastian, W. Haberle, J. Lygeros, and A. Pantazi, "Impulsive control for fast nanopositioning," *Nanotechnology*, vol. 23, no. 18, p. 135501, 2012.

[71] A. Sebastian and S. O. R. Moheimani, "Signal transformation approach to fast nanopositioning," *Review of Scientific Instruments*, vol. 80, p. 076101, 2009.

[72] V. Ugrinovskii and I. Petersen, "Finite horizon minimax optimal control of stochastic partially observed time varying uncertain systems," in *Proceedings of the Conference on Decision and Control*, vol. 4, 1997, pp. 3938–3943 vol.4.

[73] ——, "Finite horizon minimax optimal control of stochastic partially observed

time varying uncertain systems." *Mathematics of Control, Signals and Systems*, vol. 12, pp. 1–23, 1999.

[74] I. Petersen, M. James, and P. Dupuis, "Minimax optimal control of stochastic uncertain systems with relative entropy constraints," *IEEE Transactions on Automatic Control*, vol. 45, no. 3, pp. 398–412, 2000.

[75] I. R. Petersen, V. Ugrinovski, and A. V. Savkin, *Robust control design using H-$\infty$ methods*. London: Springer, 2000.

[76] A. V. Savkin and I. R. Petersen, "Minimax optimal control of uncertain systems with structured uncertainty," *International Journal of Robust and Nonlinear Control*, vol. 5, pp. 119–137, 1995.

[77] T. McKelvey, H. Akay, and L. Ljung, "Subspace-based identification of infinite-dimensional multivariable systems from frequency-response data," *Automatica*, vol. 32, no. 6, pp. 885 – 902, 1996.

[78] S. K. Das, H. R. Pota, and I. R. Petersen, "Multi-variable resonant controller for fast atomic force microscopy," in *Proc. Australian Control Conference*, Sydney, Australia, Nov 2012, pp. 448–453.

[79] S. S. Aphale, A. J. Fleming, and S. O. R. Moheimani, "Integral resonant control of collocated smart structures," *Smart Materials and Structures*, vol. 16, no. 2, pp. 439–446, January 2007.

[80] M. Green and D. J. N. Limebeer, *Linear Robust Control*. Prentice-Hall, 1995.

[81] J. Maess, A. J. Fleming, and F. Allgower, "Model-based vibration suppression in piezoelectric tube scanners through induced voltage feedback," in *American Control Conference, 2008*, June, pp. 2022–2027.

[82] N. Chuang, I. Petersen, and H. Pota, "Robust $H^\infty$ control in fast atomic force microscopy," in *American Control Conference (ACC)*, Jul 2011, pp. 2258 –2265.